Theory of heat transfer in nanostructures : microscopic and phenomenological approaches

Jonathan Wise

To cite this version:

Jonathan Wise. Theory of heat transfer in nanostructures : microscopic and phenomenological approaches. Quantum Physics [quant-ph]. Université Grenoble Alpes [2020-..], 2021. English. NNT : 2021GRALY090 . tel-03736234

HAL Id: tel-03736234
https://theses.hal.science/tel-03736234v1

Submitted on 22 Jul 2022

Université Grenoble Alpes

THÈSE

Pour obtenir le grade de

DOCTEUR DE L'UNIVERSITÉ GRENOBLE ALPES

Spécialité : Physique de la Matière Condensée et du Rayonnement

Arrêtée ministériel : 25 mai 2016

Présentée par

Jonathan WISE

Thèse dirigée par **Denis BASKO**
et codirigéee par **Wolfgang BELZIG**

préparée au sein du **Laboratoire de Physique et de Modélisation des Milieux Condensés**
dans **l'École Doctorale Physique**

Théorie du transfert de chaleur dans des nanostructures : approches microscopique et phénoménologique

Theory of heat transfer in nanostructures: microscopic and phenomenological approaches

Thèse soutenue publiquement le **20 décembre 2021**,
devant le jury composé de :

Jean-Jacques GREFFET
Laboratoire Charles Fabry, Institute d'Optique (CNRS / Université Paris-Saclay), Rapporteur

Jukka PEKOLA
Aalto University, Rapporteur

Gianluigi CATELANI
Forschungszentrum Jülich, Examinateur

Hervé COURTOIS
Institut Néel (CNRS / Université Grenoble Alpes), Examinateur

Bart VAN TIGGELEN
Laboratoire de Physique et de Modélisation des Milieux Condensés, Président

Denis BASKO
Laboratoire de Physique et de Modélisation des Milieux Condensés, Directeur de thèse

Wolfgang BELZIG
University of Konstanz, Co-Directeur de thèse

Acknowledgements

First of all I would like to thank all members of the jury for devoting their time, whether it be in person or virtually, both in advance of and during my thesis defense. Thank you to Denis Basko for being an immensely dedicated thesis supervisor who has taught me a great deal, both about the details of theoretical condensed matter physics but also about the general development of a rigorous line of inquiry in scientific research. Thanks also to Wolfgang Belzig and Jukka Pekola for useful and broadening discussions during research visits.

I have enjoyed my time at LPMMC, and would like to thank all its members past and present, permanent and non-permanent. Thank you to the 'old guard' – Étienne, Nico, Davide, Piero and Joan – for passing on a special lab dynamic, and to those with whom we made it our own – Amit, Giovanni, Anastasia, Kostas, Ale, Carlo, Olmo and Théotime. Thanks for sharing the office life (even if we weren't as 'present' as we expected for a significant portion...) but also for the beers, meals, hikes, runs, Chartreuses, wedding (!), musical chairs, karaoke sessions and volleyball games. Thanks also to the 'newcomers' – Côme, Romuald, Aniket, Francesco (x2), Victor and Guillaume. Merci à Nathan, avec qui j'ai apprécié de collaborer et de papoter. Grand merci à Camille et Habiba à LPMMC, et à Angélique et Florence à l'Institut Néel, dont la chaleureuse présence a toujours été appréciée dans la gestion des questions administratives.

Thank you to the QuESTech gang, for the fun trips and interesting discussions. Thanks in particular to the Grenoble guys, David and Danial, and to my fellow theorist Danilo for welcoming me in Konstanz. A special word for Erika, who helped make administrative matters run smoothly and without whom the project would not have been the same.

J'aimerais remercier également ma coloc, Maëlys, qui m'a aidé énormément dès mon arrivée en France – même avec mes valises le premier jour. C'était un plaisir de partager l'appart avec toi. Merci infiniment pour tous les cours de français autour des repas, sans lesquels je n'arriverais pas à écrire ces mots. Un grand merci à la nature dont nous avons de la chance d'être entouré ici à Grenoble, la vie en montagne est splendide.

I would like to thank my parents, whose truly constant love, support and encouragement I appreciate so much and would not be here without. To my brother, Dan, who was and in some sense remains the original role model, thank you for always being there and offering helpful advice. And to my grandad, Papa, for being a constant source of inspiration.

Thank you Em for the loving mixture of support, motivation and distraction.

Contents

General introduction

Energy, in its multitude of forms and manifestations, is at the heart of describing almost all physical, chemical and biological phenomena. Whether it be the orbits of the planets, the stability of an atom, or the function of a cell – energy is always at play. If we wish to describe these phenomena as scientists, we need therefore to understand how energy behaves. In addition to satisfying general curiosity about the world, an understanding of energy is also practically advantageous. As humans we have learned how to exploit energy by directing it in its useful form, work, towards a host of tasks that make life easier or enhanced in some way. Moreover, we have developed the tools of thermodynamics to extract additional energy to that which our bodies can provide from other sources, resulting in inventions such as the combustion engine that eventually led to the industrial revolution.

Both the natural and human-induced phenomena described above rely on the transfer and transformation of energy, from one place or object to another, from one form to another. The energy transfer may take place via a variety of mechanisms, or channels, and in this work we focus on one channel: radiation. The random motion of electric charges in a body establish electromagnetic fields that may be felt and do work on charges in another body, resulting in the transfer of energy. Unlike other channels of heat transfer where some physical contact between bodies is required, radiation may occur between bodies that are spatially separated. In this case, the energy under discussion is often referred to as heat since the transfer is typically irreversible. A full classical description of the electromagnetic fields was given in the 19th century by Maxwell's equations. However, the full ramifications of this description on how energy may be exchanged via radiation are still being uncovered. At large length scales the transfer is governed by emission and absorption of real propagating photons. However, at small length scales, known as the near field, evanescent waves may carry heat which corresponds to photon tunnelling. This near-field radiative heat transfer is the primary focus of this thesis.

The difference between the heat transfer between objects via radiation in the near field vs the far field is due to the differing character of the relevant electromagnetic waves. In the far field, we have the typical picture of radiation corresponding to travelling waves whose speed and attenuation is determined by the medium through which they move. On the other hand, in the near field the radiation is dominated by evanescent waves, those which are pinned to the material surface but leak out a small distance into the region of space surrounding the object. The evanescent waves typically result in a significant enhancement of the heat current between bodies in the near field. However, exactly how the radiative heat transfer behaves is dependent on more than just the length scale. In particular, it is depends on how the materials interact with the electromagnetic field, which may itself depend on the temperature. For materials like metals, such descriptions enter into the rich field of condensed matter physics. Despite the principles of radiative heat transfer as outlined above being well-understood, the existence of a plethora of different materials as well as geometries and temperature scales that are practically relevant and realisable means that there is still much to investigate.

On a general level, there is renewed interest in theoretical descriptions of the near field due to the advancement of modern nanofabrication methods. The continued miniaturisation of electronics calls for a proper theoretical understanding of heat flow at small scales. For example, it is essential to know how heat shall be dissipated in a nanometric transistor since overheating or heat leakage may cause device instability or failure. On the other hand, there are prospects for how near-field radiative heat transfer may be advantageous, for example in near-field thermophotovoltaics, a novel form of electricity production that involves placing a photovoltaic cell within the near field of a hot emitter. The recent advent of two, one and even zero-dimensional material bodies, whose emissive and absorptive behaviour may radically differ due to the reduced dimensionality, also increases the pertinence of these otherwise merely academic studies.

In this work we address some of the important questions regarding radiative heat transfer. For example, does confinement in one or several dimensions impede the motion of the relevant charges altering how they may excite and be excited by electromagnetic fields? Does the nonlocality in the material response play a role? Do the charges exhibit collective excitations, and if so how are they damped? How does the radiative heat current between bodies fluctuate, and what can we learn by measuring these fluctuations? Rather than performing material-specific studies whose conclusions may be only narrowly applicable, we attempt to use general models that encode widely-present physical phenomena. In addition, we perform analytical calculations under various approximation schemes, allowing a clear view of what impact the physical ingredients of the model may have. We focus on a two-dimensional geometry, due to its newfound relevance thanks to novel 2D materials but also due to the ease of calculations with respect to the three-dimensional case. Our theoretical studies could in principle be used to inform future experimental investigations or even aid novel device design.

The structure of the thesis is as follows: In Ch. 1 we provide a brief history of the attempts to describe radiative heat transfer, going on to give the foundations of the primary framework used today, fluctuational electrodynamics. We discuss the general implications of fluctuational electrodynamics regarding the origins of near-field behaviours in evanescent waves. Finally we provide a brief review of modern advances in near-field radiative heat transfer, which we use to highlight the motivations to address the specific problems covered in this thesis. In Ch. 2 we perform a general study in the framework of fluctuational electrodynamics of the average heat current exchanged by two-dimensional parallel metallic layers. By performing an analytical calculation of all the contributions to the radiative heat current including both traveling and evanescent waves of both electric and magnetic fields, we seek to quantify when the electromagnetic interaction is dominated by electrostatics, known as the Coulomb limit. Having clarified this issue, in Ch. 3 we work in the Coulomb limit and explore the roles played by material disorder, spatial dispersion in the material response and collective electron density excitations known as surface plasmons. Motivated by the possibility of a dominant resonant heat transfer channel via surface plasmons, we investigate in Ch. 4 the fluctuations of the radiative heat current in the same system of two-dimensional layers, but also in a simpler zero-dimensional one modelled by an electric circuit. We attempt to see what information is accessible via the noise, since this could provide an experimental probe of the importance of resonant modes. Details of some of the longer calculations are included in Appendices A–D.

Publications related to this thesis

- J. L. Wise, D. M. Basko, and F. W. J. Hekking, Role of disorder in plasmon-assisted near-field heat transfer between two-dimensional metals, *Phys. Rev. B*, **101**, 205411, May 2020
  doi:10.1103/PhysRevB.101.205411
- J. L. Wise and D. M. Basko, Near field versus far field in radiative heat transfer between two-dimensional metals, *Phys. Rev. B*, **103**, 165423, Apr 2021
  doi:10.1103/PhysRevB.103.165423

Introduction générale

L'énergie, dans sa multitude de formes et de manifestations, est au cœur de la description de presque tous les phénomènes physiques, chimiques et biologiques. Qu'il s'agisse des orbites des planètes, de la stabilité d'un atome ou de la fonction d'une cellule, l'énergie est toujours en jeu. Si nous voulons décrire ces phénomènes en tant que scientifiques, nous devons donc comprendre comment l'énergie se comporte. En plus de satisfaire la curiosité générale sur le monde, la compréhension de l'énergie présente également des avantages pratiques. En tant que humains, nous avons appris à exploiter l'énergie en la dirigeant sous sa forme utile, le travail, vers un grand nombre de tâches qui facilitent ou améliorent la vie d'une manière ou d'une autre. De plus, nous avons développé les outils de la thermodynamique pour extraire de l'énergie supplémentaire à celle que notre corps peut fournir à partir d'autres sources, ce qui a donné lieu à des inventions telles que le moteur à combustion qui a finalement conduit à la révolution industrielle.

Les phénomènes naturels et induits par l'homme décrits ci-dessus reposent tous sur le transfert et la transformation de l'énergie, d'un lieu ou d'un objet à un autre, d'une forme à une autre. Le transfert d'énergie peut s'effectuer via une variété de mécanismes, ou canaux, et dans ce travail, nous nous concentrons sur un canal : le rayonnement. Le mouvement aléatoire des charges électriques dans un corps crée des champs électromagnétiques qui peuvent être ressentis et agir sur les charges d'un autre corps, entraînant un transfert d'énergie. Contrairement à d'autres canaux de transfert de chaleur où un contact physique entre les corps est nécessaire, le rayonnement peut se produire entre des corps séparés dans l'espace. Dans ce cas, l'énergie en question est souvent appelée chaleur car le transfert est généralement irréversible. Une description classique complète des champs électromagnétiques a été donnée au 19e siècle par les équations de Maxwell. Cependant, les ramifications complètes de cette description sur la façon dont l'énergie peut être échangée par rayonnement sont encore en cours de découverte. Aux grandes échelles de longueur, le transfert est régi par l'émission et l'absorption de photons réels propagatives. Cependant, à de petites échelles de longueur, appelées champ proche, les ondes évanescentes peuvent transporter de la chaleur qui correspond au transfert par l'effet tunnel. Ce transfert de chaleur radiative en champ proche est l'objet principal de cette thèse.

La différence entre le transfert de chaleur entre objets par rayonnement en champ proche et en champ lointain est due au caractère différent des ondes électromagnétiques concernées. Dans le champ lointain, nous avons l'image typique du rayonnement correspondant à des ondes dont la vitesse de propagation et l'atténuation sont déterminées par le milieu qu'elles traversent. En revanche, dans le champ proche, le rayonnement est dominé par les ondes évanescentes, c'est-à-dire celles qui sont fixées à la surface du matériau mais qui s'échappent sur une petite distance dans la région de l'espace entourant l'objet. Les ondes évanescentes entraînent généralement une augmentation significative du courant thermique entre les corps dans le champ proche. Cependant, le comportement exact du transfert de chaleur radiatif ne dépend pas uniquement de l'échelle de longueur. En particulier, il dépend de la façon dont les matériaux interagissent avec le champ électromagnétique, qui peut lui-même dépendre de la température. Pour des matériaux comme les métaux, ces descriptions entrent dans le riche domaine de la physique de la matière condensée. Bien que les principes du transfert radiatif de chaleur décrits ci-dessus soient bien compris, l'existence d'une pléthore de matériaux différents ainsi que de géométries et d'échelles de température pertinentes et réalisables dans les expériences signifie qu'il reste encore beaucoup à étudier.

D'une manière générale, les descriptions théoriques du champ proche suscitent un regain d'intérêt en raison des progrès des méthodes modernes de nanofabrication. La miniaturisation continue de l'électronique exige une bonne compréhension théorique du flux thermique à petite échelle. Par exemple, il est essentiel de savoir comment la chaleur sera dissipée dans un transistor nanométrique, car une surchauffe ou une fuite de chaleur peut entraîner l'instabilité ou la défaillance du dispositif. D'autre part, il existe des perspectives sur la façon dont le transfert de chaleur radiative en champ proche peut être avantageux, par exemple dans la thermophotovoltaïque en champ proche, une nouvelle forme de production d'électricité qui consiste à placer une cellule photovoltaïque dans le champ proche d'un émetteur chaud. L'avènement récent de corps matériels à deux, une et même zéro dimensions, dont le comportement émissif et absorbant peut différer radicalement en raison de la dimensionnalité réduite, accroît également la pertinence de ces études, par ailleurs purement académiques.

Dans ce travail, nous abordons certaines questions importantes concernant le transfert de chaleur radiatif. Par exemple, le confinement dans une ou plusieurs dimensions empêche-t-il le mouvement des charges pertinentes, modifiant la façon dont elles peuvent exciter et être excitées par les champs électromagnétiques ? La non-localité de la réponse du matériau joue-t-elle un rôle ? Les charges présentent-elles des excitations collectives et, dans ce cas, comment sont-elles amorties ? Comment fluctue le courant thermique radiatif entre les corps, et que pouvons-nous apprendre en mesurant ces fluctuations ? Plutôt que de réaliser des études spécifiques à un matériau dont les conclusions pourraient n'être applicables que de manière limitée, nous essayons d'utiliser des modèles généraux qui codent des phénomènes physiques largement répandus. En outre, nous effectuons des calculs analytiques selon différents schémas d'approximation, ce qui permet d'avoir une vision claire de l'impact que peuvent avoir les ingrédients physiques du modèle. Nous nous concentrons sur une géométrie bidimensionnelle, en raison de sa nouvelle pertinence grâce aux nouveaux matériaux 2D, mais aussi en raison de la facilité des calculs par rapport au cas tridimensionnel. Nos études théoriques pourraient en principe être utilisées pour informer les futures recherches expérimentales ou même aider à la conception de nouveaux dispositifs.

La structure de la thèse est la suivante : Au Ch. 1, nous présentons un bref historique des tentatives de description du transfert de chaleur radiatif, puis nous donnons les bases du principal cadre utilisé aujourd'hui, l'électrodynamique fluctuationnelle. Nous discutons des implications générales de l'électrodynamique fluctuationnelle concernant les origines des comportements de champ proche dans les ondes évanescentes. Enfin, nous fournissons une brève revue des avancées modernes dans le transfert de chaleur radiatif en champ proche, que nous utilisons pour mettre en évidence les motivations pour aborder les problèmes spécifiques couverts dans cette thèse. Dans le Ch. 2, nous effectuons une étude générale dans le cadre de l'électrodynamique fluctuationnelle du courant thermique moyen échangé par des couches métalliques parallèles bidimensionnelles. En effectuant un calcul analytique de toutes les contributions au courant thermique radiatif, y compris les ondes propagatives et évanescentes des champs électriques et magnétiques, nous cherchons à quantifier le moment où l'interaction électromagnétique est dominée par l'électrostatique, connu comme la limite de Coulomb. Après avoir clarifié cette question, dans le Ch. 3 nous travaillons dans la limite de Coulomb et explorons les rôles joués par le désordre du matériau, la dispersion spatiale dans la réponse du matériau et les excitations collectives de densité électronique connues sous le nom de plasmons de surface. Motivés par la possibilité d'un canal de transfert de chaleur résonnant dominant via les plasmons de surface, nous étudions au Ch. 4 les fluctuations du courant thermique radiatif dans le même système de couches bidimensionnelles, mais aussi dans un système plus simple de dimension zéro modélisé par un circuit électrique. Nous essayons de voir quelles informations sont accessibles via le bruit, car cela pourrait fournir une sonde expérimentale de l'importance des modes résonants. Les détails de certains des calculs les plus longs sont inclus dans les annexes A–D.

Publications liées à cette thèse

- J. L. Wise, D. M. Basko, and F. W. J. Hekking, Role of disorder in plasmon-assisted near-field heat transfer between two-dimensional metals, *Phys. Rev. B*, **101**, 205411, May 2020
  doi:10.1103/PhysRevB.101.205411
- J. L. Wise and D. M. Basko, Near field versus far field in radiative heat transfer between two-dimensional metals, *Phys. Rev. B*, **103**, 165423, Apr 2021
  doi:10.1103/PhysRevB.103.165423

1

Introduction and history of radiative heat transfer

Contents

1.1 Historical background

The transfer of energy is essential for both natural processes and human inventions. Although energy may take many forms – for example chemical or gravitational – thermal energy, that which is related to the random kinetic motion of particles, is ubiquitous in all areas of life. It is therefore highly advantageous to understand how this thermal energy, or heat, may be transferred. The temperature of an object is a measure of its thermal energy and objects with different temperatures may exchange heat, eventually altering the temperatures of both objects. This heat exchange may occur naturally or be induced, and there are roughly three main mechanisms by which it may be achieved, as depicted in Fig. 1.1.

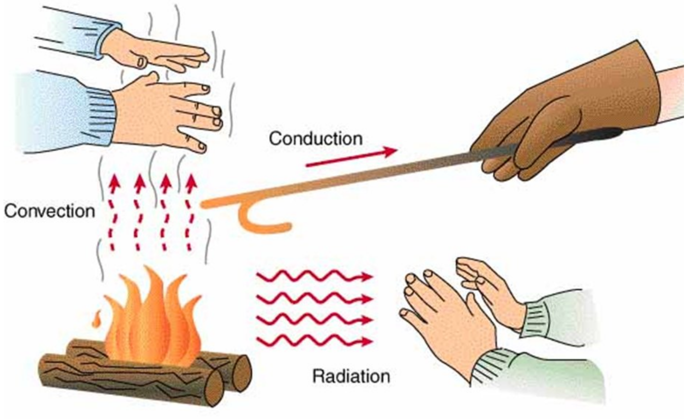

Figure 1.1: Illustration of the three main physical mechanisms of heat transfer: convection, conduction and radiation [Soffar19].

Convection describes the transfer of heat via the collective motion of particles in a homogenous fluid or gas. For example, in Fig. 1.1 the hot air particles surrounding the fire rise due to buoyancy forces displacing colder particles resulting in a flow of heat upwards. If the heat transfer is due to the movement of another type of matter dissolved or suspended in the fluid, it may be known as advection. Here the heat transfer is mediated by the transfer of matter – i.e. hot particles possessing lots of thermal energy ‘carry heat away’ by moving to another point in space, while the space that they leave behind is filled by colder particles hence creating a net transfer of thermal energy in the direction of motion of the hot particles. Convection is usually the dominant mechanism of heat transfer in fluids, for example Earth’s atmosphere.

Conversely, conduction describes the process of heat transfer via collisions of individual particles with higher energies with those of lower energies – it is not accompanied by the transfer of mass. In each collision some energy is transferred from particle to particle, eventually resulting in a spatial diffusion of heat through space, for example, in a material. In conduction, the microscopic motion of particles is important, but the transfer of heat is not driven by macroscopic mass transfer like in convection. Heat conduction within a metal, for example, is due to collisions between electrons and/or phonons, and is well-described by Fourier's law which states [baron de Fourier22]

$$\mathbf{J} = -\kappa \nabla T, \tag{1.1}$$

where $\mathbf{J}$ is the (vector) local heat current density, ∇T is the temperature gradient, and κ is the thermal conductivity which may be found from Wiedemann-Franz law [Franz53]. Heat is transferred via conduction from left to right in the metal bar in Fig. 1.1, where the temperature gradient is indicated by the changing colour. Conduction is usually the dominant mechanism of heat transfer for solid materials in contact with one and other.

Finally, objects separated by a gap devoid of matter, i.e. a vacuum, may still exchange heat. Contrary to the previous mechanisms, heat transfer via radiation does not involve movement or collisions of massive particles and is instead mediated by electromagnetic fields. Radiative heat transfer is what warms the hands on the bottom right in Fig. 1.1. The importance of this mechanism cannot be understated, since it is only via radiation that energy from the Sun – the source of all life on earth – reaches us. It is also the most recent mechanism to be accurately explained by physical laws, and constitutes the principal phenomenon investigated in this thesis.

The developments of classical electromagnetism and thermodynamics were two of the great successes of 19th century physics, however around the turn of the 20th century there were some important phenomena that remained unexplained. One unanswered question was how bodies radiate heat. In particular, the focus was on black-body radiation, where a black body is an idealised object that absorbs all radiation regardless of frequency or angle of incidence. Attempts to solve this problem via classical theories of equipartition of energy and electromagnetism led naturally to the Rayleigh-Jeans law for the spectrum of radiation [Kutner03]. Although reliable at low frequency, this description reveals an unphysical divergence in the radiation intensity at high frequency, known as the ultraviolet catastrophe.

Planck famously solved the problem by (reluctantly) postulating that bodies may only emit heat in finite packets of energy $\Delta E = \hbar\omega$ where $\hbar$ is what would become known as the famous (reduced, $\hbar = h/2\pi$) Planck's constant and ω is the (angular, $\omega = 2\pi\nu$) wave frequency. In other words, the electromagnetic fields of Maxwell needed to be quantised. In this way, Planck arrived in 1900 at the expression for the radiation spectrum of a blackbody at temperature T [Planck00]:

$$L^0_\omega(T)\, d\omega = \frac{\omega^2}{4\pi^3 c^2} \frac{\hbar\omega}{e^{\hbar\omega/k_B T} - 1} d\omega, \tag{1.2}$$

where c is the speed of light in vacuum and k_B is the Boltzmann constant. In his description of the photoelectric effect in 1905, Einstein relied on the same postulate of the quantisation of light, in what is sometimes regarded as the birth of quantum mechanics [Einstein05]. The finite packets of light later became known as photons and the idea of light behaving as a particle, rather than a wave as described by Maxwell's equations, proved to be revolutionary. Planck's law removed the ultraviolet catastrophe, faithfully matching experimental data of the spectra of stars at both low and high frequency. Simple manipulations of the expression Eq. (1.2) lead naturally to two previously observed laws on black-body radiation from a body at temperature T:

1. By differentiation we find Wien's law for the wavelength of the peak of the radiation spectrum [Wien96]:
$$\lambda_{\max} = \frac{b}{T}, \tag{1.3}$$
where $b = 2.90\,\mathrm{mm\,K}$ is a transcendental number.

2. By integration we find the Stefan-Boltzmann law for the power emitted per unit area [Boltzmann84]:
$$J(T) = \sigma T^4, \tag{1.4}$$
where $\sigma = 2\pi^5 k_B^4/(15c^2h^3)$ is the Stefan-Boltzmann constant.

Real bodies are not perfect absorbers, and their deviation from black-body radiative efficiency is described by the material emissivity. The emissivity may be incorporated into the theory of Planckian radiative heat transfer, leading to a modified expression for the power emitted by a given realistic body, away from the Stefan-Boltzmann law, Eq. (1.4).

Even with the added notion of emissivity, the Planckian approach described above, based on the particle nature of light, is fundamentally limited. The reason for this limitation is related to one of the central debates of 20th century physics: wave-particle duality. Although the photon picture appeared to solve various outstanding problems in physics, it still had to be rationalised with the irrefutable wave-like behaviour of light that was readily observed (reflection, diffraction etc.). As the development of quantum physics gradually showed, the interplay between the importance of the two descriptions – wave and particle, classical and quantum – is determined by the length or energy scales of each particular system.

In the context of radiative heat transfer, Planck's law may fail when the physical length scale of a problem decreases towards that of the dominant wavelength of light, the thermal wavelength of photons, $\lambda\!\!\!^-_T = \hbar c/T$ (taking $k_B = 1$), where $\lambda\!\!\!^-_T \approx \lambda_{\max}$ of Wien's law, Eq. (1.3). At length scales smaller than $\lambda\!\!\!^-_T$, also known as the near field, wave-like characteristics absent from Planck's law may result in photon tunnelling between bodies, which may contribute significantly to the radiative heat transfer. Indeed, a more complete theory than Planck's law is needed to accurately predict radiative heat transfer between closely spaced bodies, and this is the subject of the next section.

1.2 Fluctuational electrodynamics

The framework used to study radiative heat transfer between bodies is known as fluctuational electrodynamics (FE). This phenomenological theory combines the theories of random quantum and thermal fluctuations with Maxwell's description of the electromagnetic fields. The theory of fluctuations encodes Planck's corpuscular nature of light, while Maxwell's equations ensure that the wave-like behaviour is taken into account. FE is a semi-classical scheme in the sense that the electromagnetic fields are treated classically, but quantum fluctuations are included – indicated by the presence of $\hbar$ in the fluctuation dissipation theorem. As long as the quantum system may be represented as a collection of harmonic oscillators – which is always the case for a system whose response is linear – the quantum fields obey the same equations as the corresponding classical ones, and so nothing is lost when applying Maxwell's equations.

The resulting FE is a theory that may be used to reliably predict the heat transfer across (in principle) all length scales. We note also that the framework of FE allows one to calculate not only the energy transfer (heat), but also the momentum transfer (forces) between isolated bodies. These phenomena, known as Casimir effects, have been extensively studied: see the original papers by Casimir [Casimir48b, Casimir48a], the seminal paper connecting the force to fluctuating currents by Lifshitz [Lifshitz56], and more recent reviews [Mostepanenko97, Joulain05, Volokitin07] and references therein. However, here we tell the story of FE in the context of heat transfer.

Based on the early work in this direction by Rytov in the 1950s [Rytov53, Rytov89], the theory of FE was first successfully applied to calculate radiative heat transfer by Polder and Van Hove in 1971 [Polder71]. Since then, FE has been applied to predict the heat transfer in many systems based on different geometries, materials and temperature regimes. A brief timeline of the works most relevant to this thesis is given in Sec. 1.5.1, as well as related experiments in Sec. 1.5.2. First we detail the ingredients and steps of the phenomenological theory of FE, which is illustrated in Fig. 1.2.

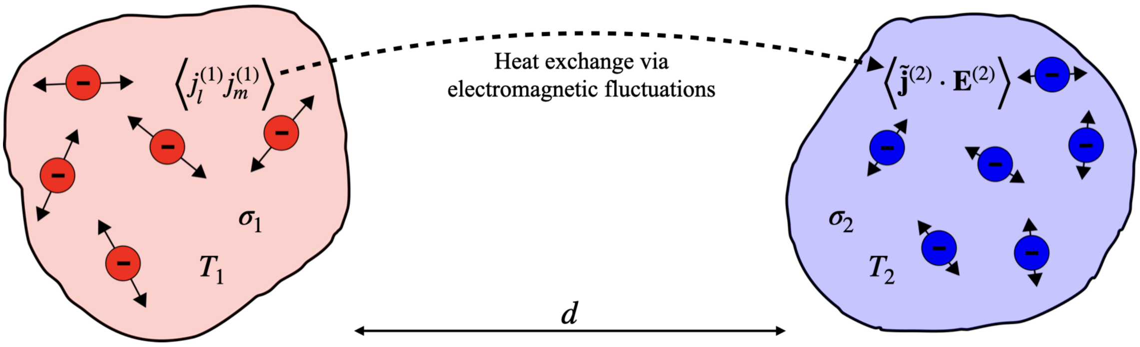

Figure 1.2: Schematic of radiative heat transfer between two metals, described through the framework of fluctuational electrodynamics. The bodies are described by their electrical conductivities, σ_1 and σ_2, and are at thermal equilibrium with temperatures T_1 and T_2, respectively. In principle the bodies may have arbitrary shape and they are spatially separated by some gap, d. Illustrated by the arrow is the heat transferred via electromagnetic fields from body 1 to body 2: The thermal fluctuations of electrons in body 1 give rise to current fluctuations that are described by the FDT. These current sources determine the electromagnetic fields that are felt by the charges in body 2. The dissipation in body 2 due to the presence of the fluctuating currents in body 1 is given by the induced current multiplied by the electric field. The same process should then be imagined in reverse, where the fluctuating currents in body 2 lead to dissipation in body 1, where the difference gives the net heat transfer between the bodies.

For a material in thermal equilibrium at temperature T, charges (ions or electrons) move randomly due to quantum (zero-point) and thermal fluctuations. The motion of these charges drives random fluctuating currents. Although the average of these currents vanishes, their presence affects the electromagnetic field present inside and outside of the material. In particular, the electromagnetic field due to current fluctuations in one body may do work on charges in a second body, spatially separated from the first. This work eventually manifests itself as dissipation, known as Joule heating, in the second body. The same process occurs in reverse where dissipation in the first body occurs due to current fluctuations in the second, and a net heat current between the bodies may be calculated. In the following subsections the key ingredients and steps mentioned in this paragraph are detailed in the following order:

1. **Material response function:** the key ingredient that describes all aspects of the material's behaviour in the presence of an electromagnetic field

2. **Fluctuation dissipation theorem:** the fundamental result describing the statistics of the random fluctuating currents in the material that arise as a result of the random thermal motion of charges

3. **Maxwell's equations:** the standard dynamical equations that describe how the electromagnetic fields produced by the currents fill the given geometry

4. **Joule heating:** the calculation of the quantity of interest, the heat transfer between spatially separated objects via the electromagnetic fields

1.2.1 Material response function

The first essential ingredient is a description of how the material interacts with external electromagnetic fields, also known as the material's optical response. The material response function may be defined in terms of the induced charge density or current density, but in general it describes the willingness of the relevant charges in the material to be influenced by the presence of an electromagnetic field. In the framework of linear response theory the current response function of a given material, known as the electrical conductivity tensor, σ_{lm}, is defined in terms of the current density induced due to the presence of an external electric field via the relation [Bruus04]

$$j_l(\mathbf{r},t) = \int dt' \int d\mathbf{r}'\, \sigma_{lm}(\mathbf{r},t;\mathbf{r}',t')E_m(\mathbf{r}',t'), \tag{1.5}$$

where l,m are Cartesian indices (summation is implied over the repeated index, m). The conductivity is the linear response coefficient for the current density, and as shown describes the ease with which currents are established in a material when placed in an electric field – its inverse is the resistivity. Considering instead of the current the response in the charge density, the density response function, Π, is defined in terms of the charge density induced due to the presence of an external potential via the analogous relation [Bruus04]

$$\rho(\mathbf{r},t) = \int dt' \int d\mathbf{r}'\, \Pi(\mathbf{r},t;\mathbf{r}',t')\phi(\mathbf{r}',t'). \tag{1.6}$$

The density response function, Π, describes how the charge is redistributed in a material upon application of an external electromagnetic potential, or in other words the material's propensity to acquire an electric dipole moment. The density response function is an important quantity because, via the dielectric function, it describes the ability of a material to screen an external potential.

The two response functions Eqs. (1.5) and (1.6) are related due to the continuity equation that expresses the fundamental law of conservation of charge in the material [Landau75]:

$$\nabla\cdot\mathbf{j}(\mathbf{r},t)+\frac{\partial\rho(\mathbf{r},t)}{\partial t}=0. \tag{1.7}$$

Naively one may think that the formulation of FE may therefore be carried out equivalently either in terms of currents and fields, or densities and potentials. However, the formulation of FE in terms of current is the more complete one, since in the density description the contributions made by transverse currents (i.e. zero divergence) are not taken into account.

It is also useful to introduce here another quantity used to describe the reshuffling of the charges inside a medium in response to the application of an external field, the electric polarisation vector, **P** (not to be confused with the polarisation direction of waves). **P** may be defined inside a medium via the definitions (equivalent by the continuity equation (1.7)):

$$\rho(\mathbf{r},t)=-\nabla\cdot\mathbf{P}(\mathbf{r},t),\Longleftrightarrow\mathbf{j}(\mathbf{r},t)=\frac{\partial\mathbf{P}(\mathbf{r},t)}{\partial t}, \tag{1.8}$$

where **P** gives the dipole moment per unit volume of the medium subject to an external field. In the formulation of Maxwell's equations in the presence of dielectric media, the polarisation often appears in the definition of the electric induction, or displacement field, $\mathbf{D}=\mathbf{E}+4\pi\mathbf{P}$ (we use CGS units throughout, unless stated otherwise).

In general the response function for a particular material object may be very complicated. In space and time invariant systems (such is the case for homogenous, isotropic materials in equilibrium) the dependence on the coordinates reduces, for example for the conductivity, to: $\sigma(\mathbf{r},t;\mathbf{r}',t')\to\sigma(\mathbf{r}-\mathbf{r}',t-t')$ with $\sigma=0$ for $t<t'$ due to causality. The dependence on two spatial coordinates and two time coordinates shows that the response may nonetheless be nonlocal. That is, the response at a given point in space within the material at a certain time may depend on the perturbation at some other point elsewhere in the material at some earlier time. Inserting the time and space invariant form of σ into Eq. (1.5) we notice the form of a convolution. It is therefore advantageous to work in Fourier space, where the Fourier transform in space and time are defined as

$$\sigma(\mathbf{k},\omega)=\int_{-\infty}^{\infty}dt\int d^d\mathbf{r}\,\sigma(\mathbf{r}-\mathbf{r}',t-t')e^{-i\mathbf{k}\cdot(\mathbf{r}-\mathbf{r}')+i\omega(t-t')}, \tag{1.9}$$

where d is the dimension of the material, $\mathbf{k}$ is the d-dimensional wavevector and ω is the frequency of the perturbation – i.e. the electric field. By the convolution theorem the integral equation Eq. (1.5) therefore becomes an algebraic equation in Fourier space:

$$j_l(\mathbf{k},\omega)=\sigma_{lm}(\mathbf{k},\omega)E_m(\mathbf{k},\omega), \tag{1.10}$$

highlighting the utility of working in Fourier space in space and time invariant systems.

The aforementioned spatial and temporal nonlocality is encoded in the conductivity's dependence on $\mathbf{k}$ and ω. The dependence on ω, known as frequency dispersion, represents memory effects in the material, while the dependence on $\mathbf{k}$, known as spatial dispersion, represents force spreading phenomena [Landau84]. From the continuity equation (1.7) and the fact that the electric field is given by the gradient of the scalar potential, we may relate the previously defined density response function appearing in Eq. (1.6) to the conductivity tensor of Eq. (1.9):

$$i\omega e^2 \Pi(\mathbf{k},\omega) = k_l k_m \sigma_{lm}(\mathbf{k},\omega), \tag{1.11}$$

where e is the electron charge.

For metals, which represent the focus of this work, the temporal dispersion is often significant while the spatial dispersion tends only to be significant at microscopic length scales. Spatial dispersion is therefore often neglected, in other words assuming a point-like spatial dependence of the conductivity $\sim \delta(\mathbf{r}-\mathbf{r}')$, leading to no $\mathbf{k}$-dependence in Eq. (1.9). In this case, the conductivity in a metal is well described by the Drude model, where the longitudinal (diagonal) conductivity is given by

$$\sigma(\omega) = \frac{e^2 \nu D}{1 - i\omega\tau}, \tag{1.12}$$

where ν is the electron density of states at the Fermi level, and $D = v_F^2\tau/2$ is the diffusion coefficient given in terms of the Fermi velocity v_F and electron momentum relaxation time τ. Equation (1.12) is very general and is a result of electron scattering with impurities – it may be derived by semi-classical transport equation or by a quantum diagrammatic approach [Bruus04]. Although using a local model simplifies the calculation, work has been done to investigate the role of spatial dispersion on radiative heat transfer [Chapuis08c], and we investigate this further in Ch. 3.

The most direct method of calculation of the response function is the famous Kubo formula [Kubo57a, Kubo57b, Bruus04], however under certain conditions one may also use the semiclassical Boltzmann kinetic equation [Abrikosov88], as in App. D. Further discussion of methods of calculating the response function are found in Sec. 2.1 and App. D. We see in the following subsections 1.2.2-1.2.4 that the material response function, once known, plays a crucial role in FE.

1.2.2 Fluctuation dissipation theorem

The material response functions described in the previous section pertain to the more general framework of linear response theory. In particular, they describe the average response of a particular observable of a system in equilibrium to the application of an external perturbation, to linear order in the perturbation. The remarkable result of the fluctuation dissipation theorem is that these very same response functions describe the random fluctuations of the corresponding observables, *present even in the absence* of the perturbation. This is the fundamental result used to describe the random current density fluctuations that act as the source of thermal radiation in FE.

The perturbations considered in linear response theory take the form $\hat{V} = -f_i(t)\hat{x}_i$, where f_i is a periodic external force of the form $f_i(t) = \frac{1}{2}\left[f_{0i}e^{-i\omega t} + f_{0i}^{*}e^{i\omega t}\right]$ which couples to the coordinate, or observable, x_i, described by the operator $\hat{x}_i$ [Landau80]. The generalised susceptibility is defined as the kernel giving the average response of the coordinate upon application of a set of forces, $\bar{x}_i = \alpha_{ik} f_k$, i.e. α_{ik} describes how susceptible the coordinate x_i is to the influence of the force f_k. Following basic arguments for quantum mechanical transition probabilities and averaging over the Gibbs ensemble for a system in equilibrium at temperature T, it is possible to arrive at the expression for the fluctuations of the coordinates [Landau80]

$$\frac{1}{2}\left\langle \hat{x}_i(t)\hat{x}_k(t') + \hat{x}_k(t')\hat{x}_i(t)\right\rangle = \int_{-\infty}^{\infty}\frac{d\omega}{2\pi}\frac{1}{2}i\hbar\left[\alpha_{ki}^{*}(\omega) - \alpha_{ik}(\omega)\right]\coth\frac{\hbar\omega}{2T}e^{-i\omega(t-t')}, \quad (1.13)$$

which represents the fluctuation dissipation theorem, where $\hat{x}_i(t)$ are Heisenberg operators and we have used the property of the generalised susceptibility, $\alpha(-\omega) = \alpha^{*}(\omega)$. First derived by Callen in 1951 [Callen51], Eq. (1.13) describes either the fluctuations of a given observable (if $i = k$) or the correlation between two different observables (if $i \neq k$) in terms of the components of the generalised susceptibility and the system temperature. These fluctuations are present with or without the presence of the external force, i.e. regardless of whether $\bar{x}_i$ is non-zero. The term in square brackets of Eq. (1.13) may be shown to describe the dissipative processes of the system, hence expressing a deep connection between random fluctuations and energy dissipation. Noting that $(1/2)\coth(\hbar\omega/2T) = 1/2 + \mathcal{N}(\omega)$, where $\mathcal{N}(\omega) = 1/(e^{\hbar\omega/T} - 1)$ is the Bose-Einstein distribution function, we identify the average energy of a harmonic oscillator – the same function that appears in Planck's law, Eq. (1.2).

The formalism briefly introduced above may be applied to a wide range of physical problems. For example, the Brownian motion of a particle in a fluid is explained by the coupling of the particle coordinates to random Langevin forces whose statistics are given by FDT [Joulain05]. For the problem of electromagnetic fluctuations in the presence of a medium, the corresponding force-coordinate pair is an external electric field, **E**, which couples to the polarisation vector, **P**. The average response in the coordinate, **P**, is given in terms of the external force, **E**, via the generalised susceptibility, labelled χ:

$$P_i(\mathbf{r},t) = \int dt' \int \mathbf{dr}'\chi_{ik}(\mathbf{r},t;\mathbf{r}',t')E_k(\mathbf{r}',\mathbf{t}'), \quad (1.14)$$

By the FDT, we may therefore write down the fluctuations of the polarisation vector, present even in the absence of an external electric field (generalising Eq. (1.13) for spatially distributed quantities):

$$\left\langle P_i(\mathbf{r},t)P_k(\mathbf{r}',t')\right\rangle = \int_{-\infty}^{\infty}\frac{d\omega}{2\pi}\frac{1}{2}i\hbar\left[\chi_{ki}^{*}(\mathbf{r}',\mathbf{r},\omega) - \chi_{ik}(\mathbf{r},\mathbf{r}',\omega)\right]\coth\frac{\hbar\omega}{2T}e^{-i\omega(t-t')}. \quad (1.15)$$

Specifying to a three-dimensional translationally invariant system we introduce the Fourier transform in space and use Eq. (1.8) to rewrite the FDT for current fluctuations as

$$\langle j_i(\mathbf{r},t)\, j_k(\mathbf{r}',t')\rangle = \int \frac{d^3\mathbf{k}}{(2\pi)^3} \int_{-\infty}^{\infty} \frac{d\omega}{2\pi}\, \hbar\omega \,\mathrm{Re}\,\sigma_{ik}(\mathbf{k},\omega) \coth\frac{\hbar\omega}{2T} e^{i\mathbf{k}(\mathbf{r}-\mathbf{r}')-i\omega(t-t')}, \tag{1.16}$$

where we have used that $\sigma_{ik}(\omega) = -i\omega\chi_{ik}(\omega)$ via the definition of the polarisation vector. The fluctuating current sources, whose statistics are given by FDT Eq. (1.16), enter directly into Maxwell's equations and eventually result in radiative heat transfer via Joule heating.

1.2.3 Maxwell's equations

The fluctuating currents of the previous section in one body act as source terms for the electromagnetic field experienced by another, spatially separated body. To calculate the field in the presence of dielectric media with intrinsic fluctuations, we solve Maxwell's equations. Solutions to these equations correspond to a complete picture of the electromagnetic system. We utilise Maxwell's equations for monochromatic field components of frequency ω [Landau84]

$$\nabla\cdot\mathbf{E}(\mathbf{r},\omega) = 4\pi\rho(\mathbf{r},\omega), \tag{1.17a}$$

$$\nabla\cdot\mathbf{B}(\mathbf{r},\omega) = 0, \tag{1.17b}$$

$$\nabla\wedge\mathbf{E}(\mathbf{r},\omega) = \frac{i\omega}{c}\mathbf{B}(\mathbf{r},\omega) \tag{1.17c}$$

$$\nabla\wedge\mathbf{B}(\mathbf{r},\omega) = \frac{1}{c}\left[4\pi\mathbf{j}(\mathbf{r},\omega) - i\omega\mathbf{E}(\mathbf{r},\omega)\right], \tag{1.17d}$$

where all contributions to the currents and densities are present in ρ and $\mathbf{j}$. In particular, $\mathbf{j}$ consists of the sum of two contributions: (i) the induced current due to the electric field present at the position $\mathbf{r}$, given in general by Eq. (1.5) and (ii) the randomly fluctuating currents whose correlation is described by the FDT of Eq. (1.16). In the spirit of the previous sections, the contributions (i) and (ii) may be seen as the induced current, and the intrinsic fluctuations, respectively. We note that the Coulomb limit, that which describes electrostatics, is obtained from Eqs. (1.17) by sending $c \to \infty$. We note also that sometimes, authors choose to define the electric displacement field, $\mathbf{D}$, as mentioned previously, which takes into account the induced current, via the relation:

$$\mathbf{D}(\mathbf{r},\omega) = \int d\mathbf{r}'\, \varepsilon(\mathbf{r},\mathbf{r}',\omega)\mathbf{E}(\mathbf{r}',\omega), \tag{1.18}$$

where the dielectric function is defined by

$$\varepsilon(\omega) = 1 + 4\pi\chi(\omega) = 1 - \frac{4\pi\sigma(\omega)}{i\omega}. \tag{1.19}$$

The properties of the dielectric function regarding spatial locality are therefore given by those of the conductivity. However, we continue with Maxwell's equations as given in Eqs. (1.17), with the geometry of the problem encoded in $\sigma(\mathbf{r},\mathbf{r}',\omega)$ – i.e. σ is only non-zero within the charge containing bodies.

One may in principle proceed to solve Maxwell's equations and construct **E** and **B** everywhere ensuring the fields satisfy the regular boundary conditions at interfaces between media [Landau84]: continuity of the normal **B**-field and tangential **E**-field, and jumps in the normal **E**-field and the tangential **B**-field given by the total surface charge and current densities, respectively.

The energy current density pertaining to an electromagnetic wave is given by the Poynting vector, **S**:[Landau84]

$$\mathbf{S}(\mathbf{r},\omega)=\frac{c}{4\pi}\mathbf{E}(\mathbf{r},\omega)\wedge\mathbf{B}(\mathbf{r},\omega). \tag{1.20}$$

Since in a travelling wave the electric and magnetic field components are transverse, we note that the Poynting vector points in the direction of propagation of the wave, giving rise to the idea of energy being 'carried' from one point in space to another by the fields. The Poynting vector is ultimately responsible for heat transfer by radiation, and is therefore central to this topic.

1.2.4 Joule heating

Finally, we wish to calculate the quantity of interest, namely, the heat deposited into a body at temperature T_1 (body 1), via radiation when in the presence of another body at temperature T_2 (body 2). Although the theory of dissipation in systems with linear response appears to arise naturally, there is nonetheless some subtlety regarding the quantity of interest. As a reminder, for a system perturbed by a periodic external force as described in Sec. 1.2.2, the dissipation due to the force may be shown to be given by:

$$Q=\frac{i}{4}\omega\left[\alpha^*_{ki}(\omega)-\alpha_{ik}(\omega)\right]f_{0k}f^*_{0i}, \tag{1.21}$$

where indeed we note the appearance in square brackets of the exact same object as in the FDT, Eq. (1.13), hence justifying its name. For the case of heat deposited via radiation into body 1, we begin by writing the expression of the total work done by the field on the charges inside the body:

$$J_1=\int_1 d\mathbf{r}\,\langle\mathbf{j}_1(\mathbf{r},t)\cdot\mathbf{E}_1(\mathbf{r},t)\rangle, \tag{1.22}$$

where $\langle . \rangle$ denotes an average over the fluctuating sources whose statistics are controlled by the FDT [Eq. (1.16)] and **r** spans the volume of body 1. The current and electric field in Eq. (1.22) may be split into additive contributions. The field, $\mathbf{E}_1$, consists of two contributions: (i) the field present in body 1 due to the current fluctuations in body 2, denoted $\mathbf{E}_1^{(2)}$, and (ii) the field present in body 1 due to the current fluctuations in body 1, $\mathbf{E}_1^{(1)}$. The current, $\mathbf{j}_1$, therefore consists of three contributions: the two induced currents given by Eq. (1.5) that are associated to the fields (i) and (ii), as well as the intrinsic fluctuations, $\mathbf{j}_1^{\text{fl.}}$. Decomposing the current and field in Eq. (1.22) in this way leads to the expression (suppressing for brevity all arguments, integrals over intermediate space and time variables and sums over tensorial indices):

$$J_1 = \int_1 d\mathbf{r} \left\langle \left(\mathbf{j}_1^{\text{fl.}} + \sigma_1 \mathbf{E}_1^{(1)}\right) \cdot \mathbf{E}_1^{(1)} \right\rangle + \left\langle \sigma_1 \mathbf{E}_1^{(2)} \cdot \mathbf{E}_1^{(2)} \right\rangle, \tag{1.23}$$

where cross terms involving current fluctuations in opposing bodies have been evaluated to give zero since the fluctuations in each body are independent. The two separate contributions in Eq. (1.23) have distinct physical interpretation. The first term may be identified as the energy emitted by body 1, while the second term is the energy absorbed by body 1 due to fluctuations in body 2. Clearly, these two contributions to the work done inside body 1 will have opposite sign. This is illustrated schematically in Fig. 1.3 where the first term corresponds to all blue arrows (dashed and solid) leaving body 1. The second term corresponds to the solid red arrow leaving body 2 and arriving at body 1 subtract the dotted red arrow leaving body 1, corresponding to transmission. The transmission should be born in mind when writing the Joule losses in terms of the Poynting vector, as we discuss later in Sec. 1.4.

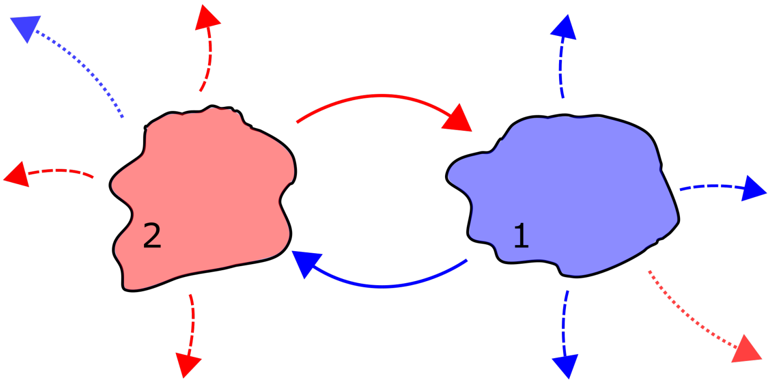

Figure 1.3: Schematic illustrating the energy exchange between body 1 and body 2 and their surroundings. The expression for the work done on charges in body 1 in Eq. (1.22) corresponds to all the arrows arriving and leaving body 1 – i.e. it includes both the energy dissipated in body 1 due to radiation from body 2 (solid red arrow from body 2 to body 1 subtract dotted red arrow leaving body 1), but also radiation emitted by body 1 (all blue arrows leaving body 1). The same picture is illustrated for the work done inside body 2. The Joule losses in body 1 given in Eq. (1.25) correspond to the solid minus the dotted red arrow, subtract the solid minus the dotted blue arrow. The importance of the dotted arrows which correspond to transmission of radiation by the bodies is dependent on the geometry of the particular problem.

One may write the corresponding expression for the work done by the fields on the charges in body 2:

$$J_2 = \int_2 d\mathbf{r} \left\langle \left(\mathbf{j}_2^{\text{fl.}} + \sigma_2 \mathbf{E}_2^{(2)}\right) \cdot \mathbf{E}_2^{(2)} \right\rangle + \left\langle \sigma_2 \mathbf{E}_2^{(1)} \cdot \mathbf{E}_2^{(1)} \right\rangle, \tag{1.24}$$

where we once again identify the two terms as the energy emitted by body 2 and the energy absorbed by body 2 due to fluctuations in body 1, respectively. The work done in body 2 is represented analogously in Fig. 1.3. Considering Eqs. (1.23) and (1.24), we recognise that due to energy balance the second term in each equation (corresponding to dissipation due to the presence of the other body) is contained (with opposite sign) within the first term of the other equation (corresponding to total energy emission). However, exactly how the first term in each equation splits into this radiation that is absorbed by the other body, and radiation that escapes to infinity is non-trivial and situation dependent. Since we are interested in energy transferred between the bodies rather than radiation lost to infinity, we may simply focus on the second two terms, defining the Joule losses in body 1 by their difference (reinstating the arguments)

$$J_{2\to 1} = \tilde{J}_1 - \tilde{J}_2 = \int_1 d\mathbf{r} \left\langle \tilde{\mathbf{j}}_1(\mathbf{r},t) \cdot \mathbf{E}_1^{(2)}(\mathbf{r},t) \right\rangle - \int_2 d\mathbf{r} \left\langle \tilde{\mathbf{j}}_2(\mathbf{r},t) \cdot \mathbf{E}_2^{(1)}(\mathbf{r},t) \right\rangle, \tag{1.25}$$

where $\tilde{\mathbf{j}}_{1,2}$ are the induced currents appearing in the second terms of Eqs. (1.23) and (1.24), respectively. In this picture, the different contributions to the heat current $\tilde{J}_{1,2}$ are seen to arise by sequentially treating one body as active (emitter) while the other is passive (receiver) – i.e. to calculate each term $\tilde{J}_{1,2}$ one needs to solve Maxwell's equations with fluctuations only in the opposing body.

With the Joule losses written in the form of Eq. (1.25) it is possible to make contact with the general result for dissipation in linear response theory, Eq. (1.21). Taking $\tilde{J}_1$ and writing the induced current explicitly in terms of the conductivity of body 1 via Eq. (1.5) leads to the expression

$$\tilde{J}_1 = \int_0^\infty \frac{d\omega}{2\pi} \int \frac{d\mathbf{k}}{(2\pi)^d} \left[\sigma_{ki}^*(\mathbf{k},\omega) + \sigma_{ik}(\mathbf{k},\omega)\right] E_k(\mathbf{k},\omega) E_i^*(\mathbf{k},\omega), \tag{1.26}$$

where we have specified to the case of a d-dimensional translationally invariant body 1. Rewriting the conductivity in terms of the generalised susceptibility results in the general form given in Eq. (1.21). This expression for the Joule losses Eq. (1.25) concludes the explanation of the phenomenological theory of FE for the purposes of radiative heat transfer.

1.3 Extensions and validity of FE

1.3.1 FE in circuits

In the above description, FE has been set up for macroscopic bodies that have a relevant, but simple, geometry. When one can neglect the details of the internal structure of the bodies, it is often desirable to represent the physical system by an effective circuit, where lumped elements such as resistors, capacitors and inductors mimic the behaviour of the real material bodies. Photonic heat transfer in such circuits has been measured experimentally – in particular in Refs. [Meschke06, Timofeev09], the authors confirmed the thermal conductance quantum (predicted in Ref. [Pendry83]) in a microscale circuit at low temperatures. For a review of the recent advances in field of quantum thermal transport in circuits, see Ref. [Pekola21].

A version of FE has been developed to treat the problem of photonic heat transfer in circuits [Schmidt04, Pascal11]. Notably, this theory allows one to calculate the heat current between dissipative impedances held at different temperatures, depending on the circuit that couples the two. Some examples of these circuits are shown in Fig. 1.4.

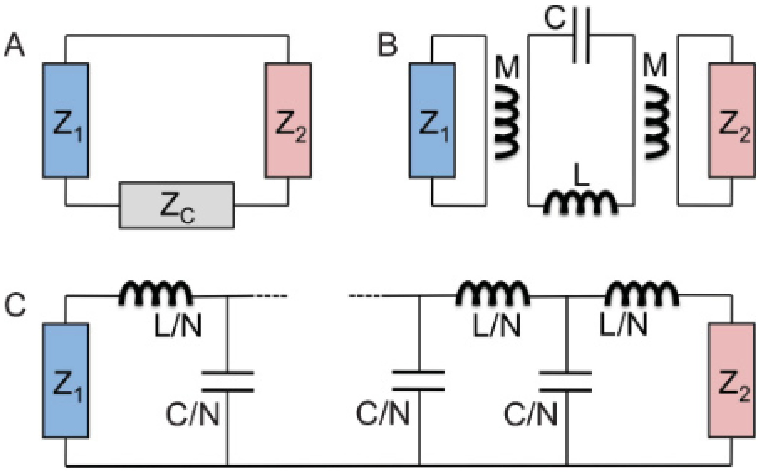

Figure 1.4: Examples of circuits with different types of coupling, treatable via circuit FE [Pascal11]. A: two dissipative impedances, Z_1 and Z_2, ($\mathrm{Re}\, Z_{1,2} \neq 0$) coupled by a reactive impedance, Z_c (i.e. $\mathrm{Re}\, Z_c = 0$). B: Z_1 and Z_2 are coupled via mutual inductances, M, to an LC resonator. C: Z_1 and Z_2 are coupled via a transmission line of length N.

Here we briefly describe the analogy between the macroscopic FE developed in the previous subsections, and the circuit FE used to calculate photonic heat transfer in circuits like those of Fig. 1.4. The bodies transferring heat are here represented by the different coloured impedances, Z_1 and Z_2, which may be thought of as baths where dissipation may take place. For the key ingredients and steps of macroscopic FE (Secs. 1.2.1-1.2.4), we provide the circuit FE equivalent:

1. **Material response function** ⇒ Instead of the response functions that describe how the materials respond in the presence of an external electromagnetic field, the impedances Z_1 and Z_2 describe the behaviour of the baths in the presence of applied voltages and currents. In the simplest case Z_1 and Z_2 may be just resistors, but in analogy to Eq. (1.5) we have the general definition for the complex impedance, $Z(\omega)$, defined to give the current, I, induced upon application of an alternating (complex) voltage, V:
$$I = \frac{1}{Z(\omega)} V, \tag{1.27}$$
where we note that $1/Z$, known as the admittance, is the circuit equivalent of the material conductivity.

2. **Fluctuation dissipation theorem** ⇒ The current that passes through the dissipative elements Z_1 and Z_2 may once again be decomposed into a linear response due to an applied potential difference, and intrinsic fluctuations. For the fluctuations, one may view each dissipative element as being associated with a fluctuating current source connected in parallel. These thermal current fluctuations are known as Johnson-Nyquist noise, which satisfy the fluctuation dissipation theorem (in direct analogy

with Eq. (1.16) for the current density fluctuations):

$$\langle I_i(t) I_j(t') \rangle = \delta_{ij} \int_{-\infty}^{\infty} \frac{d\omega}{2\pi} \hbar\omega \, \mathrm{Re} \, \frac{1}{Z_i(\omega)} \coth \frac{\hbar\omega}{2T_i} e^{-i\omega(t-t')}, \tag{1.28}$$

where $i, j = 1, 2$ label the elements and δ_{ij} indicates that the intrinsic current fluctuations in each dissipative element are independent, as in macroscopic FE. This expression reflects the fact that the impedances Z_1 and Z_2 act as photonic reservoirs, characterised by Bose-Einstein distribution functions at temperatures T_1 and T_2.

3. **Maxwell's equations** ⇒ Rather than solving Maxwell's equations for the electromagnetic fields in the presence of the material bodies, the circuit problem is solved via Kirchoff's laws for the conservation of charge (in the form of current) at circuit nodes and conservation of energy (in the form of potential difference) around closed loops. The solutions are determined by the circuit structure that couple the baths Z_1 and Z_2. Recalling the physical nature of different circuit elements it is possible to make the connection between different lumped elements, and the underlying electromagnetic mechanisms. In particular, coupling directly via capacitors (for example, taking $Z_c = 1/i\omega C$ in the top left circuit of Fig. 1.4) represents electrostatic coupling of charge density fluctuations, while coupling via inductors (for example, the top right circuit of Fig. 1.4) represents magnetostatic coupling of transverse current fluctuations.

4. **Joule heating** ⇒ Finally, the Joule losses of macroscopic FE correspond to the Ohmic dissipation that occurs in $Z_{1,2}$ as a result of the established current and potential difference. The well known expression for the dissipation in, say Z_1, is given by [in analogy with Eq. (1.22)]

$$P_{2\to 1} = \langle I_1(t) V_1(t) \rangle, \tag{1.29}$$

where there is not the same subtlety around the work done as in the macroscopic case (Fig. 1.3), since all the energy is confined to the circuit.

The description of circuit FE given above allows one to calculate heat transfer between dissipative elements of a circuit. This is applied in Ch. 3 where we discuss the applicability of the effective circuit model for a real physical system.

1.3.2 Fluctuations of the heat transfer

In all of the above discussion of FE, the quantity of interest is the average heat current between spatially separated bodies held at different temperatures. While accurate prediction of the *average* of a physical quantity is important for applications and experiments, there is often more information to be learned about the system via the *fluctuations* around the average, also known as the noise. In the context of electrical current, the noise has been studied to reveal information about the conduction mechanisms and the nature of charge carriers [Landauer98]. Although the calculation of fluctuations is in general more difficult since it involves higher order moments of the electromagnetic fields, the theory of FE has recently been applied to radiative heat current noise [Biehs18, Herz20]. Just as for the average, FE predicts fluctuations that differ significantly in the near field (see Sec. 1.4 for the definition) compared to those predicted by the Planckian approach.

There have been some works on heat current noise in particular systems, where typically one calculates the full counting statistics of the energy transferred in a given time interval. The heat current average and fluctuations may be accessed via the cumulants of the appropriate generating functional of the theory. For example, Ref. [Tang18] investigates numerically the heat current statistics between two semi-infinite metallic bodies in the Coulomb limit, revealing significant deviations in the fluctuations at large temperature differences compared to linear response results given in terms of heat conductance. In circuits, Ref. [Golubev15] develops a theory for the full counting statistics of photon mediated heat exchange between two metallic resistors. The results for the low frequency noise differ from the classical case for both low and high temperatures. Ref. [Karimi21] investigates finite frequency heat current noise in circuits and proposes a modulation procedure to allow experimental observation of the high frequency behaviour. Despite these advances, the question of how to extract information on the nature of heat-carrying excitations remains largely open (see Sec. 4.3.3).

1.3.3 Validity of FE

Finally, we discuss briefly the validity of FE. Although it is a phenomenological theory, based on linear response and a macroscopic description of the materials and fields, FE may be justified microscopically for the average heat current via nonequilibrium Green's functions (NEGFs) [Ojanen07, Ojanen08, Zhang18, Kamenev18]. The NEGFs are used to describe the many-body electron system that constitute the radiating bodies, where the electron-electron interactions responsible for the heat transfer may be treated via diagrammatic perturbation theory in the random phase approximation (RPA), which is valid for for sufficiently high electron density [Bruus04]. In App. C this procedure is performed for two-dimensional metallic layers in the Coulomb limit. The current fluctuations obeying FDT introduced as sources in FE arise naturally in the microscopic theory so long as each radiating body is in equilibrium with itself, but not with the other one. Here, equilibrium means that each body has its own homogenous temperature profile (i.e. there are no temperature gradients inside each body), while the total system represents a nonequilibrium steady state. The fact that the microscopic approach coincides with FE represents an equivalence of Maxwell's equations and the full electromagnetic interaction between electrons in RPA [Abrikosov75]. We add that a similar microscopic justification for FE for the case of noise is apparently still lacking, and we approach this problem in Ch. 4.

The assumption of homogenous temperature profiles may be interrogated – indeed one may imagine the appearance of 'hot-spots' near a material surface where the fields penetrate. By introducing in the model a physical mechanism for radiation-conduction coupling (this is how the radiative heat is actually dissipated), one may observe the establishment of inhomogeneous temperature profiles according to the size and shapes of the bodies, as well as the timescales of the relevant processes [Reina20]. For two slabs of semiconductor, this inhomogeneity is found to reduce the radiative heat transfer compared to that predicted by FE, however the discrepancy is generally only significant for slabs $> 1\,\mu$m thickness, indicating that the FE approach is sufficient in a wide terrain of experimental contexts.

1.4 Travelling and evanescent waves

All the work of the previous Sec. 1.2 establishing the framework of FE is worthwhile because it captures the contributions of all types of electromagnetic wave to the radiative heat transfer. Namely, the solutions of Maxwell's equations will include both travelling and evanescent waves which contribute additively. Conversely, the Planckian approach briefly recalled in Sec. 1.1 only takes into account travelling waves and hence does not provide reliable predictions in all settings. Here we briefly illustrate this fundamental difference in wave character and mention when we may expect the evanescent waves to play a role.

To simplify the illustration of the two possible wave characters, we restrict ourselves to a planar geometry. The two bodies transferring heat are infinite in extent in, say, the $x-y$ plane, but are restricted in the normal, or z, direction – for example parallel two-dimensional sheets, or three-dimensional half-spaces, both separated by some gap (see Fig. 1.5). In these cases the in-plane symmetry means that there is zero average lateral heat transfer (since each body is in equilibrium) and we seek the heat current in the z direction.

We take Maxwell's equations Eqns. (1.17) in vacuum which result in the wave equation for the electric field

$$\nabla^2\mathbf{E}(\mathbf{r},\omega) = -\frac{\omega^2}{c^2}\mathbf{E}(\mathbf{r},\omega), \tag{1.30}$$

and identically for the magnetic field. The solutions to this equation are plane waves, with spatial variation of the type $\mathbf{E}(\mathbf{r}) = \mathbf{E}_0 e^{i\mathbf{k}\cdot\mathbf{r}}$, where $\mathbf{k}$ is the three-dimensional wavevector. In general the wavevector may be decomposed into in-plane and z components, which according to Eq. (1.30) satisfy the relation: $|\mathbf{k}|^2 = k_\parallel^2 + k_z^2 = (\omega/c)^2$. Focusing on the z direction, it is therefore indicative to write the equation

$$k_z = \pm\sqrt{\frac{\omega^2}{c^2} - k_\parallel^2}, \tag{1.31}$$

revealing that k_z may be either real or imaginary, according to the relation between $k_\parallel$ and ω. For $k_\parallel < |\omega|/c$, the normal component is real, and so the wave travels, or propagates, in the z direction (as well as in x and y directions according to $\mathbf{k}_\parallel$). These waves may be reflected between bodies (perhaps multiple times leading to Fabry-Perot modes) before being absorbed, as shown in Fig. 1.5 (a). The travelling waves give the 'radiant' contribution to the heat transfer, which corresponds to the fraction of black body radiation predicted by Planck's law according to the material emissivity. According to the geometry of the problem, this energy may escape to infinity.

If instead $k_\parallel > |\omega|/c$, then $k_z = i|k_z|$ is imaginary and the wave propagation is confined to the plane, while the field strength decays exponentially in the z-direction according to $e^{-|k_z|z}$, as shown in Fig. 1.5 (b). The wave travels along the surface of the material, or in other words the field amplitude is oscillatory in the plane, while it decreases rapidly to zero away from the surface – this is known as an evanescent wave. Although evanescent waves do not propagate in the z-direction, and therefore may not carry energy away to infinity through the vacuum, they do contribute to the energy density of the field close to the material surface. When two bodies are placed in close vicinity of one and other, evanescent waves on the surface of each body may be 'felt' by the other body, and lead to a contribution to the heat transfer – this process is known as photon tunnelling. Although this mechanism is inherently 'non-radiative', the evanescent wave contribution is nonetheless referred to as a form of radiative heat transfer, since the transfer of heat occurs via the electromagnetic field (see Fig. 1.1).

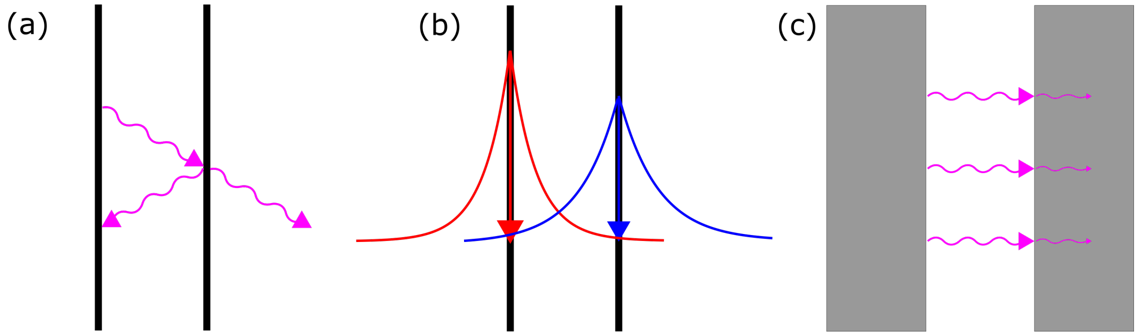

Figure 1.5: Illustrations of the possible wave types and phenomenon for planar geometries: (a) and (b) show two-dimensional layers while (c) is three-dimensional semi-infinite bodies. (a): $k_{\parallel} < |\omega|/c$ leads to reflection and transmission of travelling waves. Finite transmission means some energy may 'escape' to infinity. (b): $k_{\parallel} > |\omega|/c$ leads to the formation of evanescent waves that travel along the hot (red) and cold (blue) layers. The exponential decay of the field strength away from the body surfaces is indicated. (c): for semi-infinite bodies the incoming radiation is entirely attenuated within the body, leading to an equivalence of the Joule losses and the average Poynting vector in the gap.

The two contributions to the heat transfer from travelling and evanescent waves are additive and therefore either one may be dominant. The travelling waves are known to dominate when bodies are separated by large distances, where the relevant length scale is the decay scale of the evanescent waves, $|k_z|^{-1}$. This decay scale is often, but not always, determined by the thermal wavelength of photons at the temperature of the source, $\lambda\!\!\!^{-}_T = \hbar c/T$ (for example, $\lambda\!\!\!^{-}_T = 7.6\,\mu$m at $T = 300\,$K). So for bodies at higher temperatures, the field strength of evanescent waves is larger at the surface, but decays faster away from the surface, as indicated in Fig. 1.5 (b). In the near field, where the separation is less than the thermal wavelength, we may expect evanescent wave dominance, leading to a significant enhancement of the overall heat current predicted by Planckian theory including material emissivity, which is said to be valid only in the far field (separation larger than the thermal wavelength). Since its earliest predictions by Polder and Van Hove [Polder71], this enhanced near-field radiative heat transfer has become a burgeoning field of research. A brief timeline of theoretical and experimental works as well as a discussion of some applications of these advances is given in Sec. 1.5. The competition between near-field and far-field contributions is investigated thoroughly in Ch. 2.

We make an important remark regarding the different planar geometries shown in Fig. 1.5. In the case of semi-infinite bodies [Fig. 1.5 (c)], all the energy carried by the electromagnetic field in the gap is eventually dissipated in the material, and therefore the Joule losses [as defined in Eq. (1.25)] per unit area are equal to the average of the z-component of the Poynting vector, Eq. (1.20), in the gap. In the case of metals, the absorption occurs very quickly on the scale of the skin depth [Abrikosov88], but even if the absorption is slow (for example, in dielectrics), the field has nowhere to escape so will eventually be attenuated via the Joule heating. On the contrary, for two-dimensional layers or finite width slabs, there may be a part of the energy which is transmitted by the media and escapes to infinity [Fig. 1.5 (a)]. In these cases the Joule losses are therefore not equal to the Poynting vector in the gap, but rather the Poynting vector in the gap minus the Poynting vector on the other side of the medium. Whether the radiation transmitted by the medium escapes or not is dependent on the particular experimental setup, and so in order to compare experiment to theory one must take careful note of how the measurement is taken (discussed further in Sec. 2.2.5).

Finally, we discuss briefly which frequencies give particularly strong contributions to the heat transfer. This is determined by the energetic behaviour of the relevant charge carriers, or the dispersion relation, of the material. As postulated by Planck, energy may only be received and emitted in finite packets, and the size of these packets corresponds to energy level transitions in the material. For a metal, the behaviour of the interacting unbound electrons responsible for the heat transfer may be found via perturbation theory in the random phase approximation (RPA). In this picture, the energy is stored in electron-hole excitations around the Fermi surface allowing a continuum of radiation to be emitted and absorbed [Bruus04]. The electron-hole excitations represent pairs of fermions, and are therefore bosonic in their statistics as reflected by the appearance of the Bose-Einstein distribution function in the FDT.

Meanwhile, the electrons may also form collective charge density oscillations known as plasmons [Bruus04]. Similarly to phonons which describe collective oscillations of ions in a material, plasmons may be thought of as quasi-particles that may be created or destroyed via the absorption or emission of radiation of a particular frequency and wavevector, determined by the plasmon dispersion relation. Plasmon excitations may therefore lead to resonances in the absorption and emission spectra, and eventually provide the dominant channel for heat transfer depending on the material and experimental parameters. For three-dimensional metals, plasmons may propagate either through the bulk, or along the surface as evanescent waves. Bulk plasmons are typically activated at higher frequencies than surface plasmons and are therefore less likely to play a significant role in the heat transfer [Abrikosov88]. Information about all the material excitations is encoded in the response functions – in particular, plasmons appear as damped poles in response functions dressed by interactions with the field. The potential role of surface plasmons in radiative heat transfer represents an active area of research (see Sec. 1.5) to which this thesis contributes in Ch. 3.

1.5 Near-field enhancement

In the previous sections we have described the most common framework used to solve problems of radiative heat transfer: fluctuational electrodynamics. This framework has been used to reveal that radiative heat transfer may be different, and in particular enhanced, with respect to the Planckian picture. Typically this enhancement occurs in the near field, where the evanescent waves not accounted for in Planck's law provide the dominant channel of heat transfer. We note immediately that there exists in the literature two similar measures for the near-field enhancement: the ratio of the total radiative heat current with respect to (i) the heat current exchanged by black bodies given by Stefan Boltzmann, and (ii) the actual far-field radiative heat current based on the material emissivity (less than black-body radiation since no real material is a perfect emitter/absorber). Although quantitatively different, both measures (i) and (ii) correspond to an increase in the radiative heat transfer due to the dominance of separation dependent evanescent wave contributions.

Numerous theoretical works have been devoted to the calculation of this enhancement, and also to the identification of the physical mechanisms responsible. Meanwhile, a wide range of experiments have been conducted using different materials, geometries and temperatures in order to probe these effects. Excellent review papers are available [Joulain05, Volokitin07, Basu09, Song15a, Cuevas18, Biehs21], however in this section we give historical context and discuss the most important theoretical and experimental advances that set the stage for the original work contained in this thesis. We also provide a discussion of possible applications of near-field radiative heat transfer, which represents a growing field of technological research and development.

1.5.1 Theoretical studies

The prediction of near-field enhancement of radiative heat transfer dates to the earliest works by Rytov himself [Rytov53], where he suggests that the energy flow between bodies could increase "without limit" as the spatial separation between them decreases. This points immediately to the principal difference of near-field radiative heat transfer, to that of the far field: dependence on the body separation, d. In the far field in the planar geometry the heat transfer does not depend on d, while near-field contributions increase as bodies move closer. As discussed in Sec. 1.4, this reflects the fact that in the near field the waves responsible for transferring heat are evanescent, whose strength decays exponentially with d – in the particle picture of light this process may be seen as photon tunnelling. Typically, this dependence on d is what facilitates the enhancement of the heat transfer with respect to the far field, where the transfer is independent of the separation [as in the Stefan-Boltzmann law, Eq. (1.4)].

After some only partially successful attempts to calculate near-field radiative heat transfer [Emslie62, Cravalho67, Olivei68], Polder and Van Hove provided the first complete study of radiative heat current via FE between three-dimensional metals [Polder71]. In this seminal work the authors treat the case of two chromium half-spaces described by local Drude optical response separated by a vacuum gap – the geometry considered here of three-dimensional semi-infinite half-spaces would go on to be the most studied. The contributions of evanescent and travelling waves of transverse electric (TE) and transverse magnetic (TM) polarisations are separated naturally. The authors provide semi-analytical results in terms of integrals but also give approximate closed-form expressions in limiting cases revealing the dependence of the heat current on temperature and separation (these expressions are rederived in this thesis in App. B). The major results of Ref. [Polder71] have been beautifully reproduced in Ref. [Song15a], as shown in Fig. 1.6.

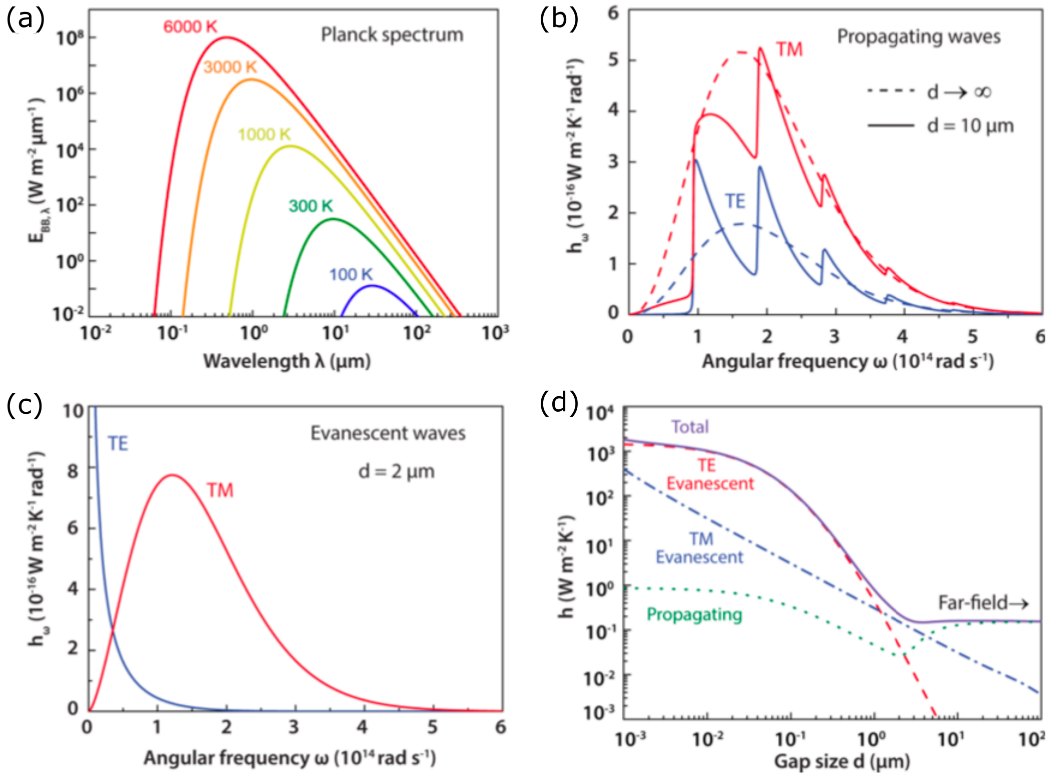

Figure 1.6: Numerical results for radiative heat transfer between two chromium half-spaces around room temperature as studied in Ref. [Polder71], reproduced in Fig. 1 of Ref. [Song15a]. (a) Black-body spectral power given by Planck's law [closely related to Eq. (1.2)] in terms of wavelength for a variety of temperatures. (b) The spectral heat transfer coefficient as a function of frequency, h_ω, defined as the derivative with respect to temperature of the heat transfer spectrum for propagating waves of both polarisations for gap sizes $d = 10\,\mu m$ and $d \to \infty$. The solid lines clearly indicate the effects of wave interference. (c) h_ω for evanescent waves of both polarisations for gap size $d = 2\,\mu m$. (d) Total heat transfer coefficients, h, for the different wave types and polarisations, as well as the total indicating the vast enhancement of the heat transfer in the near field over the far-field result predicted by Planck's law. Material parameters for the chromium bodies described by Drude conductivity come from Ref. [Polder71].

As shown in Fig. 1.6 (d), the work of Ref. [Polder71] concludes that depending on the separation either the TM or TE evanescent contribution may dominate the heat transfer in the near field (remember $\lambda_T = 7.6\,\mu$m at $T = 300$ K) and be responsible for the enhancement over the far-field result. At separations of a few microns it is the TM polarisation [see Fig. 1.6 (c)] while at even smaller nanometric separations TE evanescent waves provide the dominant contribution that results in an enhancement by many orders of magnitude with respect to the far-field result. This dramatic divergence from the Planckian theory becomes a familiar theme in the subsequent field of near-field radiative heat transfer. Although illuminating, the work of Polder and Van Hove calculated only the derivative with respect to temperature of the heat current, and so was only valid for small temperature differences between materials. They also did not address the possible effects of spatial dispersion in the material conductivity.

After some further contributions by Caren [Caren72a, Caren72b, Caren74], the next pioneering work came from Levin, Polevoi and Rytov [Levin80]. This very general study investigated good conductors in the three-dimensional half-space geometry in the normal and anomalous skin effect regimes, allowing in principle for anisotropic media with spatial dispersion. Unlike in Polder and Van Hove, the heat current itself is calculated meaning there is no restriction on the difference in temperature of the two bodies. Results are given in terms of generalised surface impedance tensors and the authors indicate that spatial dispersion in the conductivity could play a role at very small separations.

Fairly few papers on radiative heat transfer appeared in the following years. Loomis and Maris performed a calculation similar to that of Polder and Van Hove investigating the role of the dc conductivity of Drude metals on the temperature and separation dependence of the heat current [Loomis94]. Pendry offered an alternative viewpoint on the subject of near-field radiative heat transfer [Pendry99], in which he considered different wave vectors as channels for heat transfer via tunnelling, and suggested an upper limit for the heat flux through each channel related to quantum information theory. Around the turn of the millennium, the field was reinvigorated by a variety of works. In Ref. [Volokitin01] the heat current between three-dimensional half-spaces is first cast in a simple general form in terms of the material reflectivities – we derive the analogous, almost identical expression for the heat current between two-dimensional layers in Sec. 2.1.

The continued reinvigoration of the field of radiative heat transfer has largely been driven by investigations into the roles played by two material-dependent phenomena:

- Collective excitations, in particular resonant surface waves
- Spatial dispersion in the conductivity, representing spatial nonlocality in the material response

Coupled with the emergence of new geometries made experimentally relevant through modern fabrication methods and the advent of two-dimensional materials, the above phenomena have inspired the growth of the field of near-field radiative heat transfer in the 21st century. Below we review some of the most significant advances made in the context of this thesis.

The first avenue of exploration taken by theoretical works on radiative heat transfer has to do with collective phenomena, notably resonant surface waves. In doing so, works appear focussing not only on metals (as in the aforementioned papers) where the (low frequency) optical response is determined by conduction electrons, but also on dielectrics, where optical phonons are responsible for heat exchange. For dielectrics, the phonons represent the resonant excitations, while in metals they are surface plasmons.

The phonons and surface plasmons describe collective oscillations of the crystal lattice and electron densities, respectively. These excitations couple to electromagnetic surface waves, forming surface phonon polaritons (SPhPs) and surface plasmon polaritons (SPPs), respectively. These are manifested by peaks in the emission and absorption spectra of the materials, and so depending on the parameters and experimental conditions they may provide a significant channel for radiative heat exchange. Meanwhile, more complex geometries are also studied, motivated by the concurrent experimental realisations that shall be discussed in Sec. 1.5.2. For some examples of theoretical works one may see Ref. [Volokitin01] for a sphere and a plane, Ref. [Narayanaswamy08a] for arbitrary sized spheres or Refs. [Chapuis08a, Chapuis08b] for nanoparticles.

As mentioned, the materials treated in the literature essentially fall into one of two categories: metals and doped semiconductors, where the charge carriers are free, or dielectrics, where they are bound. The focus in this thesis is on metals, however we briefly mention some notable contributions to the study of radiative heat transfer via SPhPs in polar dielectrics. Mulet et. al [Mulet01b, Mulet02] showed that the already enhanced near-field heat transfer between a small spherical particle and a semi-infinite bulk may be even further enhanced if either the surface or the particle support resonant surface waves, in which case the heat transfer becomes almost monochromatic. Similarly, Ref. [Francoeur08] investigated radiative heat transfer between a thin film and a semi-infinite half-space of silicon carbide (SiC). As shown in Fig. 1.7, the heat transfer is essentially monochromatic at the resonant frequency given by the SPhP dispersion of the system. In fact, the resonance comes about via the coupling inside the film of the evanescent waves on the opposing surfaces of the film, and therefore the SPhP contribution increases as the SiC film thickness decreases – as shown in the inset of Fig. 1.7.

Another numerical study investigated the effect of adding a thin dielectric film to a metallic emitter [Fu09] reporting that the heat transferred to a metallic receiver may actually decrease as a result. This is because although the SPhPs enhance the contribution of TM polarisation (SPhPs and SPPs exist only in TM polarisation for nonmagnetic materials [Joulain05]), the dominant TE contribution (TE is known to be dominant for metals in the near field, as found in Refs. [Polder71, Chapuis08a] and we investigate later in Ch. 2) is actually reduced as the effective distance between the metals increases due to the dielectric film.

The behaviour and potential role of surface plasmon polaritons (SPPs) in metals is very similar to the above discussion of SPhPs in dielectrics. Ref. [Biehs07] looked at the effect of adding a metallic film to various dielectric and metal substrates, providing estimates for the effect that the added surface plasmon coupling may have on the separation dependence of the near-field energy density. Recently, many studies have found that SPPs may dominate the radiative heat transfer between two-dimensional materials such as graphene and hexagonal boron nitride monolayers [Svetovoy12, Ilic12, Rodriguez-López15, Jiang17, Zhao17, Zhang19] – the materials are doped such that the charge carriers are free. Similarly, radiative heat transfer between highly doped silicon has been shown to be dominated at sufficiently small separations by a SPP contribution [Rousseau09a]. On the other hand, working in the Coulomb limit Ref. [Mahan17] con-

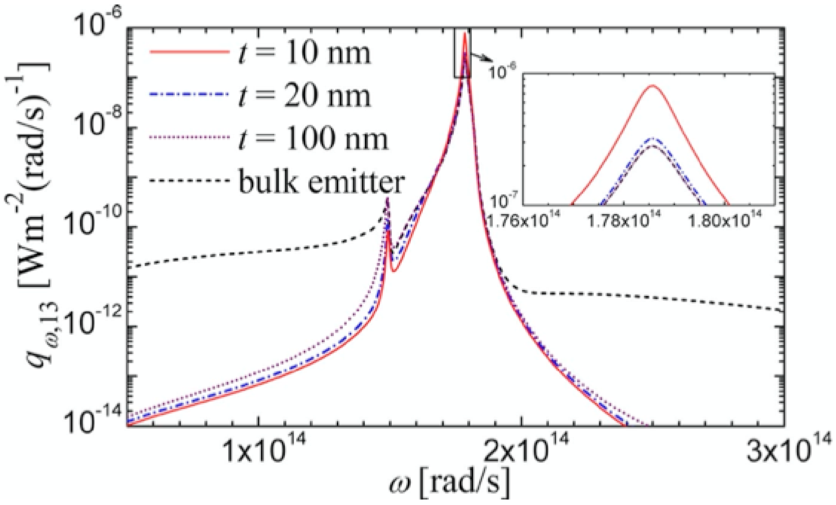

Figure 1.7: Numerical calculation of the spectrum of the radiative heat flux between a SiC film of thickness t (imagined to be suspended in vacuum at 300 *K, emitter) and bulk SiC (at* 0 *K, receiver) separated by a* 10 *nm vacuum gap. The large peak corresponds to the resonant frequency of the SPhP of the SiC emitter, while the small peak corresponds to the tunnelling of regular evanescent waves. The contribution of the former increases as the film thickness, t, decreases (since the coupling of surface waves on opposite sides of the film increase with decreasing thickness), while that of the latter decreases as the film thickness (and therefore volume) decreases. Fig. 2 in Ref. [Francoeur08].*

cluded that surface plasmons were unimportant for the heat transfer between semi-infinite metallic half-spaces. Whether or not plasmons make a substantial contribution to the heat transfer may depend on the energy scales in the problem – for room temperature the thermal photons typically responsible for energy exchange are at around 25 meV, while a surface plasmon of a typical bulk metal may have energy larger than 2 eV so will not be excited [Rousseau09a]. For doped semiconductors and two-dimensional materials the plasmon frequency may be tuned allowing one to modulate the resulting heat transfer [Svetovoy12].

Regarding the effects of spatial dispersion in the conductivity, Chapuis et al. [Chapuis08c] studied its effect on near-field radiative heat transfer between semi-infinite metallic half-spaces by using two different nonlocal models for the dielectric function. The main conclusion of the work is that the effects of spatial dispersion are negligible for gaps larger than a few nanometers, while for even smaller gaps the nonlocality produces a saturation in the radiative heat flux as $d \to 0$. This is in contrast with the divergence as $\sim 1/d^n$ with some power n predicted by the local theory, whose physicality has been debated (see Ref. [Pan00] and the associated comment Ref. [Mulet01a], and also the discussion in Ref. [Joulain05]). Ref. [Svetovoy12] also implemented a nonlocal dielectric function in their numerical study of graphene, however the effects of the spatial dispersion are difficult to extract – we perform an analytical calculation using the same nonlocal model in Ch. 3.

Finally, of particular interest to this thesis are two recent theoretical studies focusing on two-dimensional metal layers, which is a system that has received far less attention than the three-dimensional one. Ref. [Kamenev18] performed an analytical calculation in the Coulomb limit ($c \to \infty$, where c is the speed of light) comprising contributions coming from clean and diffusive limits of the metallic conductivity. Treating the disorder in this way the author reported no plasmonic contribution to the radiative heat transfer between the layers. On the other hand, treating the full electromagnetic interaction Ref. [Wang19] provides a numerical study of ultrathin films of silver modelled by a local Drude conductivity. The authors report a dominant contribution that is associated with optical and acoustic branches of the coupled surface plasmons in the system, exhibited by the peaks in the energy transmission coefficient seen in Fig. 1.8 (b).

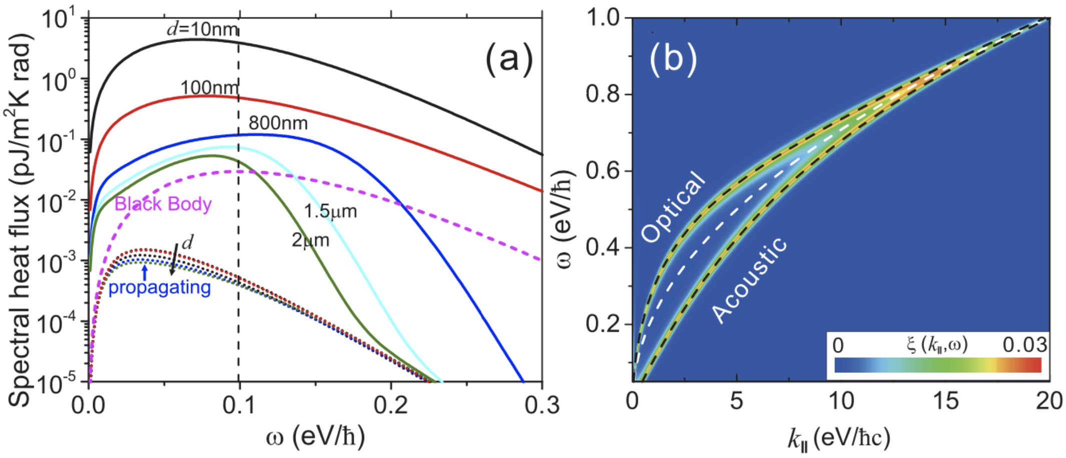

Figure 1.8: Results of a simulation of radiative heat transfer between two theoretically imagined silver monoloayers, held near room temperature. (a) Spectral heat flux [the same quantity seen in Figs. 1.6 (b) and (c)] for different gap sizes. Solid lines are the total heat flux while the dotted lines give the contributions from travelling waves only. Note that the x-axis scale is linear while the y-axis scale is logarithmic. (b) The energy transmission coefficient for $d = 50\,nm$ *indicating the optical and acoustic plasmon branches that come about due to the splitting of the dispersion relation of plasmons in a single silver monolayer, shown by the white dotted line. Fig. 2 in Ref. [Wang19].*

Ref. [Wang19] concludes that the effect of plasmons diminishes as the number of atomic layers of silver (i.e. the layer thickness) increases, in agreement with previous works. The general focus of this and many of the works in recent years has been on including precise details of particular materials leading to detailed and sometimes heavy numerical simulations. In our work we perform analytical calculations using more general, widely-applicable models. In doing so, we find that we are able to make conclusions about physical ingredients such as surface plasmons and spatial dispersion that have not been seen in these previous works.

1.5.2 Experimental studies

Ever since its theoretical prediction researchers have attempted to design experiments to observe the near-field enhancement of radiative heat transfer. The experiments have varied widely in terms of the materials used, size of the setup and temperature range probed. One interesting classification of the experiments performed to date may be seen in Fig. 1.9.

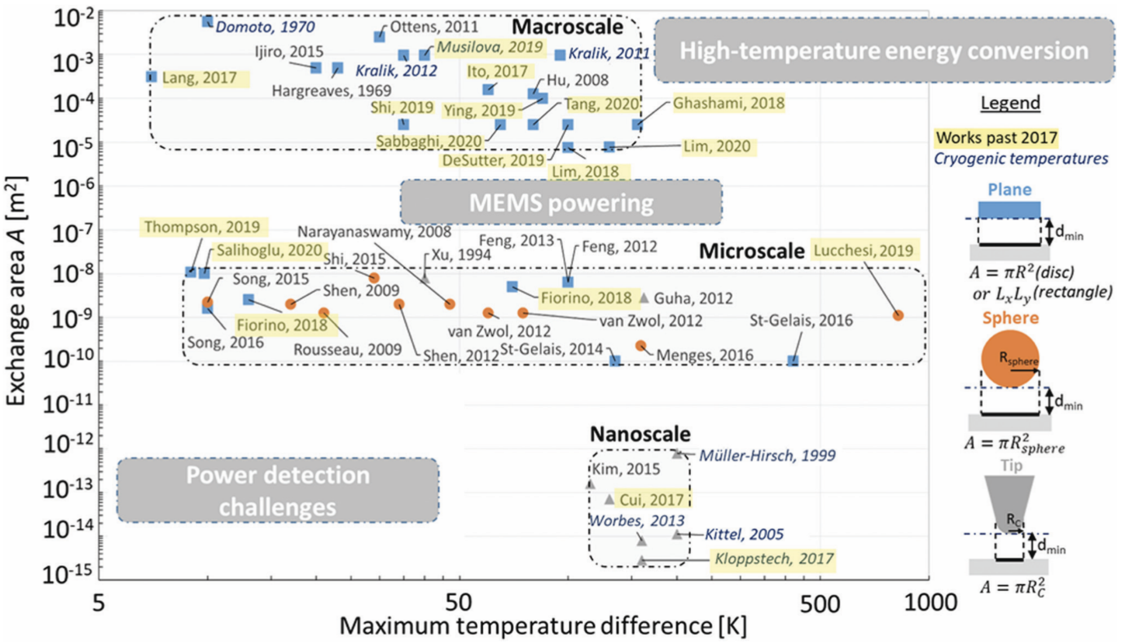

Figure 1.9: Classification of experiments on near-field radiative heat transfer according to heat exchange area and temperature difference between emitter and receiver. Also indicated is the geometry of each corresponding experiment: parallel plates, sphere-plate or tip-plate. Fig. 2 in Ref. [Lucchesi21].

As shown in Fig. 1.9, the classification of experiments according to exchange area and temperature difference leads to the fairly natural separation of the three main geometries investigated: parallel plates, sphere-plate and tip-plate. The work of this thesis focuses on macroscopic parallel plates (upper dot-dashed rectangle of Fig. 1.9), and so in this section we briefly sketch the history focusing on some of these experiments.

While proposing some of the earliest theoretical attempts to incorporate evanescent wave contributions [Cravalho67], the same group reported the first near-field heat transfer measurements between parallel plates [Cravalho68, Domoto70]. Their experiment consisted of parallel copper disks immersed in liquid helium with the top disk being heated by a few degrees via resistors to act as the emitter. The radiative heat current was estimated by measuring the increase in temperature of the receiver. Modifying the spatial separation between 2 mm and 10 μm the heat current was observed to increase as the separation decreased, the hallmark feature of near-field radiative heat transfer. However, due to the lack of a complete theoretical description at the time, it was difficult to draw strong conclusions and the experiment suffered from a lack of control over the parallelism of the disks.

Hargreaves performed a similar experiment where he measured the heat current between 100 nm thick chromium layers on pyrex disks separated by vacuum [Hargreaves69]. His preliminary results [Hargreaves69] followed by more precise measurements reported in his PhD thesis [Hargreaves73] represented the first experiment performed at room temperature. The emitter and receiver plate temperatures were measured by embedded thermistors and the heat current was estimated by the heat input required to keep the emitter at a constant temperature. As shown in Fig. 1.10 (adapted in Ref. [Song15a] from Hargreaves' thesis [Hargreaves73]), the heat current exhibited a strong dependence on the gap size and matched rather well the theory from Polder and Van Hove [Polder71] (dashed curves). Experimental control over the separation and the parallelism of the plates was ensured by piezolelectric ceramic tubes, which could be adjusted according to capacitance measurements at three different locations between the layers, indicated in the schematic in Fig. 1.10 (inset).

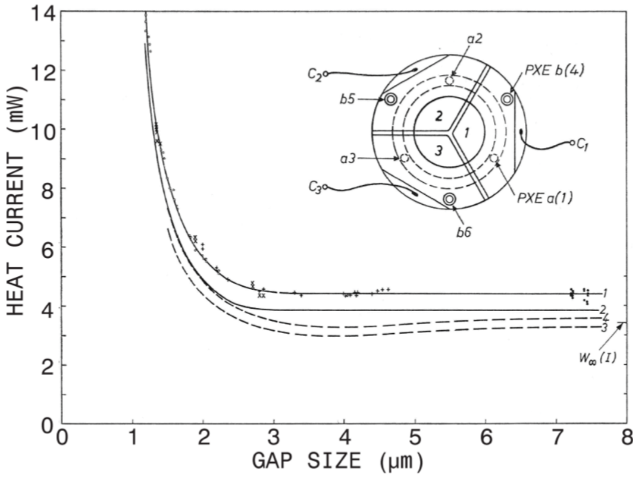

Figure 1.10: Results for heat current versus gap size between chromium-coated surfaces at 313 K *and* 295 K*, adapted in Ref. [Song15a] from Hargreaves' thesis [Hargreaves73]. Solid lines are fits to the experimental data before (1) and after (2) accounting for heat losses to the environment, while dashed lines are theoretical results from Ref. [Polder71] with Drude model values from literature (3) and fitted empirically (4). Inset: schematic top view of receiver surface indicating the three sectors that couple to analogous areas on the emitter surface to act as capacitors to tune surface parallelism.*

Issues around plate parallelism and surface roughness persisted preventing sub-micron gap sizes, which led to a long drought in experiments on the parallel plates geometry. In the meantime, the development of the scanning tunnelling microscope and atomic force microscope inspired interest in near-field heat transfer in the tip-plate geometry. Using a nanometric sharp tip and a planar sample allowed experimenters to delve deeper into the near field reaching minimum gap sizes of ~ 1 nm, without the technical challenges of alignment. The trade-off was that the radiative heat currents associated with such small exchange areas (see lower dot-dashed rectangle, Fig. 1.9) become extremely small and so the method of measurement must have a high resolution.

Nevertheless a wave of experimental research followed in near-field radiative heat transfer in systems of this geometry, including the inventions of scanning thermal profiler [Williams86, Xu94] and scanning thermal microscope [Müller-Hirsch99] (for a more detailed discussion see Ref. [Song15a]). A particular study by Kittel et al. [Kittel05] measured the heat transfer in a scanning thermal microscope setup comprised of a gold tip and a gold or gallium nitride surface. The separation between the room temperature tip and the 100 K surface was decreased from 200 nm down to 1 nm, revealing enhancement of 3 orders of magnitude relative to far-field values. Interestingly, the heat current appears to saturate for gaps less than 10 nm, in contrast to the power-law divergent behaviour at vanishing separation predicted by earlier studies [Polder71, Pan00]. As mentioned in the previous section, this effect was subsequently attributed to spatial dispersion in the material response [Kittel05, Chapuis08c].

Sphere-plate geometries [Narayanaswamy08b, Shen09, Rousseau09b, van Zwol12a, van Zwol12b, Song15b, Lucchesi19] and integrated microelectromechanical systems (MEMS) [St-Gelais14, St-Gelais16] have also been heavily investigated due both to the reduced technical challenge surrounding alignment compared to the macroscopic parallel plates geometry, and larger exchange area compared to tip-plate setups. In some sense these setups represent a compromise that has allowed the experimental exploration of some of the outstanding phenomena related to near-field radiative heat transfer. However, a small number of modern experiments have nonetheless been devised to further probe the elegantly simple geometry of parallel plates. Other than its theoretical simplicity, the interest in this old problem has also been rekindled due to the development of thin film fabrication techniques and the advent of two-dimensional materials. We describe some of these modern experiments, to which we explicitly compare our theoretical work in Ch. 2, in the following paragraphs.

After some experiments on dielectrics [Hu08, Ottens11] exhibited strong enhancement beyond the blackbody radiation limit due to SPhPs, the first investigation of macroscopic metal plates in around 40 years was due to Kralik et al. [Kralik12]. In particular, they performed measurements of heat transfer between two 150 nm thick tungsten layers on 2.5 mm thick, 35 mm diameter alumina substrates over a wide range of vacuum separations ($1-500\,\mu$m) and cryogenic temperatures ($T_1 = 5\,$K, $T_2 = 10-40\,$K). As shown in Fig. 1.11 (a) [Kralik11], the hot sample is brought into the vicinity of the cold sample via a differential screw, while the parallelism between the two is carefully controlled via a mechanical equaliser. The heat flux meter at the cold sample consists of a calibration heater, a thermal resistor and a copper thermal stabilisation wing, which together provide direct access to the temperature of the cold sample itself, without influence of the substrate or sample holder beneath it. This important experimental specificity determines whether or not the radiation emitted/absorbed by the substrate should be taken into account in a theoretical model – this is discussed in more detail in Sec. 2.2.5.

The results are shown in Fig. 1.11 (b) for the heat current normalised to that of black bodies against the product of the hot temperature and the gap size, for which the authors observe a data collapse. Near-field behaviour is observed (i.e. gap size dependence) for separations less than $\lambda_{\max}/3$, with enhanced heat currents reaching 10^2 and 10^4 times the black-body and far-field values, respectively, for the smallest gap sizes. There is good agreement with numerical simulations that are based on a Drude model of parallel finite thickness metallic slabs where the material constants are used as fitting parameters.

A recent room temperature study recorded radiative heat transfer between 100 nm gold layers on two silicon microdevices, with an effective exchange area of $48 \times 48\,\mu\text{m}^2$

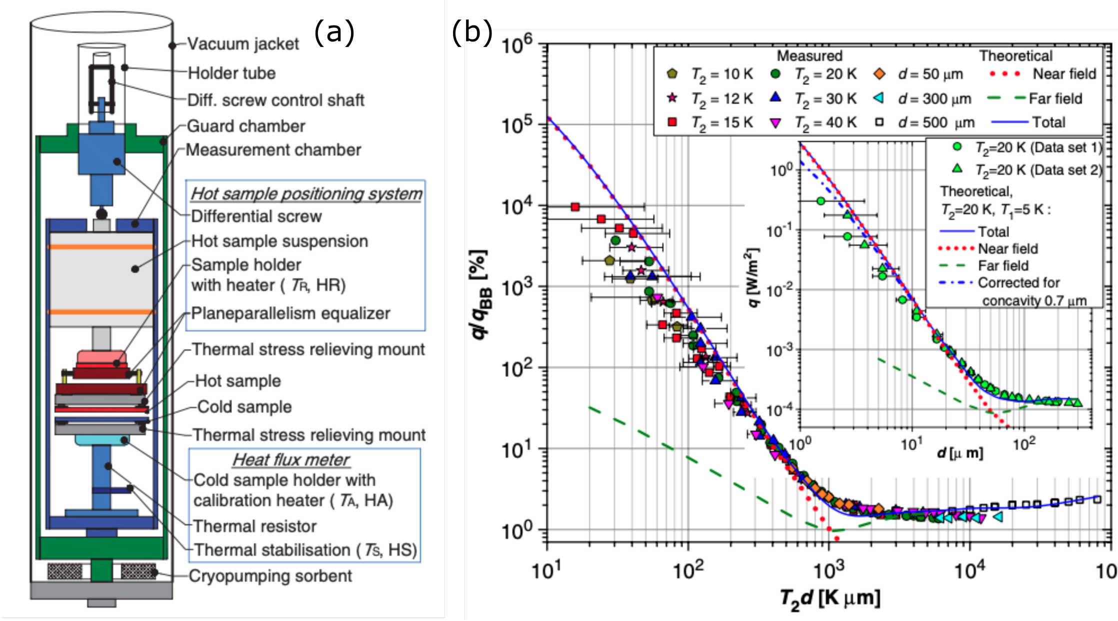

Figure 1.11: (a) Scheme of experimental apparatus used for near-field radiative heat transfer measurements between tungsten layers. Fig. 1 in Ref. [Kralik11]. (b) Results for the radiative heat current normalised to the black-body result against the product of the hot sample temperature, T_2, and the gap size, d. Lines correspond to numerical calculations based on a Drude model where the electron scattering time is used as a fitting parameter. Inset: Results from two experimental runs for $T_2 = 20\,K$. Fig. 2 in Ref. [Kralik12].

[Song16]. A custom nanopositioning system allowed the emitter and receiver to be brought within $< 100\,\text{nm}$ of each other via a piezoelectric actuator, while also precisely controlling the parallelism via a motorised goniometer. Once again by measuring temperature changes in the receiver, they observed strong gap dependence on the thermal conductance below a certain threshold, and enhancements of 10 and 10^3 times the black-body and far-field values, respectively. The data is shown along with results of theoretical modelling in Fig. 1.12 (a). The computed spectral conductance shown in Fig. 1.12 (b) are broad indicating that the near-field enhancement is a result of non-resonant evanescent modes, as expected since the surface plasmons in the gold layers are not thermally excited.

A recent work [Sabbaghi20] sought to combine the macroscopic heat exchange area of the type in Ref. [Kralik12] with the nanometer sized gaps like those of Ref. [Song16]. Sabbaghi et al. used nanosized polystyrene particles to create a fixed nanometer-sized gap between aluminium thin films of varying thicknesses $13-80\,\text{nm}$ on $5\times 5\,\text{mm}^2$ silicon substrates. The experiment is performed around room temperature, with the emitter heated such that $\Delta T = 25-65\,\text{K}$. The authors observe that the radiative heat flux increases as the film thickness decreases, and for the thinnest films and largest temperature difference they obtain similar order of magnitude enhancements over far-field (6.4×) and black-body (420×) results as previous works.

The fixed gap size was determined via fitting heat transfer measurements for bare silicon separated by the same solution of polystyrene particles, which led to a large degree

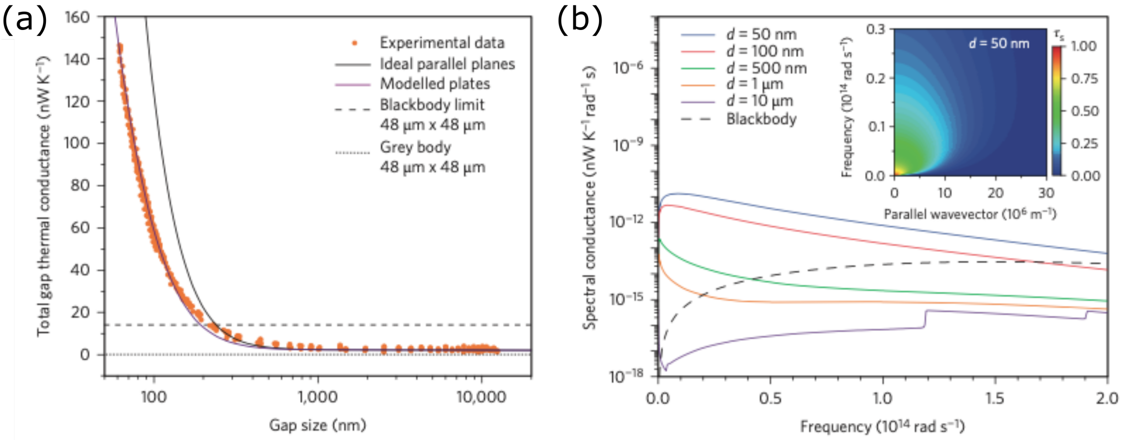

Figure 1.12: (a) Experimentally measured radiative thermal conductance between gold layers as well as computational data based on a Drude model for the dielectric function from Ref. [Ordal83]. (b) Computed spectral conductance curves indicating contributions from a broad range of frequencies. Inset: Radiative heat transfer transmission coefficient for the TE modes at $d = 50\,\text{nm}$. Fig. 4 in Ref. [Song16].

of uncertainty: $d = 215^{+55}_{-50}\,\text{nm}$. Considering the high sensitivity to gap size expected in the near-field regime, this uncertainty made comparisons to theory unconvincing. In particular, we question the experimental observation that the thermal conductance is independent of the layer thickness in Sec. 2.3. In addition, according to the experimental setup the receiver temperature was actually measured behind the substrate, meaning the radiation associated with the silicon should also be taken into account.

We make one general comment on the experiments discussed on conventional metal films [Kralik12, Song16, Sabbaghi20] regarding the plate thickness. The numerical simulations that usually accompany the experimental results are generally performed for finite thickness slabs. While more precise they become computationally heavy, and in order to make theoretical progress analytically one should determine whether, according to the thickness, the plates better correspond to three-dimensional half-spaces (like those most studied, e.g. Ref. [Polder71]) or two-dimensional sheets (like those studied in the remainder of this thesis). Even for thin films, it is not a priori clear which is the appropriate approximate model, and one must compare the plate thickness to material skin depth (see Sec. 2.3 for a continued discussion).

The question of three-dimensional half-spaces versus two-dimensional sheets is self-evident when regarding atomically thin two-dimensional materials such as graphene and transition metal dichalcogenides. A recent experiment measured radiative heat flux between $2 \times 2\,\text{cm}^2$ doped monolayer graphene sheets ($E_F = 0.27\,\text{eV}$) on insulating silicon, separated by a fixed $430 \pm 25\,\text{nm}$ vacuum gap ensured by four photoresist posts [Yang18]. As in the case of Ref. [Sabbaghi20], the temperature measurement takes place in a copper layer behind the substrate so the substrate radiation (albeit small for insulating silicon) is captured. Indeed the experimental results for the radiative heat current measured between the insulating silicon substrates with and without the graphene layers as a function of the emitter/receiver temperature difference are shown in Fig. 1.13 (a).

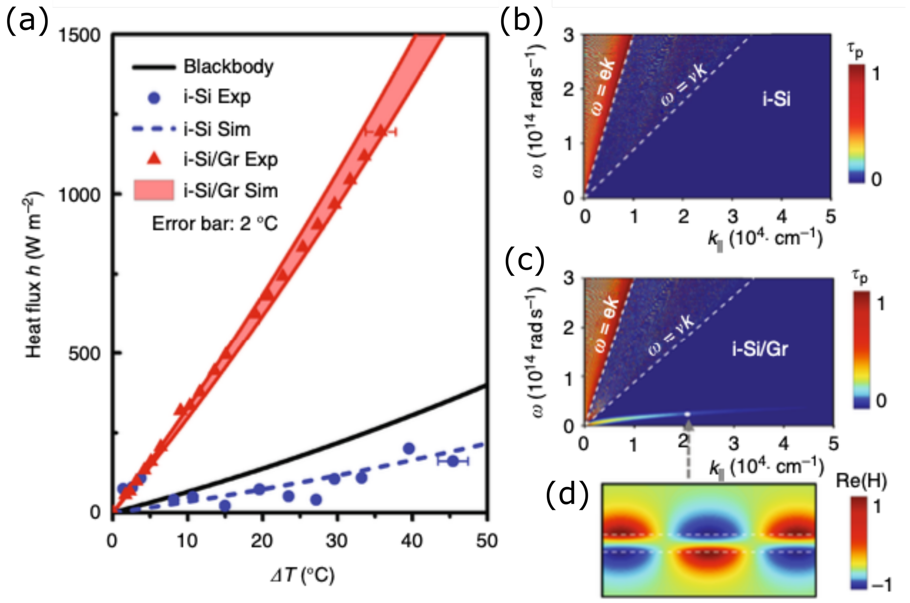

Figure 1.13: (a) Measured heat current density between insulating silicon substrates with and without layers of monolayer graphene as a function of temperature difference where the receiver temperature is $30\,^{\circ}C$*. Simulations based on measured material parameters and gap size including uncertainties. (b), (c) TM polarisation photon transmission probability for* $\Delta T = 50\,^{\circ}C$ *without and with graphene, respectively. The steep dashed lines should read* $\omega = ck$*, where* c *is the speed of light in vacuum. (d) The magnetic mode pattern of the plasmon peak at a point in the* $\omega - k_{\|}$*-plane. Fig. 3 in Ref. [Yang18].*

Fig. 1.13 (a) shows enhancement in the heat flux with respect to the black-body limit due to the presence of the graphene layers by a factor of nearly 4.5 at $\Delta T = 36\,^{\circ}\mathrm{C}$. The surface plasmons of graphene are thought to be primarily responsible for the enhancement of the radiative flux, as indicated by Figs. 1.13 (b) and (c). They show the computed TM polarisation photon transmission probability across the gap without and with the graphene layers, respectively. While the pattern inside the silicon light cone (above the line $\omega = \nu k$, where ν is the speed of light in silicon) remains largely unchanged, the addition of graphene introduces a peak outside the silicon light cone associated with a plasmonic resonance coupled to evanescent modes, i.e. a surface plasmon polariton. Yang et al. go on to repeat the experiment with doped silicon substrates where the graphene plasmons are also visible, and propose a thermophotovoltaic cell based on this heterostructure, which is an idea that will be discussed further in the next section.

1.5.3 Applications of near-field heat transfer

Now that the theoretical descriptions and experimental observations of enhanced radiative heat transfer have been discussed in the previous sections, it is important to ask what impact these phenomena may have on the real world. In this section we discuss very briefly some of the novel techniques and devices that are direct applications of the fundamental physics explored in this thesis. For more thorough discussions one may refer to the relevant sections on applications in the reviews [Basu09, Lucchesi21, Song21].

Before launching into how researchers are attempting to wield near-field radiative heat transfer to their advantage, it should be noted that its effects may also be parasitic. As the miniaturisation of electronics has progressed steadily, near-field effects not originally accounted for in device design may come into play and cause undesired behaviour. The distribution of heat is generally critical to device performance and durability, so it is vital to understand how different parts of engineered devices may exchange heat, even when galvanically isolated. One can easily imagine that the massive enhancement that has been demonstrated leads to the possibility of heat leakage, which could even result in device failure. If the trend of miniaturisation is to continue, this may prompt a redesign of certain ubiquitous micro and nanoelectronics components.

On the other hand, the radiation in the near field may be used to our advantage. Near-field radiation invites a wide variety of novel applications not only due to its increased magnitude – i.e. the enhancement that has occupied most of the previous sections – but also due to its coherence properties. As has been widely studied [Carminati99, Henkel00, Greffet02, Marquier04, Laroche05, Greffet07], depending on the materials and geometries of bodies involved, the spatial and temporal coherence of radiation in the near field may be very different to typical incoherent thermal (far-field) radiation. A particular example is the possibility of quasi-monochromatic radiation emitted by a system dominated by resonant surface waves, like those discussed previously due to SPhPs or SPPs. The concentration of energy around a particular frequency makes this radiation more desirable for certain applications than the typical broad-band radiation emitted by a black body.

The exploitation of coherence properties and enhancement of near-field radiation has led to wide-ranging applications. A nanofabrication method known as thermal lithography has been proposed as an alternative to electron bean lithography [Pendry99]. A plasmon-assisted version has been simulated [Liu05] and actually performed [Wang06] to create sub-diffraction limit patterns. Inspired by the earliest experiments on tip-plate geometries [Williams86] researchers have developed an imaging technique known as scanning thermal microscopy [De Wilde06, Kittel08] which operates without external illumination to construct an image of a material surface by detecting the local density of states of thermally excited electromagnetic modes. There has also been applications in thermal management such as near-field refrigeration [Chen15, Liu16] and rectification [Otey10, Iizuka12, Yang13, Fiorino18a], which are achieved by exploiting the chemical potential and temperature dependence of the materials' emission spectra, respectively.

As explained in Sec. 1.3.1 there is an analogue of radiative heat transfer in electric circuits, which dominates over electron-phonon and electron conduction contributions at low temperatures [Meschke06]. By continuation of the analogy, resonant photons supported by the particular circuit elements play the role of SPhPs or SPPs in real materials. In quantum circuits theoretical proposals and pioneering experimental realisations have also been made for photonic refrigeration [Kosloff14, Karimi16] (see also the earlier review [Giazotto06]) and rectification [Ronzani18, Senior20]. Here, the thermal transport properties of the system are controlled via a heat valve, for which schematic and real scanning tunnelling micrograph images are shown in Fig. 1.14. The basic structure of the device is two reservoirs (resistors) at different temperatures that are each coupled to an LC resonator, and are coupled to each other via a two-level system, realised here by a superconducting transmon qubit. Different heat management regimes are achieved by adjusting the frequencies of microwave resonators associated with each reservoir as well as the gap of the two-level system. These state of the art proposals and experiments represent significant progress at the intersection of the fields of quantum thermodynamics and quantum information.

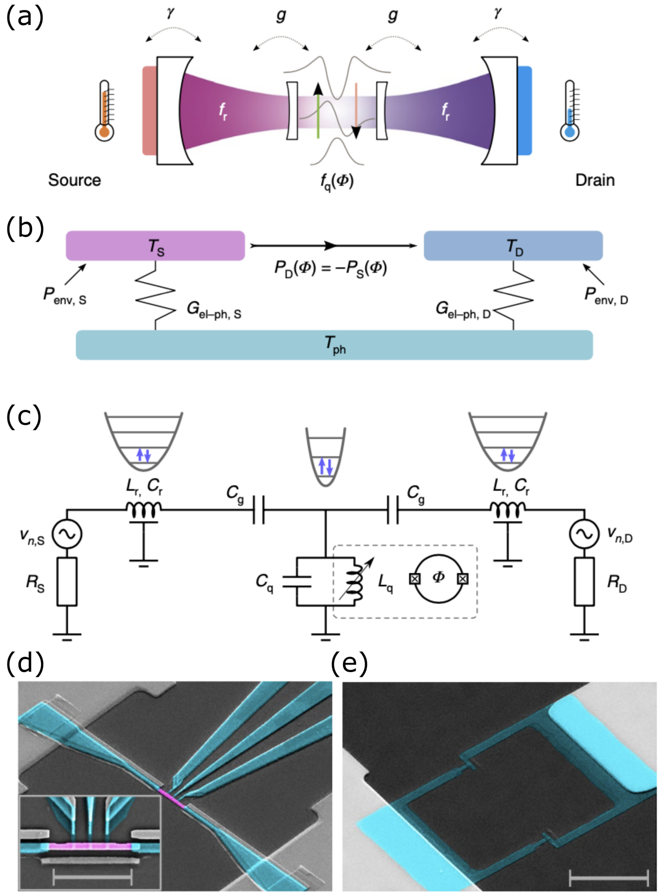

Figure 1.14: (a) Conceptual depiction of a quantum heat valve. (b) Thermal model indicating power from source to drain and the interaction of the electrons with the phonon bath of the cryostat. (c) Lumped-element idealisation of the device where capacitors C_g couple the transmon to each L_rC_r resonator. (d, e) Scanning tunnelling micrograph of a waveguide termination and the SQUID element of the transmon qubit, respectively. Fig. 1 in Ref. [Ronzani18].

One of the most exciting and relevant applications appears to be that of near-field thermophotovoltaics (TPV) – for reviews see Ref. [Basu07, Basu09, Ben-Abdallah19]. The basic idea builds on the standard model of electricity generation from radiation, but instead of placing the p-n junction photovoltaic material in the far field of the Sun, it is placed in the near field of some terrestrial thermal emitter. In this way, one may take advantage of the aforementioned enhancement and coherence of near-field radiation by choosing optimally the materials, emitter/receiver separation distance and temperature. In particular, for an emitter material that supports a resonant surface mode and as such emits quasi-monochromatically, one may try to match this to the band gap frequency of the chosen direct band gap semiconductor that forms the photovoltaic cell. By capitalising on the frequency-matched near-field heat transfer one may hope to generate more photocurrent than in a standard solar (far-field) setup. In addition, the coherence properties could in principle lead to improved device efficiency since one may design the device to minimise losses via Joule heating brought about by impinging photons that have insufficient energy to create electron-hole pairs.

A quantitative study [Laroche06] has been performed via FE to numerically evaluate the performance of an ideal TPV system comprised of a gallium antimonide receiver at 300 K and an emitter that is either tungsten or a fictitious Drude material (chosen to match the semiconductor gap) at 2000 K. The authors show that the choice of material for the emitter and receiver is non-trivial, since the angular coherence of the emitter radiation is not an intrinsic property, and rather it is affected by the presence of the receiver. Nevertheless for both emitters they report an increase in the photogeneration current by at least one order of magnitude compared to the case where the emitter is a black body at the same temperature. Ref. [Park08] performed a more realistic study in which they considered non-ideal photovoltaic cell made of an alloy of indium antimonide and gallium antimonide (300 K) due to a tungsten emitter (2000 K) and calculated the conversion efficiency (ratio of electric power generated to the radiative power absorbed by the cell) as a function of separation distance. Due to electron-hole diffusion and recombination events, they found that the conversion efficiency actually begins to decrease at separations below 10 nm. Nevertheless at $d = 10\,\mathrm{nm}$, where the conversion efficiency is estimated to be slightly above 20%, the electricity production is $1\,\mathrm{MWm}^{-2}$, which for a device with an area of just $25\,\mathrm{cm}^2$ would be enough to meet the per household USA demand (at the time) [Basu09].

In reality, it is difficult to take advantage of the resonant surface mode of the emitter because of a mismatch between its frequency and the band gap of real semiconductor materials. One proposed method of overcoming this mismatch is to add a layer of graphene on top of the receiver cell [Messina13]. The tunability of the graphene Fermi level allows one to improve the coupling between emitter and receiver, resulting in significant gains in the device efficiency as shown in Fig. 1.15 (b). Meanwhile, following closely the work of Ref. [Park08], a theoretical analysis was performed on the effect of adding a highly reflective gold mirror to the back of the photovoltaic cell [Bright14]. The authors reported moderate improvements in the device efficiency since the radiation that passes through the cell may be recycled back to the tungsten emitter, hence reducing losses.

Experimental demonstrations of near-field thermophotvoltaic devices remain scarse, however a recent investigation reported 40× the far-field electrical power output for a microscale TPV system comprised of a silicon emitter at 655 K separated by a 60 nm vacuum gap from a commercial photodiode at room temperature [Fiorino18b]. Despite the impressive enhancement, the conversion efficiency remained low (0.02%) due to high energy absorption in the receiver cell. On the question of the real-world viability of thermophotovoltaic energy generation, the elephant in the room is, of course, where does the energy to heat the emitter come from? Although the subject is often omitted in studies

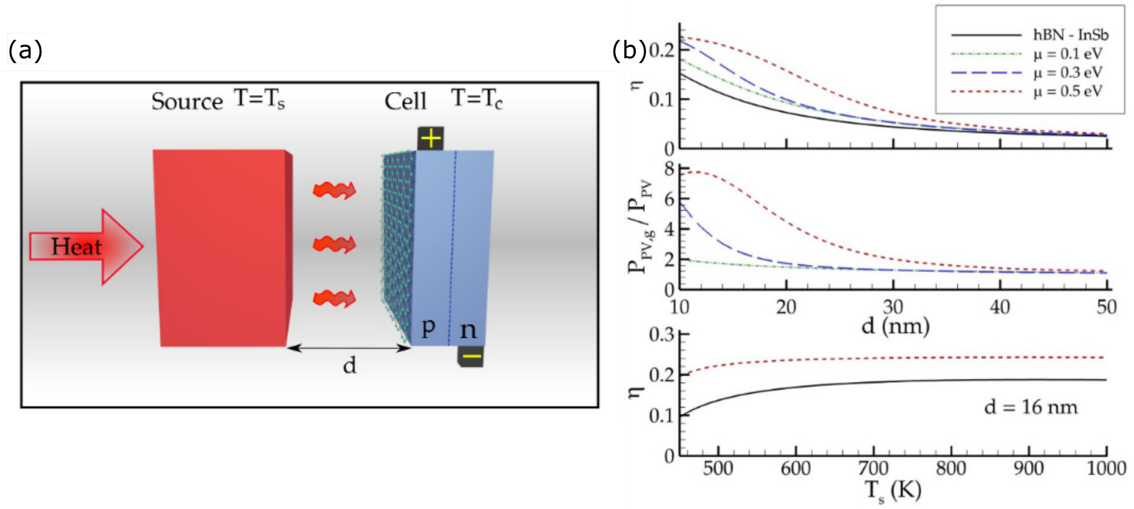

Figure 1.15: (a) Schematic of the thermovoltaic device proposed in Ref. [Messina13] comprised of a hexagonal boron nitride emitter and an indium antimonide cell with an added layer of graphene. (b) Top and middle panels: The computed conversion efficiency and the ratio of the photocurrent generated in the cell with and without the graphene at various chemical potentials, as a function of separation distance. Bottom panel: Conversion efficiency at $d = 16\,nm$ *with and without graphene as a function of source temperature. Fig. 1 and 2 in Ref. [Messina13].*

like those mentioned, there appears to be some hope of directing heat produced by other (industrial) processes that would otherwise be wasted for this task. Despite the evident challenges, researchers are optimistic that near-field thermophovoltaics will continue to improve in terms of power outputs and efficiencies, eventually providing a versatile and effective way to recover waste heat from other processes [Ben-Abdallah19].

1.6 Motivation for the thesis

In the previous sections we have seen that significant progress has been made in the field of radiative heat transfer. In particular, its enhancement due to near-field effects has now been well established theoretically for over 50 years, and it may be described within the phenomenological framework of fluctuational electrodynamics for any system whose electrodynamic response is linear. More recently, well-controlled experimental setups have been refined in various geometries that have allowed for direct confirmation of this theory, as well as the conception of novel devices that harness the near-field radiation. However, there still remain some open questions in the field. They motivate the work of this thesis.

The advent of atomically thin two-dimensional materials such as graphene and transition metal dichalcogenides – as well as the increased prevalence of metallic thin films - calls for a complete study of this formerly unrealistic geometry. As compared to the well-studied case of three-dimensional half-spaces, this geometry has the same in-plane translational invariance that makes analytical progress feasible, while also offering the possibility of observing markedly different behaviour due to the perpendicular confinement governed by the layer thickness. The combination of the wish to make analytical progress and the appearance of these new materials motivate us to focus on the two-dimensional geometry. Further, we use models that describe materials with free charge carriers (metals and doped semiconductors and semimetals) since these are the most relevant in modern micro and nanotechnologies.

In nanoscale devices operating at sub-Kelvin temperatures some new aspects of heat transfer, unimportant in macroscopic systems at room temperatures, can become relevant. On the one hand, the nanostructures often have a complicated geometry which makes microscopic simulations numerically costly. On the other hand, their size is often small compared to intrinsic length scales relevant to the heat transfer, which justifies a phenomenological description in terms of effective circuits made of lumped elements. For our model system of two-dimensional layers, we can compare the microscopic and phenomenological descriptions and check when they match.

Within the remit outlined above, we identify some open questions, to be explained in more detail below:

- Validity of the Coulomb limit
- Role of spatial dispersion
- Role of surface plasmons
- Validity of the effective circuit description

Most often, FE calculations involve the solution of the full set of Maxwell's equations, including all retardation effects. However, at short distances the electromagnetic interaction is dominated by the instantaneous Coulomb contribution. It has sometimes been assumed that the small length scales associated with the near field guarantee the validity of the Coulomb limit [Svetovoy12, Jiang17, Mahan17, Kamenev18, Zhang18], which has the advantage of simpler calculations. However, the threshold of validity has not been explicitly evaluated – i.e. how small must the body separation be to safely neglect retardation and focus on the Coulomb limit? In Ch. 2 we address this question for radiative heat transfer between two-dimensional metallic layers described by local Drude conductivity. We compute and compare asymptotic expressions for near-field and far-field contributions to the heat transfer coming from TM and TE polarisations, revealing dependencies on material and setup parameters such as conductivity, temperature and separation. From these we identify regimes with different dominant heat transfer channels and predict the length scale which determines the significance (or lackthereof) of retardation i.e. the conditions of validity of the Coulomb limit. We also interrogate the common wisdom that the evanescent contributions dominate only when the material separation is small compared to the thermal wavelength of photons. The results reveal the qualitative role played by the dc conductivity of the metals that gives rise to a classification of materials into two groups. In Ch. 2, we also remark on some of the key differences as compared to the three-dimensional case, and compare quantitatively to relevant experiments discussed previously.

A tacit assumption that often goes un-interrogated in studies of near-field radiative heat transfer is that of spatial locality of the material response (neglecting spatial dispersion in the conductivity). It is naturally assumed that nonlocal effects are important only at extremely small length scales, and authors often assume the setups they wish to describe fall above this threshold, hence ensuring the validity of simpler local models. However, once again this threshold is rarely mentioned explicitly or explored. It has been argued that the local/nonlocal length scale is given by a microscopic material property such as the material mean free path [Landau84], although some claim the threshold depends on the observable in question [Rodriguez-López15]. Spatial dispersion is included in the model of graphene in Ref. [Svetovoy12], but its effect is unclear from the numerical results. Ref. [Chapuis08c] reported the saturation of the heat current between metallic half-spaces as a direct consequence of nonlocal effects when the separation is below $\sim 1\,\mathrm{nm}$. Similar results regarding saturation at extremely small distances due to spatial dispersion are reported for two-dimensional metals in Ref. [Kamenev18]. Working in the Coulomb limit, in Ch. 3 we employ a general and under-utilised nonlocal model for the conductivity of a two-dimensional electron gas with disorder, where once again we identify distinct regimes of the heat transfer. From the details of our analytical calculation, we establish quantitatively the length scale of the local/nonlocal threshold.

While the importance of surface phonon polaritons in radiative heat transfer between dielectrics appears beyond much doubt [Joulain05, Francoeur08], the role of surface plasmon polaritons in metals, doped semiconductors and two-dimensional materials is less certain. On the one hand SPPs have been identified to play a crucial role in the enhancement of near-field radiative heat transfer in several studies. This has included theoretical works on graphene [Svetovoy12], doped semiconductor [Rousseau09a] and metal [Biehs07] films, as well as experimental observation in graphene [Yang18]. On the other hand, Ref. [Kamenev18] reported no plasmon contribution to the heat current between two-dimensional disordered conductors, and Ref. [Mahan17] explicitly claimed the contribution of SPPs to be unimportant for three-dimensional, disorder-free metallic half-spaces (both studies were in the Coulomb limit). Questions naturally arise regarding the source of this discrepancy, in particular around whether the absence of a plasmonic contribution in some studies is an artefact of the Coulomb limit or related to the model of disorder taken for the material. In the analytical calculation in Ch. 3 we find that the plasmon contribution to the heat current may in fact be dominant for two-dimensional metallic layers, but it disappears if one takes clean or diffusive limits for electron motion. We determine the conditions for which this plasmonic contribution dominates.

As discussed in Sec. 1.3.1, radiative heat transfer may be calculated in electric circuits, and in Ch. 3 we address the open question of when and how a given structure may be described by an effective circuit that is justified by a microscopic model. Using the aforementioned model for a two-dimensional electron gas with disorder, we check whether the radiative heat transfer between two metallic layers may be represented by photonic heat transfer in an effective circuit. We make qualitative observations that connect effective circuit parameters to material values from the microscopic model, and find the limits of validity of the circuit representation.

In Ch. 4, we graduate from studying the average radiative heat current to instead study its fluctuations. As discussed in Sec. 1.3.2, heat current fluctuations, or noise, remain much less well-studied both theoretically and experimentally. However, it is known that the noise of a signal may contain additional information about the system compared to the average [Landauer98]. In particular, information about the relevant excitations of a system may be visible in the fluctuations. With this in mind, we study the finite-frequency heat current noise spectrum in two systems whose radiative heat transfer may be dominated by discrete resonant modes. Firstly, we report on the recent study Ref. [Roubinowitz21] of heat current fluctuations in a zero dimensional system modelled by an effective circuit based on an experiment [Meschke06]. It has been found that the radiative heat current in such a system, which dominates over other transfer channels at low temperatures, may have a resonant character due to the structure of the circuit. Secondly, we study the system of two-dimensional metallic layers, where as shown in Ch. 3 the radiative heat current may be due to resonant surface plasmons. We calculate the finite-frequency noise spectra of these systems in Secs. 4.2 and 4.3, finding that in both cases the resonant behaviour is indeed encoded in the noise spectrum. Via measurements of receiver temperature fluctuations, these predictions provide a potential way to observe directly the importance of resonant modes.

In some sense, our wish to perform analytical calculations is in itself motivated by the generality of the open questions discussed above. Recently there have been many studies that use detailed, material-specific models that are handled numerically [Svetovoy12, Zhao17, Zhang19]. While offering precise results and perhaps insight into the role of the above physical ingredients (retardation, spatial dispersion and plasmons) in a *particular material*, it is difficult to make general conclusions from these studies that are applicable to a *wider class of materials*. By performing analytical work on widely-applicable general models, we reveal some new general conclusions on each of the physical ingredients discussed above.

2

Near field versus far field in radiative heat transfer between two-dimensional metals

Contents

2.1 Radiative heat transfer via FE

Many theoretical works have been dedicated to different material systems in the near-field regime ([Joulain05, Volokitin07, Song15a, Biehs21] and references therein), in which various models for material response have been employed and different dominant channels for heat transfer identified. The common wisdom is that the evanescent modes dominate the heat transfer when the spatial separation $d \ll \lambda\!\!\!^{-}_T \equiv \hbar c/T$, the wavelength of photons at temperature T (here $\hbar$ and c are the Planck constant and the speed of light, respectively, and we set the Boltzmann constant to unity). Indeed, for $d > \lambda\!\!\!^{-}_T$ the evanescent waves with the typical frequency $\omega \sim T/\hbar$ decay exponentially outside the material, while at $d \ll \lambda\!\!\!^{-}_T$ the region of the wave vectors k occupied by evanescent waves, $k \sim 1/d$, is larger than that of travelling states, $k \sim 1/\lambda\!\!\!^{-}_T$ [Volokitin07]. The importance of magnetic coupling in the near-field heat transfer between well-conducting metals has been emphasised [Chapuis08c, Chapuis08a]. In the extreme near-field limit, heat transfer due to the electrostatic Coulomb interaction has also been studied [Prunnila13, Mahan17, Zhang18, Wang18, Kamenev18, Ying20]. Here, we perform a calculation using the full retarded electromagnetic interaction in order to establish the conditions of validity of the Coulomb limit, and interrogate the common wisdom that evanescent waves dominate the heat transfer only if $d \ll \lambda\!\!\!^{-}_T$.

2.1.1 Model: local Drude conductivity

We consider two identical 2D metal sheets held at different temperatures T_1 and T_2, embedded in vacuum and separated by a gap of width d. A more realistic configuration would be to place a medium with a dielectric constant ε in the half-space behind each sheet, since in experiments the layers are placed on a substrate. For the sake of simplicity, we will focus on $\varepsilon = 1$ in most of the chapter, and check for the effect of the substrate when specifically needed (see Sec. 2.2.5).

We model the metal sheets as infinitely thin layers, characterised by a local 2D Drude conductivity [introduced in Eq. (1.12)],

$$\sigma(\omega) = \frac{\sigma_{2\mathrm{D}}}{1 - i\omega\tau}, \tag{2.1}$$

with τ being the electron momentum relaxation time, assumed to be temperature-independent. This is the case if τ is determined by elastic scattering on static impurities. In Ch. 3 we employ a richer model for the material conductivity including spatial dispersion, however we find that under certain conditions the simpler Drude model is sufficient for describing the radiative heat transfer. We incorporate those validity conditions here. Eq. (2.1) neglects (i) the spatial dispersion of the conductivity, and (ii) field variation over the layer thickness. For atomically thin materials, such as doped graphene or transition metal dichalcogenides, condition (ii) is irrelevant, and condition (i) holds at distances $d \gg \sqrt{a_{2\mathrm{D}}\ell}$ ($a_{2\mathrm{D}}$ and ℓ being the 2D screening radius and the electron mean free path, respectively) – see Ch. 3. For thin but macroscopic layers of conventional metals, condition (ii) imposes that the thickness must be small compared both to the typical wavelength of the waves dominating the heat transfer (which may be rather short for evanescent waves) and to the skin depth at the typical frequency of these waves, while condition (i) requires the wavelength and the skin depth to be longer than the electron mean free path in the metal.

We also emphasise that our study applies to metals only. Optical response of Drude metals and dielectrics is governed by qualitatively different physical mechanisms: conduction electrons and optical phonons, respectively, whose response is concentrated at low and high frequencies (e. g., the optical phonon frequency in SiO_2 is more than three times higher than the room temperature). We do not include the contribution of such high-frequency resonances in our model. This is a valid approximation even for bad metals at sufficiently low frequencies/temperatures, since the electronic Drude contribution to the layer polarisability diverges at low frequencies, while the optical phonon contribution stays finite. Comparing the two contributions, one can estimate the temperature below which the Drude model is sufficient for a specific material.

2.1.2 Explicit general expression for the heat current between two thin metallic sheets

Our calculation of the heat current between the metals follows the standard FE procedure set out in Sec. 1.2. The fluctuating in-plane surface currents $\mathbf{j}^{(\alpha)}(\mathbf{r},t)$ in each sheet obey the fluctuation-dissipation theorem,

$$\langle j_l(\mathbf{r},t)\, j_m(\mathbf{r}',t')\rangle = \delta_{lm}\int \frac{d^2\mathbf{k}\,d\omega}{(2\pi)^3}\,\hbar\omega\coth\frac{\hbar\omega}{2T}\,\mathrm{Re}\,\sigma(\mathbf{k},\omega)\,e^{i\mathbf{k}(\mathbf{r}-\mathbf{r}')-i\omega(t-t')}, \tag{2.2}$$

where $\mathbf{k}$ is the two-dimensional in-plane wavevector, $l,m = x,y$ label the orthogonal in-plane directions and $T = T_1$ or T_2. These currents appear as sources in Maxwell's equations, whose solution in the presence of the conducting sheets determines the fluctuating electric fields $\mathbf{E}(\mathbf{r},t)$. Then, the heat current J (per unit area) from layer 1 to layer 2 is given by the average Joule loss power (per unit area) $\langle\tilde{\mathbf{j}}^{(2)}\cdot\mathbf{E}^{(2)}\rangle - \langle\tilde{\mathbf{j}}^{(1)}\cdot\mathbf{E}^{(1)}\rangle$, where $\tilde{\mathbf{j}}^{(\alpha)}$ is the surface current in layer α, induced by the electric field $\mathbf{E}^{(\alpha)}$ in this layer, which, in turn, is produced by the fluctuating current in the other layer.

We emphasize that for thin layers, the Joule losses $\langle\tilde{\mathbf{j}}^{(2)}\cdot\mathbf{E}^{(2)}\rangle - \langle\tilde{\mathbf{j}}^{(1)}\cdot\mathbf{E}^{(1)}\rangle$ are not equal to the average normal component of the Poynting vector in the gap between the layers. The reason is that some part of the radiation emitted by layer 1 may pass through layer 2 and escape to infinity, and vice versa. Whether this escaped radiation should be included in the heat current or not, depends on the precise measurement setup, which may collect this escaped radiation or not. Our calculation thus assumes that the escaped radiation is lost. As discussed in Sec. 2.2.5, here we focus on the heat transfer from one metal to the other, so we calculate the Joule losses, not the Poynting vector. Note that for two semi-infinite metals (the most studied setup), everything is collected inside the metals, so the Poynting vector and the Joule losses match exactly.

We solve Maxwell's equations (in CGS units) for the monochromatic components of the electric and magnetic field, $\mathbf{E}_{\mathbf{k}\omega}(z)\,e^{i\mathbf{k}\mathbf{r}-i\omega t}$ and $\mathbf{B}_{\mathbf{k}\omega}(z)\,e^{i\mathbf{k}\mathbf{r}-i\omega t}$ in the planar geometry with the two metallic sheets placed at $z = z_1, z_2$ with $z_2 - z_1 = d$, while the position-dependent dielectric constant $\varepsilon(z)$ accounts for whatever (non-magnetic, isotropic) dielectric medium surrounds the layers:

$$\left(i\mathbf{k}+\mathbf{e}_z\frac{\partial}{\partial z}\right)\wedge\mathbf{E}_{\mathbf{k}\omega}=\frac{i\omega}{c}\mathbf{B}_{\mathbf{k}\omega}, \tag{2.3}$$

$$\left(i\mathbf{k}+\mathbf{e}_z\frac{\partial}{\partial z}\right)\wedge\mathbf{B}_{\mathbf{k}\omega}=\frac{4\pi}{c}\sum_{\alpha=1,2}\delta(z-z_\alpha)\left(\mathbf{j}^{(\alpha)}_{\mathbf{k}\omega}+\tilde{\mathbf{j}}^{(\alpha)}_{\mathbf{k}\omega}\right)-\frac{i\omega}{c}\varepsilon(z)\,\mathbf{E}_{\mathbf{k}\omega}, \tag{2.4}$$

where $\mathbf{e}_z$ is the unit vector in the z direction, perpendicular to the layers. The surface current in each layer $\alpha=1,2$ consists of two contributions: $\tilde{\mathbf{j}}^{(\alpha)}_{\mathbf{k}\omega}=\sigma_\alpha(\omega)\,\mathbf{E}_{\mathbf{k}\omega}(z_\alpha)$ is the induced current due to the electric field, while the fluctuating currents $\mathbf{j}^{(\alpha)}_{\mathbf{k}\omega}=(\mathbf{j}^{(\alpha)}_{-\mathbf{k},-\omega})^*$ are complex Gaussian random variables with the correlator determined by the fluctuation-dissipation theorem (2.2):

$$\langle j^{(\alpha)}_{\mathbf{k}\omega,l}\,j^{(\alpha')}_{\mathbf{k}'\omega',m}\rangle=(2\pi)^3\,\delta(\mathbf{k}+\mathbf{k}')\,\delta(\omega+\omega')\,\delta_{\alpha\alpha'}\delta_{lm}\hbar\omega\coth\frac{\hbar\omega}{2T_\alpha}\operatorname{Re}\sigma_\alpha(\mathbf{k},\omega) \tag{2.5}$$

Because of δ_{lm} on the right-hand side of this equation, current fluctuations are independent for any two orthogonal directions, so it is convenient to pass to the longitudinal and transverse basis (p and s polarisations, respectively):

$$\mathbf{j}^{(\alpha)}_{\mathbf{k}\omega}=j^{(\alpha)}_{\mathbf{k}\omega}\frac{\mathbf{k}}{k}+j^{(\alpha)}_{\mathbf{k}\omega}\frac{\mathbf{e}_z\wedge\mathbf{k}}{k}. \tag{2.6}$$

In this basis the solutions of Maxwell's equations decouple into transverse magnetic (TM) and transverse electric (TE) modes, whose contribution to the heat current is simply additive. To model different metal sheets mounted on identical dielectric substrates separated by vacuum, we take $\varepsilon(z_1<z<z_2)=1$, $\varepsilon(z<z_1)=\varepsilon(z>z_2)=\varepsilon>1$. This leads to the spatial dependence of the electric and magnetic fields $\propto e^{i\mathbf{kr}\pm iq_z z}$ for $z_1<z<z_2$, and $\propto e^{i\mathbf{kr}+iq'_z z}, e^{i\mathbf{kr}-iq'_z z}$ for $z>z_2$ and $z<z_1$, respectively. Here we defined

$$q_z=\begin{cases}\sqrt{\omega^2/c^2-k^2}\,\operatorname{sign}\omega, & |\omega|>ck,\\ i\sqrt{k^2-\omega^2/c^2}, & |\omega|<ck,\end{cases} \tag{2.7a}$$

$$q'_z=\begin{cases}\sqrt{\varepsilon\omega^2/c^2-k^2}\,\operatorname{sign}\omega, & \sqrt{\varepsilon}|\omega|>ck,\\ i\sqrt{k^2-\varepsilon\omega^2/c^2}, & \sqrt{\varepsilon}|\omega|<ck.\end{cases} \tag{2.7b}$$

At $|\omega|>ck$, the metallic layers are coupled by travelling waves, while for $|\omega|<ck$ the solutions in the gap are evanescent waves, where the fields' strength decays away from the layers. The solutions are matched at $z=z_1$ and $z=z_2$ using the standard boundary conditions: continuity of the in-plane component of the electric field $\mathbf{E}_\parallel$, and a jump in the magnetic field in-plane component, determined by the total surface current (the fluctuating sources as well as the induced current $\sigma\mathbf{E}_\parallel$). The heat current from, say, sheet 2 to the sheet 1 is given by the average Joule loss power per unit area, $J(T_1,T_2)=\langle\tilde{\mathbf{j}}^{(1)}\cdot\mathbf{E}_\parallel(z_1)\rangle-\langle\tilde{\mathbf{j}}^{(2)}\cdot\mathbf{E}_\parallel(z_2)\rangle$, determined unambiguously due to the continuity of $\mathbf{E}_\parallel(z)$.

For a temperature-independent relaxation time this heat current splits into $J(T_1,T_2) = J(T_2) - J(T_1)$, where

$$J(T) = \int_0^\infty \frac{d\omega}{2\pi} \frac{\hbar\omega}{e^{\hbar\omega/T} - 1} \int \frac{d^2\mathbf{k}}{(2\pi)^2} \sum_{j=p,s} \frac{a_{1j} a_{2j} \, |e^{iq_z d}|^2}{|1 - r_{1j} r_{2j} e^{2iq_z d}|^2} \tag{2.8}$$

is expressed in terms of reflectivities $r_{\alpha j}$ and emissivities $a_{\alpha j}$ for the p and s polarisations:

$$r_{\alpha p} = \frac{q_z - q_z'/\varepsilon + 4\pi\sigma_\alpha q_z q_z'/(\varepsilon\omega)}{q_z + q_z'/\varepsilon + 4\pi\sigma_\alpha q_z q_z'/(\varepsilon\omega)}, \tag{2.9a}$$

$$a_{\alpha p} = \frac{4|q_z||q_z'/\varepsilon|^2 (4\pi \operatorname{Re}\sigma_\alpha/\omega)}{|q_z + q_z'/\varepsilon + 4\pi\sigma_\alpha q_z q_z'/(\varepsilon\omega)|^2}, \tag{2.9b}$$

$$r_{\alpha s} = \frac{q_z - q_z' - 4\pi\omega\sigma_\alpha/c^2}{q_z + q_z' + 4\pi\omega\sigma_\alpha/c^2}, \tag{2.9c}$$

$$a_{\alpha s} = \frac{4|q_z|(4\pi\omega \operatorname{Re}\sigma_\alpha/c^2)}{|q_z + q_z' + 4\pi\omega\sigma_\alpha/c^2|^2}. \tag{2.9d}$$

The emissivities can also be written as

$$a_{\alpha p} = (1 - |r_{\alpha p}|^2)\,\theta(|\omega| - ck) + 2\operatorname{Im} r_{\alpha p}\,\theta(ck - |\omega|) - \left|\frac{q_z'}{\varepsilon q_z}\right| |t_{\alpha p}|^2\,\theta(\sqrt{\varepsilon}|\omega| - ck), \tag{2.10a}$$

$$a_{\alpha s} = (1 - |r_{\alpha s}|^2)\,\theta(|\omega| - ck) + 2\operatorname{Im} r_{\alpha s}\,\theta(ck - |\omega|) - \left|\frac{q_z'}{q_z}\right| |t_{\alpha s}|^2\,\theta(\sqrt{\varepsilon}|\omega| - ck), \tag{2.10b}$$

where $\theta(x)$ is the Heaviside step function, and $t_{\alpha j}$ are the transmittivities:

$$t_{\alpha p} = \frac{2q_z}{q_z + q_z'/\varepsilon + 4\pi\sigma_\alpha q_z q_z'/(\varepsilon\omega)}, \tag{2.11a}$$

$$t_{\alpha s} = \frac{2q_z}{q_z + q_z' + 4\pi\omega\sigma_\alpha/c^2}. \tag{2.11b}$$

First, we note that the Stefan-Boltzmann law Eq. (1.4) is recovered from the full formula Eq. (2.8) by assuming perfect absorption of the layers (setting $r_{\alpha j} = t_{\alpha j} = 0$ leads to $a_{\alpha j} = \theta(|\omega| - ck)$, i.e. unit emissivity for travelling waves). More subtly, note the difference between Eqs. (2.10) and Eq. (2) of Ref. [Wang19], where the third term is absent in both polarisations. Without the third term, Eq. (2.8) gives the average value of the Poynting vector in the gap between the two layers, which counts the heat flux that is not absorbed by the metal, but irradiated to infinity behind it, due to the finite transmission. Eqs. (2.10) without the third term originally appeared in Ref. [Volokitin01] for the problem of heat transfer between two semi-infinite materials. In that geometry, all heat flux transmitted through the surface is eventually absorbed by the material. In the thin layer geometry, whether the transmitted flux is detected or not, depends on the specific experimental measurement scheme. In our calculation, we assume that the transmitted radiation is lost, and thus use the full Eqs. (2.10).

To summarise, in the planar geometry considered here, the solutions of Maxwell's equations are classified by in-plane wave vector $\mathbf{k}$, frequency ω, and two polarisations $p = \mathrm{TE}, \mathrm{TM}$ – transverse electric and transverse magnetic, respectively, for which the electric or the magnetic field vector is parallel to the layers and perpendicular to $\mathbf{k}$. The contributions to the heat current from modes with different $\mathbf{k}, \omega, p$ add up independently, so the heat current $J(T_1, T_2)$ is given by by an integral over $\mathbf{k}$ and ω, and a sum over the polarisations. The integral splits in two contributions: the interior of the light cone, $\omega > ck$ hosts travelling modes, while in the region $\omega < ck$ the solutions are evanescent. The resulting heat current is comprised of four additive contributions (TM and TE, travelling and evanescent). Which contribution dominates, depends on the material conductivity, as well as the system temperature and length scales.

2.1.3 Asymptotic expressions for limiting cases

For temperature-independent relaxation time, the heat current naturally splits into the difference $J(T_1, T_2) = J(T_1) - J(T_2)$. In Appendix A we perform analytically the $\mathbf{k}, \omega$ integrals in Eq. (2.8) and derive simple asymptotic expressions for $J(T)$ according to the separation and the temperature. For each expression, we can identify the dominant contribution (TM or TE, travelling or evanescent). Our results are approximate; one can describe the heat transfer much more precisely by solving Maxwell's equations for finite-thickness slabs with a material-specific frequency dependence of the conductivity and numerically evaluating the integrals, as routinely done in many works. However, simple approximate expressions (i) are rather useful when a quick estimate of the heat current is needed, and (ii) offer a general insight into the dominant physical mechanisms responsible for the heat transfer and enable one to characterise different possibilities.

The detailed analysis of different asymptotic regimes of the $\mathbf{k}, \omega$ integrals results in several asymptotic expressions for $J(T)$ in different parametric ranges of d. The magnitudes of the TM and TE travelling contributions are sensitive to the dimensionless conductivity parameter $\mathcal{G} = 2\pi\sigma_{2\mathrm{D}}/c$ (we use CGS units throughout, in SI units $\mathcal{G} = (\sigma_{2\mathrm{D}}/2)\sqrt{\mu_0/\varepsilon_0}$) so we proceed to present the results sequentially for small and large values of $\mathcal{G}$.

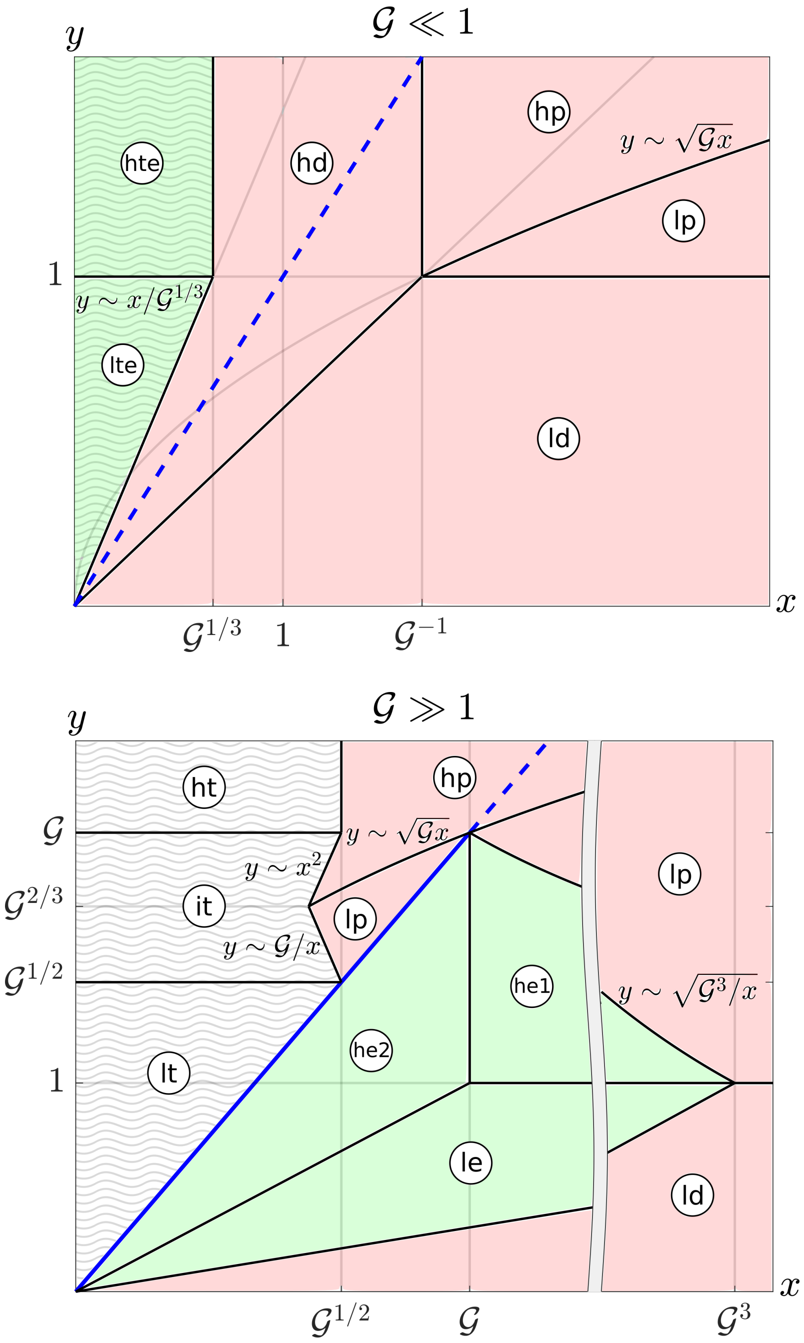

Figure 2.1: The domains of validity for asymptotic expressions, Eqs. (2.12) and (2.14) in the parameter plane $(1/d, T)$*, shown in the dimensionless variables* $x \equiv c\tau/d$*,* $y \equiv T\tau/\hbar$*. The crossovers between the regimes are governed by the dimensionless conductivity parameter* $\mathcal{G} \equiv 2\pi\sigma_{2D}/c$*, the upper and lower panels corresponding to* $\mathcal{G} \ll 1$ *and* $\mathcal{G} \gg 1$*, respectively. The encircled label of each region corresponds to the subscript at* $J(T)$ *in Eqs. (2.12) and (2.14). Solid lines indicate crossovers between different expressions; straight lines* $y/x = \mathrm{const}$ *are not labeled for readability (the coefficient can be deduced from the endpoints). The blue line (solid or dashed) corresponds to* $d \sim \lambda\!\!\!^{-}_T$*. The shading color indicates the heat being predominantly carried by TM modes (red), TE modes (green), or both (white); dominance of travelling waves is indicated by wavy hatching.*

For $\mathcal{G} \ll 1$, the asymptotic expressions for $J(T)$ are:

$$J_{\mathrm{lp}}(T) = \frac{\zeta(3)}{4\pi} \frac{T^3}{\hbar^2 c \mathcal{G} d}, \tag{2.12a}$$

$$J_{\mathrm{hp}}(T) = \frac{T}{16\pi\tau d^2} \mathcal{L}(\mathcal{G} c\tau/d), \tag{2.12b}$$

$$J_{\mathrm{ld}}(T) = \frac{\zeta(3)}{8\pi} \frac{T^3}{\hbar^2 c \mathcal{G} d}, \tag{2.12c}$$

$$J_{\mathrm{hd}}(T) = \frac{1}{16\pi} \frac{\mathcal{G} c}{d^3} T, \tag{2.12d}$$

$$J_{\mathrm{lte}}(T) = \frac{\pi^2}{15} \frac{\mathcal{G}^2}{\hbar^3 c^2} T^4 \ln \frac{1}{\mathcal{G}}, \tag{2.12e}$$

$$J_{\mathrm{hte}}(T) = \frac{1}{4\pi} \frac{\mathcal{G}^2}{c^2 \tau^3} T \ln \frac{1}{\mathcal{G}}, \tag{2.12f}$$

valid in the corresponding regions of the $(1/d, T)$ plane, schematically shown in Fig. 2.1 (upper). The contributions given by Eqs. (2.12a)–(2.12d), with labels corresponding to low-temperature plasmonic, high-temperature plasmonic, low-temperature diffusive, high-temperature diffusive, are the TM evanescent contributions that remain in the Coulomb limit ($c \to 0$) whose calculation is given in App. A.4. Their survival in the Coulomb limit is manifested by their dependence on the product $\mathcal{G} c$. Equations (2.12e) and (2.12f) (with labels corresponding to low-temperature travelling electric and high-temperature travelling electric) are the travelling TE contributions which dominate over the travelling TM contributions by the logarithmic factor $\ln(1/\mathcal{G})$. In Eqs. (2.12), $\zeta(x)$ is the Riemann zeta function, and $\mathcal{L}(x)$ is a slow logarithmic function, approximately given by (see App. A.4)

$$\mathcal{L}(x) \approx \frac{4 \ln^3 x}{1 + (\ln x)/\ln(1 + \ln x)}. \tag{2.13}$$

For $\mathcal{G} \gg 1$, in addition to the expressions given in Eqs. (2.12a)–(2.12c) we also have:

$$J_{\mathrm{le}}(T) = \frac{\pi^2}{15} \frac{\mathcal{G}^2}{\hbar^3 c^2} T^4 \ln \frac{\lambda_T}{\mathcal{G} d}, \tag{2.14a}$$

$$J_{\mathrm{he1}}(T) = \frac{1}{4\pi} \frac{\mathcal{G}^2}{c^2 \tau^3} T \ln \frac{c\tau}{\mathcal{G} d}, \tag{2.14b}$$

$$J_{\mathrm{he2}}(T) = \frac{\zeta(3)}{16\pi} \frac{c}{\mathcal{G} d^3} T, \tag{2.14c}$$

$$J_{\mathrm{lt}}(T) = \frac{\pi^2}{45} \frac{T^4}{\hbar^3 c^2 \mathcal{G}}, \tag{2.14d}$$

$$J_{\mathrm{it}}(T) = \frac{1}{12} \frac{T^2}{\hbar c^2 \tau^2}, \tag{2.14e}$$

$$J_{\mathrm{ht}}(T) = \left(\frac{\sqrt{2}}{12\pi} + \frac{1}{4\pi} \right) \frac{\mathcal{G}}{c^2 \tau^3} T, \tag{2.14f}$$

valid in the corresponding regions of the $(1/d, T)$ plane, schematically shown in Fig. 2.1 (lower). The contributions given by Eqs. (2.14a)–(2.14c) are the TE evanescent contributions, while Eqs. (2.14d)–(2.14f) are the sums of travelling contributions from both polarisations which are of the same order.

For $\mathcal{G} \gg 1$, the travelling channels support resonant Fabry-Perot (FP) modes. In (lt) and (it) regions, many sharp FP modes contribute significantly to the heat current. In the high-temperature case (ht) the FP modes are overdamped since the conductivity $\sigma(\omega)$ becomes small at high frequencies. For temperatures lower than the first mode cutoff energy, $T \ll \pi\hbar c/d$, the contributions from the FP modes are exponentially suppressed. However, the prefactor in front of the small thermal exponential turns out to be larger than the evanescent contribution (2.14c) in (he2) region. Thus, the FP additive contribution is potentially significant for $c\tau/d < \sqrt{\mathcal{G}}$, where it is dominated by the first FP mode:

$$J_{\mathrm{FP1}}(T) = \frac{\pi c T}{[2\mathcal{G} + (\pi c\tau/d)^2]d^3}\, e^{-\pi\hbar c/(Td)}. \tag{2.15}$$

2.2 Discussion of results

2.2.1 Two classes of 2D structures

As shown in Fig. 2.1, we find two qualitatively different types of behaviour, depending on the value of the two-dimensional dc conductivity σ_{2D} of the sheets. The parameter $\mathcal{G} = 2\pi\sigma_{\mathrm{2D}}/c$ characterises the impedance mismatch between a 2D metal and vacuum; its importance is not restricted to the heat transfer problem and is rather general. Notably, two distinct regimes in the behaviour of 2D plasmon polaritons for $\mathcal{G} < 1$ and $\mathcal{G} > 1$ have been identified [Govorov89, Fal'ko89, Volkov14, Muravev15, Gusikhin18, Oriekhov20]. In our heat transfer problem, we find no sharp distinction between $\mathcal{G} < 1$ and $\mathcal{G} > 1$, but rather a smooth crossover between the two limiting situations. As we shall see below, the poor metal ($\mathcal{G} \ll 1$) case may be realised by doped two-dimensional materials, while the good metal ($\mathcal{G} \gg 1$) case represents typical thin films of conventional metals. In the following subsections, we discuss in detail various observations based on the results of Sec. 2.1.3, drawing attention to the differences between the two cases of poor and good metals.

2.2.2 Near-field enhancement beyond the thermal wavelength

In Fig. 2.1, the areas with wavy hatching indicate the regions where the heat transfer is dominated by travelling wave contributions, while areas with solid colours indicate where it is evanesecent contributions that dominate. Before discussing the physical difference between the two polarisations (indicated by the colour of each region), we comment on the position of the boundary between wavy and solid regions, i.e. the crossover between travelling and evanescent wave dominance.

For $\mathcal{G} \ll 1$, the evanescent waves dominate at separations up to $d \sim \mathcal{G}^{-1/3}\lambda\!\!\!^{-}_T$, parametrically larger than the commonly used condition for the near field, $d \ll \lambda\!\!\!^{-}_T$ [$y \ll x$ in Fig. 2.1 (upper)]. One would naturally expect the exponential suppression of the evanescent waves to be significant at such separations as we enter into the far field. The reason for such counter-intuitive behaviour is that the low-temperature TM evanescent contribution is determined by $k \ll 1/d$ for which the exponential suppression is not efficient. For $\mathcal{G} \gg 1$, the commonly used inequality $d \ll \lambda\!\!\!^{-}_T$ does become the accurate condition for evanescent contribution dominance, except for high temperatures where the Drude conductivity is suppressed by high frequency.

2.2.3 The role of electrostatics and magnetostatics

The contributions by evanescent waves from the two polarisations may be understood as being due to different types of electromagnetic coupling. In the extreme near-field limit, $k \gg \omega/c$, the TM mode field is mostly electric and longitudinal, while the magnetic field is smaller by a factor $\sim \omega/(ck)$; these modes represent the electrostatic coupling by the Coulomb interaction between charge density fluctuations in the two layers. At the same time, for TE modes the field is mostly magnetic, while the electric field is smaller by a factor $\sim \omega/(ck)$; these modes represent magnetostatic coupling, where the magnetic field established by transverse current fluctuations in one layer drives eddy currents in the second layer. The commonly used Coulomb limit, given by sending $c \to \infty$, corresponds to electrostatics (no magnetic fields) and is therefore given by retaining only the TM evanescent contribution from Eq. (2.8) – this is discussed further in Ch. 3.

For $\mathcal{G} \ll 1$ the near-field transfer is dominated by the TM evanescent contribution [red shading in Fig. 2.1 (upper)], basically, by electrostatic (capacitive) coupling between the two layers. This happens because in a poor metal, the charge density response is not fast enough to dynamically screen the fluctuating Coulomb field. Moreover, the TE evanescent contributions never dominate, indicating that the Coulomb limit is valid in and beyond the near field.

For $\mathcal{G} \gg 1$ we observe that in a large part of the near-field region of the parameter plane the heat current is governed by TE evanescent modes [green shading in Fig. 2.1 (lower)], which correspond to magnetostatic (inductive) coupling between the layers. As discussed in Refs. [Chapuis08c, Chapuis08a] for bulk metals, large conductivity leads to efficient screening of the electric fields, so the magnetostatic coupling becomes more important. The electrostatic coupling takes over only at very short distances or low temperatures, $d \ll \lambda\!\!\!^{-}_T/(\pi\mathcal{G})^3$, determined by $J_{\mathrm{le}}(T) \sim J_{\mathrm{ld}}(T)$.

However, for very small d the finite layer thickness of a conventional metal may become important, and/or the assumption of the local response, Eq. (2.1), may break down. Taking, for example, a $h = 10\,$nm-thick gold film with the bulk plasma frequency $\omega_p = 0.6 \times 10^{16}\,\mathrm{s}^{-1}$ and relaxation time $\tau = 6\,$fs [Ordal85] we may use the relation $4\pi\sigma_{2\mathrm{D}} = \omega_p^2 \tau h$ (found from Eqs. (1.12) and (1.19) and the fact that $\sigma_{2\mathrm{D}} = \sigma_{3\mathrm{D}} h$ for a local model) to arrive at the estimate $\mathcal{G} \approx 3.6$. Since $\lambda\!\!\!^{-}_T = 7.6\,\mu$m at $T = 300$ K, in such structure the predicted crossover to electrostatics occurs at a few nanometers. We note that in the (ld) regime, the heat transfer is mainly determined by rather small wave vectors $k \sim (\mathcal{G}\lambda\!\!\!^{-}_T d)^{-1/2}$ (App. A.4), so that even at $d = 1\,$nm we obtain $1/k \gtrsim 100\,$nm, and the local response assumption should still be formally valid. However, at nanometric distances other physical effects may come into play (electron or phonon tunnelling, surface roughness, etc.), so for ultrathin films of conventional metal we expect the Coulomb mechanism to be relevant mostly at low temperatures. These kind of low temperature regimes are explored in many experimental mesoscopic physics scenarios. Taking, for example, the 10 nm thick gold films discussed above with $\mathcal{G} \approx 3.6$ we find at $T = 0.1\,\mathrm{K}$, the crossover between electrostatics and magnetostatics occurs at $d \approx 16\,\mu\mathrm{m}$, where the thermal conductance per unit area is $\sim 2 \times 10^{-8}\,\mathrm{W\,K^{-1}m^{-2}}$. The result is similar for other very well conducting metals such as copper and silver. Note however that the crossover length scale decreases quickly ($\propto 1/h^3$) with increasing film thickness.

2.2.4 Comparison to the bulk case

The results presented in the previous section show two qualitatively different pictures of the near-field heat transfer between two metallic layers, depending on the value of their dimensionless 2D dc conductivity: for $\mathcal{G} \ll 1$, the heat transfer is mostly due to electrostatic coupling between the layers, up to distances significanly exceeding $\lambda\!\!\!^{-}_T$, while for $\mathcal{G} \gg 1$ the near-field magnetostatic coupling dominates up to distances $d \sim \lambda\!\!\!^{-}_T$, in close analogy with earlier results on bulk metals. This picture is consistent with the results of Ref. [Wang19] where the very same problem of radiative heat transfer between parallel 2D layers was studied numerically. There, a distinction was made between thin and thick metallic films. In this formulation $\mathcal{G}$ is proportional to the layer thickness h (in the local approximation, the 2D conductivity is simply $\sigma_{\mathrm{2D}} = \sigma_{\mathrm{3D}}h$, where σ_{3D} is the bulk conductivity). In Ref. [Wang19], the heat transfer between two theoretically imagined atomic monolayers of silver, described by a 2D Drude model with $\mathcal{G} \approx 2$, is found to be driven by TM evanescent waves, while for thicker films it is TE evanescent waves.

The peculiarity of the 2D geometry is that the 2D conductivity can be compared to two universal scales. One is the speed of light, hence the dimensionless parameter $\mathcal{G} = 2\pi\sigma_{\mathrm{2D}}/c$ we introduced earlier. The other universal scale is the conductance quantum, $e^2/(2\pi\hbar)$. For $\sigma_{\mathrm{2D}} \lesssim e^2/(2\pi\hbar)$, or $\mathcal{G} \lesssim e^2/(\hbar c) \approx 1/137$, the disorder is too strong, so the metallic conduction is destroyed by localization effects [Altshuler85, Lee85]. Thus, the poor metal regime discussed above, can be realised in the interval $1/137 \lesssim \mathcal{G} \ll 1$.

The situation is quite different for the bulk metal case. The 3D conductivity σ_{3D} has the dimensionality of the inverse time, so that $1/(4\pi\sigma_{\mathrm{3D}})$ (in CGS units, while in SI it is $\varepsilon_0/\sigma_{\mathrm{3D}}$) would have the meaning of the RC time needed to dissolve a charge density perturbation if the conductivity were frequency independent. In conventional metals $1/(4\pi\sigma_{\mathrm{3D}})$ is extremely short (in the attosecond range). Still, one can compare $4\pi\sigma_{\mathrm{3D}}$ to other scales. One is the electron relaxation time τ; typically, $4\pi\sigma_{\mathrm{3D}}\tau = \omega_p^2\tau^2 \gg 1$ (ω_p being the bulk plasma frequency). Moreover, at $T \ll \hbar/\tau$ the relaxation time drops out of the problem, so one cannot construct a dimensionless parameter out of σ_{3D}, which could produce different 'asymptotic maps' of the kind shown in Fig. 2.1. The bulk case turns out to be somewhat similar to the 2D case with $\mathcal{G} \gg 1$.

To see the reason for this similarity, let us recall the asymptotic expressions for the heat current between semi-infinite bulk metals, assuming $T\tau \ll \hbar$ (the derivation can be found in Ref. [Polder71], we also give it in Appendix B):

$$J_a(T) = \frac{\pi^2}{60}\,\frac{\hbar(T/\hbar)^4}{(2\pi\sigma_{\mathrm{3D}})^2 d^2}\ln\frac{2\pi\sigma_{\mathrm{3D}}}{T/\hbar}, \qquad d \ll \frac{\delta_T^3}{\lambdabar_T^2}, \tag{2.16a}$$

$$J_b(T) = \frac{\zeta(3)}{4\pi^2}\,\frac{2\pi\sigma_{\mathrm{3D}}\hbar(T/\hbar)^3}{c^2}, \qquad \frac{\delta_T^3}{\lambdabar_T^2} \ll d \ll \delta_T, \tag{2.16b}$$

$$J_c(T) = \frac{3\,\zeta(3)}{4\pi^2}\,\frac{c^2 T}{2\pi\sigma_{\mathrm{3D}} d^4}\ln\frac{d}{\delta_T}, \qquad \delta_T \ll d \ll (\lambdabar_T^2\delta_T)^{1/3}, \tag{2.16c}$$

$$J_d(T) = \frac{75\,\zeta(7/2)}{256\sqrt{\pi}}\,\frac{\hbar(T/\hbar)^{7/2}}{\sqrt{2\pi\sigma_{\mathrm{3D}}}\,cd}, \qquad (\lambdabar_T^2\delta_T)^{1/3} \ll d \ll \lambdabar_T, \tag{2.16d}$$

$$J_e(T) = \frac{35\,\zeta(9/2)}{16\pi^{3/2}}\,\frac{\hbar(T/\hbar)^{9/2}}{\sqrt{2\pi\sigma_{\mathrm{3D}}}\,c^2}, \qquad \lambdabar_T \ll d, \tag{2.16e}$$

where the parametric intervals of d are conveniently defined in terms of two length scales: the thermal wavelength $\lambdabar_T = \hbar c/T$ and the normal skin depth at the thermal frequency, $\delta_T = c/\sqrt{2\pi\sigma_{\mathrm{3D}}T/\hbar} \ll \lambdabar_T$. The shortest-distance expression (2.16a) is determined by the TM evanescent contribution and corresponds to the Coulomb limit (indeed, it does not contain the speed of light); however, the length scale $\delta_T^3/\lambdabar_T^2$ is extremely short: for $4\pi\sigma_{\mathrm{3D}} = 10^{17}\,\mathrm{s}^{-1}$ at $T = 300\,\mathrm{K}$, we have $\delta_T = 0.22\,\mu\mathrm{m}$ and $\lambdabar_T = 7.6\,\mu\mathrm{m}$, so $\delta_T^3/\lambdabar_T^2 \sim 2\,\text{Å}$ and becomes even smaller at lower temperatures, invalidating the local approximation and making Eq. (2.16a) irrelevant for conventional metals. Equations (2.16b) and (2.16c) originate from the TE evanescent contribution and correspond to magnetostatic coupling [Chapuis08c]. Equation (2.16d) contains both TM evanescent and TM travelling contributions which are of the same order at such distances (only the evanescent one was evaluated in Ref. [Polder71]); in fact, for both contributions the integral is dominated by wave vectors k very close to ω/c, and the fields vary weakly across the gap so there is no sharp physical distinction between travelling and evanescent waves. Finally, Eq. (2.16e) comes from the TE and TM travelling waves and is contributed by many Fabry-Perot modes inside the gap.

It is easy to see that by the order of magnitude, Eqs. (2.16b), (2.16c), (2.16d) and (2.16e) can be obtained from Eqs. (2.14a), (2.14c), (2.12c) and (2.14d), respectively, by replacing $\mathcal{G} = 2\pi\sigma_{\mathrm{2D}}/c \to 2\pi\sigma_{\mathrm{3D}}\delta_\omega/c$, where the skin depth $\delta_\omega = c/\sqrt{2\pi\sigma_{\mathrm{3D}}\omega}$ corresponds to the typical frequency scale determining the integral: it is δ_T for Eqs. (2.16b), (2.16d) and (2.16e), determined by frequencies $\omega \sim T/\hbar$, and $\delta_\omega \sim d$ for Eq. (2.16c), where the frequency integral is logarithmic, with the lower cutoff corresponding to $\delta_\omega \sim d$ (see Appendix B for details). This replacement roughly corresponds to modelling the semi-infinite metal as an effective metallic layer whose thickness corresponds to the field penetration depth. Such an effective layer is characterised by the dimensionless $\mathcal{G}_{\mathrm{eff}} \sim \sqrt{2\pi\sigma_{\mathrm{3D}}/\omega}$, so that $\mathcal{G}_{\mathrm{eff}} \gg 1$ for conventional metals and reasonable temperatures. We note that this effective layer analogy should be used with caution, since the frequency dependence of δ_ω sometimes makes the convergence scale of the frequency integral different from the case of fixed layer thickness.

2.2.5 Role of the substrates

The expressions given in Sec. 2.1.3 correspond to the heat transferred from one metallic sheet to the other, not including the radiation transmitted behind each sheet. In an experiment, this transmitted radiation can be absorbed by dielectric substrates (even if the absorption by the dielectric material is very weak, the transmitted radiation can still be absorbed if the substrate is thick enough) or captured by some background parts of the structure. Whether the transmitted radiation should be included in the measured heat current or not, depends on the specific measurement scheme. The measurement can be done directly on the metallic layers as, for example, in Ref. [Kralik12]; the radiation absorbed in the substrate leads to a very weak heating of the latter since this absorption occurs in a large volume, and has little effect on the metallic layers. The opposite example is Ref. [Yang18], where the measurement was actually performed behind the substrate, so that all radiation was collected, and good thermal contact between graphene sheets and the substrate was ensured.

If radiation absorbed by the thick dielectric substrate is included, one should also include radiation emitted by the substrate, which is equivalent to adding an incident black-body heat flux

$$J_{\mathrm{bb}}(T) = \frac{\pi^2}{60}\,\frac{T^4}{c^2\hbar^3}. \tag{2.17}$$

Its effect is especially important for $\mathcal{G} \ll 1$ since the transmission of each sheet is close to unity in this case. For thick dielectric substrates with dielectric constant $\varepsilon = 1$ and an infinitesimal imaginary part, almost all incident black-body heat flux is transmitted through the sheets and absorbed on the other side, so the far-field expressions $J_{\mathrm{lte}}(T)$ and $J_{\mathrm{hte}}(T)$, Eqs. (2.12e) and (2.12f), should be replaced by Eq. (2.17). This starts to dominate over the near-field contribution $J_{\mathrm{hd}}(T)$ at shorter distances, $d \sim \bar{\lambda}_T \mathcal{G}^{1/3} \ll \bar{\lambda}_T$. This is natural, since the near-field contribution is still determined by the sheets, while the far-field transfer is essentially between the substrates.

For $\mathcal{G} \gg 1$, the low-temperature far-field expression (2.14d) remains valid, since the layer transmission is too small. At intermediate temperatures, $\sqrt{\mathcal{G}} \ll T\tau/\hbar \ll \mathcal{G}$, the sheet transmission is still small, but it is already larger than the absorption, so the far-field contribution is determined by the fraction of the black-body radiation entering the Fabry-Perot resonator, $J(T) \sim J_{\mathrm{bb}}(T)\,(T\tau/\hbar G)^2$, which is larger than $J_{\mathrm{it}}(T)$, Eq. (2.14e). At $T\tau/\hbar \gg 1$ the conductivity at relevant frequencies is so small, that the transmission of the layers is close to 1, and instead of Eq. (2.14f) the far-field heat current is the black-body one, Eq. (2.17).

2.2.6 Quantifying the near-field enhancement of the heat transfer

When studying radiative heat transfer between objects, one is often interested in comparing it to the radiative transfer between black bodies of the same geometry. In the planar geometry considered here, the black-body heat current is given by Eq. (2.17) and does not depend on d. Metals are not perfect emitters/absorbers, so in the far field they exchange less heat than black bodies. This is seen by comparing the far-field expressions (2.12e), (2.12f), (2.14d)–(2.14f), which are all d independent, to Eq. (2.17). At the lowest temperatures, we have $J_{\mathrm{lte}}(T)/J_{\mathrm{bb}}(T) = 4\mathcal{G}^2\ln(1/\mathcal{G})$ and $J_{\mathrm{lt}}(T)/J_{\mathrm{bb}}(T) = 4/(3\mathcal{G})$, for $\mathcal{G} \ll 1$ and $\mathcal{G} \gg 1$, respectively. At higher temperatures, even smaller values are obtained. Only at $\mathcal{G} \sim 1$ the metallic sheets approach the black-body limit in the far field, due to impedance matching with vacuum.

However, it is well known that the coupling of evanescent modes can lead to significant, d-dependent contributions to the heat transfer between closely spaced conducting bodies, resulting in an overall enhancement of the radiative power compared to the black-body result ([Joulain05, Volokitin07, Song15a, Biehs21] and references therein). So there are two competing effects: the far-field contribution is weaker than that of black bodies due to metals being imperfect emitters, meanwhile between metals there is an extra contribution from the evanescent waves that dominates in the near field (evanescent waves do not contribute to black-body radiation into the vacuum). To assess when the near-field contribution leads to an enhancement over the black-body result, one needs to compare various near-field expressions in Sec. 2.1.3 to Eq. (2.17). For example, at the lowest temperatures, $J_{\mathrm{hd}}(T)$ and $J_{\mathrm{he2}}(T)$ [Eqs. (2.12d) and (2.14c)] overcome the black-body current at $d \lesssim \lambda\!\!\!^{-}_T\mathcal{G}^{1/3}$ and $d \lesssim \lambda\!\!\!^{-}_T\mathcal{G}^{-1/3}$, respectively, for $\mathcal{G} \ll 1$ and $\mathcal{G} \gg 1$.

The strongest enhancement is obtained at small separations (since the near-field contribution always grows with decreasing d) and low temperatures (since the black-body expression has the highest power of temperature). Thus, we need the ratio of Eqs. (2.12c) and (2.17):

$$\frac{J_{\mathrm{ld}}(T)}{J_{\mathrm{bb}}(T)} = \frac{15\,\zeta(3)}{2\pi^3}\,\frac{1}{\mathcal{G}}\,\frac{\lambda\!\!\!^{-}_T}{d}. \tag{2.18}$$

Note that the enhancement is stronger for smaller $\mathcal{G}$; indeed, in this regime the near-field transfer is dominated by the Coulomb interaction which is screened less efficiently in poorly conducting metals. Taking $T = 300\,\mathrm{K}$, $d = 10\,\mathrm{nm}$, and $\mathcal{G} = 0.01$ (we remind that for smaller values of $\mathcal{G}$ the Drude description is not valid), we obtain the ratio of 2×10^4. For bulk metals, the relevant ratio is $J_b(T)/J_{\mathrm{bb}}(T) \approx 0.19\,(4\pi\hbar\sigma_{3\mathrm{D}}/T)$ [Eq. (2.16b), since Eq. (2.16a) becomes valid at unrealistically short distances], which amounts to about 3×10^4 for $4\pi\sigma_{3\mathrm{D}} = 7\times10^{18}\,\mathrm{s}^{-1}$ (silver at room temperature).

2.3 Comparison to experiments

Values $\mathcal{G} \lesssim 1$ are characteristic of atomically thin 2D materials. This is illustrated by a recent experiment [Yang18], where two doped monolayer graphene sheets were placed on insulating silicon ($\varepsilon = 11.7$) and separated by a 400 nm wide vacuum gap. For temperatures corresponding to energies well below the Fermi energy E_F (counted from the Dirac point) the electrons in graphene can be viewed as a conventional 2D electron gas with the density of states per unit area coming from free electron theory: $\nu = 2|E_F|/(\pi\hbar^2 v_F^2)$ (including the valley and spin degeneracies). The Fermi energy of 0.27 eV and the relaxation time $\tau = 100\,\mathrm{fs}$ reported in Ref. [Yang18] give $\mathcal{G} = 0.6$. The linear thermal conductance per unit area $dJ/dT = 30\,\mathrm{W\,m^{-2}\,K^{-1}}$ was measured around room temperature. These conditions correspond to the high-temperature plasmon regime, Eq. (2.12b), where the substrate dielectric constant ε enters only inside the logarithmic function $\mathcal{L}$ (App. A). Setting $\mathcal{L} = 1$ in Eq. (2.12b) gives $dJ/dT = 11\,\mathrm{W\,m^{-2}\,K^{-1}}$, which agrees by order of magnitude with the experimental value.

Thin layers of conventional metals are typically characterised by $\mathcal{G} \gg 1$. Several experiments have been reported in the literature. In each case, it is important to compare the layer thickness h to the the skin depth δ_ω at the relevant frequency, to ensure the layers should correspond to the 2D limit, rather than the bulk one (we discuss this more in Sec. 3.2.2 and one may show that the latter is the case of Refs. [Hargreaves69, Song16]).

Heat transfer in a wide range of interlayer separations and temperatures was studied in Ref. [Kralik12] for two 150 nm thick tungsten layers on alumina substrates. The measured dc conductivity of the material $4\pi\sigma_{\mathrm{3D}} = 0.6\times 10^{18}\,\mathrm{s}^{-1}$ (constant in the temperature range of the experiment) corresponds to a value of the dimensionless conductivity parameter $\mathcal{G} \approx 150$. The skin depth at $T = 40\,\mathrm{K}$ is $\delta_T = 240\,\mathrm{nm}$, and even longer at lower temperatures, so the layers are close to the 2D limit. The separation between the layers was varied over $d = 1 - 300\,\mu\mathrm{m}$, while the temperatures were $T_1 = 5\,\mathrm{K}$ and $T_2 = 10 - 40\,\mathrm{K}$, corresponding to regions (he2) and (lt) in Fig. 2.1 (lower). It can be easily checked that in these regions, the dielectric substrate plays no role as long as $\sqrt{\varepsilon} \ll \mathcal{G}$, which clearly holds here. Although the numerical calculation accounting for the finite layer thickness does better in closely matching the experimental points (see Fig. 2 of Ref. [Kralik12]), our simple expressions (2.14c) and (2.14d) (i) agree with the observed values within a factor of 3 without any fitting parameters, (ii) give the correct distance dependence throughout the experiment, (iii) capture the observed approximate collapse of the rescaled data for $J(T)/T^4$ on a function of a single variable Td, and (iv) correctly predict the separation $d \approx 0.5\lambda\!\!\!^{-}_T$, at which the crossover between the near-field and the far-field regimes occurs, $J_{\mathrm{he2}}(T) = J_{\mathrm{le}}(T)$.

A recent publication [Sabbaghi20] presents measurements of heat transfer between two aluminium films of varying thicknesses $h = 13 - 79\,\mathrm{nm}$, separated by a fixed vacuum gap $d = 215\,\mathrm{nm}$ and attached to silicon substrates. The experiment was performed around room temperature with one film being heated such that $\Delta T = 25 - 65\,\mathrm{K}$. Taking the values $\omega_p = 1.93\times 10^{16}\,\mathrm{s}^{-1}$ and $\tau \approx 5\,\mathrm{fs}$ [Modest13] used in Ref. [Sabbaghi20] to interpret the data, we obtain $\delta_T \approx 50\,\mathrm{nm}$ and $\mathcal{G} \approx 40$ for the thinnest layer with $h = 13\,\mathrm{nm}$. Then Eq. (2.14c) predicts $dJ/dT = 250\,\mathrm{W\,m^{-2}/K}$, which agrees in order of magnitude with the reported value, $dJ/dT = 60\,\mathrm{W\,m^{-2}/K}$.

An intriguing feature of the results reported in Ref. [Sabbaghi20] is the independence of dJ/dT of the layer thickness. This agrees neither with our 2D expressions, nor with the more precise simulations done in Ref. [Sabbaghi20]. All theoretical results point to a non-monotonic dependence of the heat current on the layer thickness or dc conductivity [the latter is also true for the bulk limit expressions (2.16)]. Further experimental investigations of this dependence would be interesting.

2.4 Summary and outlook

In this chapter, we have performed an analytical calculation of the radiative heat current between two thin metallic layers, using the standard framework of fluctuational electrodynamics and a local 2D Drude model for the electromagnetic response of each layer. We have identified two different classes of such structures, distinguished by the dimensionless 2D dc conductivity $\mathcal{G} = 2\pi\sigma_{\mathrm{2D}}/c$. For poor metals with $\mathcal{G} \ll 1$, typically represented by atomically thin 2D materials, the heat transfer is dominated by evanescent modes at distances d extending well beyond $\lambdabar_T$, and the main coupling mechanism in this near-field regime is the Coulomb interaction between electrons in the two layers. Good metals with $\mathcal{G} \gg 1$, such as thin films of conventional metals, behave more similarly to the bulk limit, studied in earlier works: the crossover from near to far field occurs at $d \sim \lambdabar_T$ at not too high temperatures, and the near-field transfer is dominated by magnetostatic (inductive) coupling between the layers in a wide range of parameters. We remind that for the two-dimensional geometry considered here, the role of the substrates may be important according to the specific experimental setup, how the temperature difference is maintained, and how the heat current is measured. In relation to this, we found that our result about evanescent mode dominance beyond $\lambdabar_T$ applies only to the heat current from one sheet to the other, not including the radiation emitted and absorbed by the substrates.

We have derived several simple approximate asymptotic expressions for the heat current valid in different parametric ranges of interlayer separation distance and temperature. We quantified the degree of enhancement that may be achieved in the near field with respect to the far-field and black-body results. In agreement with previous work, we find that at small enough separations the radiative heat transfer may realistically be $\sim 10^4$ times that of black bodies. Comparing our expressions with the available experimental data, we saw that they give valid order-of-magnitude estimates of the heat current and correctly capture its dependence on the distance and temperature. Better agreement with the experimental results can be reached by a more detailed modelling of each system geometry and the dielectric response, which is strongly system-specific and lies beyond the scope of our work. Still, our approximate results offer a useful insight into the main physical mechanisms responsible for the heat transfer.

We have found that the Coulomb limit is valid for poor metals up to and even beyond the thermal wavelength, while for good metals the Coulomb interaction is predicted to dominate only at unrealistically small separations. Focusing therefore on poor metals, we are motivated to take advantage of the simplifications of the Coulomb limit to investigate a richer model for the material response at small separations. In particular, we are motivated to study the effect of nonlocality in the material response, which is expected to play a role at extremely small separations where the local Drude model may fail. This nonlocality, manifested by spatial dispersion in the conductivity, is investigated in the next chapter, where not only do we reveal quantitatively the limits of validity of the local Drude model, but also we identify the regions in parameter space where the dominant heat transfer channel is provided by surface plasmons.

Dans ce chapitre, nous avons effectué un calcul analytique du courant thermique radiatif entre deux couches métalliques minces, en utilisant le cadre standard de l'électrodynamique fluctuationnelle et le modèle de Drude 2D local pour la réponse électromagnétique de chaque couche. Nous avons identifié deux classes différentes de telles structures, distinguées par la conductivité dc 2D adimensionnelle $\mathcal{G} = 2\pi\sigma_{\mathrm{2D}}/c$. Pour les mauvais métaux avec $\mathcal{G} \ll 1$, typiquement représentés par des matériaux 2D atomiquement minces, le transfert de chaleur est dominé par des modes évanescents à des distances d s'étendant bien au-delà de $\lambda\!\!\!^{-}_T$, et le principal mécanisme de couplage dans ce régime de champ proche est l'interaction de Coulomb entre les électrons dans les deux couches. Les bons métaux avec $\mathcal{G} \gg 1$, tels que les couches minces de métaux conventionnels, se comportent de manière plus similaire à la limite 3D, étudiée dans des travaux antérieurs : le passage du champ proche au champ lointain se produit à $d \sim \lambda\!\!\!^{-}_T$ à des températures pas trop élevées, et le transfert en champ proche est dominé par le couplage magnétostatique (inductif) entre les couches dans une large gamme de paramètres. Nous rappelons que pour la géométrie bidimensionnelle considérée ici, le rôle des substrats peut être important en fonction du montage expérimental spécifique, de la façon dont la différence de température est maintenue et de la façon dont le courant thermique est mesuré. À cet égard, nous avons constaté que notre résultat concernant la dominance du mode évanescent au-delà de$\lambda\!\!\!^{-}_T$ ne s'applique qu'au courant thermique d'une feuille à l'autre, sans tenir compte du rayonnement émis et absorbé par les substrats.

Nous avons dérivé plusieurs expressions asymptotiques approximatives simples pour le courant thermique, valables dans différentes plages paramétriques de distance de séparation entre les couches et de température. Nous avons quantifié le degré d'amélioration qui peut être atteint dans le champ proche par rapport au champ lointain et aux résultats du corps noir. En accord avec les travaux antérieurs, nous constatons qu'à des séparations suffisamment petites, le transfert de chaleur radiatif peut, de manière réaliste, être $\sim 10^4$ fois celui des corps noirs. En comparant nos expressions avec les données expérimentales disponibles, nous avons vu qu'elles donnent des estimations valides de l'ordre de grandeur du courant thermique et qu'elles capturent correctement sa dépendance à la distance et à la température. Un meilleur accord avec les résultats expérimentaux peut être obtenu par une modélisation plus détaillée de la géométrie de chaque système et de la réponse diélectrique, ce qui est fortement spécifique au système et dépasse le cadre de notre travail. Néanmoins, nos résultats approximatifs offrent un aperçu utile des principaux mécanismes physiques responsables du transfert de chaleur.

Nous avons constaté que la limite de Coulomb est valable pour les mauvais métaux jusqu'à et même au-delà de la longueur d'onde thermique, tandis que pour les bons métaux, l'interaction de Coulomb ne devrait dominer que pour des séparations irréalisablement petites. En nous concentrant donc sur les mauvais métaux, nous sommes motivés pour profiter des simplifications de la limite de Coulomb pour étudier un modèle plus riche pour la réponse du matériau. En particulier, nous sommes motivés pour étudier l'effet de la non-localité dans la réponse du matériau, qui devrait jouer un rôle à des séparations extrêmement petites où le modèle local de Drude peut échouer. Cette non-localité, qui se manifeste par une dispersion spatiale de la conductivité, est étudiée dans le chapitre suivant, où non seulement nous révélons quantitativement les limites de validité du modèle local de Drude, mais où nous identifions également les régions de l'espace des paramètres où le canal de transfert de chaleur dominant est fourni par les plasmons de surface.

3

Role of disorder in plasmon-assisted near-field heat transfer between two-dimensional metals

Contents

3.1 Radiative heat transfer in the Coulomb limit

Having clarified in the previous chapter the role of retardation in the electromagnetic interaction, we here focus on the case where it is unimportant: the Coulomb limit, where only the electrostatic contribution to the interaction is retained. Valid at sufficiently small distances, many studies of the radiative heat transfer have been carried out in the Coulomb limit. In particular, in several works dedicated to different materials in the near-field regime, the important role played by collective plasmon excitations has been pointed out [Rousseau09a, Svetovoy12, Ilic12, Rodriguez-López15, Yu17, Jiang17, Zhao17, Zhang19, Wang19]. However, Ref. [Mahan17] concluded that surface plasmons were unimportant for the heat transfer between two bulk semi-infinite metals, and in Ref. [Kamenev18] no plasmon contribution was reported for heat current between two thin metallic layers in the clean and diffusive limits. Here we revisit the problem of radiative heat transfer between two thin parallel metallic sheets in the Coulomb limit, and establish definitively the role of surface plasmons. Building on previous investigations including the effects of spatial dispersion [Chapuis08c], we employ a nonlocal model for the material response function which interpolates between clean and diffuse levels of disorder in the material.

3.1.1 Caroli formula

For radiative heat transfer between parallel two-dimensional layers, the Coulomb limit corresponds to taking the limit $c \to \infty$ in the general equation Eq. (2.8). Regarding Eq. (2.8) and the way in which c enters into the emmissivities in Eqs. (2.9b), (2.9d), we see that the heat current in the Coulomb limit is equivalent to retaining only the TM evanescent contribution from the full retarded calculation. Eq. (2.8) for the heat current per unit area then reduces to the well known formula [Yu17, Jiang17, Zhang18, Wang18, Kamenev18]:

$$J(T_1,T_2) = \int_0^\infty \frac{d\omega}{\pi} \int \frac{d^2\mathbf{k}}{(2\pi)^2} \hbar\omega \left[\mathcal{N}_2(\omega) - \mathcal{N}_1(\omega)\right] \mathcal{T}(\mathbf{k},\omega), \tag{3.1}$$

$$\mathcal{T}(\mathbf{k},\omega) = 2\left|V_{12}(\mathbf{k},\omega)\right|^2 \operatorname{Im}\Pi_1(\mathbf{k},\omega) \operatorname{Im}\Pi_2(\mathbf{k},\omega), \tag{3.2}$$

often called the Caroli formula, in analogy to a similar expression for electron current across a tunnel junction [Caroli71]. In Eq. (3.1), $\mathcal{N}_{1,2}(\omega) = 1/[\exp(\hbar\omega/T_{1,2}) - 1]$ are the Bose distribution functions in the two layers. In Eq. (3.2),

$$V_{12}(\mathbf{k},\omega) = \frac{v_{\mathbf{k}} e^{-qd}}{(1 - v_{\mathbf{k}}\Pi_1)(1 - v_{\mathbf{k}}\Pi_2) - v_{\mathbf{k}}^2 \Pi_1 \Pi_2 e^{-2kd}} \tag{3.3}$$

is the Coulomb interaction between the layers, screened in the random-phase approximation (RPA), with $v_{\mathbf{k}} = 2\pi e^2/k$ being the bare 2D Coulomb potential and $e < 0$ the electron charge. Finally, $\Pi_1(\mathbf{k},\omega)$ and $\Pi_2(\mathbf{k},\omega)$ are the susceptibilities determining the linear response $\delta\rho_i(\mathbf{r},t) = \Pi_i(\mathbf{k},\omega)\, e\varphi_{\mathbf{k},\omega}\, e^{i\mathbf{kr} - i\omega t}$ of the 2D electron density ρ_i in the corresponding layer $i = 1,2$ to a perturbing electrostatic potential $\varphi_{\mathbf{k},\omega}\, e^{i\mathbf{kr} - i\omega t}$ applied to that layer. As discussed in Sec. 1.2.1, the density response function is related to the in-plane longitudinal optical conductivity, $\sigma(\mathbf{k},\omega) = (i\omega/k^2)e^2\Pi(\mathbf{k},\omega)$, where the $\mathbf{k}$-dependence represents the spatial dispersion that was not taken into account in Ch. 2 where we used the simple Drude model, Eq. (2.1). As we have seen here, Eq. (3.1) can be derived from the Coulomb limit of fluctuational dynamics. In Appendix C we also derive it from non-equilibrium Green's function formalism, hence providing a microscopic justification for the phenomenological fluctuational electrodynamics.

3.1.2 Model: 2D electron gas with impurity scattering

The density response functions encode all material characteristics of the two layers. We model each layer as a degenerate isotropic 2D electron gas with short-range impurities. Such a system can be characterised by three parameters: (i) ν, the electronic density of states per unit area at the Fermi level including both spin projections, whose energy dependence is neglected; (ii) v_F, the Fermi velocity; and (iii) τ, the elastic scattering time. The Fermi momentum p_F is assumed to be the largest momentum scale, $p_F/\hbar \gg k, \omega/v_F, T/(\hbar v_F), 1/(v_F\tau)$. This assumption is economical in view of making analytical progress, and sufficient since we will always consider temperatures much lower than the Fermi energy – going to higher temperatures would require use of the more complicated Lindhard functions [Mihaila11, Stern67]). Under these assumptions, the density response function of each layer is temperature-independent and given by [Zala01]

$$\Pi(\mathbf{k},\omega) = -\nu\left[1+\frac{i\omega\tau}{\sqrt{(1-i\omega\tau)^2+(v_Fk\tau)^2}-1}\right], \tag{3.4}$$

for an arbitrary relation between ω, v_Fk, and τ. Equation (3.4) interpolates between two well-known expressions corresponding to the clean limit ($\tau \to \infty$) and the diffusive limit ($\omega, v_Fk \ll 1/\tau$):

$$\Pi(\mathbf{k},\omega) = -\nu\left[1+\frac{i\omega}{\sqrt{(v_Fk)^2-\omega^2}}\right] \quad \text{(clean)}, \tag{3.5a}$$

$$\Pi(\mathbf{k},\omega) = -\frac{\nu Dk^2}{Dk^2-i\omega} \quad \text{(diffusive)}, \tag{3.5b}$$

where $D = v_F^2\tau/2$ is the diffusion coefficient. Equation (3.4) corresponds to a 2D analog of Mermin's prescription [Mermin70], which was recently used to model the response in monolayer graphene [Jablan09, Svetovoy12]. In Appendix D we give a derivation of Eq. (3.4) based on the Boltzmann equation for electrons scattering on impurities. Equation (3.4) may also be found by resummation of Feynman diagrams for impurity scattering [Bruus04]. In spite of several assumptions underlying Eq. (3.4), its simplicity enables one to obtain an important insight into the interplay between the spatial dispersion [that is, the $\mathbf{k}$ dependence of the conductivity $\sigma(\mathbf{k},\omega)$] and the impurity scattering. For simplicity we also assume the two metals to be identical.

The three independent material parameters, introduced above, define two important length scales: (i) the 2D screening length $1/\kappa = (2\pi e^2\nu)^{-1}$, and (ii) the mean free path

$\ell = v_F \tau$. Typically, the screening length is very short, so we assume $\kappa\ell \gg 1$ and $\kappa d \gg 1$. The mean free path can vary from several nanometers to several microns, and may be larger or smaller than the separation d between the two layers.

3.1.3 Asymptotic expressions for limiting cases

In the isotropic model, formulated above, Eq. (3.1) represents a two-dimensional integral over k and ω. This integral can be rather straightforwardly evaluated numerically, but much better insight into relevant physics is obtained by studying different asymptotics of the integral in various parameter regimes. The latter approach was adopted in Ref. [Kamenev18] using the two limiting expressions (3.5a) and (3.5b). It turns out, however, that these expressions miss the plasmon contribution.

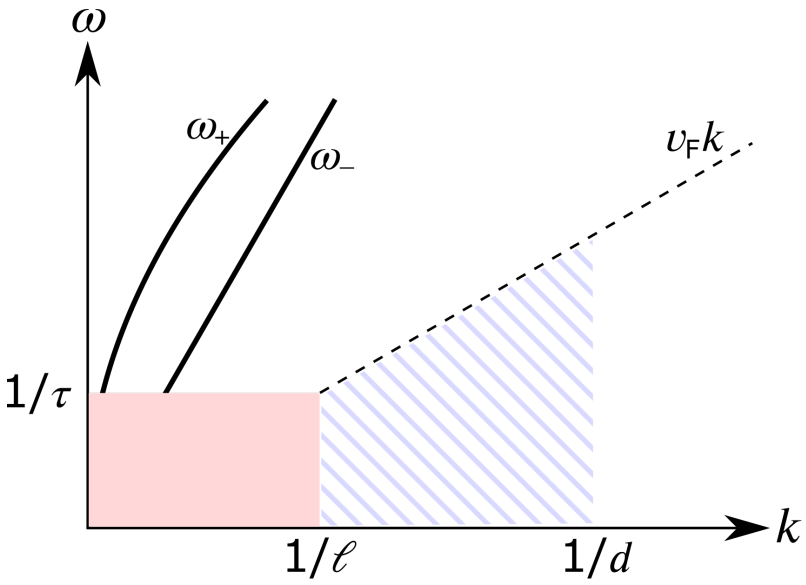

Figure 3.1: A schematic picture showing the behaviour of $\mathcal{T}(k,\omega)$ *[Eq. (3.2)] in the* (k,ω) *plane for* $d \ll \ell$*. For* $k \gg 1/d$ *(to the right of the hatched area),* $\mathcal{T}(k,\omega)$ *is suppressed by the factor* e^{-kd}*. In the hatched area,* $\mathcal{T}(k,\omega)$ *is well approximated by the clean limit expression (3.5a), while the shaded area* $k\ell \ll 1$, $\omega\tau \ll 1$ *corresponds to the diffusive limit (3.5b). In the white region above the shaded and hatched areas (*$\omega \gg 1/\tau$, $\omega > v_F k$*) the integrand is small except, maybe, in the vicinity of the symmetric and antisymmetric plasmon dispersions (upper and lower solid lines, respectively) where* $|V_{12}|^2$ *is peaked.*

We show schematically the behaviour of of $\mathcal{T}(k,\omega)$ [Eq. (3.2)] in the (k,ω) plane for $d \ll \ell$ in Fig. 3.1. At large $\omega \gtrsim \max\{T_1,T_2\}/\hbar$, the integrand in Eq. (3.1) is suppressed by the Bose function at ω, and this cutoff may be positioned anywhere in Fig. 3.1, depending on the temperatures. At large $k \gtrsim 1/d$, the integrand is suppressed by e^{-kd} in the numerator of Eq. (3.3); Fig. 3.1 corresponds to the case $d \ll \ell$, but for larger d the spatial cutoff may shift to the diffusive shaded area.

The strongly coupled plasmon modes (in the case of identical layers, symmetric and antisymmetric, denoted by "±") manifest themselves as poles of $V_{12}(k,\omega)$. In the clean limit, $\tau \to \infty$, the plasmon frequencies are real and given by (for $k \ll \kappa$)

$$\omega_\pm = v_F \sqrt{\kappa k \frac{1 \pm e^{-kd}}{2}}. \tag{3.6}$$

At finite τ, but such that $\omega_\pm \tau \gg 1$, the poles acquire a small imaginary part, so $|V_{12}(k,\omega)|^2$ is peaked around the dispersions (3.6). At $\omega_\pm \tau \lesssim 1$, when the diffusive expression (3.5b) applies, the plasmons are overdamped and do not produce a separate contribution to the integral. In the strictly clean limit, $\tau \to \infty$, their contribution vanishes as well, since for $\omega > v_F k$ the integrand vanishes because $\mathrm{Im}\,\Pi(k, \omega > v_F k) = 0$. In Refs. [Mahan17, Kamenev18], the authors focussed on the clean and diffusive limits and therefore missed the plasmon contribution.

For temperature-independent $\Pi(\mathbf{k},\omega)$, Eq. (3.1) naturally splits into the difference $J(T_1,T_2) = J(T_2) - J(T_1)$. A detailed analysis of different asymptotic regimes for the integral in Eq. (3.1) (given in App. A.4) results in several asymptotic expressions for $J(T)$:

$$J_{\mathrm{lc}}(T) = \frac{\pi^2}{60} \frac{T^4}{\hbar^3 v_F^2 (\kappa d)^2} \ln \frac{v_F}{Td}, \tag{3.7a}$$

$$J_{\mathrm{hc}}(T) = \frac{\pi^2}{900} \frac{v_F}{d^3} \frac{T}{(\kappa d)^2}, \tag{3.7b}$$

$$J_{\mathrm{lp}}(T) = \frac{\zeta(3)}{4\pi} \frac{T^3}{\hbar^2 D \kappa d}, \tag{3.7c}$$

$$J_{\mathrm{hp}}(T) = \frac{T}{16\pi\tau d^2} \mathcal{L}(\ell^2 \kappa/4d), \tag{3.7d}$$

$$J_{\mathrm{ld}}(T) = \frac{\zeta(3)}{8\pi} \frac{T^3}{\hbar^2 D \kappa d}, \tag{3.7e}$$

$$J_{\mathrm{hd}}(T) = \frac{1}{16\pi} \frac{D\kappa}{d^3} T. \tag{3.7f}$$

In the labels “l" and “h” denote low and high temperature, while “c", “p", and “d” stand for clean, plasmonic, and diffusive, respectively. Here $\zeta(x)$ is the Riemann zeta function, and $\mathcal{L}(x)$ is a slow logarithmic function defined in Eq. (A.37). For moderate values of $\ln(\ell^2\kappa/4d) < 10$, it can be approximated with 10% precision as

$$\mathcal{L}(x) \approx \frac{4 \ln^3 x}{1 + (\ln x)/\ln(1 + \ln x)}. \tag{3.8}$$

Figure 3.2 schematically shows the domains of validity for expressions (3.7) in the $(1/d, T)$ plane. The clean and diffusive regimes were also identified in Ref. [Kamenev18].

Each of the above regimes is characterised by typical scales of k and ω, which are found to dominate the integral in Eq. (3.1) – see App. A.4. Namely, $k \sim 1/d$ in the all high temperature cases, $T/(\hbar v_F \sqrt{\kappa d})$ in the low temperature plasmonic case and $\sqrt{T/(\hbar D \kappa d)}$ in the low temperature diffusive case. In the low temperature clean case, the momentum integral is logarithmic, determined by the whole interval $T/(\hbar v_F) < k < 1/d$. In order for the results to be valid for some real sample with a finite in-plane size, this size should be much larger than the corresponding convergence scale $1/k$ specified here. The convergence scale of the frequency integral is $\omega \sim T/\hbar$ in all low temperature cases, while in the high temperature cases it is $v_F\sqrt{\kappa/d}$ in the plasmonic case, $D\kappa/d$ in the diffusive case, and v_F/d in the clean case. In all three high-temperature regions, one can approximate the Bose distribution as $\mathcal{N}(\omega) \approx T/(\hbar\omega)$, so the density fluctuations can be treated classically and the resulting $J(T) \propto T$.

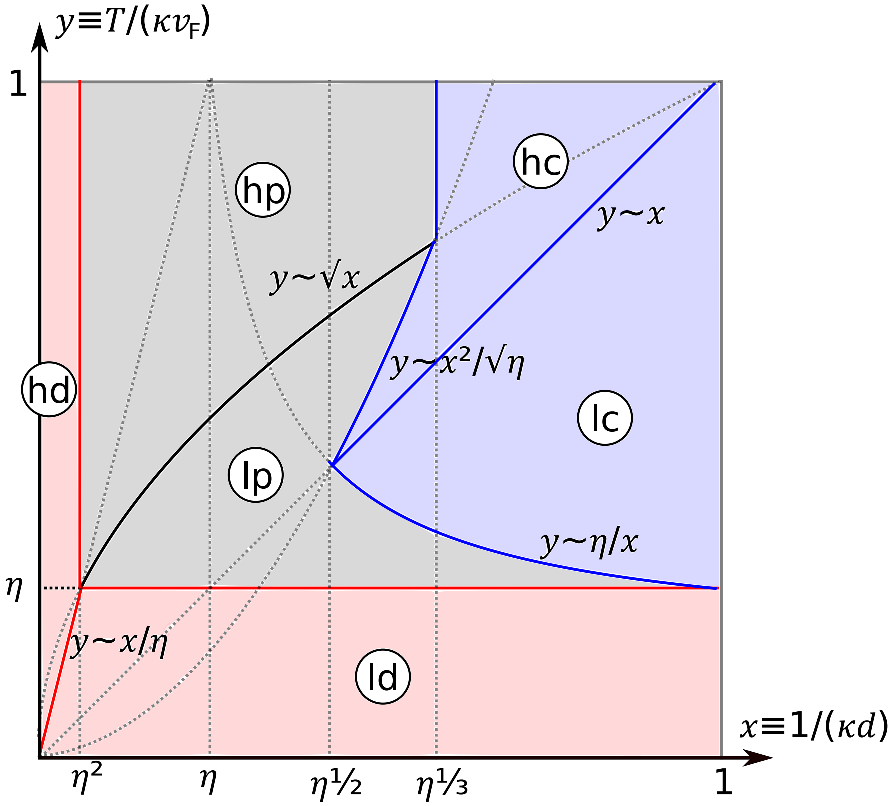

Figure 3.2: The regions in which clean (blue), plasmonic (grey) and diffusive (red), contributions are dominant in the heat current and the domains of validity for asymptotic expressions (3.7) in the parameter plane $(1/d, T)$*, shown in the dimensionless variables* $x \equiv 1/(\kappa d)$*,* $y \equiv T/(\hbar\kappa v_F)$*. The boundaries between the regimes are governed by a single dimensionless material parameter* $\eta = 1/(\kappa\ell) \ll 1$*.*

3.2 Discussion of the results

3.2.1 Roles of coupled surface plasmons and spatial dispersion

As shown in Fig. 3.2, plasmon contributions dominate in a parametrically wide region of the parameter space. Crucially, this behaviour is captured by neither of the limiting expressions (3.5a) nor (3.5b), but by the leading term of the small k expansion of the full expression (3.4). This is equivalent to using the Drude expression for the optical conductivity, $\sigma(\omega) = e^2 \nu D/(1 - i\omega\tau)$, that is, neglecting the spatial dispersion. We note that our modelling does contain finite Landau damping of the plasmons via excitation of electron hole pairs. However, due to the large plasmon velocity this damping only occurs to extremely high energy plasmons that lie above the thermal cut-off and therefore do not play an important role in the heat transfer. We find that the spatial dispersion can also be neglected to describe the diffusive contribution, where once again the Drude expression for the conductivity is sufficient – the details may be found in App. A.4. This is why the contributions given by Eqs. (3.7c)–(3.7f) could be used in the previous chapter for the TM evanescent contribution to the full retarded calculation, in Eqs. (2.12a)–(2.12d).

Here, in the Coulomb limit, we find that the spatial dispersion becomes important only in the clean region where $J(T)$ is dominated by the hatched area in Fig. 3.1. Observing the relevant regions in Fig. 3.2, we see that the spatial dispersion may be safely neglected at all temperatures for $d \gg \sqrt{a_{2\mathrm{D}}\ell}$, where $a_{2\mathrm{D}} = 1/\kappa$ is the 2D electron screening radius, and down to even smaller separations at low temperature. For sufficiently large separations, the dominant heat transfer behaviour is described by a Drude model for the layer conductivity, as quoted in Sec. 2.1.1. One may ask how the length scale determining the importance of spatial dispersion discussed here compares with that of the validity of the Coulomb limit discussed in Ch. 2, which is $\lambda\!\!\!^{-}_T/\mathcal{G}^{1/3}$ for the poor metals that may correspond to the two-dimensional materials addressed in this investigation. The former is expected to be significantly smaller than the latter hence ensuring the compatibility of the two conclusions on the thresholds of the Coulomb limit and spatial dispersion. This may be verified explicitly by taking, for example, the parameters of the experiment on graphene monolayers in Ref. [Yang18].

In the literature on near-field radiative heat transfer, there has been a debate about the separation dependence as bodies are brought vanishingly close to one and other [Pan00, Mulet01a]. While local models predict a divergence of the heat current at small distances (for example, Ref. [Polder71]), it has been shown numerically that spatial dispersion in the conductivity leads to a more physical saturation at $d \to 0$ [Chapuis08c]. In all of our final expressions, including those relevant at the smallest separations J_{ld} and J_{lc}, we have assumed $d \gg 1/\kappa$. However, by relaxing this assumption Ref. [Kamenev18] showed analytically that these contributions do indeed saturate as $d \to 0$.

3.2.2 Generality of the results

The above results were derived for a specific model of a 2D metal, described in Sec. 3.1.2. We now discuss how sensitive these results are to the details of the model.

Expressions (3.7) were obtained for two identical metallic layers. If they are different, but the material parameters ν, v_F and τ are of the same order, our expressions are still valid as order-of-magnitude estimates. In particular, this applies to the plasmon contribution: the plasmons remain strongly hybridised even when the bare plasmonic dispersions of each layer do not match exactly. The case when the two materials are strongly different, is beyond the scope of this work.

One assumption used in the derivation of Eq. (3.4) is that the electron scattering is dominated by short-range impurities. If it is relaxed, Eq. (3.4) is not valid quantitatively (see Appendix D). Note, however, that in the clean regimes (lc, hc), the result is not sensitive to the electron scattering at all, so expressions (3.7a) and (3.7b) remain quantitatively valid. In the other four regimes (ld, hd, lp, hp, and crossovers between them) it is sufficient to use only the local Drude conductivity $\sigma(\omega)$, which is very general. Thus, all information about the electron scattering, needed to describe these regimes, is encoded in the momentum relaxation time τ, and expressions (3.7c)–(3.7f) remain valid for any disorder (weak enough, not to induce Anderson localisation effects).

If the electron momentum relaxation is due to some inelastic scattering mechanism (such as electron-phonon), the relaxation time acquires a temperature dependence. Then, the screened Coulomb interaction depends on both temperatures through the respective polarisation operators, so the heat current can no longer be written as $J(T_1,T_2) = J(T_2) - J(T_1)$. Even if the layers are made of the same material, when kept at different temperatures, they should be treated as different because their inelastic scattering times are different. If the two temperatures are of the same order, our expressions can still be used as order-of-magnitude estimates; the situation when they are strongly different is beyond the scope of this work.

Another strong assumption behind Eq. (3.4) is the strictly 2D character of the electron motion, valid for atomically thin materials. For a metallic slab whose thickness h exceeds a few Fermi wavelengths, several electronic transverse modes contribute to the density response, making Eq. (3.4) invalid even in the clean limit. However, in electrodynamics, the conditions for a material slab to be described as an infinitely thin layer with *some* density response function $\Pi(\mathbf{k},\omega)$, are much weaker. Namely, (i) the normal component of the electric field should not penetrate inside the slab, since the description in terms of a 2D density response function implies that the electrons respond only to the in-plane component, and (ii) the in-plane component should be approximately constant over the slab thickness. Condition (i) is usually satisfied in conventional metals at frequencies below the bulk plasma frequency ω_p (typically, several eV), when the normal electric field component is screened on the length scale of the bulk screening radius (typically, on the atomic scale). Condition (ii) requires the layer thickness h to be smaller compared to both $1/k$ and the skin depth $\delta(\omega)$ in the corresponding regime of the skin effect [Lifshitz81]. The relevant values of k and ω are determined by the convergence scales of the corresponding integrals [as specified after Eqs. (3.7)]. Note that in all cases the 2D response function must satisfy $\Pi(k \ll 1/h, \omega = 0) = -\nu$, where $\nu = \nu_{3D}h$ is determined by the bulk density of states per unit volume, ν_{3D}. This defines $\kappa = 2\pi e^2\nu$, as before.

3.2.3 Numerical verification of analytical expressions

As discussed in Sec. 2.3, there are fairly few experiments on near-field heat transfer in the parallel plate geometry, and those that do exist are typically close to the crossover where retardation may play a role and so their analysis was included in the previous chapter. In order to illustrate the various behaviours and crossovers indicated in Fig. 3.2 in the Coulomb limit, and to verify our asymptotic expressions (3.7), we therefore evaluate numerically the integral in Eq. (3.1) using the full response function (3.4).

To describe clean and plasmonic regimes, we take parameters typical for doped graphene. If the temperature is well below the Fermi energy E_F (counted from the Dirac point) the electrons in graphene can be viewed as a conventional 2D electron gas with the density of states per unit area $\nu = 2|E_F|/(\pi\hbar^2 v_F^2)$, including the valley and spin degeneracies. In Fig. 3.3, we plot $J(T)$ taking $v_F = 10^6\,\mathrm{m\,s^{-1}}$ [Yang18] for two sets of parameters corresponding to $1/(\kappa d) \approx \eta^{1/3} = 0.034$, and $1/(\kappa d) \approx \eta^{1/2}$ [we remind that $\eta \equiv 1/(\kappa\ell)$].

To study the diffusive crossover for realistic materials, we introduce dielectric screening. Equation (3.3), written for metallic layers surrounded by vacuum, can be generalised to the situation when the layers are embedded in a dielectric medium. This generalisation is particularly simple when the medium is characterised by a uniaxially anisotropic dielectric constant, $\varepsilon_\parallel$ in the plane parallel to the layers, and $\varepsilon_\perp$ along the z direction, perpendicular to the layers. The solution of the Poisson equation in such a medium gives the 2D Coulomb potential at a distance z from a charged layer:

$$v_{\mathbf{k}}(z) = \frac{2\pi e^2}{\sqrt{\varepsilon_\parallel \varepsilon_\perp}\, k}\, e^{-\sqrt{\varepsilon_\parallel/\varepsilon_\perp}\, k|z|}. \tag{3.9}$$

Thus, in all expressions (3.7) it is sufficient to rescale

$$\kappa \to \frac{\kappa}{\sqrt{\varepsilon_\parallel \varepsilon_\perp}}, \quad d \to \sqrt{\varepsilon_\parallel/\varepsilon_\perp}\, d. \tag{3.10}$$

In Fig. 3.4 we show the crossover between low- and high-temperature diffusive asymptotics (3.7e) and (3.7f) for two hole-doped tungsten diselenide monolayers embedded in boron nitride. The valence band of $\mathrm{WSe_2}$ is parabolic with the hole effective mass m_h being about half of the free electron mass. The spin degeneracy is lifted by a strong spin-orbit coupling, so only valley degeneracy remains, and the density of states per unit area is $\nu = m_h/(\hbar^2\pi)$. We take $E_F = 50\,\mathrm{meV}$ and a very short $\ell = 2\,\mathrm{nm}$, still consistent with $\kappa\ell \gg 1$, $p_F\ell/\hbar \gg 1$. The taken separation $d = 100\,\mathrm{nm}$ corresponds to $1/(\kappa d) = 0.006$, well below $\eta^2 = 0.1$, and hence to the diffusive region.

We are not showing the high-temperature clean and plasmonic regimes; for realistic material parameters, they correspond to temperatures so high that the assumptions behind our model (degenerate Fermi gas, near-field Coulomb regime) are no longer valid. However, we checked numerically the validity of the asymptotic expressions (3.7b) and (3.7d) for $J_{\mathrm{hc}}(T)$ and $J_{\mathrm{hp}}(T)$.

3.3 On the possibility of an effective circuit description for two-dimensional metals

Often, complicated structures can be described in terms of effective electric circuits made of lumped elements (capacitors, inductors, and resistors) [Pekola21]. In this approach, all details of the structure's geometry are hidden inside the effective circuit parameters, resulting in a much simpler description (provided that such reduction is valid). As discussed in Sec. 1.3.1, the theory of heat transfer in electric circuits was developed in Ref. [Pascal11]. In the circuit analog of the fluctuational electrodynamics, dissipative circuit elements represent thermal baths and provide thermal voltage fluctuations (Johnson-Nyquist noise), while reactive elements mediate the electromagnetic interactions, result-

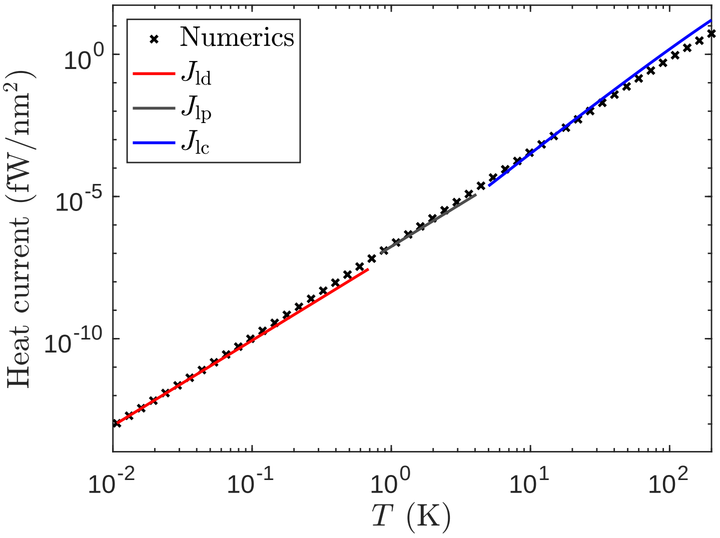

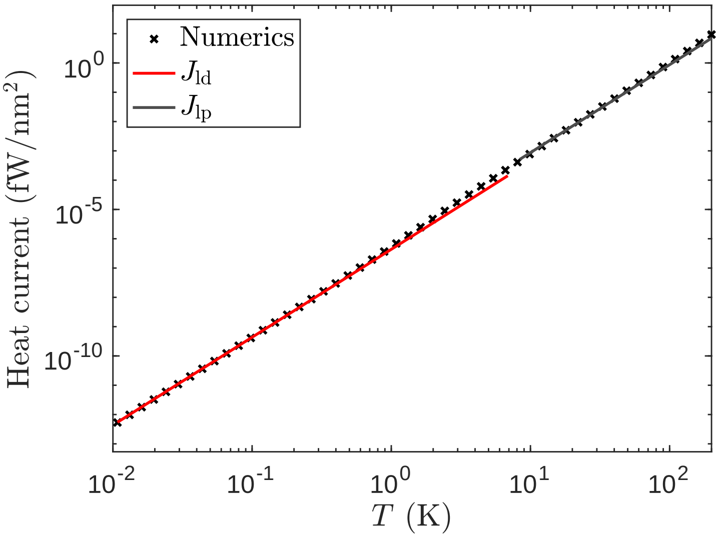

Figure 3.3: Power per unit area as a function of temperature, $J(T)$, for $\nu = 0.29\,eV^{-1}nm^{-2}$, $v_F = 10^6\,m/s$, and $\ell = 10\,\mu\text{m}$, $d = 10\,nm$ (upper panel), $\ell = 1\,\mu\text{m}$, $d = 20\,nm$ (lower panel), characteristic of two graphene monolayers with Fermi energy $E_F = 0.2\,eV$, suspended in vacuum (the 2D screening length $\kappa^{-1} = 0.4\,nm$, the Fermi momentum $p_F/\hbar = 0.3\,nm^{-1}$). The black crosses show numerical results, while the red, black and blue solid lines represent Eqs. (3.7e), (3.7c) and (3.7a), respectively.

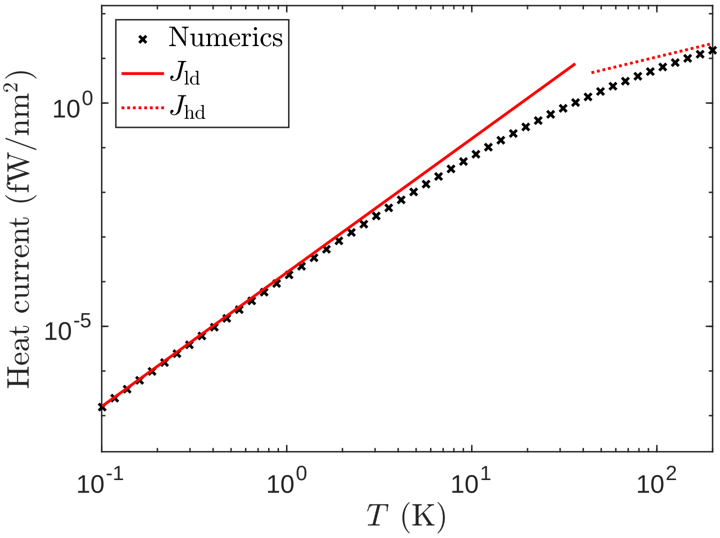

Figure 3.4: Power per unit area as a function of temperature, $J(T)$, *for* $\nu = 2.1\,eV^{-1}nm^{-2}$, $v_F = 0.94\times10^5$ *m/s, and* $\ell = 2\,\mu$m, $d = 100\,nm$, *characteristic of two WSe*$_2$ *monolayers with Fermi energy* $E_F = 50\,meV$, *embedded in boron nitride with* $\varepsilon_\| = 7$, $\varepsilon_\perp = 5$ *[Geick66] (the 2D screening length* $\kappa^{-1} = 0.3\,nm$, *the Fermi momentum* $p_F/\hbar = 1.6\,nm^{-1}$*). The black crosses show the numerical integration results, while the solid and dashed red lines represent expressions (3.7e) and (3.7f), respectively.*

ing in energy exchange between the baths. We check now whether such a circuit approach can be applied to the heat transfer between two metallic layers.

Let us focus on the diffusive regime. As we have seen, the dynamics of density excitations is overdamped in this regime, so it is natural to consider a circuit made of resistors and capacitors only, such as shown in Fig. 3.5 (a). Indeed, the electronic excitations in each layer constitute a dissipative bath analogous to a resistor. To mimic charge oscillations within each layer, the resistor should be shunted by a capacitor. The Coulomb interaction between the layers resembles that between the plates of a capacitor, so the two RC contours are connected by two coupling capacitors C_c.

For the circuit in Fig. 3.5 (a), the power transferred from resistor R_2 to resistor R_1 is given by [Pascal11]

$$P(T_1,T_2) = \int_0^\infty \frac{d\omega}{\pi}\,\hbar\omega\,[\mathcal{N}_2(\omega)-\mathcal{N}_1(\omega)]\,\mathcal{T}(\omega), \tag{3.11}$$

$$\mathcal{T}(\omega) = \frac{2\,\mathrm{Re}\,Z_1(\omega)\,\mathrm{Re}\,Z_2(\omega)}{|Z_1(\omega)+Z_2(\omega)-2/(i\omega C_c)|^2}, \tag{3.12}$$

where $Z_{1,2}(\omega) = (1/R_{1,2} - i\omega C_{1,2})^{-1}$ is the impedance of each RC contour. As for the layers, for simplicity we assume the two subsystems to be identical: $R_1 = R_2 = R$, $C_1 = C_2 = C$. Writing the transmission as

$$\mathcal{T}(\omega) = \frac{\omega^2(RC_c)^2}{2[1+\omega^2(RC)^2][1+\omega^2R^2(C+C_c)^2]}, \tag{3.13}$$

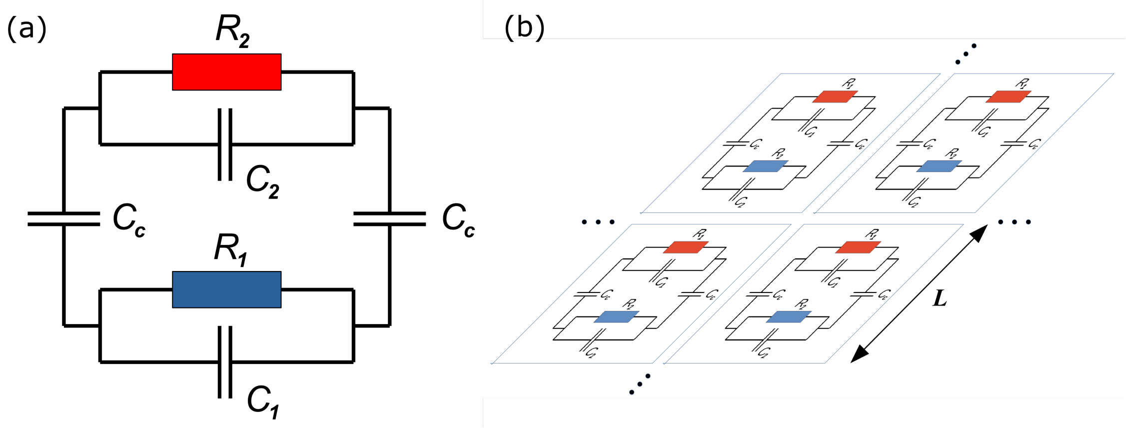

Figure 3.5: Circuit representation of two parallel metallic layers. (a) The elementary RC circuit whose heat transfer is governed by the transmission coefficient given in Eq. (3.12). (b) The infinite 2D system represented as a tiling of the elementary circuits, each one corresponding to a region of size L.

we obtain the following asymptotic expressions for the transferred power $P(T_1, T_2) = P(T_2) - P(T_1)$:

$$P(T) = \frac{\pi^3}{30}(RC_c)^2\frac{T^4}{\hbar^3}, \qquad T/\hbar \ll \frac{1}{R(C+C_c)}. \tag{3.14a}$$

$$P(T) = \frac{\pi}{12}\frac{T^2}{\hbar}, \qquad \frac{1}{R(C+C_c)} \ll T/\hbar \ll \frac{1}{RC}, \tag{3.14b}$$

$$P(T) = \frac{C_c^2}{4(C+C_c)(2C+C_c)}\frac{T}{RC}, \qquad T/\hbar \gg \frac{1}{RC}. \tag{3.14c}$$

Differentiating the expression (3.14b) we note the appearance of the thermal conductance quantum, $\partial P(T)/\partial T = \pi T/6\hbar \equiv G_Q$. This highlights the fact that the circuit model represents a system with only one heat transfer channel (namely the zero wavevector channel), which in this regime achieves the maximum thermal conductance [Pendry83]; in the high and low temperature regimes the thermal conductance is much smaller than G_Q because the transmission coefficient is small. This intermediate "universal" regime, where the power depends only on the temperature, but not on the circuit, is present only when $C \ll C_c$.

To relate results (3.14) to those of Sec. 3.1.3 for parallel layers, it is important to realise that while Eqs. (3.14) give the full transferred power, Eqs. (3.7) give the power *per unit area*. To make a meaningful comparison we must therefore invoke a length scale L, such that the infinite sample can be divided into squares of size L. Then Eqs. (3.14) describe the power transferred in each square, and the contributions of different squares can be added up independently, as schematically shown in Fig. 3.5 (b). Thus, the relevant length scale should be associated with the typical convergence scale of the k integral in Eq. (3.1).

In the diffusive regime, it is natural to associate the resistance R to the resistance per square $1/\sigma_{2D}$ of each metallic layer, $R \sim 1/\sigma_{2D} = 2\pi/(\kappa D)$. The coupling capacitance is associated to the geometric capacitance between the two layers, $C_c \sim L^2/d$, where the in-plane length scale $L \gtrsim d$ must be invoked because the capacitance is proportional to the area. The capacitance C should be associated to an intrinsic property of each layer, so $C \sim L$, the only intrinsic length scale of the layer. Recalling the convergence scales of the k integral in Sec. A.4.2, we associate $L \sim \sqrt{\hbar D\kappa d/T}$ and $L \sim d$ in the low- and high-temperature diffusive regimes, respectively. Then Eqs. (3.14a) and (3.14c) match Eqs. (3.7e) and (3.7f) at low and high temperatures, respectively. Expression (3.14b) does not correspond to any parametric region because at $T/\hbar \gg D\kappa/d$ the two capacitances become of the same order.

Thus, while the proposed effective RC circuit does capture the qualitative picture of the heat transfer in the diffusive regime, one cannot completely disregard the 2D geometry of the system. This geometry manifests itself in the appearance of the length scale L, which must supplement the circuit picture in order to reproduce the temperature dependence of the heat current. Moreover, this length scale is temperature-dependent, so one cannot represent a given system by a given array of elementary circuits in the whole temperature range. This strongly limits the usefulness of the circuit analogy for large 2D samples.

However, the situation is different for 2D samples whose lateral size is smaller than the length scale L deduced above. Indeed, consider a rectangular sample with side lengths W_x and W_y, such that $d \ll W_x, W_y \ll L$, which is only possible in the low-temperature diffusive regime. Then integration over the continuum of diffusion modes labelled by $\mathbf{k}$ in Eq. (3.1) should be replaced by a sum over discrete modes with $k_x = \pm n\pi/W_x$ and $k_y = \pm m\pi/W_y$, where n and m are integers. This sum is dominated by the first non-zero modes $k_x = \pm\pi/W_x$, $k_y = 0$ and $k_x = 0$, $k_y = \pm\pi/W_y$, leading to the expression for the total power

$$P_{\mathrm{ld}}(T) = \frac{1}{15\pi} \frac{W_x^4 + W_y^4}{(D\kappa d)^2} \frac{T^4}{\hbar^3}. \tag{3.15}$$

Once again associating the coupling capacitance to the the geometric capacitance between the layers, $C_c \sim W_x W_y/d$, we find that the expression (3.15) matches the appropriate low-temperature circuit expression (3.14a) if the resistance is given by

$$R = \frac{1}{\pi^3} \sqrt{\frac{1}{2}\left[\left(\frac{1}{\sigma_{\mathrm{2D}}} \frac{W_x}{W_y}\right)^2 + \left(\frac{1}{\sigma_{\mathrm{2D}}} \frac{W_y}{W_x}\right)^2\right]}, \tag{3.16}$$

where the square root may be identified as the root mean square of the two directional sample resistances. Contrary to the case of large samples, we therefore find that for small samples (side lengths smaller than $L \sim \sqrt{\hbar D\kappa d/T}$), the heat transfer may be correctly modelled by an effective circuit whose parameters are determined by the system size and geometry. Taking as an estimate $L \sim d$, we obtain the typical scale $L \sim \hbar D\kappa d/T = \mathcal{G}\lambda\!\!\!^{-}_T$; using the estimates for $\mathcal{G}$ in different structures given in Sec. 2.3 we find this distance to well exceed 1 mm at $T = 1\,\mathrm{K}$.

This points to a more general result regarding the validity of modelling the heat transfer in a physical system by heat transfer in an effective circuits. Essentially, if the size of the physical system is smaller than the length scale of photons responsible for the heat transfer (i.e. the scale that determines the integral in the microscopic theory) then a zero-dimensional effective circuit model is appropriate. However, the choice of circuit elements in such a circuit must come from a prior knowledge of the dominant physical mechanisms at play – for example, for weakly damped density excitations one would also require inductors. This prior knowledge would be difficult to access without first performing the microscopic calculation, somewhat limiting the circuit approach.

3.4 Summary and outlook

We have studied the problem of heat transfer between two thin parallel metallic layers, mediated by the Coulomb interaction. Using a simple model for a 2D electron gas subject to scattering on short-range impurities, we described the crossover between clean and diffusive limits and showed that strongly coupled surface plasmons dominate the heat transfer in a parametrically wide region at sufficiently high temperatures, but their contribution is suppressed in both the clean and diffusive limits. We also clarified the role of the spatial dispersion of the optical conductivity, which turns out to be important only in the clean limit. In all other regimes, the effect of disorder is correctly captured by the relaxation time in the local Drude conductivity.

We have shown that in the diffusive limit, the heat transfer is quantitatively similar to that in an effective *RC* circuit. However, for this analogy to be meaningful for large sheets, one must specify a length scale. This length scale should correspond to the size of regions where the transfer occurs independently. In other words, each region can be described by a separate circuit, and contributions from different regions add up. This length scale must be determined from the microscopic theory and turns out to be temperature-dependent. This greatly limits the usefulness of the circuit analogy for large sheets, especially when the two temperatures are strongly different. However, for sheets smaller than the length scale discussed above, we find that an effective circuit picture may be used to calculate the heat current, where the circuit parameters are determined by the system size and geometry. The circuit description is therefore more useful for systems with small spatial dimensions.

We have seen from the details of our calculation that the average heat current may be dominated by a surface plasmon channel. Although it is possible to test this in an experiment by comparing the dependence on separation and temperature to our asymptotic expressions, in reality this is a somewhat weak demonstration of the importance of plasmons since many of the expressions have similar dependences – crucially, the resonant behaviour responsible for the heat transfer is not reflected in the final expressions for the *average*. In the next chapter we study an observable where the resonant behaviour may be more explicitly manifested: the *fluctuations*. In the surface plasmon regime we calculate the fluctuation, or noise, spectrum of the heat current, in the hope of recovering resonant signatures linked to plasmons that could be measured experimentally.

Nous avons étudié le problème du transfert de chaleur entre deux fines couches métalliques parallèles, médié par l'interaction de Coulomb. En utilisant un modèle simple pour un gaz d'électrons 2D soumis à la diffusion sur des impuretés à courte portée, nous avons décrit le passage entre les limites propre et diffusive et montré que les plasmons de surface fortement couplés dominent le transfert de chaleur dans une région paramétriquement large à des températures suffisamment élevées, mais que leur contribution disparait dans les limites propre et diffusive. Nous avons également clarifié le rôle de la dispersion spatiale de la conductivité optique, qui s'avère être importante uniquement dans la limite propre. Dans tous les autres régimes, l'effet du désordre est correctement capturé par le temps de relaxation dans la conductivité de Drude locale.

Nous avons montré que dans la limite diffusive, le transfert de chaleur est quantitativement similaire à celui d'un circuit effectif *RC*. Cependant, pour que cette analogie soit significative pour des grands échantillons, il faut spécifier une échelle de longueur. Cette échelle de longueur doit correspondre à la taille des régions où le transfert se produit indépendamment. En d'autres termes, chaque région peut être décrite par un circuit séparé, et les contributions des différentes régions s'additionnent. Cette échelle de longueur doit être déterminée à partir de la théorie microscopique et s'avère dépendre de la température. Cela limite considérablement l'utilité de l'analogie du circuit pour les grands échantillons, surtout lorsque les deux températures sont fortement différentes. Cependant, pour des échantillons plus petits que l'échelle de longueur discutée ci-dessus, nous constatons qu'une image d'un circuit effectif peut être utilisée pour calculer le courant thermique, où les paramètres du circuit sont déterminés par la taille et la géométrie du système. La description du circuit est donc plus utile pour les systèmes de petites dimensions spatiales.

Nous avons vu dans les détails de notre calcul que le courant thermique moyen peut être dominé par un canal plasmonique. Bien qu'il soit possible de tester cela dans une expérience en comparant la dépendance de la séparation et de la température à nos expressions asymptotiques, il s'agit en réalité d'une démonstration un peu faible de l'importance des plasmons puisque de nombreuses expressions ont des dépendances similaires – de manière cruciale, le comportement résonant responsable du transfert de chaleur n'est pas reflété dans les expressions finales pour le *moyen*. Dans le chapitre suivant, nous étudions une observable où le comportement résonant peut se manifester plus explicitement : les *fluctuations*. Dans le régime des plasmons de surface, nous tentons de calculer le spectre de fluctuations, ou de bruit, du courant thermique, dans l'espoir de retrouver des résonances liées aux plasmons qui pourraient être mesurées expérimentalement.

4

Noise spectrum of the heat current

Contents

4.1 Why study the noise spectrum?

For a more complete understanding of the behaviour of a physical quantity pertaining to a system, one needs not only to study its average, but also its fluctuations, or noise. These fluctuations about the average occur due to correlations in time and perhaps space of the sources of the signal. It is well known that noise may contain additional physical information about a particular system as compared to the average. For example, by studying electric current noise, researchers have been able to probe the effects of interaction on electron dynamics [Landauer98]. However, studying noise is in general more complex than the average signal, and there are often many possible ways for the fluctuations to be characterised. We introduce here some of the measures associated with studying fluctuations and discuss what has been done so far on the topic of radiative heat current noise.

We found in chapters 2 and 3 that the average radiative heat current exhibits many different behaviours not predicted by Planckian theory. A few theoretical works have started to confirm that the same is true of the fluctuations. A recent work conducted in the framework of fluctuational electrodynamics studied the variance of the Poynting vector, S_z, between semi-infinite bodies, given by [Biehs18]

$$\sigma_S^2 = \langle S_z^2 \rangle - \langle S_z \rangle^2, \tag{4.1}$$

where the Poynting vector S_z is always taken at coinciding positions and times. The variance therefore gives a measure of the magnitude of the fluctuations happening over all frequency scales. They show that like the average heat current, the variance obtains a separation dependence in the near field due to evanescent wave coupling. In Ref. [Herz20] the authors also study the variance of the Poynting vector developing a general trace formula for bodies of arbitrary shape. They apply their theory to heat transfer between closely spaced dielectric nanoparticles where they are able to show analytically that the separation dependence of the standard deviation (square root of the variance) is the same as that of the average heat flux.

To go beyond the average and the variance of a quantity, one may study the low-frequency fluctuations via the full counting statistics (FCS). In FCS, one constructs a generating functional with a counting field, from which the moments of arbitrarily high order may be found via differentiation. The FCS of photonic heat current between resistors in a circuit model has been developed in Ref. [Golubev15], while in Ref. [Tang18] the authors study the FCS of near-field radiative heat transfer between metals in the Coulomb limit working in the framework of nonequilibrium Green's functions. From the FCS they are able to verify some important thermodynamic properties, e.g. that the probability of backwards heat flow from the cold body to the hot body is exponentially suppressed with respect to the forward heat flow [Tang18].

The variance and higher order moments discussed so far give information about magnitude of fluctuations but do not say over which frequency or time scale they occur. This scale determines whether the fluctuations are measurable for both technical and fundamental reasons. Technically, the measurement apparatus used in a heat current experiment has some finite time resolution – one can imagine a time series of measurements with some minimum spacing between each measurements. If the fluctuations happen over timescales shorter than the experimental resolution, the signal will appear smooth with the noise averaged out.

On a more fundamental level, the timescale of heat current fluctuations is important since it brings into question the physical definition of heat itself. Instead of measuring the heat current directly like one would for, say, electrical current, the heat absorbed by a body, dQ, is inferred from the measured change in its temperature, dT, via the relation $dQ = \mathcal{C}\,dT$, where $\mathcal{C}$ is the absorbing body's heat capacity. While this correspondence is clearly meaningful for the average heat, the situation is more subtle for the fluctuations. Whether or not the thermodynamic quantity temperature may actually fluctuate, and therefore be measured to give an accurate picture of heat current fluctuations, has been debated [Landau80, Kittel88, Day97]. Imagine a system that is receiving energy via a noisy incoming heat current. The system temperature is only well-defined on time scales that are larger than the system's local equilibration time, which is the time it takes for particles to collide sufficiently in order to establish the equilibrium distribution function, e.g. Fermi-Dirac for electrons in a small but macroscopic region of the sample. For time scales shorter than this time, the temperature is ill-defined and therefore finite frequency fluctuations in the Joule losses may only be meaningful for frequencies slower than the equilibration rate. Typically, this rate is slower than the thermal rate $\tau_T^{-1} = T/\hbar$, so experiments tend to be limited to observing only the zero or low-frequency fluctuations.

A recent experiment measured the time dependent temperature of electrons in the absorber (normal metal) of a nano-calirometer at low temperatures [Karimi20]. The electrons receive a fluctuating heat current via coupling to a phonon bath. With an experimental time resolution of $100\,\mu$s the authors show that under equilibrium conditions the low-frequency electron temperature fluctuations obey a fluctuation dissipation theorem. Regarding the electron equilibration time, the authors have a good separation of time scales ensuring that the measured temperature fluctuations illustrate the incoming fluctuating heat current.

Bearing in mind the importance of these timescales, equal time correlation functions such as the variance are clearly not enough to fully understand the fluctuations. In Ref. [Biehs18] the authors do evaluate numerically the time resolved correlation function $\langle S_z(t) S_z(t') \rangle$ indicating the timescale over which the fluctuations occur. For blackbody radiation, the typical timescale is given by the thermal time $\tau_T = \hbar/T$ which for room temperature is very short; $\tau_T \approx 25\,\text{fs}$ at $T = 300\,\text{K}$ so the fluctuations appear as structureless white noise on practical timescales. On the other hand, they find that for SiC bodies whose near-field heat exchange is dominated by surface phonon polaritons, the heat current is temporally correlated over a much longer time. However, this interesting fact which opens the possibility to observe a nontrivial structure of the noise was not analysed in detail in Ref. [Biehs18]. Here we want to perform such a study and focus on situations where the heat transfer is mediated by a narrow resonance in the transmission.

In our work, we study the fluctuation spectrum of the Joule losses, defined by the

Fourier transform

$$S(\mathbf{K},\Omega) = \int_{-\infty}^{\infty} d(t-t')e^{i\Omega(t-t')} \int d(\mathbf{r}-\mathbf{r}')e^{-i\mathbf{K}\cdot(\mathbf{r}-\mathbf{r}')} S(\mathbf{r}-\mathbf{r}',t-t'), \tag{4.2}$$

where the space- and time-resolved symmetrised heat current correlator is given by

$$S(\mathbf{r}-\mathbf{r}',t-t') = \frac{1}{2}\left\langle \left\{ J(\mathbf{r},t), J(\mathbf{r}',t') \right\} \right\rangle - \langle J(\mathbf{r},t)\rangle^2, \tag{4.3}$$

where $J(\mathbf{r},t)$ gives the heat current absorbed (per unit area) by a macroscopic receiving body that arrives at position $\mathbf{r}$ and time t – i.e. in general $J(\mathbf{r},t) = \mathbf{j}(\mathbf{r},t)\cdot\mathbf{E}(\mathbf{r},t)$. For three-dimensional semi-infinite bodies, $J(\mathbf{r},t)$ is given by the divergence of the total Poynting vector, while for two-dimensional layers it is equal to the jump in the normal component of the Poynting vector at the absorbing layer. Notice that the correlation function Eq. (4.3) depends only on coordinate and time differences since we assume a translationally invariant system in a steady state. The variation of the corresponding spectrum Eq. (4.2) in wavevector and frequency describes the relative significance of fluctuations on different length and time scales.

Based on the discussion above regarding the manifestation of heat current by temperature change, the spectrum Eq. (4.2) should be used only under certain conditions. For heat exchange between metals at temperatures T_1 and T_2 with $T_2 > T_1$, we should have $\Omega \ll 1/\tau_{\text{eq.}} \ll T_1/\hbar$ where $\tau_{\text{eq.}}$ is the local electron equilibration time. This inequality reflects the fact that heat current fluctuations are only detectable if they occur slowly enough such that the temperature of the body is always well-defined – i.e. the temperature 'reacts' to the noisy incoming heat current.

In a realistic experiment, the electrons and phonons in the metal may interact not only with each other but also with the substrate or leads. In the following we assume that the phonons in the metal are in thermal equilibrium with the substrate, which itself is in thermal equilibrium with the cryostat. The electrons on the other hand are perturbed by the incoming radiation so they are not in thermal equilibrium with the phonons nor the cryostat. We shall choose to focus on the case $T_2 \gg T_1$, where the dominant contribution to the fluctuations comes from the correlations of fluctuating sources in body 2, rather than those in body 1. Then, the fluctuations of the incoming heat are strong enough not to be drowned out by the internal energy fluctuations present in the receiving body.

We are particularly interested in studying noise where resonant modes are expected to be important, since the resonant behaviour will likely leave a signature on the noise spectrum. Revealing these signatures in observable quantities should provide a route to experimental demonstrations of the resonant modes themselves. We remind the reader that our study in Ch. 3 showed that the average radiative heat current between two-dimensional metallic layers in the Coulomb limit may be dominated by a surface plasmon channel over a parametrically wide region. However, as mentioned in Sec. 3.4, the resonant behaviour responsible is not easily identified empirically in the results for the average current – the temperature and separation dependence of the final expression is not necessarily different than for regimes dominated by continuum excitations – see expressions J_{ld} and J_{lp} in Eq. (3.7). We therefore study in Sec. 4.3 the noise spectrum of the type of (4.2) of the heat current in this physical system focusing on the low-temperature plasmon regime, in the hope of revealing more explicit signatures of the resonant collective behaviour that would be potentially measurable. We start, however, in Sec. 4.2 with a simpler example of a zero-dimensional system represented by an effective circuit. As we will see, the general structure of the expressions is quite analogous in the two cases, but the absence of spatial variables makes the calculations simpler in the circuit model.

4.2 Heat current noise spectrum in a superconducting resonator

A recent experiment measured the heat exchange between two small pieces of normal metal held at different temperatures connected by superconducting leads interrupted by SQUIDs (superconducting quantum interference device) [Meschke06]. The superconducting leads are ideal insulators against conventional electronic thermal conduction, and the experiment was conducted at sub-Kelvin temperatures such that heat transport via phonons is frozen out. The dominant channel for heat exchange between the metals is therefore radiation via photons in the superconducting resonator. We stress that the photons here pass through the superconducting material, not vacuum, and therefore have some material-dependent velocity. For the linear response of heat transfer to a temperature gradient the authors of Ref. [Meschke06] confirm the apparition of the universal thermal conductance quantum [Pendry83] for photonic heat transfer.

In the experiment described above, the metals are much smaller than the thermal wavelength of photons in the resonator at the low temperatures used for the investigation. Moreover, the physics of the system in Ref. [Meschke06] may be expected to be dominated by the near field; indeed taking the overall system size $L \sim 50\,\mu\mathrm{m}$ and the thermal wavelength of photons $\lambdabar_T = 2.3\,\mathrm{cm}$ at $T = 100\,\mathrm{mK}$ we have the ratio $L/\lambdabar_T = 2\times 10^{-3} \ll 1$. As discussed in Sec. 3.3, the experiment in Ref. [Meschke06] may therefore be represented by an effective zero-dimensional electrical circuit comprised of lumped elements [Pascal11]. For our calculation we choose the circuit in Fig. 4.1 (a). The normal metals are represented by resistors held at different temperatures, and the superconducting resonator by an LC contour coupled to each resistor via mutual inductances. The magnitudes of the mutual inductances play the role of the coupling constant.

The average radiative heat current in such circuits is fairly well understood (see, for example Ref. [Pascal11]) and heat current fluctuations have begun to be addressed (for a review see Ref. [Pekola21]) – the finite frequency heat current noise spectrum has even been analysed in some circuits in thermal equilibrium [Karimi21]. However, the case of an out-of-equilibrium circuit whose transmission has a resonance has not yet been studied. A student performing a Masters internship under the co-supervision of D. M. Basko and myself has recently solved this problem. In their internship report Ref. [Roubinowitz21] the author has provided a quantum description of this circuit and has calculated the spectrum of heat current fluctuations. We present (without derivation) some of the results here, focusing on the exposition of a resonant feature in the heat current noise, which is due to the nature of the coupling being that of a harmonic oscillator. These results will help us understand the more complex two-dimensional structure studied in Sec. 4.3.

4.2.1 Heat current noise correlator

The circuit of Fig. 4.1 (a) is described as a collection of quantum harmonic oscillators. The LC loop constitutes a single harmonic oscillator whose conjugate variables are the charge stored by the capacitor and the magnetic flux threading the loop. The fundamental frequency of the oscillator is given by $\omega_0 = 1/\sqrt{LC}$. Each resistor acts as a thermal bath which may be described by a large ensemble of independent harmonic oscillators whose eigenfrequencies form a continuous spectrum. The quantum mechanical circuit representation of a resistor is therefore a parallel chain of LC series, as shown in Fig. 4.1 (b) where the current through the resistor $a = 1,2$ is denoted I_a and the continuum limit $N \to \infty$ must be taken. Defining properly the operator $\hat{I}_a$, we may verify that in the continuum limit it indeed fluctuates according to the fluctuation dissipation theorem, yielding the so-called Johnson-Nyquist noise. As discussed in Sec. 1.3.1, the Johnson-Nyquist noise is the circuit analogue of the charge density fluctuations that drive radiative heat transfer in macroscopic bodies.

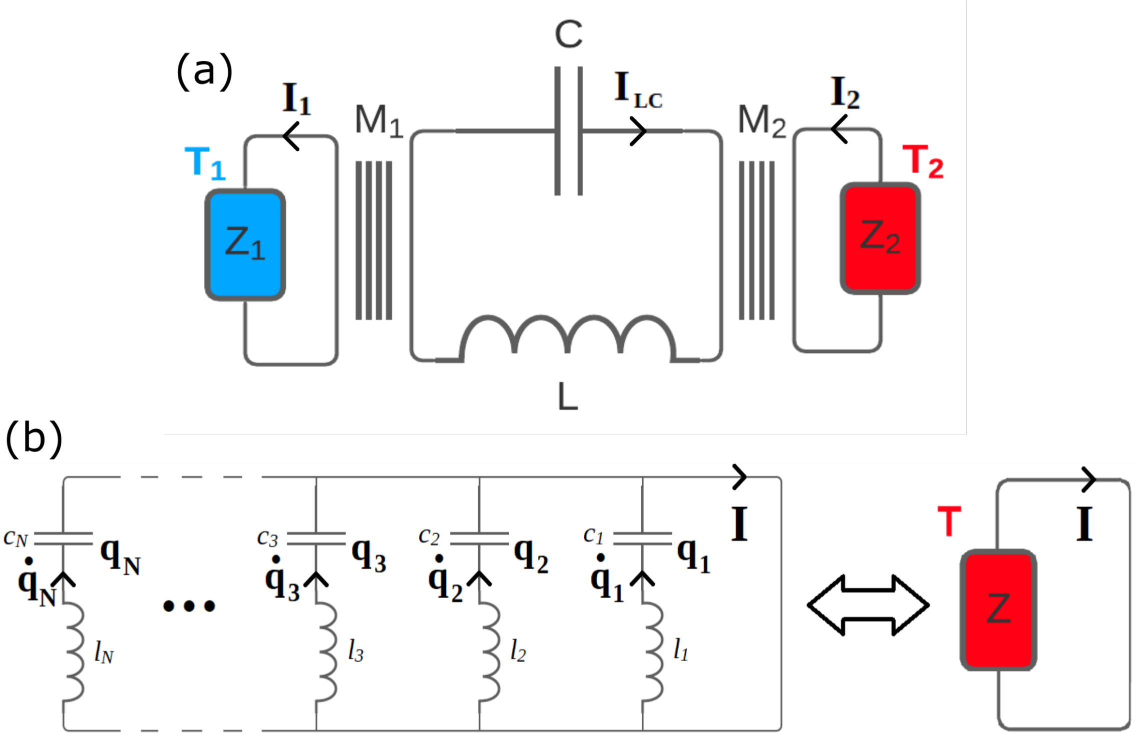

Figure 4.1: (a) Effective circuit used to model two small pieces of metal exchanging heat by radiation via a superconducting resonator. The pieces of metal may be represented simply by resistors, however here we denote them as general frequency dependent impedances $Z_{1,2}(\omega)$. (b) Circuit representation of an impedance as an ensemble of N LC loops that allows a quantum mechanical description in terms of charge q_k and current $\dot{q}_k$ in each loop characterised by capacitance c_k and inductance l_k.

We formalise what was written above, by writing the Langrangian for the full circuit of Fig. 4.1 (a):

$$\begin{aligned}\mathcal{L} = &\frac{L}{2}\dot{Q}^2 - \frac{Q^2}{2C} + \\ &+ \sum_{a=1,2}\sum_{k=1}^{N}\left(\frac{l_{a,k}}{2}\dot{q}_{a,k}^2 - \frac{q_{a,k}^2}{2c_{a,k}}\right) \\ &+ M_2\dot{Q}\sum_{k=1}^{N}\dot{q}_{2,k} - M_1\dot{Q}\sum_{k=1}^{N}\dot{q}_{1,k},\end{aligned} \tag{4.4}$$

The first line corresponds to the LC loop, whose Lagrangian is that of a harmonic oscillator where Q is the charge stored by the capacitor. The second line denotes the loops containing the impedances $Z_{1,2}(\omega)$, each of which may be thought of as a long chain of LC loops connected in parallel, where in the Lagrangian $l_{a,k}$ and $c_{a,k}$ are the inductance and capacitance in the k-th loop of impedance Z_a, and $q_{a,k}$ is the charge stored at the corresponding capacitor [see Fig. 4.1 (b)]. By computing the auto-correlation function of the current through the impedances when decoupled from the rest of the circuit, it is possible to show that the macroscopic impedance is related to the constituent inductances and capacitances via

$$\frac{1}{Z_a(\omega)} = \sum_{k=1}^{N}\left(-i\omega l_{a,k} - \frac{1}{i\omega c_{a,k}}\right)^{-1}. \tag{4.5}$$

In the continuum limit ($N \to \infty$), $Z_a(\omega)$ becomes a smooth function of ω. Finally, the third line in Eq. (4.4) represents the coupling of the loops containing the impedances $Z_{1,2}(\omega)$ with the central LC loop via mutual inductances. The inductive coupling is given simply by the product of the currents in the coupled loops, where the sign of the coupling constant M_a depends on the choice of convention for the directions of the different currents in the circuit (the observable quantity will not depend on this arbitrary choice). From the classical Lagrangian (4.4) we may write the expression for the heat dissipated in impedance 1

$$\begin{aligned}P_{2\to 1} &= \frac{d}{dt}\sum_{n=1}^{N}\left[\frac{l_{1,k}}{2}\dot{q}_{1,k}^2 + \frac{q_{1,k}^2}{2c_{1,k}}\right], && (4.6)\\ &= I_1 M_1\frac{dI_{LC}}{dt}, && (4.7)\end{aligned}$$

where we identify that the power dissipated in Z_1 is given by the product of the current through it, I_1, and the electromotive force exerted on the loop, $M_1\, dI_{LC}/dt$ [see Fig. 4.1 (a)]. This expression for the dissipation in the impedance is analogous to $J = \mathbf{j}\cdot\mathbf{E}$ in a continuous medium. The Langrangian (4.4) is quadratic, i.e. we may write

$$\mathcal{L} = \frac{1}{2}\left[\dot{\mathbf{q}}^T\mathbf{L}\dot{\mathbf{q}} - \mathbf{q}^T\mathbf{C}^{-1}\mathbf{q}\right], \tag{4.8}$$

where $\mathbf{q}$ and $\dot{\mathbf{q}}$ are column vectors of length $2N+1$ and $\mathbf{L}$ and $\mathbf{C}$ are the corresponding inductance and conductance matrices. Passing from the Lagrangian to the Hamiltonian and performing the canonical quantisation leads to the desired representation of the circuit as a system of coupled quantum harmonic oscillators. The quantum mechanical operator for the heat current in impedance Z_1 is:

$$\hat{P}_{2\to 1}(t) = \frac{1}{2}\left\{\hat{I}_1(t), M_1 \frac{d\hat{I}_{LC}(t)}{dt}\right\}, \tag{4.9}$$

where $\{.\}$ is the anticommutator and the current operators are in the Heisenberg representation. They may be found by solving the appropriate Heisenberg equations of motion, which take the form of quantum Langevin equations whose random forces are nothing but the Johnson-Nyquist current noise associated with each resistor.

The moments of the power transferred may then be calculated by taking the average of operators in the Heisenberg representation over the noninteracting density matrix, which just takes the form of a tensor product of the uncoupled loops: $\hat{\rho} = \hat{\rho}_1 \otimes \hat{\rho}_{LC} \otimes \hat{\rho}_2$, assuming that the couplings $M_{1,2}$ were turned on adiabatically in the remote past. The average power transferred is found to be given by

$$\langle \hat{P}_{2\to 1}(t)\rangle = \int_{-\infty}^{\infty} \frac{d\omega}{2\pi} \hbar\omega \left|\tilde{U}^R_{12}(\omega)\right|^2 \mathrm{Re}\,\frac{1}{Z_1(\omega)}\,\mathrm{Re}\,\frac{1}{Z_2(\omega)} \left[\coth\frac{\hbar\omega}{2T_2} - \coth\frac{\hbar\omega}{2T_1}\right], \tag{4.10}$$

where the result does not depend on time, as expected for the average in a steady state. Here, we have introduced the notation

$$\tilde{U}^R_{ab}(\omega) = \frac{i\omega^3 C M_a M_b}{1 - \omega^2 LC - i\omega^3 C\left[M_1^2/Z_1(\omega) + M_2^2/Z_2(\omega)\right]}, \tag{4.11}$$

in order to make connections to expressions in Sec. 4.3. Notice the similarity to the Caroli formula for the average heat current between parallel layers, Eq. (3.1), where the only difference is the additional integration over wavevector brought about by the spatial dimension. The term here $\tilde{U}^R_{12}$ describes the coupling between the two impedances via the circuit, and is directly analogous to the RPA screened interaction term, Eq. (3.3), that describes the coupling of the electrons in the metallic layers. As with the Caroli formula, the heat transfer splits into two terms: $P(T_1,T_2) = P(T_2) - P(T_1)$, where the resulting form of $P(T)$ depends on the circuit parameters and the temperature.

The fluctuations in time of the power transferred to impedance 1 may be characterised by the symmetrised correlator

$$S(t-t') = \frac{1}{2}\left\langle\left\{\hat{P}_{2\to 1}(t), \hat{P}_{2\to 1}(t')\right\}\right\rangle - \left\langle\hat{P}_{2\to 1}(t)\right\rangle^2, \tag{4.12}$$

where the correlator depends only on the time difference since we assume to be in a steady state. Plugging in the operators and performing the average leads to the following general expression

$$\begin{aligned}S(t-t') = -\frac{\hbar^2}{4}\int_{-\infty}^{\infty}\frac{d\omega}{2\pi}\int_{-\infty}^{\infty}\frac{d\omega'}{2\pi}e^{-i(\omega+\omega')(t-t')}&\\ \times\sum_{a,b}\Bigg[\underbrace{\left(\delta_{1a}+\frac{1}{Z_1}\tilde{U}^R_{1a}\right)D^K_{I_aI_b}\left(\delta_{b1}+\tilde{U}^A_{b1}\frac{1}{Z_1^*}\right)}_{\omega}\underbrace{\tilde{U}^R_{1a}D^K_{I_aI_b}\tilde{U}^A_{b1}}_{\omega'}&\\ +\underbrace{\tilde{U}^R_{1a}D^K_{I_aI_b}\left(\delta_{b1}+\tilde{U}^A_{b1}\frac{1}{Z_1^*}\right)}_{\omega}\underbrace{\left(\delta_{1a}+\frac{1}{Z_1}\tilde{U}^R_{1a}\right)D^K_{I_aI_b}\tilde{U}^A_{b1}}_{\omega'}\Bigg]&+\left[D^K_{I_aI_b}\to D^{R-A}_{I_aI_b}\right],\end{aligned} \tag{4.13}$$

where $\tilde{U}^A_{ab} = [\tilde{U}^R_{ba}]^*$ and we have introduced the notations

$$D^K_{I_aI_b}(\omega) = -i\delta_{ab}\,\mathrm{Re}\,\frac{2\omega}{Z_a(\omega)}\coth\frac{\hbar\omega}{2T_\alpha}, \tag{4.14a}$$

$$D^{R-A}_{I_aI_b}(\omega) = -i\delta_{ab}\,\mathrm{Re}\,\frac{2\omega}{Z_a(\omega)}, \tag{4.14b}$$

which is once again for comparison with results in Sec. 4.3. For the spectrum of the fluctuations, we seek the Fourier transform

$$S(\Omega) = \int_{-\infty}^{\infty} d(t-t')\,e^{i\Omega(t-t')}S(t-t'). \tag{4.15}$$

We focus on the case where $T_2 \gg T_1$, such that the dominant terms in the spectrum (4.13) are those which contain the product of two hyperbolic cotangents both with arguments involving T_2. i.e. $D^K_{I_2I_2}D^K_{I_2I_2}$. Taking only these terms leads to a divergence that is saved by taking also the corresponding term in $D^{R-A}_{I_2I_2}D^{R-A}_{I_2I_2}$, which according to Eqs. (4.14) contributes the same but with 1 in place of the product of hyperbolic cotangents. As we shall see in Sec. 4.3, D^{R-A} represents a commutator, and therefore it is only non-zero in a quantum mechanical calculation. We see then that in a classical electrodynamics calculation we would arrive at this unphysical divergence, and in order to correctly calculate the heat current noise a quantum mechanical treatment is required. In this case of $T_2 \gg T_1$ where we take $a = b = 2$ we notice that the Kronecker delta functions in Eq. (4.13) do not contribute, resulting in the expression

$$\begin{aligned}S(\Omega) = \hbar^2\int_{-\infty}^{\infty}\frac{d\omega}{2\pi}\left[1+\coth\frac{\hbar\omega}{2T_2}\coth\frac{\hbar(\Omega-\omega)}{2T_2}\right]\omega\,(\Omega-\omega)&\\ \times\mathrm{Re}\,\frac{1}{Z_2(\omega)}\,\mathrm{Re}\,\frac{1}{Z_2(\Omega-\omega)}\left|\tilde{U}^R_{12}(\omega)\tilde{U}^R_{12}(\Omega-\omega)\right|^2&\\ \times\left[\frac{1}{|Z_1(\omega)|^2}+\frac{1}{Z_1(\omega)^*}\frac{1}{Z_1(\Omega-\omega)}\right].&\end{aligned} \tag{4.16}$$

From these general results Eqs. (4.10) and (4.16), it is possible to evaluate the integrals revealing different regimes of behaviour for the average heat current and its fluctuations according to the circuit parameters and the temperatures. In the following section we focus on the case where the heat current is dominated by a resonance associated with the LC loop fundamental frequency.

4.2.2 Resonant feature in the noise spectrum

We specify to the case where the impedances are replaced by simple resistors, i.e. $Z_{1,2}(\omega) = R_{1,2}$. In the expression for the average heat current (4.10), we notice the appearance of the complicated factor $|\tilde{U}^R_{12}(\omega)|^2$. We note that for sufficiently small $M_{1,2}$, the function $|\tilde{U}_{12}(\omega)|^2$ is highly peaked in the vicinity of $\omega = \omega_0 \equiv LC$, corresponding to resonant heat transfer via photons whose frequency matches the fundamental frequency of the LC resonator, ω_0. This resonant behaviour may be captured by approximating $\left|\tilde{U}_{12}(\omega)\right|^2$ as a Lorentzian, and setting $\omega \to \omega_0$ in all non-resonant factors. This leads to the contribution

$$
\begin{aligned}
P_{\text{res.}}(T) &= \frac{\hbar\omega_0}{2\pi}\frac{\gamma_1\gamma_2}{e^{\hbar\omega_0/T}-1}\int_0^\infty \frac{d\omega}{(\omega-\omega_0)^2+\left(\frac{\gamma_1+\gamma_2}{2}\right)^2} \\
&= \frac{\gamma_1\gamma_2}{\gamma_1+\gamma_2}T, \qquad (4.17)
\end{aligned}
$$

where $\gamma_a = \omega_0^2 M_a^2/R_a L$ is the damping rate associated with each resistance loop, and we assume weak damping such that $\gamma_{1,2} \ll \omega_0$ which translates into the condition on the mutual inductances $M_{1,2} \ll \sqrt{R_{1,2}L/\omega_0}$. In the final expression we have expanded the hyperbolic cotangent in Eq. (4.10) for $T \gg \hbar\omega_0$, while for lower temperatures the contribution is exponentially suppressed. It is found that the contribution (4.17) dominates over other non-resonant contributions to the average heat current in the temperature window: $\hbar\omega_0 \ll T \ll \hbar\omega_0(\omega_0/\gamma)^{1/3}$, where $\gamma = \gamma_1+\gamma_2$.

For $T_2 \gg T_1$ we regard the heat current spectrum in the regime described above where resonant transfer dominates, i.e. $\hbar\omega_0 \ll T_2 \ll \hbar\omega_0(\omega_0/\gamma)^{1/3}$. In the expression (4.16) we have once again the appearance of the resonant coupling terms. In particular, $|\tilde{U}^R_{12}(\omega)|^2$ is highly peaked at $\omega = \pm\omega_0$ and $|\tilde{U}^R_{12}(\Omega-\omega)|^2$ is peaked at $\omega = \Omega \pm \omega_0$. The overlap of these peaks results in resonant contributions to the heat current spectrum. Focusing on the case where we have $\Omega \ll \omega_0 \ll T_2/\hbar$, these contributions may be evaluated by approximating the coupling terms as Lorentzians (just as for the average heat current) and setting non-resonant terms to the centres of the Lorentzians. The resulting products of Lorentzians may be integrated leading to the following contribution to the noise spectrum

$$
S_{\text{res.}}(\Omega) = 2\frac{\gamma^2}{\Omega^2+\gamma^2}\frac{\gamma_1^2\gamma_2^2}{\gamma^3}T_2^2, \qquad (4.18)
$$

where we see a Lorentzian resonant feature at $\Omega = 0$ with width γ. There is also a frequency-independent (structureless) background contribution to the heat current noise spectrum, to which the resonant contribution (4.18) should be added. We notice that the resonant contribution (4.18) may be written in terms of the average resonant heat current expression (4.17) as

$$S_{\text{res.}}(\Omega) = 2\hbar\omega_0 P_{\text{res.}}(T_2)\,\mathcal{F}\,s(\Omega), \tag{4.19}$$

where we have defined the Fano factor

$$\mathcal{F} = \frac{T_2}{\hbar\omega_0}\frac{\gamma_1\gamma_2}{\gamma^2} \gg 1, \tag{4.20}$$

and the dimensionless function encoding the structure of the noise

$$s(\Omega) = \frac{\gamma^2}{\Omega^2+\gamma^2}. \tag{4.21}$$

We notice that for $\gamma_1 = \gamma_2$ we have $s(\Omega = 0) = 1$ and Eq. (4.19) has the form of an energy current shot noise. Shot noise is a well-known regime of behaviour for charge current through a potential barrier, where for low frequency the noise is frequency independent and given simply by twice the product of the average charge current and the magnitude of the charge carriers, $2e\langle I\rangle$ [Blanter00]. Here in Eq. (4.19) we see the situation is analogous since we have the product of the average energy current and the energy of photons, $\hbar\omega_0$. The additional large Fano factor enhances the noise with respect to shot noise, reflecting bunching of the photons in the superconductor (as is typical for bosons). The physical meaning of the final term in Eq. (4.21) is that the fluctuations of the heat current around its average value – in other words, momentary overheating or overcooling events – dissolve on a timescale $1/\gamma$.

In an experimental setup like that of Ref. [Meschke06], revealing these signatures in heat current noise behaviour may provide a way to confirm the significance of a resonant photonic heat transfer channel. However, as we discussed previously the measurability depends on many factors, most notably the time resolution of the experiment which should be small compared to the width of the resonant feature. We shall see in the next section that the situation for radiative heat current between two-dimensional metallic layers is quite analogous, where the resonant behaviour is due to the emission and absorption of surface plasmons.

4.3 Heat current noise spectrum for two-dimensional metals

In this section we study the heat current noise spectrum between two-dimensional metallic layers in the Coulomb limit. As found in Ch. 3, in a particular parametric region the main contribution to the radiative heat current comes from the emission and absorption of antisymmetric surface plasmons – see J_{lp} in Fig. 3.2. We give a microscopic derivation of the radiative heat current fluctuations in the framework of nonequilibrium Green's functions. We include in the following Sec. 4.3.1 some details of the derivation before discussion in Sec. 4.3.2 of the main result concerning a resonant feature in the spectrum due to dominant surface plasmons.

4.3.1 Heat current noise correlator

For the physical system of two galvanically isolated bodies held at different temperatures T_1 and T_2, the Joule losses in body 1 given in electrodynamics by $\mathbf{j}\cdot\mathbf{E}$, where $\mathbf{j}$ is the electric current and $\mathbf{E}$ is the electric field. We write it here in the Coulomb limit as the operator (see App. C.1 for details)

$$\hat{J}(\mathbf{r},t) = -\int d\mathbf{r}'\, \hat{j}_i(\mathbf{r},t)\nabla^i_{\mathbf{r}} V_0(\mathbf{r}-\mathbf{r}')\hat{\rho}(\mathbf{r}',t), \tag{4.22}$$

where the operators $\hat{j}_i$ and $\hat{\rho}$ are the particle current and particle density, respectively, and $V_0(\mathbf{r}-\mathbf{r}')$ is the bare Coulomb interaction with the electrical charge, e^2, absorbed. The position $\mathbf{r}$ resides in layer 1, while the integration variable $\mathbf{r}'$ extends over the whole volume including both layers. The domain of integration represents the fact that dissipation is caused in layer 1 due to fields produced by density fluctuations either in layer 2, or elsewhere in layer 1 – the latter gives no contribution to the average heat current since each subsystem is assumed to have a homogenous temperature (when averaged over time).

For the fluctuations, we are interested in the symmetrised heat current correlator

$$S(\mathbf{r},\mathbf{r}',t-t') = \frac{1}{2}\left\langle \left\{ \hat{J}(\mathbf{r},t), \hat{J}(\mathbf{r}',t') \right\} \right\rangle - \langle \hat{J}(\mathbf{r},t)\rangle^2, \tag{4.23}$$

where $\{.\}$ is the anticommutator and we have assumed a steady state so the correlator depends only on the time difference. In the Keldysh formalism, the operators appearing in Eq. (4.23) $\hat{J}(\mathbf{r},t)$ are in the Heisenberg picture including both intra- and inter-layer Coulomb interactions, and the ensemble average $\langle . \rangle$ should be taken over the noninteracting density matrix, which is built of a tensor product of the noninteracting hamiltonians, $\hat{\rho} = e^{-\hat{H}_1/T_1} \otimes e^{-\hat{H}_2/T_2}$, since the interactions are assumed to be adiabatically switched on in the remote past. To evaluate the correlator, we employ a generating functional approach in the framework of nonequilibrium Green's functions, where the resulting averages contained in Eq. (4.23) may be found by functional differentiation. The procedure may be found in App. C.4, which results in the following general expression for the fluctuations:

$$\begin{aligned} S(\mathbf{r},\mathbf{r}',t-t') = -\frac{\hbar^2}{4}\int\limits_{-\infty}^{\infty}\frac{d\omega}{2\pi}\int\limits_{-\infty}^{\infty}\frac{d\omega'}{2\pi} e^{-i(\omega+\omega')(t-t')}\int d\mathbf{r_1}\int d\mathbf{r_2}\nabla^i_{\mathbf{r}}V_0(\mathbf{r}-\mathbf{r}_1)\nabla^k_{\mathbf{r}'}V_0(\mathbf{r}'-\mathbf{r}_2) \\ \times\Big[\tilde{D}^K_{j_ij_k}(\mathbf{r},\mathbf{r}',\omega)\tilde{D}^K_{\rho\rho}(\mathbf{r}_1,\mathbf{r}_2,\omega') + \tilde{D}^{R-A}_{j_ij_k}(\mathbf{r},\mathbf{r}',\omega)\tilde{D}^{R-A}_{\rho\rho}(\mathbf{r}_1,\mathbf{r}_2,\omega') \\ + \tilde{D}^K_{\rho j_k}(\mathbf{r}_1,\mathbf{r}',\omega)\tilde{D}^K_{j_i\rho}(\mathbf{r},\mathbf{r}_2,\omega') + \tilde{D}^{R-A}_{\rho j_k}(\mathbf{r}_1,\mathbf{r}',\omega)\tilde{D}^{R-A}_{j_i\rho}(\mathbf{r},\mathbf{r}_2,\omega')\Big], \end{aligned} \tag{4.24}$$

where the spatial integrations are over the volumes of both layers and we have introduced the retarded (R), advanced (A) and Keldysh (K) components of the contour ordered Green's functions (GFs). For two arbitrary operators $A(\mathbf{r},t)$ and $B(\mathbf{r},t)$ the GFs are constructed in the time domain according to

$$D^R_{AB}(\mathbf{r},\mathbf{r}';t,t') = -\frac{i}{\hbar}\theta(t-t')\left[\langle A(\mathbf{r},t)B(\mathbf{r}',t')\rangle - \langle B(\mathbf{r}',t')A(\mathbf{r},t)\rangle\right], \tag{4.25a}$$

$$D^A_{AB}(\mathbf{r},\mathbf{r}';t,t') = -\frac{i}{\hbar}\theta(t'-t)\left[\langle B(\mathbf{r}',t')A(\mathbf{r},t)\rangle - \langle A(\mathbf{r},t)B(\mathbf{r}',t')\rangle\right], \tag{4.25b}$$

$$D^K_{AB}(\mathbf{r},\mathbf{r}';t,t') = -\frac{i}{\hbar}\left[\langle A(\mathbf{r},t)B(\mathbf{r}',t')\rangle + \langle B(\mathbf{r}',t')A(\mathbf{r},t)\rangle\right], \tag{4.25c}$$

and in Eq. (4.24) we have defined $D^{R-A} = D^R - D^A$. From the above definitions we see explicitly that D^{R-A} is a commutator, and is therefore a strictly quantum object as mentioned in the previous section. These components (4.25) may be collected into a triangular matrix form

$$D = \begin{pmatrix} 0 & D^A \\ D^R & D^K \end{pmatrix}, \tag{4.26}$$

where in what follows the lack of a superscript implies a matrix. In a steady state the GFs depend only on time difference, leading to the Fourier transform:

$$D_{AB}(\mathbf{r},\mathbf{r}',\omega) = \int_{-\infty}^{\infty} d(t-t')\, e^{i\omega(t-t')} D_{AB}(\mathbf{r},\mathbf{r}',t-t'). \tag{4.27}$$

On a final point of notation, we may have GFs with tilde like those appearing in Eq. (4.24), and those without. $\tilde{D}$ are GFs dressed by Coulomb interactions, i.e. the Heisenberg evolution of the operators is taken with the full interacting Hamiltonian. D are noninteracting GFs, where the Heisenberg evolution is taken without any electron-electron interactions. In the random phase approximation, the dressed density-density GF is given by the infinite series

$$\tilde{D}_{\rho\rho} = D_{\rho\rho} + D_{\rho\rho}\begin{pmatrix} 0 & V_0 \\ V_0 & 0 \end{pmatrix} D_{\rho\rho} + D_{\rho\rho}\begin{pmatrix} 0 & V_0 \\ V_0 & 0 \end{pmatrix} D_{\rho\rho}\begin{pmatrix} 0 & V_0 \\ V_0 & 0 \end{pmatrix} D_{\rho\rho} + \ldots \tag{4.28}$$

where integration over intermediate spatial variables is implied and $D^R_{\rho\rho} \equiv \Pi$ is the density response function already met in Sec. 3.1.2. Summation of the geometric series in Eq. (4.28) is equivalent to Dyson's equation for the dressed GF

$$\tilde{D}_{\rho\rho} = D_{\rho\rho} + D_{\rho\rho}\sigma_1 V_0 \tilde{D}_{\rho\rho}, \tag{4.29}$$

where σ_1 is the first Pauli matrix that gives the correct matrix structure in this basis. Similarly to Eq. (4.29), we may write an iterative equation for the screened Coulomb interaction

$$V_{RPA} = V_0\sigma_1 + V_0\sigma_1 D_{\rho\rho} V_{RPA}, \tag{4.30}$$

The retarded component of the above is what appeared in the Caroli formula for the average heat current in Eq. (3.3). Inverting both equations (4.29) and (4.30) leads to expressions for the components of the dressed GF $\tilde{D}_{\rho\rho}$ and screened interaction V_{RPA} in terms of components of the noninteracting GF $D_{\rho\rho}$ and the bare interaction V_0:

$$\begin{pmatrix} 0 & \tilde{D}^A \\ \tilde{D}^R & \tilde{D}^K \end{pmatrix} = \begin{pmatrix} 0 & D^A(\mathbb{1}-V_0D^A)^{-1} \\ D^R(\mathbb{1}-V_0D^R)^{-1} & (\mathbb{1}-D^RV_0)^{-1}D^K(\mathbb{1}-V_0D^A)^{-1} \end{pmatrix}, \tag{4.31}$$

$$\begin{pmatrix} V^K_{RPA} & V^R_{RPA} \\ V^A_{RPA} & 0 \end{pmatrix} = \begin{pmatrix} (\mathbb{1}-V_0D^R)^{-1}V_0D^K(\mathbb{1}-V_0D^A)^{-1} & (\mathbb{1}-V_0D^R)^{-1}V_0 \\ (\mathbb{1}-V_0D^A)^{-1}V_0 & 0 \end{pmatrix}, \tag{4.32}$$

where integrations over intermediate spatial variables is always implied and $\mathbb{1} = \delta(\mathbf{r}-\mathbf{r}')$ is the Dirac delta function playing the role of the unit operator in the coordinate space. We seek an expression analogous to the Caroli formula for the average heat current, Eq. (3.1), that gives the fluctuations in terms of the known objects. So it is useful to write the dressed GF in terms of the screened interaction, i.e. combining Eqs. (4.29) and (4.30):

$$\tilde{D}_{\rho\rho} = D_{\rho\rho} + D_{\rho\rho}V_{RPA}D_{\rho\rho}. \tag{4.33}$$

The above equations (4.29)–(4.33) refer to the density-density GF, $D_{\rho\rho}$, while the other current-density, density-current and current-current GFs appearing in Eq. (4.24) are related via the continuity equation,

$$\overrightarrow{\nabla}^i_{\mathbf{r}} j_i(\mathbf{r},t) + \frac{\partial\rho(\mathbf{r},t)}{\partial t} = 0, \tag{4.34}$$

which leads to the relations:

$$D_{\rho\rho}(\mathbf{r},\mathbf{r}',\omega) = \frac{1}{\omega^2}\overrightarrow{\nabla}^i_{\mathbf{r}} D_{j_ij_k}(\mathbf{r},\mathbf{r}',\omega)\overleftarrow{\nabla}^k_{\mathbf{r}'}, \tag{4.35a}$$

$$D_{j_i\rho}(\mathbf{r},\mathbf{r}',\omega) = -\frac{1}{i\omega} D_{j_ij_k}(\mathbf{r},\mathbf{r}',\omega)\overleftarrow{\nabla}^k_{\mathbf{r}'}, \tag{4.35b}$$

$$D_{\rho j_k}(\mathbf{r},\mathbf{r}',\omega) = \frac{1}{i\omega}\overrightarrow{\nabla}^i_{\mathbf{r}} D_{j_ij_k}(\mathbf{r},\mathbf{r}',\omega), \tag{4.35c}$$

where the gradient operators $\overrightarrow{\nabla}$ and $\overleftarrow{\nabla}$ act in the direction of the arrow.

It is convenient to express the final expression Eq. (4.24) in terms of bare current-current GFs and retarded and advanced components of the RPA screened interaction potentials. The detailed manipulations are included in App. C.4, but here we sketch briefly the procedure in words: Taking the first term of the first line of Eq. (4.24), we notice that we may immediately write the gradients on the outside of the integral and replace $V_0\tilde{D}^K_{\rho\rho}V_0 = V^R_{RPA}D^K_{\rho\rho}V^A_{RPA}$ via Dyson's equations, Eqs. (4.31) and (4.32). We replace the density-density GF by current-current GF via Eq. (4.35a), where the gradient operators act on integration variables and so their direction may be flipped via integration by parts to act on the newly introduced RPA screened interaction potentials. Finally $\tilde{D}^K_{j_ij_k}$ is found via its own Dyson equation where we employ Eqs. (4.35) to write everything in terms of current-current GFs. The second term in the first line of Eq. (4.24) is found by the observation that $\tilde{D}^{R-A}$ obeys the same equations as $\tilde{D}^K$, and the second line is approached in the same way as the first. Performing these manipulations as shown in App. C.4 we obtain the following expression for the correlator

$$
\begin{aligned}
S(\mathbf{r},\mathbf{r}',t-t') = &-\frac{\hbar^2}{4}\int_{-\infty}^{\infty}\frac{d\omega}{2\pi}\int_{-\infty}^{\infty}\frac{d\omega'}{2\pi}e^{i(\omega+\omega')(t-t')} \\
&\times\Bigg[\underbrace{\left(\mathbb{1}+\frac{1}{\omega^2}D^R V_\nabla^R\right)D^K\left(\mathbb{1}+\frac{1}{\omega^2}V_\nabla^A D^A\right)}_{\mathbf{r},\mathbf{r}',\omega}\underbrace{\frac{1}{\omega'^2}V_\nabla^R D^K V_\nabla^A}_{\mathbf{r},\mathbf{r}',\omega'} \\
&+\underbrace{\frac{1}{\omega}V_\nabla^R D^K\left(\mathbb{1}+\frac{1}{\omega^2}V_\nabla^A D^A\right)}_{\mathbf{r},\mathbf{r}',\omega}\underbrace{\left(\mathbb{1}+\frac{1}{\omega'^2}D^R V_\nabla^R\right)\frac{1}{\omega'}D^K V_\nabla^A}_{\mathbf{r},\mathbf{r}',\omega'}\Bigg] + \left[D^K\to D^{R-A}\right],
\end{aligned}
\tag{4.36}
$$

where all GFs D are noninteracting current-current and tensors V_∇ are RPA screened interaction terms sandwiched by gradients acting on either side, which may be seen as dipole-dipole interactions. Once again integration of intermediate spatial variables over the whole volume is implied, while the coordinates $\mathbf{r}$ and $\mathbf{r}'$ which appear as indicated reside necessarily in body 1 due to the definition of the heat current operator, Eq. (4.22). Due to the presence of Cartesian indices on the current-current GFs and the gradient terms, the unit operator $\mathbb{1}$ now includes also the Kronecker delta in the Cartesian indices, $\mathbb{1}=\delta(\mathbf{r}-\mathbf{r}')\delta_{ik}$.

As long as the Coulomb limit is justified, expression (4.36) is valid for bodies of arbitrary shape, size and dimension – it may even be used if there are more than two bodies. To specify to the case of two-dimensional parallel layers separated by a distance d, the geometry is encoded in the bare GFs appearing in Eq. (4.36):

$$
\begin{aligned}
D^{R(A)}_{j_i j_l}(\mathbf{r},\mathbf{r}',\omega) = &\int\frac{d^2\mathbf{k}}{(2\pi)^2}e^{i\mathbf{k}\cdot(\mathbf{r}_\parallel-\mathbf{r}'_\parallel)}\frac{k_i k_l}{k^4}\omega^2 \\
&\times\left[\Pi_1^{(*)}(\mathbf{k},\omega)\delta(z)\delta(z')+\Pi_2^{(*)}(\mathbf{k},\omega)\delta(z-d)\delta(z'-d)\right],
\end{aligned}
\tag{4.37a}
$$

$$
\begin{aligned}
D^{K}_{j_i j_l}(\mathbf{r},\mathbf{r}',\omega) = &\int\frac{d^2\mathbf{k}}{(2\pi)^2}e^{i\mathbf{k}\cdot(\mathbf{r}_\parallel-\mathbf{r}'_\parallel)}\frac{k_i k_l}{k^4}\omega^2(2i) \\
&\times\left[\operatorname{Im}\Pi_1(\mathbf{k},\omega)\delta(z)\delta(z')\coth\frac{\hbar\omega}{2T_1}+\operatorname{Im}\Pi_2(\mathbf{k},\omega)\delta(z-d)\delta(z'-d)\coth\frac{\hbar\omega}{2T_2}\right],
\end{aligned}
\tag{4.37b}
$$

where we used Eq. (4.35a) to go back to density-density GFs and the relation for bosons in equilibrium that relates the Keldysh component to the occupation number. We also used that $D^R_{\rho\rho}(\mathbf{k},\omega)=\Pi(\mathbf{k},\omega)$ and $D^A_{\rho\rho}(\mathbf{k},\omega)=\Pi^*(\mathbf{k},\omega)$. The Coulomb limit is reflected in Eqs. (4.37) since it assumes only longitudinal modes ($\mathbf{j}$ parallel to $\mathbf{k}$) contribute to Eq. (4.36). Going beyond the Coulomb limit, the inclusion of also the transverse conductivity would account for transverse electric (TE) modes representing magnetostatic coupling as discussed in Ch. 2. According to Eqs. (4.37) the correlator now bears the in-plane translational symmetry: $S(\mathbf{r},\mathbf{r}',t-t') = S_{2\mathrm{D}}(\mathbf{r}_\parallel - \mathbf{r}'_\parallel, t-t')\delta(z)\delta(z')$.

Just as we found for the average heat current in Sec. 3.1.3, the general equation for the fluctuations Eq. (4.36) will lead to a range of different behaviours according to the temperatures T_1 and T_2 and layer separation d. For $T_2 \gg T_1$, the dominant contribution to Eq. (4.36) comes from taking only the term in $\coth \hbar\omega/2T_2$ in Eq. (4.37b). This corresponds to considering only fields induced by charge fluctuations in layer 2. In this case we notice that the terms $\mathbb{1}$ in Eq. (4.36) do not contribute since the Dirac delta functions always have mismatched z coordinates ($\mathbf{r}$ and $\mathbf{r}'$ reside on layer 1 while the integration variables reside in layer 2).

Inserting Eqs. (4.37a) and (4.37b) for $T_2 \gg T_1$ into Eq. (4.36) and taking the Fourier transform in the form

$$S_{2\mathrm{D}}(\mathbf{K},\Omega) = \int_{-\infty}^{\infty} d(t-t')e^{i\Omega(t-t')} \int d^2(\mathbf{r}_\parallel - \mathbf{r}'_\parallel) e^{-i\mathbf{K}\cdot(\mathbf{r}_\parallel - \mathbf{r}'_\parallel)} S(\mathbf{r}_\parallel - \mathbf{r}'_\parallel, t-t'), \tag{4.38}$$

leads to the spectrum

$$\begin{aligned} S_{2\mathrm{D}}(\mathbf{K},\Omega) = \int_{-\infty}^{\infty} \frac{d\omega}{2\pi} \int \frac{d^2\mathbf{k}}{(2\pi)^2} \left[1 + \coth\frac{\hbar\omega}{2T_2}\coth\frac{\hbar(\Omega-\omega)}{2T_2}\right] [(\mathbf{K}-\mathbf{k})\cdot\mathbf{k}]^2 \\ \times \operatorname{Im}\Pi_2^R(\mathbf{K}-\mathbf{k},\Omega-\omega)\operatorname{Im}\Pi_2^R(\mathbf{k},\omega)\left|V_{12}^R(\mathbf{K}-\mathbf{k},\Omega-\omega)V_{12}^R(\mathbf{k},\omega)\right|^2 \\ \times \left[\frac{\omega^2}{|\mathbf{k}|^4}\left|\Pi_1^R(\mathbf{k},\omega)\right|^2 + \frac{\omega(\Omega-\omega)}{|\mathbf{K}-\mathbf{k}|^2|\mathbf{k}|^2}\Pi_1^R(\mathbf{K}-\mathbf{k},\Omega-\omega)\Pi_1^A(\mathbf{k},\omega)\right], \end{aligned} \tag{4.39}$$

The two terms in square brackets arise from the two lines of Eq. (4.36), which themselves may be traced back to the two lines of Eq. (4.24). The screened inter-layer interaction term V_{12}^R is the same as in the calculation of the average heat current, and is given explicitly in Eq. (3.3). We may notice the correspondence between Eqs. (4.36) and (4.39) for two-dimensional layers and the analogous expressions for the heat current noise in a circuit presented in the previous section, Eqs. (4.13) and (4.16). The only major difference is the additional integration over wavevector in the case of the two-dimensional layers, while the circuit model may be thought of as zero-dimensional.

4.3.2 Plasmon resonance feature in the noise spectrum

We see from Eq. (4.39) that there are many possible regimes of behaviour for the noise spectrum, valid for different values of Ω and $\mathbf{K}$ according to the temperature T_2 and the material parameters encoded in $\Pi_{1,2}$. We specify to the case where the two layers are identical, i.e. $\Pi_1 = \Pi_2$. Rather than computing the full map of behaviour resulting from Eq. (4.39), we focus on the regime where we know that the main radiative heat transfer channel is emission and absorption of surface plasmons – in particular, in the low-temperature regime J_{lp} of Fig. 3.2 where the antisymmetric plasmon gives the dominant contribution. Here, as discussed in App. A.4.1, the screened interaction $|V_{12}|^2$ is highly peaked in the vicinity of the antisymmetric surface plasmon dispersion, and the spatial dispersion in the conductivity does not play a role. In order to pick up the contribution, the integrand was approximated as a Lorentzian centred at the linear plasmon dispersion, $\omega = v_- k$, with $v_- = v_F\sqrt{\kappa d/2}$ the antisymmetric plasmon speed [see Eq. (3.6)], and width $1/\tau$.

Analogously, in the same region of validity $1/\tau \ll T_2/\hbar \ll v_F\sqrt{\kappa/d}$, we may approximate the integrand in Eq. (4.39) as a product of two Lorentzians corresponding to the two factors of $|V_{12}|^2$, whose centres are for $\omega > 0$ at $k = \omega/v_-$ and the solution of $|\mathbf{K}-\mathbf{k}| = (\omega-\Omega)/v_-$. For Ω, $v_- K \ll T_2/\hbar$, we expand the $\mathbf{k}$ integral in plane polar coordinates approximating $|\mathbf{K}-\mathbf{k}| \approx k - K\cos\phi$ and set all non-singular terms in k to the centres of the Lorentzians. There is an identical contribution from $\omega < 0$, leading to the total expression

$$\begin{aligned}
S_{\mathrm{2D}}(\mathbf{K},\Omega) = {} & -\frac{\hbar^2\tau^4 {v_-}^2(4+\Omega^2\tau^2)}{64(\kappa d)^2}\int_0^\infty \frac{d\omega}{2\pi}\left(1+\coth\frac{\hbar\omega}{2T_2}\coth\frac{\hbar(\Omega-\omega)}{2T_2}\right)\\
& \times \frac{(\omega-\Omega)^5\omega^6}{\left[1+(\Omega-\omega)^2\tau^2\right]^2\left[1+\omega^2\tau^2\right]^2}\\
& \times \int_0^{2\pi}\frac{d\phi}{2\pi}\int_0^\infty\frac{d\varpi}{2\pi}\frac{1}{(\varpi-\omega)^2+(\frac{1}{2\tau})^2}\,\frac{1}{(\varpi-\omega-Kv_-\cos\phi+\Omega)^2+(\frac{1}{2\tau})^2},
\end{aligned} \tag{4.40}$$

where we made the change of variables $\varpi = v_- k$. We extend the lower limit of integration over ϖ to $-\infty$ and integrate over the product of Lorentzians, resulting in another Lorentzian in $\cos\phi$ which may be integrated exactly. The remaining integral in ω is determined by the temperature so according to $T_2/\hbar \gg 1/\tau$ we may neglect unity in the denominator in the second line of Eq. (4.40) and since $T_2/\hbar \gg \Omega$ we approximate everywhere $\omega - \Omega \approx \omega$ leading to an integral that may be done exactly, leading to the final expression

$$S_{\mathrm{2D}}(\mathbf{K},\Omega) = \frac{3\pi^3\zeta(3)}{64}\,\mathrm{Im}\left[\frac{1}{\sqrt{(\Omega-i/\tau)^2-(v_-K)^2}}\right]\frac{4+\Omega^2\tau^2}{d\sigma_{\mathrm{DC}}\tau}\,\frac{T_2^4}{\hbar^2}, \tag{4.41}$$

where we observe immediately the resonant structure of the spectrum in the vicinity of the antisymmetric plasmon dispersion, $\Omega = v_- K$, with a width $1/\tau$. The spectrum in Eq. (4.41) is a function of the dimensionless variables $X = v_-\tau K$ and $Y = \Omega\tau$, and may be written in terms of the expression for the average heat current in the low-temperature plasmon regime given in Eq. (3.7c), resulting in

$$S_{\mathrm{2D}}(X,Y) = 2\pi^5 J_{\mathrm{lp}}(T_2)\,T_2\,s_{\mathrm{2D}}(X,Y), \tag{4.42}$$

where we introduced the dimensionless function containing the structure of the noise

$$s_{\mathrm{2D}}(X,Y) = \left[1+(Y/2)^2\right]\mathrm{Im}\left[\frac{1}{\sqrt{(Y-i)^2-X^2}}\right], \tag{4.43}$$

In Eq. (4.42) we may once again make the connection to the famous shot noise [Blanter00], as discussed in the previous section for heat current noise through a circuit. For $\Omega = K = 0$ we have that $s_{2\mathrm{D}}(0,0) = 1$ and the heat current fluctuations are simply given as twice the product of the average energy current and the average energy of carriers, given by temperature. The large prefactor π^5 indicates bunching of plasmons (bosons), as we found in the case of photonic heat current in a zero-dimensional system in Sec. 4.2. However, here there is no variable Fano factor like $T_2/(\hbar\omega_0)$ in Eq. (4.20) since the frequency integral is determined by $\omega \sim T_2/\hbar$.

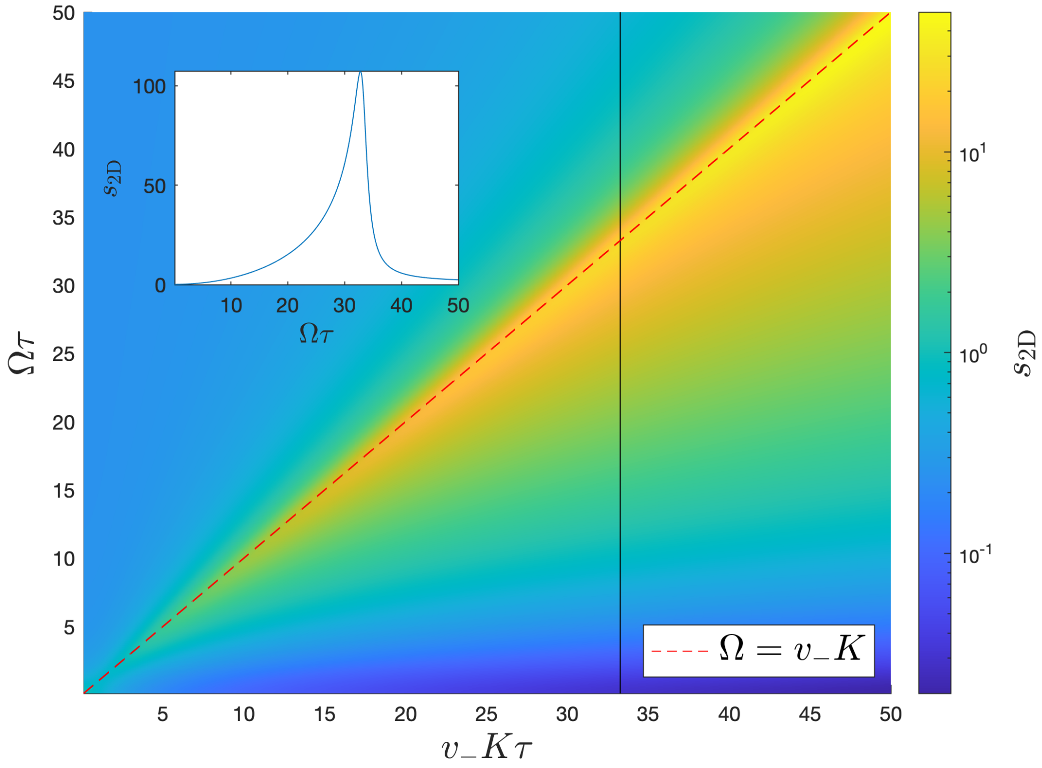

Figure 4.2: Plasmonic noise spectrum resonant feature given by the dimensionless expression (4.43) in terms of the dimensionless parameters $X = v_-\tau K$ and $Y = \Omega\tau$. We observe clearly a resonant feature at the antisymmetric plasmon dispersion $\Omega = v_- K$. Inset: Indicates the dimensionless spectrum value $s_{2\mathrm{D}}$ for fixed wavevector along the vertical black line of the main plot as a function of frequency.

In Fig. 4.2 we plot the dimensionless function (4.43) indicating the resonant feature. As shown, the noise spectrum varies by several orders of magnitude close to the plasmon resonance, which may provide a clear experimental signature of surface plasmons' contribution to the radiative heat transfer. The width of the resonant feature is simply related to the surface plasmon lifetime. This indicates that in order to detect the resonant peak in an experiment, one requires temporal resolution shorter than this lifetime. While for a typical Fermi liquid the quasiparticle lifetime is very short, for resonant modes it may be increased significantly, meaning the resonant feature could be visible experimentally.

4.3.3 Observability of the heat current noise

We have shown in the previous section that the structure of the heat current noise spectrum may contain information about the system excitations and their relaxation properties. However, in order to extract this information, we must ask whether the noise spectrum is observable in an experiment. This question may be both fundamentally nontrivial as discussed in Sec. 4.1 and situation dependent, since the answer depends on the measurement technique. Typically, the heat current absorbed is inferred from measurements of the changing temperature of the receiving body. Fluctuations of the heat current may therefore be sought in the fluctuations of the temperature, as investigated experimentally in Ref. [Karimi20] for the temperature of electrons exchanging heat with a phonon bath. In this section we investigate how the fluctuations of the radiative heat current between two-dimensional layers are translated into temperature fluctuations of the receiving layer, and what this means for the experimental observability.

Without the incoming radiation, the receiving layer is held at a uniform temperature T_1 by coupling to some external bath. Here, the phonons in the layer represent the bath, since the phonons are assumed to be in equilibrium with the substrate/cryostat of the experimental setup. The addition of the space- and time-varying incident radiation causes the electron temperature field in the layer, $T_1(\mathbf{r},t)$, to vary according to the heat transport equation

$$\mathcal{C}\frac{\partial T_1(\mathbf{r},t)}{\partial t} = \kappa\nabla_{\mathbf{r}}^2 T_1(\mathbf{r},t) + J(\mathbf{r},t) - J_{\text{ph.}}(\mathbf{r},t), \tag{4.44}$$

where $\mathcal{C}$ is the heat capacity (per unit area), κ is the thermal conductivity, $J(\mathbf{r},t)$ is the incoming radiative heat current absorbed by the electrons and $J_{\text{ph.}}(\mathbf{r},t)$ is the energy current given by electrons to phonons in the layer. Equation (4.44) is the classical diffusion equation for the energy density inside the layer, written in terms of the temperature field. The temperature field may be written in terms of the change with respect to the constant bath temperature brought about by the incoming radiation: $T_1(\mathbf{r},t) = T_1 + \Delta T_1(\mathbf{r},t)$. The radiative source and phonon sink terms may be further decomposed into an average value and fluctuations, via the expressions

$$J_{\text{ph.}}(\mathbf{r},t) = G_{\text{th.}}\Delta T_1(\mathbf{r},t) + \delta J_{\text{ph.}}(\mathbf{r},t), \tag{4.45a}$$

$$J(\mathbf{r},t) = \langle J\rangle + \delta J(\mathbf{r},t), \tag{4.45b}$$

where $G_{\text{th.}}$ is the electron-phonon heat conductance (per unit area) of the layer. The fluctuations of the heat exchange between electrons and phonons defined by

$$S_{\text{ph.}}(\mathbf{K},\Omega) = \int_{-\infty}^{\infty} d(t-t')\, e^{i\Omega(t-t')} \int d(\mathbf{r}-\mathbf{r}')\, e^{-i\mathbf{K}(\mathbf{r}-\mathbf{r}')}\langle \delta J_{\text{ph.}}(\mathbf{r},t)\delta J_{\text{ph.}}(\mathbf{r}',t')\rangle, \tag{4.46}$$

has been calculated in Ref. [Pekola18] where it is shown to satisfy the general fluctuation dissipation theorem $S_{\text{ph.}}(\mathbf{K},\Omega) = 2T_1^2 G_{\text{th.}}$, which is valid up to frequencies Ω on the order of the temperature. It is convenient to further decompose the total change in the layer temperature, $\Delta T_1(\mathbf{r},t)$ into a uniform response to the average incoming heat current and fluctuations, i.e. $\Delta T_1(\mathbf{r},t) = \langle J\rangle/G_{\text{th.}} + \delta T_1(\mathbf{r},t)$. Substituting this redefinition and the expressions (4.45) into the transport equation (4.44) leads to the equation

$$\mathcal{C}\frac{\partial \delta T_1(\mathbf{r},t)}{\partial t} = \kappa\nabla_{\mathbf{r}}^2\delta T_1(\mathbf{r},t) - G_{\text{th.}}\delta T_1(\mathbf{r},t) + \delta J(\mathbf{r},t) - \delta J_{\text{ph.}}(\mathbf{r},t). \tag{4.47}$$

which is solved by going to Fourier space resulting in the expression

$$\delta T_1(\mathbf{k},\omega) = \frac{\delta J(\mathbf{k},\omega) - \delta J_{\text{ph.}}(\mathbf{k},\omega)}{(G_{\text{th.}} + \kappa k^2) - i\omega\mathcal{C}}. \tag{4.48}$$

Just as for the radiative heat current in Eq. (4.38), we seek the spectrum for the temperature fluctuations in the form

$$S_{T_1}(\mathbf{K},\Omega) = \int_{-\infty}^{\infty} d(t-t')\, e^{i\Omega(t-t')} \int d^2(\mathbf{r}-\mathbf{r}')\, e^{-i\mathbf{K}\cdot(\mathbf{r}-\mathbf{r}')} \langle \delta T_1(\mathbf{r},t)\delta T_1(\mathbf{r}',t')\rangle, \tag{4.49}$$

where we once again use the fact that the object in angular brackets above depends only on the difference in the space and time coordinates due to the temporal and in-plane translational invariance. Plugging in the solution for the temperature fluctuations Eq. (4.48) leads to the temperature fluctuation spectrum

$$S_{T_1}(\mathbf{K},\Omega) = \frac{S_{\text{2D}}(\mathbf{K},\Omega) + S_{\text{ph.}}(\mathbf{K},\Omega)}{(G_{\text{th.}} + \kappa K^2)^2 + \Omega^2\mathcal{C}^2}, \tag{4.50}$$

where we have used the fact that the radiative heat current and the heat exchange between electrons and phonons are uncorrelated. So the temperature fluctuation spectrum is given by a sum of contributions from the incoming radiative heat current and the heat exchange with phonons, modulated by a frequency and wavevector dependent denominator that depends on the receiving material's thermal properties.

The expression (4.50) determines the conditions for which the features of the radiative heat current noise spectrum in Eq. (4.41) are observable in measurements of temperature fluctuations. In particular Eq. (4.50) gives rise to two conditions: (i) in the numerator, the radiative contribution to the spectrum should not be too small in comparison with the phonon contribution, and (ii) $S_{T_1}(\mathbf{K},\Omega)$ should not be too strongly suppressed by the denominator at frequencies and wavevectors corresponding to the interesting features of $S_{\text{2D}}(\mathbf{K},\Omega)$. Condition (i) means we should compare the overall magnitude of $S_{\text{2D}}(\mathbf{K},\Omega)$ with $2T_1^2G_{\text{th.}}$. Analysing Fig. 4.2, we see that the resonant feature of $S_{\text{2D}}(\mathbf{K},\Omega)$ becomes pronounced at scales above $\Omega \sim 1/\tau$ and $K \sim 1/(v_-\tau)$. Condition (ii) implies that the denominator in Eq. (4.50) should be roughly flat over these scales, i.e. we require $1/\tau \lesssim G_{\text{th.}}/\mathcal{C}$ and $1/(v_-\tau) \lesssim \sqrt{G_{\text{th.}}/\kappa}$.

To evaluate the feasibility of satisfying the conditions formulated above, we take the example of doped graphene monolayers where plasmon dominated radiative heat transfer has been observed (see the discussion in Sec. 2.3 of Ref. [Yang18]). We require estimates for the material parameters appearing in the denominator of Eq. (4.50). The thermal conductivity is estimated from the Drude electrical conductivity via the Wiedemann-Franz law as $\kappa = (\pi/3)E_F\tau T_1/\hbar^2$, and the heat capacity per unit area is found from free electron theory as $\mathcal{C} = (2\pi/3)E_F T_1/(\hbar^2 v_F^2)$. Meanwhile, the thermal conductance between electrons and phonons $G_{\mathrm{th.}}$ may be estimated from experimental data on graphene monolayers at low temperatures in Ref. [Fong13], where it shown that $\langle J_{\mathrm{ph.}}\rangle = \Sigma(T_1^3 - T_{\mathrm{ph.}}^3)$, with $T_{\mathrm{ph.}}$ the phonon (bath) temperature and $\Sigma \approx 1.25\,\mathrm{W\,K^{-3}\,m^{-2}}$. This leads to the expression for the thermal conductance $G_{\mathrm{th.}} = 3\Sigma T_1^2$, which is shown to be roughly independent of Fermi energy away from the Dirac point – see Fig. 3 (b) of Ref. [Fong13].

We may now use the conditions (i) and (ii) formulated above to test when the radiative heat current fluctuations will be visible in the temperature fluctuations of the receiving layer. Using the known value $v_F = 10^6\,\mathrm{m\,s^{-1}}$ [Yang18] and taking Fermi energy $E_F = 100\,\mathrm{meV}$, we find that the frequency scale in the denominator of $S_{T_1}(\mathbf{K},\Omega)$ to be $G_{\mathrm{th.}}/\mathcal{C} = (6.5\times 10^9)T_1/(1\,\mathrm{K})\,\mathrm{s^{-1}}$. Taking a mean free path of $\ell = 3\,\mu\mathrm{m}$ we find then that condition (ii) on frequency $1/\tau \lesssim G_{\mathrm{th.}}/\mathcal{C}$ is satisfied for temperatures $T_1 \gtrsim 50\,\mathrm{K}$. In this regime, we may check that the corresponding condition on wavevector $1/(v_-\tau) \lesssim \sqrt{G_{\mathrm{th.}}/\kappa}$ is satisfied automatically since for $G_{\mathrm{th.}}/\mathcal{C} \sim 1/\tau$, we have $\sqrt{G_{\mathrm{th.}}/\kappa} \sim 1/(v_F\tau) \gg 1/(v_-\tau)$. For lower temperatures or smaller mean free paths, the denominator of $S_{T_1}(\mathbf{K},\Omega)$ does indeed mask the interesting resonant feature of $S_{2\mathrm{D}}(\mathbf{K},\Omega)$. Condition (i) regarding the relative magnitude of the two contributions in the numerator of $S_{T_1}(\mathbf{K},\Omega)$ is easily satisfied – for example, taking $T_2 = 300\,\mathrm{K}$ and $d = 430\,\mathrm{nm}$ as in Ref. [Yang18] we find $S_{2\mathrm{D}}(\mathbf{K},\Omega)/S_{\mathrm{ph.}}(\mathbf{K},\Omega) \sim 10^4$.

The overall difficulty in the observability of the resonant feature in the radiative heat current spectrum stems from the fact that it only appears at relatively high frequencies, $\Omega \gtrsim 1/\tau$. This could have been expected since we know from Sec. 3.2 that the plasmon contribution to the heat current is overdamped at lower frequencies. We have subsequently found that there is a tradeoff in terms of the value of the thermal conductance between electrons and phonons. If $G_{\mathrm{th.}}$ is too large, the electrons lose their energy to the phonons too quickly such that the resulting electron temperature fluctuations are dominated by the contribution from this “internal” heat exchange. On the other hand, if $G_{\mathrm{th.}}$ is too small, the high frequency resonant feature of the incoming radiative heat current noise is masked because the thermal response of the metal is too slow, so the heat current fluctuations are effectively averaged out.

4.4 Summary and outlook

In this chapter we have moved on from the study of the average radiative heat current to instead discuss its fluctuations, or noise. We have focused on two systems that exhibit a resonant heat transfer channel that is dominant under certain conditions. The first was a zero-dimensional system modelled quantum mechanically by an electric circuit, while the second was a system of parallel two-dimensional metallic layers, as studied in Chs. 2 and 3. The general forms of the expressions for the heat current noise in the two systems is found to be quite analogous.

Focusing on the case where the heat transfer in the system is dominated by thermal fluctuations in the hotter body (i.e. when the temperatures are strongly different), we find that for both systems a resonant signature is imprinted on the noise spectrum. These signatures reflect the detail of the resonant transfer channel: for the circuit we found a

Lorentzian resonance at zero frequency, and for the parallel layers we find a resonance at the antisymmetric plasmon dispersion. The additional spatial dimension of the parallel layers meant that the resonance has a different shape. At low frequency (and wavevector) we find a heat current shot noise-like regime in both systems. Finally, for the system of two-dimensional layers we discussed the observability of the plasmonic resonant feature of the heat current noise spectrum, finding that in certain situations the electron-phonon coupling in the material may lead to the resonant feature being masked in the measured temperature fluctuations. Generally, the resonant feature in the noise spectrum is easier to observe in cleaner systems where the plasmon damping is weak. We hope that this work paves the way for more experimental and theoretical investigation into finite frequency heat current fluctuations in systems with a resonant transfer channel.

Dans ce chapitre, nous sommes passés de l'étude du courant thermique radiatif moyen à celle de ses fluctuations, ou bruit. Nous nous sommes concentrés sur deux systèmes qui présentent un canal de transfert de chaleur résonant dominant dans certaines conditions. Le premier était un système de dimension zéro modélisé par un circuit électrique quantique, tandis que le second était un système de couches métalliques bidimensionnelles parallèles, tel qu'étudié dans les chapitres 2 et 3. Les formes générales des expressions pour le bruit du courant de chaleur dans les deux systèmes s'avèrent être assez analogues.

En se concentrant sur le cas où le transfert de chaleur dans le système est dominé par les fluctuations thermiques dans le corps le plus chaud (c'est-à-dire lorsque les températures sont fortement différentes), nous trouvons que pour les deux systèmes une signature résonante est imprimée sur le spectre de bruit. Ces signatures reflètent le détail du canal de transfert résonant : pour le circuit, nous avons trouvé une résonance lorentzienne liée à fréquence zero, et pour les couches parallèles, nous trouvons une résonance à la dispersion du plasmon antisymétrique. En raison de la dimension spatiale supplémentaire des couches parallèles, la résonance a une forme différente. À basse fréquence (et vecteur d'onde), nous trouvons un régime semblable au bruit de grenaille thermique dans les deux systèmes. Enfin, pour le système de couches bidimensionnelles, nous avons discuté de l'observabilité de la résonance plasmonique dans le spectre de bruit du courant thermique, en constatant que dans certaines situations, le couplage électron-phonon dans le matériau peut conduire à ce que la caractéristique de résonance soit masquée dans les fluctuations de température mesurées. Généralement, la résonance dans le spectre du bruit est plus facile à observer dans des systèmes propres où l'amortissement du plasmon est faible. Nous espérons que ce travail ouvre la voie à d'autres recherches expérimentales et théoriques sur les fluctuations de courant thermique à fréquence finie dans les systèmes avec un canal de transfert résonant.

General conclusion and outlook

In this thesis we have performed detailed studies of radiative heat transfer between spatially separated bodies. We focused on performing analytical calculations using general models in order to reveal the roles and interplay of key physical ingredients. The work has led to many interesting conclusions regarding radiative heat transfer behaviour that we summarise here. Our findings also stimulate further research in a number of open questions which we also mention.

Working in the framework of fluctuational electrodynamics, we studied the average radiative heat current between two-dimensional metallic layers characterised by Drude conductivity separated by a vacuum gap. We were able to see explicitly the origins of the sometimes many order of magnitude enhancement of the heat current due to evanescent waves. The decaying character of the evanescent waves is reflected in the heat current's dependence on the body separation of the analytical expressions obtained. The calculation revealed the existence of two classes of materials: For poor metals such as doped semiconductors and atomically thin two-dimensional materials, the heat current at layer separations up to and even beyond the thermal wavelength of photons is dominated by electrostatic coupling of electrons between the layers. Meanwhile, for good metals such as thin films of conventional metal the heat current in the near field is primarily dominated by magnetostatic coupling, where the magnetic field established by transverse current fluctuations in one layer drives eddy currents that cause dissipation in the other layer – this behaviour is reminiscent of what had already been discovered for bulk three-dimensional metals. Our theoretical results showed order of magnitude agreement with experimental data, indicating that they could be useful in providing quick estimates of the heat current in a given context and revealing the main physical mechanisms responsible.

Focusing on the Coulomb limit shown mainly to be relevant for poor metals, we studied the same problem of average radiative heat current between parallel layers, but with a richer model for the material response. Modelling the layers as an interacting two-dimensional electron gas with elastic impurity scattering, we showed that collective charge density excitations known as surface plasmons become coupled in the near field and may contribute significantly to the radiative heat transfer. We find that the disorder, if too weak or too strong has a tendency to mask this plasmon contribution but that it nonetheless may be expected to dominate for a wide class of parameters. This kind of plasmonic heat transport may be utilised in the design of novel devices where control over the heat flow may be tuned via material parameters. We find that the surface plasmon contribution is not sensitive to nonlocality in the material response, which only plays a role at extremely small body separations. We explored the possibility of representing the heat transfer in a physical system like that described above by an effective circuit without spatial dimension. As may be expected this analogy is limited for large objects, while for objects that are small compared to the characteristic length scale of the relevant heat carriers we find that an effective circuit picture may indeed be used. This is in support of what is commonly done when studying electric charge current in nanometric systems via an effective circuit.

In an attempt to delve deeper into the characteristics of radiative heat transfer, we studied its fluctuations. In particular, we were motivated to study the fluctuations in systems whose heat transfer may be dominated by a resonant channel since while effectively invisible in the average heat current signal, it was expected that this resonant behaviour would be imprinted in the fluctuations' frequency spectrum. This signature could be visible when compared to the structureless noise that one expects from processes involving continuum excitations. First, we reported on findings of a study of an effective zero-dimensional system modelled by an electric circuit, where the heat transfer may be dominated by photons at the natural frequency of a superconducting resonator. It was shown that to capture the behaviour of the heat current fluctuations a fully quantum description of the system is necessary, and that indeed the finite-frequency heat current noise spectrum exhibits a signature of the resonance in the transmission that could potentially be measurable. Subsequently, we have worked in the framework of nonequilibrium Green's functions to calculate the finite frequency and wavevector heat current noise spectrum for the system of two-dimensional metallic layers separated by a gap. The general structure of the noise is reminiscent of the simpler zero-dimensional case, and here we also find a resonant feature in the noise due to the aforementioned resonant heat transfer channel via the emission and absorption of surface plasmons. The resonant feature encodes details of the collective excitations themselves both in the form of their dispersion relation but also their lifetime. If measured, this type of feature would provide a demonstration of the important role played by these collective excitations in the heat transfer, but also provide a general method of probing the character of the excitations themselves. We have briefly discussed the observability of the heat current noise resonant feature via temperature measurements, finding that according to the material parameters the feature may actually be masked due to the dynamics controlling the temperature relaxation.

The problem of heat current noise (radiative or otherwise) remains subtle with many open questions. In particular, there remains much to explore on the question of its measurability. Since the heat current signal itself is generally inferred from measurements of temperature in a receiving body, one needs to explore exactly how and over what timescale this heat-to-temperature correspondence takes place. This involves questions not only of technical and experimental capability in terms of measurement resolution, but also fundamental questions related to thermal equilibration and energy-time uncertainty. Indeed, one may consider the case of observing heat current fluctuations when the electrons are out of equilibrium and therefore do not have a well-defined temperature. In this case it may be possible to construct a theory that takes into account the out-of-equilibrium electron dynamics to infer the heat current from measurements of some other observable which is well-defined such as, for example, electric current.

A rare regime of electron dynamical behaviour known as electron hydrodynamics has recently realised experimentally in graphene [Gallagher19]. This fluid-like behaviour may occur only in extremely clean samples, where the dominant collisions are those between the electrons themselves, rather than with impurities or phonons. We have not addressed the hydrodynamic regime in this work, since our calculations do not explicitly take electron-electron collisions into account. The question of radiative heat transfer for hydrodynamic electrons therefore remains open and would be interesting to investigate.

Although we have tackled a variety of problems regarding radiative heat transfer, they have all nonetheless been harmonic. We have considered only linear electrodynamics, and only ever linear circuit elements, meaning all the systems studied eventually amount to collections of harmonic oscillators. For conventional metals at high temperatures, the linear approximation holds very well. However, in nanoscale structures operating at sub-Kelvin temperatures nonlinearities are expected to become important. The study of heat transfer in systems with a nonlinearity is likely to reveal rich physics. For example, average heat transport between reservoirs coupled via a two-level system has been shown to display radically different behaviours depending on the relation between the temperature and the two-level energy splitting [Ruokola11], as well as the mechanism and strength of the coupling of the two-level system to the baths [Yamamoto18, Xu21]. This kind of a system has been realised experimentally [Ronzani18], where the two-level system is achieved by a superconducting transmon qubit, whose level separation may be tuned via an external magnetic field allowing for the modulation of heat flow. The investigation of radiative heat current fluctuations through a two-level system remains an open question whose answer may have significant implications on the design of novel devices based on nonlinear elements of this type.

Conclusion générale et perspectives

Dans cette thèse, nous avons réalisé des études détaillées sur le transfert de chaleur radiative entre des corps séparés dans l'espace. Nous nous sommes concentrés sur la réalisation de calculs analytiques en utilisant des modèles généraux afin de révéler les rôles et l'interaction des ingrédients physiques clés. Ce travail a conduit à de nombreuses conclusions intéressantes concernant le comportement du transfert de chaleur radiatif que nous résumons ici. Nos résultats stimulent également la recherche dans un certain nombre de questions ouvertes que nous mentionnons également.

En travaillant dans le cadre de l'électrodynamique fluctuante, nous avons étudié le courant thermique radiatif moyen entre des couches métalliques bidimensionnelles caractérisées par une conductivité de Drude et séparées par un vide. Nous avons pu voir explicitement les origines de l'augmentation parfois de plusieurs ordres de grandeur du courant thermique due aux ondes évanescentes. Le caractère décroissant des ondes évanescentes est reflété dans la dépendance du courant thermique par rapport à la séparation des corps des expressions analytiques obtenues. Le calcul a révélé l'existence de deux classes de matériaux : Pour les mauvais métaux tels que les semi-conducteurs dopés et les matériaux bidimensionnels atomiquement minces, le courant thermique à des separations de couches jusqu'à et même au-delà de la longueur d'onde thermique des photons est dominé par le couplage électrostatique des électrons entre les couches. En revanche, pour les bons métaux tels que les films minces de métaux classiques, le courant thermique dans le champ proche est principalement dominé par le couplage magnétostatique, où le champ magnétique établi par les fluctuations de courant transversales dans une couche entraîne des courants de Foucault qui provoquent une dissipation dans l'autre couche - ce comportement rappelle ce qui a déjà été découvert pour les métaux tridimensionnels massifs. Nos résultats théoriques ont montré un accord d'ordre de grandeur avec les données expérimentales, indiquant qu'ils pourraient être utiles pour fournir des estimations rapides du courant thermique dans un contexte donné et révéler les principaux mécanismes physiques responsables.

En nous concentrant sur la limite de Coulomb, qui s'avère principalement pertinente pour les mauvais métaux, nous avons étudié le même problème de courant thermique radiatif moyen entre des couches parallèles, mais avec un modèle plus riche pour la réponse du matériau. En modélisant les couches comme un gaz d'électrons bidimensionnel en interaction avec une diffusion élastique des impuretés, nous avons montré que les excitations collectives de densité de charge connues sous le nom de plasmons de surface deviennent couplées dans le champ proche et peuvent contribuer de manière significative au transfert de chaleur radiatif. Nous avons constaté que le désordre, s'il est trop faible ou trop fort, a tendance à masquer cette contribution plasmonique, mais qu'on peut néanmoins s'attendre à ce qu'elle domine pour une large classe de paramètres. Ce type de transport de chaleur plasmonique peut être utilisé dans la conception de nouveaux dispositifs où le contrôle du flux de chaleur peut être réglé par des paramètres matériels. Nous constatons que la contribution des plasmons de surface n'est pas sensible à la nonlocalité dans la réponse du matériau, qui ne joue un rôle que pour des séparations de corps extrêmement petites. Nous avons exploré la possibilité de représenter le transfert de chaleur dans un système physique comme celui décrit ci-dessus par un circuit effectif sans dimension spatiale. Comme on peut s'y attendre, cette analogie est limitée aux objets de grande taille, alors que pour les objets de petite taille par rapport à l'échelle de longueur caractéristique des transporteurs de chaleur concernés, nous constatons qu'une image de circuit effectif peut effectivement être utilisée. Cela va dans le sens de ce qui est généralement fait lors de l'étude du courant de charge électrique dans les systèmes nanométriques via un circuit effectif.

Dans le but d'approfondir les caractéristiques du transfert de chaleur radiatif, nous avons étudié ses fluctuations. En particulier, nous avons été motivés pour étudier les fluctuations dans des systèmes dont le transfert de chaleur peut être dominé par un canal résonnant. En effet, bien qu'invisible dans le signal moyen du courant thermique, on s'attendait à ce que ce comportement résonnant soit imprimé dans le spectre de fréquence des fluctuations. Cette signature pourrait être visible par rapport au bruit sans structure que l'on attend des processus impliquant des excitations continues. Nous avons d'abord présenté les résultats d'une étude d'un système effectif de dimension zéro modélisé par un circuit électrique, où le transfert de chaleur peut être dominé par des photons à la fréquence naturelle d'un résonateur supraconducteur. Il a été démontré que pour capturer le comportement des fluctuations du courant thermique, une description entièrement quantique du système est nécessaire, et qu'en effet le spectre de bruit du courant thermique à fréquence finie présente une signature de la résonance dans la transmission qui pourrait potentiellement être mesurable. Par la suite, nous avons travaillé dans le cadre des fonctions de Green de non-équilibre pour calculer le spectre de bruit du courant thermique à fréquence finie et à vecteur d'onde pour le système de couches métalliques bidimensionnelles séparées par un espace. La structure générale du bruit rappelle le cas plus simple de la dimension zéro, et ici nous trouvons également une caractéristique résonante dans le bruit due au canal de transfert de chaleur résonant mentionné ci-dessus via l'émission et l'absorption de plasmons de surface. La caractéristique résonante code les détails des excitations collectives elles-mêmes, à la fois sous la forme de leur relation de dispersion et de leur durée de vie. S'il était mesuré, ce type de caractéristique fournirait une démonstration du rôle important joué par ces excitations collectives dans le transfert de chaleur, mais aussi une méthode générale pour sonder le caractère des excitations elles-mêmes. Nous avons brièvement discuté de l'observabilité de la caractéristique résonante du bruit du courant thermique par le biais de mesures de température, en constatant que selon les paramètres du matériau, la caractéristique peut en fait être masquée en raison de la dynamique contrôlant la relaxation de température.

Le problème du bruit du courant thermique (radiatif ou autre) reste subtil avec de nombreuses questions ouvertes. En particulier, il reste beaucoup à explorer sur la question de sa mesurabilité. Puisque le signal du courant thermique lui-même est généralement déduit des mesures de la température dans un corps récepteur, il faut explorer exactement comment et sur quelle échelle de temps cette correspondance chaleur-température a lieu. Cela implique non seulement des questions de capacité technique et expérimentale en termes de résolution de mesure, mais aussi des questions fondamentales liées à l'équilibre thermique et à l'incertitude énergie-temps. En effet, on peut envisager le cas de l'observation des fluctuations du courant thermique lorsque les électrons sont hors d'équilibre et n'ont donc pas une température bien définie. Dans ce cas, il peut être possible de construire une théorie qui prend en compte la dynamique des électrons hors équilibre pour déduire le courant thermique à partir des mesures d'une autre observable bien définie comme, par exemple, le courant électrique.

Un régime rare de comportement dynamique des électrons, connu sous le nom des électrons hydrodynamiques, a récemment été réalisé expérimentalement dans le graphène [Gallagher19]. Ce comportement de type fluide ne peut se produire que dans des échantillons extrêmement propres, où les collisions dominantes sont celles entre les électrons eux-mêmes, plutôt qu'avec des impuretés ou des phonons. Nous n'avons pas abordé le régime hydrodynamique dans ce travail, car nos calculs ne prennent pas explicitement en compte les collisions électron-électron. La question du transfert de chaleur radiatif pour les électrons hydrodynamiques reste donc ouverte et serait intéressante à étudier.

Bien que nous ayons abordé une variété de problèmes concernant le transfert de chaleur radiative, ils ont néanmoins tous été harmoniques. Nous n'avons considéré que l'électrodynamique linéaire, et seulement des éléments de circuit toujours linéaires, ce qui signifie que tous les systèmes étudiés se résument finalement à des collections d'oscillateurs harmoniques. L'étude du transfert de chaleur dans des systèmes présentant une non-linéarité est susceptible de révéler une physique riche. Par exemple, il a été démontré que le transport de chaleur moyen entre des réservoirs couplés par un système à deux niveaux présente des comportements radicalement différents selon la relation entre la température et le fractionnement d'énergie à deux niveaux [Ruokola11], ainsi que le mécanisme et la force du couplage du système à deux niveaux aux bains [Yamamoto18, Xu21]. Ce type de système a été réalisé expérimentalement [Ronzani18], où le système à deux niveaux est réalisé par un qubit transmon supraconducteur, dont la séparation des niveaux peut être accordée via un champ magnétique externe permettant la modulation du flux de chaleur. L'étude des fluctuations du courant thermique radiatif à travers un système à deux niveaux reste une question ouverte dont la réponse peut avoir des implications importantes sur la conception de nouveaux dispositifs basés sur des éléments non linéaires de ce type.

Bibliography

[Abrikosov75] A. Abrikosov, L. Gorkov, and I. Dzyaloshinski. *Methods of quantum field theory in statistical physics*. Dover Books on Physics and Chemistry. Dover, New York, 1975.

[Abrikosov88] A. A. Abrikosov. *Fundamentals of the Theory of Metals*. Dover, New York, 1988.

[Altshuler85] B. L. Altshuler and A. G. Aronov. Chapter 1 - electron–electron interaction in disordered conductors. In A. Efros and M. Pollak, editors, *Electron–Electron Interactions in Disordered Systems*, volume 10 of *Modern Problems in Condensed Matter Sciences*, pages 1 – 153. North-Holland, Amsterdam, 1985. doi:https://doi.org/10.1016/B978-0-444-86916-6.50007-7.

[baron de Fourier22] J. B. J. baron de Fourier. *Théorie analytique de la chaleur*. Firmin Didot, 1822.

[Basu07] S. Basu, Y.-B. Chen, and Z. M. Zhang. Microscale radiation in thermophotovoltaic devices—a review. *International Journal of Energy Research*, 31(6-7):689–716, 2007, doi:https://doi.org/10.1002/er.1286.

[Basu09] S. Basu, Z. M. Zhang, and C. J. Fu. Review of near-field thermal radiation and its application to energy conversion. *International Journal of Energy Research*, 33(13):1203–1232, 2009, doi:https://doi.org/10.1002/er.1607.

[Ben-Abdallah19] P. Ben-Abdallah and S.-A. Biehs. Harvesting the electromagnetic energy confined close to a hot body. *Zeitschrift fur Naturforschung A*, 74(8):689–696, 2019, doi:doi:10.1515/zna-2019-0132.

[Biehs07] S. A. Biehs. Thermal heat radiation, near-field energy density and near-field radiative heat transfer of coated materials. *The European Physical Journal B*, 58(4):423–431, 2007, doi:10.1140/epjb/e2007-00254-8.

[Biehs18] S.-A. Biehs and P. Ben-Abdallah. Fluctuations of radiative heat exchange between two bodies. *Phys. Rev. B*, 97:201406, May 2018, doi:10.1103/PhysRevB.97.201406.

[Biehs21] S.-A. Biehs, R. Messina, P. S. Venkataram, A. W. Rodriguez, J. C. Cuevas, and P. Ben-Abdallah. Near-field radiative heat transfer in many-body systems. *Rev. Mod. Phys.*, 93:025009, Jun 2021, doi:10.1103/RevModPhys.93.025009.

[Blanter00] Y. Blanter and M. Büttiker. Shot noise in mesoscopic conductors. *Physics Reports*, 336(1):1–166, 2000, doi:https://doi.org/10.1016/S0370-1573(99)00123-4.

[Boltzmann84] L. Boltzmann. Ableitung des stefan'schen gesetzes, betreffend die abhängigkeit der wärmestrahlung von der temperatur aus der electromagnetischen lichttheorie. *Annalen der Physik*, 258(6):291–294, 1884, doi:https://doi.org/10.1002/andp.18842580616.

[Bright14] T. J. Bright, L. P. Wang, and Z. M. Zhang. Performance of Near-Field Thermophotovoltaic Cells Enhanced With a Backside Reflector. *Journal of Heat Transfer*, 136(6), 03 2014, doi:10.1115/1.4026455. 062701.

[Bruus04] H. Bruus and K. Flensberg. *Many-body quantum theory in condensed matter physics: an introduction*. Oxford university press, 2004.

[Callen51] H. B. Callen and T. A. Welton. Irreversibility and generalized noise. *Phys. Rev.*, 83:34–40, Jul 1951, doi:10.1103/PhysRev.83.34.

[Caren72a] R. P. Caren. Radiation Energy Density and Radiation Heat Flux in Small Rectangular Cavities. *Journal of Heat Transfer*, 94(3):289–294, 08 1972, doi:10.1115/1.3449934.

[Caren72b] R. P. Caren. Radiation Heat Transfer between Closely Spaced Metal Surfaces at Low Temperature: The Impact of Discrete Modes of the Radiation Field. *Journal of Heat Transfer*, 94(3):295–299, 08 1972, doi:10.1115/1.3449935.

[Caren74] R. Caren. Thermal radiation between closely spaced metal surfaces at low temperature due to traveling and quasi-stationary components of the radiation field. *International Journal of Heat and Mass Transfer*, 17(7):755–765, 1974, doi:https://doi.org/10.1016/0017-9310(74)90170-7.

[Carminati99] R. Carminati and J.-J. Greffet. Near-field effects in spatial coherence of thermal sources. *Phys. Rev. Lett.*, 82:1660–1663, Feb 1999, doi:10.1103/PhysRevLett.82.1660.

[Caroli71] C. Caroli, R. Combescot, P. Nozieres, and D. Saint-James. Direct calculation of the tunneling current. *Journal of Physics C:*

Solid State Physics, 4(8):916–929, jun 1971, doi:10.1088/0022-3719/4/8/018.

[Casimir48a] H. B. G. Casimir and D. Polder. The influence of retardation on the london-van der waals forces. *Phys. Rev.*, 73:360–372, Feb 1948, doi:10.1103/PhysRev.73.360.

[Casimir48b] H. B. Casimir. On the attraction between two perfectly conducting plates. In *Proc. Kon. Ned. Akad. Wet.*, volume 51, page 793, 1948.

[Chapuis08a] P.-O. Chapuis, M. Laroche, S. Volz, and J.-J. Greffet. Near-field induction heating of metallic nanoparticles due to infrared magnetic dipole contribution. *Phys. Rev. B*, 77:125402, Mar 2008, doi:10.1103/PhysRevB.77.125402.

[Chapuis08b] P.-O. Chapuis, M. Laroche, S. Volz, and J.-J. Greffet. Radiative heat transfer between metallic nanoparticles. *Applied Physics Letters*, 92(20):201906, 2008, doi:10.1063/1.2931062.

[Chapuis08c] P.-O. Chapuis, S. Volz, C. Henkel, K. Joulain, and J.-J. Greffet. Effects of spatial dispersion in near-field radiative heat transfer between two parallel metallic surfaces. *Phys. Rev. B*, 77:035431, Jan 2008, doi:10.1103/PhysRevB.77.035431.

[Chen15] K. Chen, P. Santhanam, S. Sandhu, L. Zhu, and S. Fan. Heat-flux control and solid-state cooling by regulating chemical potential of photons in near-field electromagnetic heat transfer. *Phys. Rev. B*, 91:134301, Apr 2015, doi:10.1103/PhysRevB.91.134301.

[Cravalho67] E. G. Cravalho, C. L. Tien, and R. P. Caren. Effect of Small Spacings on Radiative Transfer Between Two Dielectrics. *Journal of Heat Transfer*, 89(4):351–358, 11 1967, doi:10.1115/1.3614396.

[Cravalho68] E. Cravalho, G. Domoto, and C. Tien. Measurements of thermal radiation of solids at liquid-helium temperatures. In *3rd Thermophysics Conference*, page 774, 1968.

[Cuevas18] J. C. Cuevas and F. J. García-Vidal. Radiative heat transfer. *ACS Photonics*, 5(10):3896–3915, 2018, doi:10.1021/acsphotonics.8b01031.

[Day97] P. Day, I. Hahn, T. C. P. Chui, A. W. Harter, D. Rowe, and J. A. Lipa. The fluctuation-imposed limit for temperature measurement. *Journal of Low Temperature Physics*, 107(3):359, 1997, doi:10.1007/BF02397463.

[De Wilde06] Y. De Wilde, F. Formanek, R. Carminati, B. Gralak, P.-A. Lemoine, K. Joulain, J.-P. Mulet, Y. Chen, and J.-J. Greffet. Thermal radiation scanning tunnelling microscopy. *Nature*, 444(7120):740–743, 2006, doi:10.1038/nature05265.

[Domoto70] G. A. Domoto, R. F. Boehm, and C. L. Tien. Experimental Investigation of Radiative Transfer Between Metallic Surfaces at Cryogenic Temperatures. *Journal of Heat Transfer*, 92(3):412–416, 08 1970, doi:10.1115/1.3449677.

[Einstein05] A. Einstein. On a heuristic point of view toward the emission and transformation of light. *Ann. Phys*, 17:132, 1905.

[Emslie62] A. G. Emslie. In P. E. Glaser, editor, *Aerodynamically Heated Structures*. Prentice-Hall, Englewood Cliffs, NJ, 1962.

[Fal'ko89] V. I. Fal'ko and D. I. Khmel'nitskii. What if a film conductivity exceeds the speed of light? *Sov. Phys. JETP*, 68(6):1150, 1989.

[Fiorino18a] A. Fiorino, D. Thompson, L. Zhu, R. Mittapally, S.-A. Biehs, O. Bezencenet, N. El-Bondry, S. Bansropun, P. Ben-Abdallah, E. Meyhofer, and P. Reddy. A thermal diode based on nanoscale thermal radiation. *ACS Nano*, 12(6):5774–5779, 2018, doi:10.1021/acsnano.8b01645. PMID: 29790344.

[Fiorino18b] A. Fiorino, L. Zhu, D. Thompson, R. Mittapally, P. Reddy, and E. Meyhofer. Nanogap near-field thermophotovoltaics. *Nature Nanotechnology*, 13(9):806–811, 2018, doi:10.1038/s41565-018-0172-5.

[Fong13] K. C. Fong, E. E. Wollman, H. Ravi, W. Chen, A. A. Clerk, M. D. Shaw, H. G. Leduc, and K. C. Schwab. Measurement of the electronic thermal conductance channels and heat capacity of graphene at low temperature. *Phys. Rev. X*, 3:041008, Oct 2013, doi:10.1103/PhysRevX.3.041008.

[Francoeur08] M. Francoeur, M. P. Mengüç, and R. Vaillon. Near-field radiative heat transfer enhancement via surface phonon polaritons coupling in thin films. *Applied Physics Letters*, 93(4):043109, 2008, doi:10.1063/1.2963195.

[Franz53] R. Franz and G. Wiedemann. Ueber die wärme-leitungsfähigkeit der metalle. *Annalen der Physik*, 165(8):497–531, 1853, doi:https://doi.org/10.1002/andp.18531650802.

[Fu06] C. Fu and Z. Zhang. Nanoscale radiation heat transfer for silicon at different doping levels. *International Jour-*

nal of Heat and Mass Transfer, 49(9):1703–1718, 2006, doi:https://doi.org/10.1016/j.ijheatmasstransfer.2005.09.037.

[Fu09] C. Fu and W. Tan. Near-field radiative heat transfer between two plane surfaces with one having a dielectric coating. *Journal of Quantitative Spectroscopy and Radiative Transfer*, 110(12):1027–1036, 2009, doi:https://doi.org/10.1016/j.jqsrt.2009.02.007.

[Gallagher19] P. Gallagher, C.-S. Yang, T. Lyu, F. Tian, R. Kou, H. Zhang, K. Watanabe, T. Taniguchi, and F. Wang. Quantum-critical conductivity of the dirac fluid in graphene. *Science*, 364(6436):158–162, 2019, doi:10.1126/science.aat8687.

[Geick66] R. Geick, C. H. Perry, and G. Rupprecht. Normal modes in hexagonal boron nitride. *Phys. Rev.*, 146:543–547, Jun 1966, doi:10.1103/PhysRev.146.543.

[Giazotto06] F. Giazotto, T. T. Heikkilä, A. Luukanen, A. M. Savin, and J. P. Pekola. Opportunities for mesoscopics in thermometry and refrigeration: Physics and applications. *Rev. Mod. Phys.*, 78:217–274, Mar 2006, doi:10.1103/RevModPhys.78.217.

[Golubev15] D. S. Golubev and J. P. Pekola. Statistics of heat exchange between two resistors. *Phys. Rev. B*, 92:085412, Aug 2015, doi:10.1103/PhysRevB.92.085412.

[Govorov89] A. O. Govorov and A. V. Chaplik. Retardation effects in the relaxation of a two-dimensional electron plasma. *Sov. Phys. JETP*, 68(6):1143, 1989.

[Greffet02] J.-J. Greffet, R. Carminati, K. Joulain, J.-P. Mulet, S. Mainguy, and Y. Chen. Coherent emission of light by thermal sources. *Nature*, 416(6876):61–64, 2002, doi:10.1038/416061a.

[Greffet07] J.-J. Greffet and C. Henkel. Coherent thermal radiation. *Contemporary Physics*, 48(4):183–194, 2007, doi:10.1080/00107510701690380.

[Gusikhin18] P. A. Gusikhin, V. M. Muravev, A. A. Zagitova, and I. V. Kukushkin. Drastic reduction of plasmon damping in two-dimensional electron disks. *Phys. Rev. Lett.*, 121:176804, Oct 2018, doi:10.1103/PhysRevLett.121.176804.

[Hargreaves69] C. M. Hargreaves. Anomalous radiative transfer between closely-spaced bodies. *Physics Letters A*, 30(9):491 – 492, 1969, doi:https://doi.org/10.1016/0375-9601(69)90264-3. More precise measurements were described in the Ph. D. Thesis of C.

M. Hargreaves (University of Leiden, 1973), reproduced in Ref. [Song15a].

[Hargreaves73] C. M. Hargreaves. PhD thesis, University of Leiden, 1973.

[Henkel00] C. Henkel, K. Joulain, R. Carminati, and J.-J. Greffet. Spatial coherence of thermal near fields. *Optics Communications*, 186(1):57–67, 2000, doi:https://doi.org/10.1016/S0030-4018(00)01048-8.

[Herz20] F. Herz, C. Kathmann, and S.-A. Biehs. General trace formula for heat flux fluctuations. *EPL (Europhysics Letters)*, 130(4):44003, Jun 2020, doi:10.1209/0295-5075/130/44003.

[Hu08] L. Hu, A. Narayanaswamy, X. Chen, and G. Chen. Near-field thermal radiation between two closely spaced glass plates exceeding planck's blackbody radiation law. *Applied Physics Letters*, 92(13):133106, 2008, doi:10.1063/1.2905286.

[Iizuka12] H. Iizuka and S. Fan. Rectification of evanescent heat transfer between dielectric-coated and uncoated silicon carbide plates. *Journal of Applied Physics*, 112(2):024304, 2012, doi:10.1063/1.4737465.

[Ilic12] O. Ilic, M. Jablan, J. D. Joannopoulos, I. Celanovic, H. Buljan, and M. Soljačić. Near-field thermal radiation transfer controlled by plasmons in graphene. *Phys. Rev. B*, 85:155422, Apr 2012, doi:10.1103/PhysRevB.85.155422.

[Jablan09] M. Jablan, H. Buljan, and M. Soljačić. Plasmonics in graphene at infrared frequencies. *Phys. Rev. B*, 80:245435, Dec 2009, doi:10.1103/PhysRevB.80.245435.

[Jiang17] J.-H. Jiang and J.-S. Wang. Caroli formalism in near-field heat transfer between parallel graphene sheets. *Phys. Rev. B*, 96:155437, Oct 2017, doi:10.1103/PhysRevB.96.155437.

[Joulain05] K. Joulain, J.-P. Mulet, F. Marquier, R. Carminati, and J.-J. Greffet. Surface electromagnetic waves thermally excited: Radiative heat transfer, coherence properties and casimir forces revisited in the near field. *Surface Science Reports*, 57(3):59 – 112, 2005, doi:https://doi.org/10.1016/j.surfrep.2004.12.002.

[Kamenev11] A. Kamenev. *Field theory of non-equilibrium systems*. Cambridge University Press, 2011.

[Kamenev18] A. Kamenev. Near-field heat transfer between disordered conductors, 2018, arXiv:1811.10187.

[Karimi16] B. Karimi and J. P. Pekola. Otto refrigerator based on a superconducting qubit: Classical and quantum performance. *Phys. Rev. B*, 94:184503, Nov 2016, doi:10.1103/PhysRevB.94.184503.

[Karimi20] B. Karimi, F. Brange, P. Samuelsson, and J. P. Pekola. Reaching the ultimate energy resolution of a quantum detector. *Nature Communications*, 11(1):367, 2020, doi:10.1038/s41467-019-14247-2.

[Karimi21] B. Karimi and J. P. Pekola. Down-conversion of quantum fluctuations of photonic heat current in a circuit, 2021, arXiv:2104.09238.

[Kittel88] C. Kittel. Temperature fluctuation: an oxymoron. *Phys. Today*, 41(5):93, 1988.

[Kittel05] A. Kittel, W. Müller-Hirsch, J. Parisi, S.-A. Biehs, D. Reddig, and M. Holthaus. Near-field heat transfer in a scanning thermal microscope. *Phys. Rev. Lett.*, 95:224301, Nov 2005, doi:10.1103/PhysRevLett.95.224301.

[Kittel08] A. Kittel, U. F. Wischnath, J. Welker, O. Huth, F. Rüting, and S.-A. Biehs. Near-field thermal imaging of nanostructured surfaces. *Applied Physics Letters*, 93(19):193109, 2008, doi:10.1063/1.3025140.

[Kosloff14] R. Kosloff and A. Levy. Quantum heat engines and refrigerators: Continuous devices. *Annual Review of Physical Chemistry*, 65(1):365–393, 2014, doi:10.1146/annurev-physchem-040513-103724. PMID: 24689798.

[Kralik11] T. Kralik, P. Hanzelka, V. Musilova, A. Srnka, and M. Zobac. Cryogenic apparatus for study of near-field heat transfer. *Review of Scientific Instruments*, 82(5):055106, 2011, doi:10.1063/1.3585985.

[Kralik12] T. Kralik, P. Hanzelka, M. Zobac, V. Musilova, T. Fort, and M. Horak. Strong near-field enhancement of radiative heat transfer between metallic surfaces. *Phys. Rev. Lett.*, 109:224302, Nov 2012, doi:10.1103/PhysRevLett.109.224302.

[Kubo57a] R. Kubo. Statistical-mechanical theory of irreversible processes. i. general theory and simple applications to magnetic and conduction problems. *Journal of the Physical Society of Japan*, 12(6):570–586, 1957, doi:10.1143/JPSJ.12.570.

[Kubo57b] R. Kubo, M. Yokota, and S. Nakajima. Statistical-mechanical theory of irreversible processes. ii. response to thermal disturbance. *Journal of the Physical Society of Japan*, 12(11):1203–1211, 1957, doi:10.1143/JPSJ.12.1203.

[Kutner03] M. L. Kutner. *Astronomy: A physical perspective*. Cambridge University Press, 2003.

[Landau75] L. D. Landau and E. M. Lifshitz. *The Classical Theory of Fields*, volume 2 of *Course of Theoretical Physics*. Butterworth-Heinemann, 4 edition, Jan. 1975. URL `http://www.worldcat.org/isbn/0750627689`.

[Landau80] L. D. Landau and E. M. Lifshitz. *Statistical Physics*, volume 5 of *Course of Theoretical Physics*. Butterworth-Heinemann, 3 edition, Jan. 1980. URL `http://www.worldcat.org/isbn/0750633727`.

[Landau84] L. D. Landau, E. M. Lifshitz, and L. P. Pitaevskii. *Electrodynamics of continous media*, volume 8 of *Course of Theoretical Physics*. Butterworth-Heinemann, 1984.

[Landauer98] R. Landauer. The noise is the signal. *Nature*, 392(6677):658–659, 1998, doi:10.1038/33551.

[Laroche05] M. Laroche, C. Arnold, F. Marquier, R. Carminati, J.-J. Greffet, S. Collin, N. Bardou, and J.-L. Pelouard. Highly directional radiation generated by a tungsten thermal source. *Opt. Lett.*, 30(19):2623–2625, Oct 2005, doi:10.1364/OL.30.002623.

[Laroche06] M. Laroche, R. Carminati, and J.-J. Greffet. Near-field thermophotovoltaic energy conversion. *Journal of Applied Physics*, 100(6):063704, 2006, doi:10.1063/1.2234560.

[Lee85] P. A. Lee and T. V. Ramakrishnan. Disordered electronic systems. *Rev. Mod. Phys.*, 57:287–337, Apr 1985, doi:10.1103/RevModPhys.57.287.

[Levin80] M. L. Levin, V. G. Polevoi, and S. M. Rytov. Contribution to the theory of heat exchange due to a fluctuating electromagnetic field. *Sov. Phys. JETP*, 52(6):1054, December 1980.

[Lifshitz56] E. M. Lifshitz. The theory of molecular attractive forces between solids. *Sov. Phys. JETP*, 2(1):73, January 1956.

[Lifshitz81] E. M. Lifshitz and L. P. Pitaevskii. *Physical Kinetics*, volume 10 of *Course of Theoretical Physics*. Butterworth-Heinemann, Oxford, 1981. We remind here of the main regimes for the skin effect. If the bulk mean free path $\ell_{3D} \ll c/\omega_p$, where ω_p is the bulk plasma frequency, the skin depth δ can be found from the local 3D Drude conductivity $\sigma_{3\mathrm{D}}(\omega) = (4\pi)^{-1}\omega_p^2\tau/(1-i\omega\tau)$: $\delta \sim (c/\omega_p)/\sqrt{\omega\tau}$ for $\omega \ll 1/\tau$ and $\delta \sim c/\omega_p$ for $\omega \gg 1/\tau$. For a sufficiently clean metal with $\ell_{3\mathrm{D}} \gg c/\omega_p$, the above expressions for δ work for $\omega \ll (c/\omega_p\ell_{3\mathrm{D}})^2/\tau$ and $\omega \gg (v_F/c)\omega_p$, respectively, while in the interval $(c/\omega_p\ell_{3\mathrm{D}})^2/\tau \ll \omega \ll (v_F/c)\omega_p$ one has the anomalous skin effect with nonlocal response and $\delta \sim (c/\omega_p)^{2/3}(v_F/\omega)^{1/3}$.

[Liu05] Z.-W. Liu, Q.-H. Wei, and X. Zhang. Surface plasmon interference nanolithography. *Nano Letters*, 5(5):957–961, 2005, doi:10.1021/nl0506094. PMID: 15884902.

[Liu16] X. Liu and Z. M. Zhang. High-performance electroluminescent refrigeration enabled by photon tunneling. *Nano Energy*, 26:353–359, 2016, doi:https://doi.org/10.1016/j.nanoen.2016.05.049.

[Loomis94] J. J. Loomis and H. J. Maris. Theory of heat transfer by evanescent electromagnetic waves. *Phys. Rev. B*, 50:18517–18524, Dec 1994, doi:10.1103/PhysRevB.50.18517.

[Lucchesi19] C. Lucchesi, D. Cakiroglu, J. P. Perez, T. Taliercio, E. Tournié, P. O. Chapuis, and R. Vaillon. Harnessing near-field thermal photons with efficient photovoltaic conversion, 2019, arXiv:1912.09394.

[Lucchesi21] C. Lucchesi, R. Vaillon, and P.-O. Chapuis. Radiative heat transfer at the nanoscale: experimental trends and challenges. *Nanoscale Horiz.*, 6:201–208, 2021, doi:10.1039/D0NH00609B.

[Mahan17] G. D. Mahan. Tunneling of heat between metals. *Phys. Rev. B*, 95:115427, Mar 2017, doi:10.1103/PhysRevB.95.115427.

[Marquier04] F. Marquier, K. Joulain, J.-P. Mulet, R. Carminati, J.-J. Greffet, and Y. Chen. Coherent spontaneous emission of light by thermal sources. *Phys. Rev. B*, 69:155412, Apr 2004, doi:10.1103/PhysRevB.69.155412.

[Mermin70] N. D. Mermin. Lindhard dielectric function in the relaxation-time approximation. *Phys. Rev. B*, 1:2362–2363, Mar 1970, doi:10.1103/PhysRevB.1.2362.

[Meschke06] M. Meschke, W. Guichard, and J. P. Pekola. Single-mode heat conduction by photons. *Nature*, 444(7116):187–190, 2006, doi:10.1038/nature05276.

[Messina13] R. Messina and P. Ben-Abdallah. Graphene-based photovoltaic cells for near-field thermal energy conversion. *Scientific Reports*, 3(1):1383, 2013, doi:10.1038/srep01383.

[Mihaila11] B. Mihaila. Lindhard function of a d-dimensional fermi gas, 2011, 1111.5337.

[Modest13] M. F. Modest. *Radiative Heat Transfer*. Academic Press, San Diego, 2013.

[Mostepanenko97] V. M. Mostepanenko and N. N. Trunov. *The Casimir effect and its applications*. Oxford University Press, 1997.

[Mulet01a] J.-P. Mulet, K. Joulain, R. Carminati, and J.-J. Greffet. Comment on “radiative transfer over small distances from a heated metal”. *Opt. Lett.*, 26(8):480–481, Apr 2001, doi:10.1364/OL.26.000480.

[Mulet01b] J.-P. Mulet, K. Joulain, R. Carminati, and J.-J. Greffet. Nanoscale radiative heat transfer between a small particle and a plane surface. *Applied Physics Letters*, 78(19):2931–2933, 2001, doi:10.1063/1.1370118.

[Mulet02] J.-P. Mulet, K. Joulain, R. Carminati, and J.-J. Greffet. Enhanced radiative heat transfer at nanometric distances. *Microscale Thermophysical Engineering*, 6(3):209–222, 2002, doi:10.1080/10893950290053321.

[Müller-Hirsch99] W. Müller-Hirsch, A. Kraft, M. T. Hirsch, J. Parisi, and A. Kittel. Heat transfer in ultrahigh vacuum scanning thermal microscopy. *Journal of Vacuum Science & Technology A*, 17(4):1205–1210, 1999, doi:10.1116/1.581796.

[Muravev15] V. M. Muravev, P. A. Gusikhin, I. V. Andreev, and I. V. Kukushkin. Novel relativistic plasma excitations in a gated two-dimensional electron system. *Phys. Rev. Lett.*, 114:106805, Mar 2015, doi:10.1103/PhysRevLett.114.106805.

[Narayanaswamy08a] A. Narayanaswamy and G. Chen. Thermal near-field radiative transfer between two spheres. *Phys. Rev. B*, 77:075125, Feb 2008, doi:10.1103/PhysRevB.77.075125.

[Narayanaswamy08b] A. Narayanaswamy, S. Shen, and G. Chen. Near-field radiative heat transfer between a sphere and a substrate. *Phys. Rev. B*, 78:115303, Sep 2008, doi:10.1103/PhysRevB.78.115303.

[Ojanen07] T. Ojanen and T. T. Heikkilä. Photon heat transport in low-dimensional nanostructures. *Phys. Rev. B*, 76:073414, Aug 2007, doi:10.1103/PhysRevB.76.073414.

[Ojanen08] T. Ojanen and A.-P. Jauho. Mesoscopic photon heat transistor. *Phys. Rev. Lett.*, 100:155902, Apr 2008, doi:10.1103/PhysRevLett.100.155902.

[Olivei68] A. Olivei. Transfert d’énergie thermique rayonnante entre deux diélectriques aux très basses températures. *Rev. Phys. Appl. (Paris)*, 3(3):225–230, 1968, doi:10.1051/rphysap:0196800303022500.

[Ordal83] M. A. Ordal, L. L. Long, R. J. Bell, S. E. Bell, R. R. Bell, R. W. Alexander, and C. A. Ward. Optical properties of the metals al, co, cu, au, fe, pb, ni, pd, pt, ag, ti, and w in the infrared and far infrared. *Appl. Opt.*, 22(7):1099–1119, Apr 1983, doi:10.1364/AO.22.001099.

[Ordal85] M. A. Ordal, R. J. Bell, R. W. Alexander, L. L. Long, and M. R. Querry. Optical properties of fourteen metals in the infrared and far infrared: Al, co, cu, au, fe, pb, mo, ni, pd, pt, ag, ti, v, and w. *Appl. Opt.*, 24(24):4493–4499, Dec 1985, doi:10.1364/AO.24.004493.

[Oriekhov20] D. O. Oriekhov and L. S. Levitov. Plasmon resonances and tachyon ghost modes in highly conducting sheets. *Phys. Rev. B*, 101:245136, Jun 2020, doi:10.1103/PhysRevB.101.245136.

[Otey10] C. R. Otey, W. T. Lau, and S. Fan. Thermal rectification through vacuum. *Phys. Rev. Lett.*, 104:154301, Apr 2010, doi:10.1103/PhysRevLett.104.154301.

[Ottens11] R. S. Ottens, V. Quetschke, S. Wise, A. A. Alemi, R. Lundock, G. Mueller, D. H. Reitze, D. B. Tanner, and B. F. Whiting. Near-field radiative heat transfer between macroscopic planar surfaces. *Phys. Rev. Lett.*, 107:014301, Jun 2011, doi:10.1103/PhysRevLett.107.014301.

[Pan00] J. L. Pan. Radiative transfer over small distances from a heated metal. *Opt. Lett.*, 25(6):369–371, Mar 2000, doi:10.1364/OL.25.000369.

[Park08] K. Park, S. Basu, W. King, and Z. Zhang. Performance analysis of near-field thermophotovoltaic devices considering absorption distribution. *Journal of Quantitative Spectroscopy and Radiative Transfer*, 109(2):305–316, 2008, doi:https://doi.org/10.1016/j.jqsrt.2007.08.022. The Fifth International Symposium on Radiative Transfer.

[Pascal11] L. M. A. Pascal, H. Courtois, and F. W. J. Hekking. Circuit approach to photonic heat transport. *Phys. Rev. B*, 83:125113, Mar 2011, doi:10.1103/PhysRevB.83.125113.

[Pekola18] J. P. Pekola and B. Karimi. Quantum noise of electron–phonon heat current. *Journal of Low Temperature Physics*, 191(5):373–379, 2018, doi:10.1007/s10909-018-1854-y.

[Pekola21] J. P. Pekola and B. Karimi. Colloquium: Quantum heat transport in condensed matter systems, 2021, 2107.12936.

[Pendry83] J. B. Pendry. Quantum limits to the flow of information and entropy. *Journal of Physics A: Mathematical and General*, 16(10):2161–2171, jul 1983, doi:10.1088/0305-4470/16/10/012.

[Pendry99] J. B. Pendry. Radiative exchange of heat between nanostructures. *Journal of Physics: Condensed Matter*, 11(35):6621–6633, aug 1999, doi:10.1088/0953-8984/11/35/301.

[Planck00] M. Planck. On the theory of the energy distribution law of the normal spectrum. *Verh. Deut. Phys. Ges*, 2:237–245, 1900.

[Polder71] D. Polder and M. Van Hove. Theory of radiative heat transfer between closely spaced bodies. *Phys. Rev. B*, 4:3303–3314, Nov 1971, doi:10.1103/PhysRevB.4.3303.

[Prunnila13] M. Prunnila and S. J. Laakso. Interlayer heat transfer in bilayer carrier systems. *New Journal of Physics*, 15(3):033043, mar 2013, doi:10.1088/1367-2630/15/3/033043.

[Reina20] M. Reina, R. Messina, and P. Ben-Abdallah. Conduction-radiation coupling between two closely separated solids. *Phys. Rev. Lett.*, 125:224302, Nov 2020, doi:10.1103/PhysRevLett.125.224302.

[Rodriguez-López15] P. Rodriguez-López, W.-K. Tse, and D. A. R. Dalvit. Radiative heat transfer in 2d dirac materials. *Journal of Physics: Condensed Matter*, 27(21):214019, may 2015, doi:10.1088/0953-8984/27/21/214019.

[Ronzani18] A. Ronzani, B. Karimi, J. Senior, Y.-C. Chang, J. T. Peltonen, C. Chen, and J. P. Pekola. Tunable photonic heat transport in a quantum heat valve. *Nature Physics*, 14(10):991–995, 2018, doi:10.1038/s41567-018-0199-4.

[Roubinowitz21] N. Roubinowitz. Fluctuations of radiative heat transfer in a nanometric system. Master's thesis, École Normale Supérieure Paris-Saclay, July 2021. Internship carried out at LPMMC, Grenoble under the supervision of D. M. Basko and J. L. Wise.

[Rousseau09a] E. Rousseau, M. Laroche, and J.-J. Greffet. Radiative heat transfer at nanoscale mediated by surface plasmons for highly doped silicon. *Applied Physics Letters*, 95(23):231913, 2009, doi:10.1063/1.3271681.

[Rousseau09b] E. Rousseau, A. Siria, G. Jourdan, S. Volz, F. Comin, J. Chevrier, and J.-J. Greffet. Radiative heat transfer at the nanoscale. *Nature Photonics*, 3(9):514–517, 2009, doi:10.1038/nphoton.2009.144.

[Ruokola11] T. Ruokola and T. Ojanen. Thermal conductance in a spin-boson model: Cotunneling and low-temperature properties. *Phys. Rev. B*, 83:045417, Jan 2011, doi:10.1103/PhysRevB.83.045417.

[Rytov53] S. M. Rytov. *Theory of electric fluctuations and thermal radiation*. Air Force Cambrige Research Center, Bedford, MA, 1953.

[Rytov89] S. M. Rytov, Y. A. Kravtsov, and V. I. Tatarskii. *Principles of statistical radiophysics*. Springer-Verlag, Berlin Heidelberg, 1989.

[Sabbaghi20] P. Sabbaghi, L. Long, X. Ying, L. Lambert, S. Taylor, C. Messner, and L. Wang. Super-planckian radiative heat transfer between macroscale metallic surfaces due to near-field and thin-film effects. *Journal of Applied Physics*, 128(2):025305, 2020, doi:10.1063/5.0008259.

[Schmidt04] D. R. Schmidt, R. J. Schoelkopf, and A. N. Cleland. Photon-mediated thermal relaxation of electrons in nanostructures. *Phys. Rev. Lett.*, 93:045901, Jul 2004, doi:10.1103/PhysRevLett.93.045901.

[Senior20] J. Senior, A. Gubaydullin, B. Karimi, J. T. Peltonen, J. Ankerhold, and J. P. Pekola. Heat rectification via a superconducting artificial atom. *Communications Physics*, 3(1):40, 2020, doi:10.1038/s42005-020-0307-5.

[Shen09] S. Shen, A. Narayanaswamy, and G. Chen. Surface phonon polaritons mediated energy transfer between nanoscale gaps. *Nano Letters*, 9(8):2909–2913, 2009, doi:10.1021/nl901208v. PMID: 19719110.

[Soffar19] H. Soffar, Nov 2019. URL `https://www.online-sciences.com/the-energy`.

[Song15a] B. Song, A. Fiorino, E. Meyhofer, and P. Reddy. Near-field radiative thermal transport: From theory to experiment. *AIP Advances*, 5(5):053503, 2015, doi:10.1063/1.4919048.

[Song15b] B. Song, Y. Ganjeh, S. Sadat, D. Thompson, A. Fiorino, V. Fernández-Hurtado, J. Feist, F. J. Garcia-Vidal, J. C. Cuevas, P. Reddy, and E. Meyhofer. Enhancement of near-field radiative heat transfer using polar dielectric thin films. *Nature Nanotechnology*, 10(3):253–258, 2015, doi:10.1038/nnano.2015.6.

[Song16] B. Song, D. Thompson, A. Fiorino, Y. Ganjeh, P. Reddy, and E. Meyhofer. Radiative heat conductances between dielectric and metallic parallel plates with nanoscale gaps. *Nature Nanotechnology*, 11(6):509–514, 2016, doi:10.1038/nnano.2016.17.

[Song21] J. Song, Q. Cheng, B. Zhang, L. Lu, X. Zhou, Z. Luo, and R. Hu. Many-body near-field radiative heat transfer: methods, functionalities and applications. *Reports on Progress in Physics*, 84(3):036501, mar 2021, doi:10.1088/1361-6633/abe52b.

[St-Gelais14] R. St-Gelais, B. Guha, L. Zhu, S. Fan, and M. Lipson. Demonstration of strong near-field radiative heat transfer between integrated nanostructures. *Nano Letters*, 14(12):6971–6975, 2014, doi:10.1021/nl503236k. PMID: 25420115.

[St-Gelais16] R. St-Gelais, L. Zhu, S. Fan, and M. Lipson. Near-field radiative heat transfer between parallel structures in the deep subwavelength regime. *Nature Nanotechnology*, 11(6):515–519, 2016, doi:10.1038/nnano.2016.20.

[Stern67] F. Stern. Polarizability of a two-dimensional electron gas. *Phys. Rev. Lett.*, 18:546–548, Apr 1967, doi:10.1103/PhysRevLett.18.546.

[Svetovoy12] V. B. Svetovoy, P. J. van Zwol, and J. Chevrier. Plasmon enhanced near-field radiative heat transfer for graphene covered dielectrics. *Phys. Rev. B*, 85:155418, Apr 2012, doi:10.1103/PhysRevB.85.155418.

[Tang18] G. Tang and J.-S. Wang. Heat transfer statistics in extreme-near-field radiation. *Phys. Rev. B*, 98:125401, Sep 2018, doi:10.1103/PhysRevB.98.125401.

[Timofeev09] A. V. Timofeev, M. Helle, M. Meschke, M. Möttönen, and J. P. Pekola. Electronic refrigeration at the quantum limit. *Phys. Rev. Lett.*, 102:200801, May 2009, doi:10.1103/PhysRevLett.102.200801.

[van Zwol12a] P. J. van Zwol, L. Ranno, and J. Chevrier. Tuning near field radiative heat flux through surface excitations with a metal insulator transition. *Phys. Rev. Lett.*, 108:234301, Jun 2012, doi:10.1103/PhysRevLett.108.234301.

[van Zwol12b] P. J. van Zwol, S. Thiele, C. Berger, W. A. de Heer, and J. Chevrier. Nanoscale radiative heat flow due to surface plasmons in graphene and doped silicon. *Phys. Rev. Lett.*, 109:264301, Dec 2012, doi:10.1103/PhysRevLett.109.264301.

[Volkov14] V. A. Volkov and V. N. Pavlov. Radiative plasmon polaritons in multilayer structures with a two-dimensional electron gas. *JETP Letters*, 99(2):93–98, 2014, doi:10.1134/S0021364014020118.

[Volokitin01] A. I. Volokitin and B. N. J. Persson. Radiative heat transfer between nanostructures. *Phys. Rev. B*, 63:205404, Apr 2001, doi:10.1103/PhysRevB.63.205404.

[Volokitin07] A. I. Volokitin and B. N. J. Persson. Near-field radiative heat transfer and noncontact friction. *Rev. Mod. Phys.*, 79:1291–1329, Oct 2007, doi:10.1103/RevModPhys.79.1291.

[Wang06] L. Wang, S. M. Uppuluri, E. X. Jin, and X. Xu. Nanolithography using high transmission nanoscale bowtie apertures. *Nano Letters*, 6(3):361–364, 2006, doi:10.1021/nl052371p. PMID: 16522023.

[Wang18] J.-S. Wang, Z.-Q. Zhang, and J.-T. Lü. Coulomb-force-mediated heat transfer in the near field: Geometric effect. *Phys. Rev. E*, 98:012118, Jul 2018, doi:10.1103/PhysRevE.98.012118.

[Wang19] L. Wang, M. Bie, W. Cai, L. Ge, Z. Ji, Y. Jia, K. Gong, X. Zhang, J. Wang, and J. Xu. Giant near-field radiative heat transfer between ultrathin metallic films. *Opt. Express*, 27(25):36790–36798, Dec 2019, doi:10.1364/OE.27.036790.

[Wien96] W. Wien. Ueber die energievertheilung im emissionsspectrum eines schwarzen körpers. *Annalen der Physik*, 294(8):662–669, 1896, doi:https://doi.org/10.1002/andp.18962940803.

[Williams86] C. C. Williams and H. K. Wickramasinghe. Scanning thermal profiler. *Applied Physics Letters*, 49(23):1587–1589, 1986, doi:10.1063/1.97288.

[Xu94] J. B. Xu, K. Läuger, K. Dransfeld, and I. H. Wilson. Thermal sensors for investigation of heat transfer in scanning probe microscopy. *Review of Scientific Instruments*, 65(7):2262–2266, 1994, doi:10.1063/1.1145225.

[Xu21] M. Xu, J. T. Stockburger, and J. Ankerhold. Heat transport through a superconducting artificial atom. *Phys. Rev. B*, 103:104304, Mar 2021, doi:10.1103/PhysRevB.103.104304.

[Yamamoto18] T. Yamamoto, M. Kato, T. Kato, and K. Saito. Heat transport via a local two-state system near thermal equilibrium. *New Journal of Physics*, 20(9):093014, sep 2018, doi:10.1088/1367-2630/aadf09.

[Yang13] Y. Yang, S. Basu, and L. Wang. Radiation-based near-field thermal rectification with phase transition materials. *Applied Physics Letters*, 103(16):163101, 2013, doi:10.1063/1.4825168.

[Yang18] J. Yang, W. Du, Y. Su, Y. Fu, S. Gong, S. He, and Y. Ma. Observing of the super-planckian near-field thermal radiation between graphene sheets. *Nature Communications*, 9(1):4033, 2018, doi:10.1038/s41467-018-06163-8.

[Ying20] X. Ying and A. Kamenev. Plasmonic tuning of near-field heat transfer between graphene monolayers. *Phys. Rev. B*, 102:195426, Nov 2020, doi:10.1103/PhysRevB.102.195426.

[Yu17] R. Yu, A. Manjavacas, and F. J. García de Abajo. Ultrafast radiative heat transfer. *Nature Communications*, 8(1):2, 2017, doi:10.1038/s41467-016-0013-x.

[Zala01] G. Zala, B. N. Narozhny, and I. L. Aleiner. Interaction corrections at intermediate temperatures: Longitudinal conductivity and kinetic equation. *Phys. Rev. B*, 64:214204, Nov 2001, doi:10.1103/PhysRevB.64.214204.

[Zhang18] Z.-Q. Zhang, J.-T. Lü, and J.-S. Wang. Energy transfer between two vacuum-gapped metal plates: Coulomb fluctuations and electron tunneling. *Phys. Rev. B*, 97:195450, May 2018, doi:10.1103/PhysRevB.97.195450.

[Zhang19] W. B. Zhang, C. Y. Zhao, and B. X. Wang. Enhancing near-field heat transfer between composite structures through strongly coupled surface modes. *Phys. Rev. B*, 100:075425, Aug 2019, doi:10.1103/PhysRevB.100.075425.

[Zhao17] B. Zhao, B. Guizal, Z. M. Zhang, S. Fan, and M. Antezza. Near-field heat transfer between graphene/hbn multilayers. *Phys. Rev. B*, 95:245437, Jun 2017, doi:10.1103/PhysRevB.95.245437.

A

Derivation of asymptotic expressions for the radiative heat transfer between two-dimensional metallic layers

Contents

Here we derive asymptotic expressions for $J(T)$ of Eq. (2.8) for the average radiative heat current per unit area between two-dimensional metallic sheets modelled by Drude conductivity. We treat the specific case of identical sheets embedded in vacuum $[\sigma_1(\omega) = \sigma_2(\omega)$ and $\varepsilon = 1]$ and compute separately the travelling and evanescent wave contributions for each of the two polarisations. We quantify the contribution made by each wave type and polarisation in each region of the $(1/d, T)$ parameter plane, before comparing the size of the additive contributions and identifying which are dominant. It is convenient to introduce the dimensionless parameters $x \equiv c\tau/d$ and $y \equiv T\tau/\hbar$, as well as dimensionless integration variables: $\xi = |q_z|c\tau$ instead of k [noting that $k\,dk = \xi\, d\xi/(c\tau)^2$], and $\eta = \omega\tau$. For the travelling waves, the integration is over the region $0 < \xi < \eta < \infty$, while for the evanescent waves it is $0 < \xi, \eta < \infty$.

A.1 TM travelling contribution

In the dimensionless variables, the TM travelling contribution to Eq. (2.8) can be rewritten exactly as

$$J_{\mathrm{TM}}^{\mathrm{t}} = \frac{\hbar \mathcal{G}^2}{\pi^2 c^2 \tau^4} \int_0^\infty \frac{\eta^3\, d\eta}{e^{\eta/y} - 1} \int_0^\eta \frac{\xi^3\, d\xi}{D_+^p D_-^p}, \tag{A.1a}$$

$$D_\pm^p \equiv |\eta(1 - i\eta) + \mathcal{G}\xi(1 \pm e^{i\xi/x})|^2. \tag{A.1b}$$

The case $\mathcal{G} \ll 1$ is very simple to handle, since for $\varepsilon = 1$ one can neglect the reflection coefficients in the denominator of Eq. (2.8), and simply set $\mathcal{G} \to 0$ in Eq. (A.1b), since $\xi < \eta$. This gives

$$\begin{aligned} J_{\mathrm{TM}}^{\mathrm{t}} &= \frac{\hbar \sigma_{2\mathrm{D}}^2}{c^4 \tau^4} \int_0^\infty \frac{\eta^3\, d\eta}{(1+\eta^2)^2 (e^{\eta/y} - 1)} \\ &= \begin{cases} \pi^2 \mathcal{G}^2 T^4/(60\hbar^3 c^2), & y \ll 1, \\ \mathcal{G}^2 T/(16\pi c^2 \tau^3), & y \gg 1. \end{cases} \end{aligned} \tag{A.2}$$

For $\mathcal{G} \gg 1$, each layer behaves at low frequency as a well-reflecting mirror, so the structure may host Fabry-Perot modes. The Fabry-Perot modes manifest themselves as deep minima in $D_\pm^p$ at specific values of $\xi/x = \pi, 2\pi, 3\pi, \ldots$. These minima are important when $\mathcal{G}\xi \gg \eta\sqrt{1+\eta^2}$, which is precisely the condition of good reflection. Thus, a much more elaborate analysis is needed to evaluate the integral.

Let us focus on the contributions from the region $\xi \gg x$, when many modes contribute, and even if they are overdamped, $e^{i\xi/x}$ oscillates fast. In the general case (2.8) we average over the fast oscillations in the denominator which leads to the simple replacement [Fu06]:

$$\frac{a_{1j} a_{2j}}{\left|1 - r_{1j} r_{2j} e^{2iq_z d}\right|^2} \to \frac{a_{1j} a_{2j}}{1 - \left|r_{1j}\right|^2 \left|r_{2j}\right|^2}, \tag{A.3}$$

valid as long as $a_{\alpha j}$ and $r_{\alpha j}$ are smooth functions of q_z on the scale $q_z \sim 1/d$.

Applying this averaging to the contribution in Eq. (A.1a) leads to

$$J^{\mathrm{t}}_{\mathrm{TM}}=\frac{\hbar\mathcal{G}^2}{\pi^2c^2\tau^4}\int_0^\infty\frac{\eta^3\,d\eta}{e^{\eta/y}-1}\int_0^\eta\frac{\xi^3\,d\xi}{[\eta^2+\eta^4+2\mathcal{G}\xi\eta+2(\mathcal{G}\xi)^2][\eta^2+\eta^4+2\mathcal{G}\xi\eta]}. \tag{A.4}$$

Note that x dropped out, and enters only through the condition $\xi\gg x$. Note also that the ξ integral is always determined by the upper limit $\xi\sim\eta$. As for the η integral, it may converge at $\eta\sim y$ when cut off by the Bose function, or, for too large y, it may be cut off by other factors in the denominator at some $\eta\ll y$. In this latter case, one can expand the exponential in the Bose function, which becomes just y/η. We can identify three regions in y.

(i) For $y\ll\sqrt{\mathcal{G}}$, the integrals separate and converge at $\xi\sim\eta\sim y$, so the fast oscillation condition is $x\ll y$:

$$J^{\mathrm{t}}_{\mathrm{TM}}=\frac{\hbar\mathcal{G}^2}{\pi^2c^2\tau^4}\int_0^\infty\frac{\eta^3\,d\eta}{e^{\eta/y}-1}\int_0^\eta\frac{\xi^3\,d\xi}{4(\mathcal{G}\xi)^3\eta}=\frac{\pi^2T^4}{60\hbar^3c^2\mathcal{G}}. \tag{A.5}$$

(ii) For $\sqrt{\mathcal{G}}\ll y\ll\mathcal{G}$, we keep $2(\mathcal{G}\xi)^2$ in the first bracket and η^4 in the second one (again, oscillations are fast when $x\ll y$):

$$J^{\mathrm{t}}_{\mathrm{TM}}=\frac{\hbar\mathcal{G}^2}{\pi^2c^2\tau^4}\int_0^\infty\frac{\eta^3\,d\eta}{e^{\eta/y}-1}\int_0^\eta\frac{\xi^3\,d\xi}{2(\mathcal{G}\xi)^2\eta^4}=\frac{T^2}{24\hbar c^2\tau^2}. \tag{A.6}$$

(iii) For $y\gg\mathcal{G}$, we expand the Bose function, the integral converges at $\eta\sim\mathcal{G}$ (it is convenient to write $\xi=u\eta$); the oscillations are fast when $x\ll\mathcal{G}$:

$$J^{\mathrm{t}}_{\mathrm{TM}}=\frac{\hbar\mathcal{G}^2}{\pi^2c^2\tau^4}\int_0^\infty y\eta^2\,d\eta\int_0^1\frac{\eta^4u^3\,du}{[\eta^4+2(\mathcal{G}\eta)^2u^2]\eta^4}=\frac{\sqrt{2}\mathcal{G}T}{12\pi c^2\tau^3}. \tag{A.7}$$

Let us now pick the contributions from $\xi\ll x$. Then, $e^{i\xi/x}$ can be expanded (we again write $\xi=u\eta$):

$$J^{\mathrm{t}}_{\mathrm{TM}}=\frac{\hbar\mathcal{G}^2}{\pi^2c^2\tau^4}\int_0^\infty\frac{\eta^3\,d\eta}{e^{\eta/y}-1}\int_0^1\frac{u^3\,du}{[(1+2\mathcal{G}u)^2+\eta^2][1+\eta^2(1+\mathcal{G}u^2/x)^2]}. \tag{A.8}$$

There are three possible cutoff scales for η: y, $1+2\mathcal{G}u$, and $(1+\mathcal{G}u^2/x)^{-1}$. Which one of the three is effective, depends on the positioning of y with repect to other scales. Again, three cases arise.

(iv) For $y\ll1$, we can neglect η^2 in the first bracket in the denominator, so the η integral converges at $\eta\sim y$. In the second bracket, η^2 plays a role only if $\mathcal{G}u^2/x\gg1$, so the second bracket can be approximated as $1+(\mathcal{G}u^2\eta/x)^2$ for any $\mathcal{G}u^2/x$. We also assume that $\mathcal{G}u\gg1$, which will be verified afterwards. Then the denominator becomes $4\mathcal{G}^2u^2[1+$

$(\mathcal{G}u^2\eta/x)^2]$, so the u integral converges at $u \sim \min\{1, \sqrt{x/(\mathcal{G}y)}\}$, giving

$$J^{\mathrm{t}}_{\mathrm{TM}} = \frac{\hbar}{8\pi^2\mathcal{G}c\tau^3 d}\int_0^\infty \frac{\eta^2\,d\eta}{e^{\eta/y}-1}\arctan\frac{\mathcal{G}\eta}{x} = \begin{cases} \pi^2T^4/(120\hbar^3c^2), & y \ll x/\mathcal{G}, \\ \zeta(3)\,T^3/(8\pi\hbar^2c\mathcal{G}d), & y \gg x/\mathcal{G}. \end{cases} \tag{A.9}$$

The u integral converges at $u \sim 1$ and $u \sim \sqrt{x/(\mathcal{G}y)}$ in the two cases. In the first case, $y \ll x/\mathcal{G}$, the assumption $\mathcal{G}u \gg 1$, as well as the condition to expand the exponential, $uy/x \ll 1$, are satisfied automatically. In the second case, $y \gg x/\mathcal{G}$, both conditions translate into $y \ll \mathcal{G}x$.
(v) For $y \gg 1$ but $y \ll \mathcal{G}u$ we still have $\eta \sim y$, so the denominator can be approximated as $4\mathcal{G}u^2\eta^2(1+\mathcal{G}u^2/x)^2$:

$$J^{\mathrm{t}}_{\mathrm{TM}} = \frac{\hbar}{4\pi^2c^2\tau^4}\int_0^\infty \frac{\eta\,d\eta}{e^{\eta/y}-1}\int_0^1 \frac{u\,du}{[1+(\mathcal{G}/x)u^2]^2} = \frac{T^2/\hbar}{48c\tau(c\tau+\mathcal{G}d)}. \tag{A.10}$$

Since the convergence occurs at $u \sim \min\{1, \sqrt{x/\mathcal{G}}\}$, $\eta \sim y$, the assumption $y \ll \mathcal{G}u$ is satisfied if $y \ll \min\{\sqrt{\mathcal{G}x}, \mathcal{G}\}$; if so, the condition $uy/x \ll 1$ to expand the exponential is satisfied automatically. Thus, Eq. (A.10) is valid when $1 \ll y \ll \min\{\sqrt{\mathcal{G}x}, \mathcal{G}\}$.
(vi) For $y \gg 1, \mathcal{G}u$, the Bose function is y/η, so we integrate over η exactly (convergence at $\eta \sim 1+2\mathcal{G}u$), and obtain

$$J^{\mathrm{t}}_{\mathrm{TM}} = \frac{\mathcal{G}^2T}{2\pi c^2\tau^3}\int_0^1 \frac{u^3\,du}{(1+2\mathcal{G}u)[1+(\mathcal{G}/x)u^2]^2} = \begin{cases} Tx^{3/2}/(16c^2\tau^3\mathcal{G}^{1/2}), & x \ll \mathcal{G}, \\ \mathcal{G}T/(12\pi c^2\tau^3), & x \gg \mathcal{G}, \end{cases} \tag{A.11}$$

the convergence occurring at $u \sim \min\{\sqrt{x/\mathcal{G}}, 1\}$. At $x \ll \mathcal{G}$ the condition to expand $e^{i\xi/x}$ is not fulfilled, since we automatically have $\xi/x = u\eta/x \sim 1$. At $x \gg \mathcal{G}$, we have $\mathcal{G}u \gg 1$ automatically, while $u\eta/x \sim \mathcal{G}/x$, so the second expression Eq. (A.11) is valid at $x, y \gg \mathcal{G}$.

We schematically show the regions of validity of Eqs. (A.5)–(A.11) in the (x,y) plane in Fig. A.1(a). In the overlapping region at $y \gg x$ both $\xi \ll x$ and $\xi \gg x$ contributions are valid, but the Fabry-Perot contributions from $\xi \gg x$ naturally dominate. At $y \ll x$ the Fabry-Perot contributions are suppressed as $e^{-\pi x/y} = e^{-\pi\hbar c/(Td)}$, since the temperature is lower than the first Fabry-Perot mode energy $\pi\hbar c/d$. Nevertheless, it turns out that the prefactor in front of the exponential is large, so the contribution from the first mode (the one with the weakest exponential), coming from the narrow region around $\xi = \eta = \pi x$ [see Fig. A.1(b)] should be included together with the contribution from $\xi \ll x$, as long as $x, y \ll \mathcal{G}$ (otherwise, the mode is overdamped because of low reflectivity).

To pick up the first Fabry-Perot mode contribution, we approximate the Bose function by $e^{-\eta/y}$ and set $\eta = \pi x$ everywhere else in the integrand, which is a smooth function of η. We also set $\xi = \pi x$ everywhere in the integrand except the exponential $e^{i\xi/x}$ in D^p_+

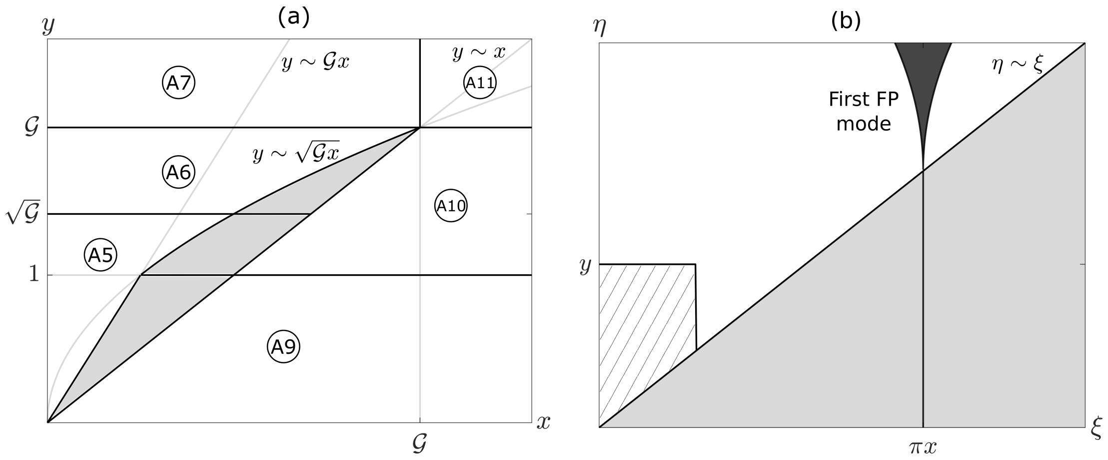

Figure A.1: (a) Regions of validity of Eqs. (A.5)–(A.11) in the (x, y) plane. In the shaded regions there are two valid contributions. (b) The (ξ, η) plane with the integration domain $\xi < \eta$ (the lightly shaded area does not belong to the integration domain). The hatched area at $\xi \ll x$ contributes to Eqs. (A.9), (A.10).

[Eq. (A.1b)]. Then we find the minimum of D_+^p as a function of ξ, reached at $\xi_{\min} = \pi x(1 - x/\mathcal{G}) + O(x^3/\mathcal{G}^2)$, and approximate near the minimum

$$
\begin{aligned}
D_+^p &= (\pi \mathcal{G} x)^2 \left| \frac{1 - i\pi x}{\mathcal{G}} + 1 + e^{i\xi/x} \right|^2 \\
&\approx (\pi x)^2 \left(1 + \frac{\pi^2 x^2}{2\mathcal{G}}\right)^2 + (\pi \mathcal{G})^2 (\xi - \xi_{\min})^2 .
\end{aligned}
\tag{A.12}
$$

Then, the integration over $\pi x < \eta < \infty$ and $-\infty < \xi - \xi_{\min} < \infty$ gives

$$
J_{\mathrm{TM}}^{\mathrm{t}} = \frac{\pi c T}{2d^3[2\mathcal{G} + (\pi c \tau/d)^2]} e^{-\pi \hbar c/(Td)} . \tag{A.13}
$$

A.2 TE travelling contribution

The TE travelling contribution to Eq. (2.8) can be rewritten exactly as

$$
J_{\mathrm{TE}}^{\mathrm{t}} = \frac{\hbar \mathcal{G}^2}{\pi^2 c^2 \tau^4} \int_0^\infty \frac{\eta^3 \, d\eta}{e^{\eta/y} - 1} \int_0^\eta \frac{\xi^3 \, d\xi}{D_+^s D_-^s} , \tag{A.14a}
$$

$$
D_\pm^s \equiv |\xi(1 - i\eta) + \mathcal{G}\eta(1 \pm e^{i\xi/x})|^2 . \tag{A.14b}
$$

For $\mathcal{G} \ll 1$, we may not simply set $\mathcal{G} \to 0$ in the denominator, as we did in the TM case: here this leads to a logarithmic divergence at $\xi \to 0$. To see how the divergence is cut off, we note that convergence scale of the η integral is the same as in the TM case: $\eta \sim y$ if $y \ll 1$ and $\eta \sim 1$ if $y \gg 1$. This gives the small-ξ cutoff scales $\xi \sim \mathcal{G}\eta$ and $\xi \sim \mathcal{G}$, respectively. As a result,

$$J^{\mathrm{t}}_{\mathrm{TE}} = \frac{\hbar\mathcal{G}^2}{\pi^2 c^2 \tau^4} \int_0^\infty \frac{\eta^3\, d\eta}{(1+\eta^2)^2 (e^{\eta/y}-1)} \ln \frac{\eta}{\min\{\mathcal{G}, \mathcal{G}\eta\}}$$
$$= \begin{cases} [(\pi^2\mathcal{G}^2T^4)/(15\hbar^3c^2)]\ln(1/\mathcal{G}), & y \ll 1, \\ [(\mathcal{G}^2T)/(4\pi c^2\tau^3)]\ln[(T\tau)/(\mathcal{G}\hbar)], & y \gg 1, \end{cases} \tag{A.15}$$

The overall map of behaviours in parameter space is therefore equivalent to the TM travelling case given in Eq. (A.2), but the TE contribution (A.15) is always dominant due to the logarithmic factors.

The calculation for $\mathcal{G} \gg 1$ is very similar to that of the TM travelling wave contribution. Focusing firstly on the cases where $\xi \gg x$ so the exponentials $e^{i\xi/x}$ oscillate fast, the averaged contribution from Eq. (A.14a) via Eq. (A.3) is given by

$$J^{\mathrm{t}}_{\mathrm{TE}} = \frac{\hbar\mathcal{G}^2}{\pi^2 c^2 \tau^4} \int_0^\infty \frac{\eta^3\, d\eta}{e^{\eta/y}-1} \int_0^\eta \frac{\xi^2\, d\xi}{\xi\,(\eta^2+1)+2\mathcal{G}\eta} \frac{1}{\xi^2\,(\eta^2+1)+2\mathcal{G}\xi\eta+2\,(\mathcal{G}\eta)^2}. \tag{A.16}$$

At low frequency the system Fabry-Perot modes are indicated, as in the TM case, in the minima in $D^s_\pm$, this time important when $\mathcal{G}\eta \gg \xi\sqrt{1+\eta^2}$. The integral in η may again converge at $\eta \sim y$ due to the Bose function, or something else if y is too large. We may identify the same regions as in the TM case.

(i) For $y \ll \sqrt{\mathcal{G}}$, we have that $\xi \sim \eta \sim y$, so the fast oscillation condition is $x \ll y$, and we may neglect all terms in the denominator containing ξ:

$$J^{\mathrm{t}}_{\mathrm{TM}} = \frac{\hbar\mathcal{G}^2}{\pi^2 c^2 \tau^4} \int_0^\infty \frac{\eta^3\, d\eta}{e^{\eta/y}-1} \int_0^\eta \frac{\xi^2\, d\xi}{4(\mathcal{G}\eta)^3} = \frac{\pi^2 T^4}{180\hbar^3c^2\mathcal{G}}. \tag{A.17}$$

(ii) For $\sqrt{\mathcal{G}} \ll y \ll \mathcal{G}$, we keep $\xi\eta^2$ in the denominator in the first line of Eq. (A.16) and $2\,(\mathcal{G}\eta)^2$ in the second line (again, oscillations are fast when $x \ll y$):

$$J^{\mathrm{t}}_{\mathrm{TE}} = \frac{\hbar\mathcal{G}^2}{\pi^2 c^2 \tau^4} \int_0^\infty \frac{\eta^3\, d\eta}{e^{\eta/y}-1} \int_0^\eta \frac{\xi^3\, d\xi}{2(\mathcal{G}\xi)^2\eta^4} = \frac{T^2}{24\hbar c^2\tau^2}. \tag{A.18}$$

(iii) For $y \gg \mathcal{G}$, we expand the Bose function to give y/η and retain $\xi\eta^2$ in the first line of Eq. (A.16) and $(\xi\eta)^2+2\,(\mathcal{G}\eta)^2$ in the second. The integrals converge at $\xi, \eta \sim \mathcal{G}$ so the oscillations are fast when $x \ll \mathcal{G}$:

$$J^{\mathrm{t}}_{\mathrm{TE}} = \frac{\hbar\mathcal{G}^2}{\pi^2 c^2 \tau^4} \int_0^\infty y\eta^2\, d\eta \int_0^\eta \frac{\xi\, d\xi}{(\xi^2+2\mathcal{G}^2)\eta^4} = \frac{\sqrt{2}\mathcal{G}T}{4\pi c^2\tau^3}. \tag{A.19}$$

For the contributions coming from $\xi \ll x$, we expand the exponential $e^{i\xi/x}$:

$$J^{\mathrm{t}}_{\mathrm{TE}} = \frac{\hbar\mathcal{G}^2}{\pi^2 c^2 \tau^4} \int_0^\infty \frac{\eta^3\, d\eta}{e^{\eta/y}-1} \frac{1}{1+\eta^2(1+\mathcal{G}/x)^2} \int_0^\eta \frac{\xi\, d\xi}{(\xi+2\mathcal{G}\eta)^2+\xi^2\eta^2}. \tag{A.20}$$

Since $\xi < \eta$ and $\mathcal{G} \gg 1$ we may neglect ξ in the first bracket of the denominator in the last line. This allows the simple integration over ξ:

$$J^{\mathrm{t}}_{\mathrm{TE}} = \frac{\hbar \mathcal{G}^2}{2\pi^2 c^2 \tau^4} \int_0^\infty \frac{\eta\, d\eta}{e^{\eta/y}-1} \frac{\ln[1+\eta^2/(2\mathcal{G})^2]}{1+\eta^2(1+\mathcal{G}/x)^2}, \tag{A.21}$$

the condition for the expansion of the exponential $e^{i\xi/x}$ becoming $\eta \ll x$.

There are three possible cutoff scales for η: y, $\mathcal{G}$, and $(1+\mathcal{G}/x)^{-1}$. Which one of the three is effective, depends on the positioning of y with repect to other scales. Again, three cases arise.

(iv) For $y \ll (1+\mathcal{G}/x)^{-1} < 1$, the logarithm is expanded for small argument and the second term in the denominator is neglected since the integral converges at $\eta \sim y$. The condition $y \ll x$ for the expansion of $e^{i\xi/x}$ is satisfied automatically:

$$J^{\mathrm{t}}_{\mathrm{TE}} = \frac{\hbar}{8\pi^2 c^2 \tau^4} \int_0^\infty \frac{\eta^3\, d\eta}{e^{\eta/y}-1} = \frac{\pi^2 T^4}{120\hbar^3 c^2}. \tag{A.22}$$

(v) For $(1+\mathcal{G}/x)^{-1} \ll y \ll \mathcal{G}$, the integral is still determined by $\eta \sim y$, but the second term in the denominator dominates. $e^{i\xi/x}$ may be expanded when $y \ll x$:

$$J^{\mathrm{t}}_{\mathrm{TE}} = \frac{\hbar}{8\pi^2 c^2 \tau^4} \frac{x^2}{(x+\mathcal{G})^2} \int_0^\infty \frac{\eta^3\, d\eta}{e^{\eta/y}-1} = \frac{T^2/\hbar}{48\,(c\tau+\mathcal{G}d)^2}. \tag{A.23}$$

(vi) For $y \gg \mathcal{G}$, the Bose function is y/η and the integral converges at $\eta \sim \mathcal{G}$ so we retain the logarithm, and $e^{i\xi/x}$ may be expanded as long as $\mathcal{G} \ll x$:

$$J^{\mathrm{t}}_{\mathrm{TE}} = \frac{\mathcal{G}^2 T\tau}{2\pi^2 c^2 \tau^4} \frac{x^2}{(x+\mathcal{G})^2} \int\limits_0^\infty \frac{d\eta}{\eta^2} \ln\left(1+\frac{\eta^2}{4\mathcal{G}^2}\right) = \frac{\mathcal{G}T}{4\pi c^2 \tau^3}. \tag{A.24}$$

We schematically show the regions of validity of Eqs. (A.17)–(A.24) for $\mathcal{G} \gg 1$ in the (x,y) plane in Fig. A.2, where there is no such overlap as in the TM case Fig. A.1(a).

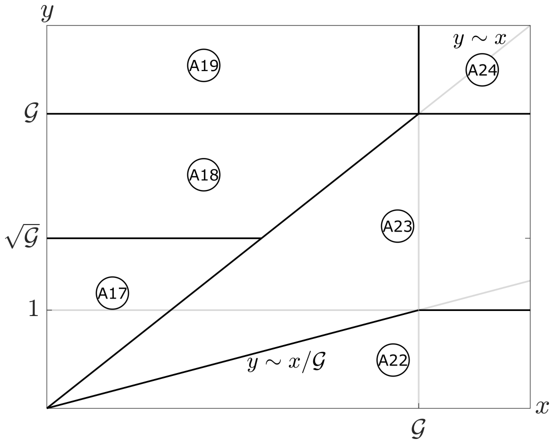

Figure A.2: Regions of validity of Eqs. (A.17)–(A.24) in the (x,y) plane.

As in the TM case, the first Fabry-Perot mode contribution should be included together with the $\xi \ll x$ contributions as long as $x, y \ll \mathcal{G}$. The same procedure is performed whereby the minimum of D^s_+ [Eq. (A.14b)] near $\xi = \pi x$ is found, allowing the integrand to be approximated by a Lorentzian. The minimum and therefore the eventual contribution is found to be identical to the TM case, Eq. (A.13).

A.3 TE evanescent contribution

The TE evanescent contribution to Eq. (2.8) can be rewritten exactly as

$$J^{\mathrm{e}}_{\mathrm{TE}} = \frac{\hbar \mathcal{G}^2}{\pi^2 c^2 \tau^4} \int_0^\infty \frac{\eta^3\, d\eta}{e^{\eta/y} - 1} \int_0^\infty \frac{e^{-2\xi/x} \xi^3\, d\xi}{\tilde{D}^s_+ \tilde{D}^s_-}, \tag{A.25a}$$

$$\tilde{D}^s_\pm \equiv |i\xi(1 - i\eta) + \mathcal{G}\eta(1 \pm e^{-\xi/x})|^2. \tag{A.25b}$$

Despite the apparent similarity to the corresponding TE travelling contribution Eq. (A.14a), there is no longer oscillatory behaviour in the denominator, so the resulting contributions are completely different. In η there are two possible decay scales: $\eta \sim y$ from the Bose function, and $\eta \sim \xi/(\mathcal{G} + \xi)$ from $\tilde{D}^s_+ \tilde{D}^s_-$.

In the low temperature case $y \ll \xi/(\mathcal{G} + \xi) < 1$ where the temperature cutoff is effective, expanding $e^{-\xi/x} \approx 1$ leads to logarithmic divergence at $\xi \to \infty$. The large ξ cutoff scale is therefore given by the decay scale of the exponential, $\xi \sim x$, leading to the result [valid for $y \ll x/(\mathcal{G} + x)$]:

$$J^{\mathrm{e}}_{\mathrm{TE}} = \frac{\hbar \mathcal{G}^2}{\pi^2 c^2 \tau^4} \int\limits_0^\infty \frac{\eta^3\, d\eta}{e^{\eta/y} - 1} \ln \frac{x}{\mathcal{G}\eta} = \frac{\pi^2 \mathcal{G}^2 T^4}{15 \hbar^3 c^2} \ln \frac{\hbar c}{\mathcal{G} T d}. \tag{A.26}$$

For high temperatures $y \gg \xi/(\mathcal{G} + \xi)$ the Bose function is y/η and it is convenient to perform integration over η first keeping $\tilde{D}^s_\pm$ exact:

$$J^{\mathrm{e}}_{\mathrm{TE}} = \frac{\mathcal{G}^2 T}{4\pi c^2 \tau^3} \int\limits_0^\infty \frac{e^{-2\xi/x} \xi^2\, d\xi}{(\mathcal{G} + \xi)[(\mathcal{G} + \xi)^2 - \mathcal{G}^2 e^{-2\xi/x})]}, \tag{A.27}$$

where the integrand may decay due to the exponential or the denominator. If $x \ll \mathcal{G}$ the exponential is clearly active and terms in ξ may be neglected in the denominator (the expansion of the Bose function is valid for $y \gg x/\mathcal{G}$):

$$J^{\mathrm{e}}_{\mathrm{TE}} = \frac{T}{4\pi^2 \mathcal{G} c^2 \tau^3} \int_0^\infty \frac{\xi^2\, d\xi}{e^{2\xi/x} - 1} = \frac{\zeta(3) c T}{16\pi \mathcal{G} d^3}. \tag{A.28}$$

If $x \gg \mathcal{G}$, expansion of $e^{-\xi/x} \approx 1$ in Eq. (A.27) again leads to logarithmic divergence at $\xi \to \infty$. As in the low temperature case, the divergence is cut off by $\xi \sim x$ (the expansion of the Bose function is valid for $y \gg 1$):

$$J^{\mathrm{e}}_{\mathrm{TE}} = \frac{\mathcal{G}^2 T}{4\pi c^2 \tau^3} \int_0^{\sim x} \frac{\xi\, d\xi}{(\xi + \mathcal{G})(\xi + 2\mathcal{G})} = \frac{\mathcal{G}^2 T}{4\pi c^2 \tau^3} \ln \frac{c\tau}{\mathcal{G} d}. \tag{A.29}$$

The domains of validity of the TE evanescent contributions are shown in Fig. A.3.

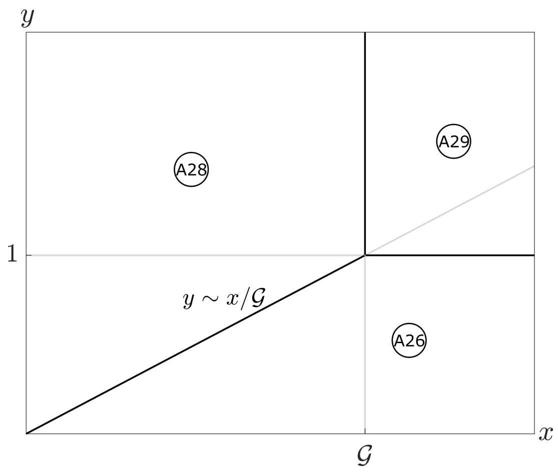

Figure A.3: Regions of validity of Eqs. (A.26)–(A.29) in the (x,y) plane.

A.4 TM evanescent contribution and approximate evaluation of the Caroli formula

On the one hand, the TM evanescent contribution to Eq. (2.8) can be rewritten exactly as

$$J^{\mathrm{e}}_{\mathrm{TM}} = \frac{\hbar\mathcal{G}^2}{\pi^2 c^2 \tau^4} \int_0^\infty \frac{\eta^3\, d\eta}{e^{\eta/y}-1} \int_0^\infty \frac{e^{-2\xi/x}\xi^3\, d\xi}{\tilde{D}^p_+ \tilde{D}^p_-}, \tag{A.30a}$$

$$\tilde{D}^p_\pm \equiv |\eta(1-i\eta) + i\mathcal{G}\xi(1\pm e^{-\xi/x})|^2. \tag{A.30b}$$

On the other hand, from the Caroli formula Eq. (3.1) for the radiative heat transfer between identical two-dimensional layers in the Coulomb limit, we have the expression

$$J(T) = \int_0^\infty \frac{d\omega}{\pi} \int \frac{d^2\mathbf{k}}{(2\pi)^2} \frac{\hbar\omega}{e^{\hbar\omega/T}-1} \mathcal{T}(\mathbf{k},\omega), \tag{A.31a}$$

$$\mathcal{T}(\mathbf{k},\omega) = 2\left|\frac{\operatorname{Im}\Pi\, v_k e^{-kd}}{[1-\Pi v_k(1-e^{-kd})][1-\Pi v_k(1+e^{-kd})]}\right|^2, \tag{A.31b}$$

where the transmission coefficient $\mathcal{T}(\mathbf{k},\omega)$ is given in terms of the bare 2D Coulomb potential, $v_{\mathbf{k}} = 2\pi e^2/k$, and the density response function of the layers, $\Pi(\mathbf{k},\omega)$. The density response function is related to the in-plane material conductivity via the general relation $\Pi(\mathbf{k},\omega) = (k^2/i\omega e^2)\sigma(\mathbf{k},\omega)$. Taking Drude conductivity $\sigma(\mathbf{k},\omega) = \sigma(\omega) = (\kappa D/2\pi)/(1-i\omega\tau)$ we see that the two expressions (A.30) and (A.31) coincide exactly. For the TM evanescent contribution in Ch. 2 we seek to evaluate the expression using the local Drude conductivity, while for the Coulomb limit calculation of Ch. 3 we employ a richer model for the material response that includes spatial dispersion [given in Eq. (3.4)]. We include here, therefore, the approximate evaluation of the integral in the more general case using the nonlocal model, in the knowledge that the contributions that are not influenced by the spatial dispersion comprise the TM evanescent contributions to the calculation using the local model, Eq. (2.8).

Using the notation of Eq. (A.31) and the nonlocal model for the density response Eq. (3.4), we analyse below the contributions from the three regions of the (k,ω) plane in

Fig. 3.1: the vicinity of the plasmon dispersions, the diffusive region, and the clean region. In each region, we separate two temperature regimes. We see that in the high-temperature regimes, the integral Eq. (3.1) is dominated by a certain frequency scale, different in each regime, but always determined by $k \sim 1/d$ and being much lower than the temperature. Then, the thermal cutoff plays no role, and one can approximate the Bose distribution $\mathcal{N}(\omega) \approx T/(\hbar\omega)$ [that is why $J(T) \propto T$ in Eqs. (A.36), (A.40) and (A.42)]. In the low-temperature regimes, it is the e^{-kd} cutoff which is ineffective, so the frequency integral is determined by $\omega \sim T/\hbar$, while the k integral converges on a scale much smaller than $1/d$. Then one can approximate $e^{-kd} \approx 1$ in the numerator of Eq. (A.31b) and $1+e^{-kd} \approx 2$, $1-e^{-kd} \approx kd$ in the denominator.

A.4.1 Plasmon contribution

As discussed earlier, the plasmon contribution comes from the region $\omega > 1/\tau, v_F k$, since otherwise the plasmons are overdamped. At such frequencies one can expand $\Pi(k,\omega)$ to the leading order in k and approximate

$$\Pi v_k = \frac{v_F^2 \kappa k}{2\omega(\omega + i/\tau)}, \tag{A.32}$$

which corresponds to neglecting the spatial dispersion in the conductivity which takes the Drude form, $\sigma(\omega) = e^2 \nu D/(1 - i\omega\tau)$. (Generally, the spatial dispersion can be neglected when $k \ll \max\{\sqrt{\omega/D}, \omega/v_F\}$.) The integral is then dominated by the vicinities of the two plasmon dispersions, where one of the factors in the denominator of Eq. (A.31b) is small. The plasmon contribution exists only if the plasmon frequencies $\omega_\pm$ [see Eq. (3.6)] at $k \sim 1/d$ (when the spatial cutoff becomes effective) exceed $1/\tau$. This gives a condition $d \ll \kappa\ell^2$ (the vertical line $x = \eta^2$ in Fig. 3.2).

Let us first consider the temperature interval $1/\tau \ll T/\hbar \ll v_F\sqrt{\kappa/d}$ (the two inequalities are consistent when $d \ll \kappa\ell^2$), where the thermal cutoff plays first leaving the spatial cutoff e^{-kd} ineffective. Then one can expand e^{-kd} and perform the k integration first, approximating the integrand by a Lorentzian in the vicinity of each pole. The remaining frequency integral can be calculated exactly:

$$\begin{aligned} J_{\text{lp}}(T) &= \int_0^\infty \frac{d\omega}{\pi} \frac{\hbar\omega}{e^{\hbar\omega/T} - 1} \frac{\omega}{4\tau v_F^2 \kappa^2} \left(\frac{\omega^2}{v_F^2} + \frac{\kappa}{d} \right) \\ &= \frac{T^3}{2\pi\hbar^2 \tau v_F^2 \kappa d} \left[\zeta(3) + 12\,\zeta(5)\,\frac{T^2 d}{\hbar^2 v_F^2 \kappa} \right]. \end{aligned} \tag{A.33}$$

Here $\zeta(x)$ is the Riemann zeta function, and the first (second) term in the square brackets comes from the antisymmetric (symmetric) plasmons, respectively. In the considered region $1/\tau \ll T/\hbar \ll v_F\sqrt{\kappa/d}$ the symmetric contribution is always small compared to the antisymmetric one.

At high temperatures, $T/\hbar \gg v_F\sqrt{\kappa/d}$, the integral is determined by the spatial factor e^{-kd}, while the thermal cutoff is ineffective so the Bose distribution $\mathcal{N}(\omega) \approx T/(\hbar\omega)$. Taking expression (A.32), Eq. (A.31b) can also be written in the form suitable for integration over ω:

$$\mathcal{T}(k,\omega)=\frac{\omega^2}{2\tau^2}\,\frac{(\omega_+^2-\omega_-^2)^2}{|\omega(\omega+i/\tau)-\omega_+^2|^2|\omega(\omega+i/\tau)-\omega_-^2|^2}. \tag{A.34}$$

Note that one cannot just do two separate Lorentzian integrals because the separation $\omega_+^2-\omega_-^2$ becomes exponentially small at $k\gtrsim 1/d$. Fortunately, the ω integral can be calculated exactly:

$$\int\limits_0^\infty \frac{d\omega}{\pi}\,\mathcal{T}(k,\omega)=\frac{1}{2\tau}\,\frac{(\omega_+^2-\omega_-^2)^2}{(\omega_+^2-\omega_-^2)^2+2(\omega_+^2+\omega_-^2)/\tau^2}. \tag{A.35}$$

Then the k integral reads as

$$\begin{aligned}J_{\mathrm{hp}}(T)&=\frac{T}{\tau}\int_0^\infty\frac{k\,dk}{4\pi}\,\frac{\ell^2\kappa k}{\ell^2\kappa k+2e^{2kd}}\\&=\frac{T}{16\pi\tau d^2}\,\mathcal{L}(\ell^2\kappa/4d),\end{aligned} \tag{A.36}$$

with the function $\mathcal{L}(x)$ defined as

$$\mathcal{L}(x)\equiv\int_0^\infty\frac{u^2\,du}{u+e^u/x}. \tag{A.37}$$

A.4.2 Diffusive contribution

Let us focus on the contribution from the shaded region in Fig. 3.1: $k\ll 1/\ell$, $\omega\ll 1/\tau$. Then one can use expression (3.5b) for $\Pi(k,\omega)$, and since we are interested in $k\lesssim 1/d\ll\kappa$, we have $Dk^2\ll D\kappa k(1\pm e^{-kd})/2$, which is again equivalent to neglecting the spatial dispersion in the conductivity. Thus, we can write

$$\mathcal{T}\approx\frac{2\omega^2(D\kappa k)^2e^{-2kd}}{[\omega^2+(D\kappa k)^2(1+e^{-kd})^2][\omega^2+(D\kappa k)^2(1-e^{-kd})^2]}. \tag{A.38}$$

At low frequencies, when the momentum integral should converge on some scale $k\ll 1/d$, the two factors in the denominator are strongly different, and it is the second factor that determines the convergence scale $k\sim\sqrt{\omega/(D\kappa d)}$. When $\omega\sim T/\hbar\ll D\kappa/d$ this scale is indeed much smaller than $1/d$, so we expand e^{-kd}, integrate over k, then over ω, and arrive at

$$\begin{aligned}J_{\mathrm{ld}}(T)&=\int_0^\infty\frac{d\omega}{\pi}\,\frac{\hbar\omega}{e^{\hbar\omega/T}-1}\,\frac{\omega^2}{2}\int_0^\infty\frac{k\,dk}{2\pi}\,\frac{1}{\omega^2+(D\kappa dk^2)^2}\\&=\frac{\zeta(3)}{8\pi}\,\frac{T^3}{\hbar^2D\kappa d},\end{aligned} \tag{A.39}$$

Moreover, the convergence scale $\sqrt{T/(\hbar D\kappa d)}\ll 1/\ell$ provided that $T/\hbar\ll\kappa d/\tau$. Thus, since we always assume $\kappa d\gg 1$, Eq. (A.39) is valid for the diffusive contribution everywhere below the horizontal line $y\sim\eta$ $(T/\hbar\sim 1/\tau)$ in Fig. 3.2.

For $T/\hbar \gg D\kappa/d$, the k integral is dominated by $k \sim 1/d$. Then the typical frequency scale of Eq. (A.38) is $\omega \sim D\kappa/d$, so for $T/\hbar \gg D\kappa/d$ the thermal cutoff is ineffective. Then we approximate $\mathcal{N}(\omega) \approx T/(\hbar\omega)$, straightforwardly integrate over ω, then over k, and arrive at

$$\begin{aligned} J_{\mathrm{hd}}(T) = T &\int_0^\infty \frac{k\,dk}{2\pi} e^{-2kd} (D\kappa k)^2 \\ &\times \int_0^\infty \frac{d\omega}{\pi} \frac{2\omega^2}{\left[\omega^2 + (D\kappa k)^2 \left(1+e^{-kd}\right)^2\right]\left[\omega^2 + (D\kappa k)^2 \left(1-e^{-kd}\right)^2\right]} \\ &= \frac{1}{16\pi} \frac{D\kappa}{d^3} T \end{aligned} \tag{A.40}$$

Note that Eq. (A.40) is valid even at $T/\hbar \gg 1/\tau$ provided that the convergence scale $\omega \sim D\kappa/d \ll 1/\tau$, that is, to the left of the vertical line $x = \eta^2$ in Fig. 3.2. As we have seen, to the right of this line the plasmon contribution becomes important.

A.4.3 Clean contribution

For $T/\hbar \gg 1/\tau$, $1/d \gg 1/\ell$, one should take into account the contribution from the hatched area in Fig. 3.1. Here one can take the limit $\tau \to \infty$ and use expression (3.5a) for $\Pi(k,\omega)$. Then, in the integration region $\omega < v_F k$, $\operatorname{Re}\Pi(k,\omega) v_k = -\kappa/k$, so one can neglect unity in both factors in the denominator of Eq. (A.31b) and write

$$\mathcal{T} \approx \frac{2}{v_k^2} \left|\frac{\operatorname{Im}\Pi}{\Pi^2}\right|^2 \frac{e^{-2kd}}{(1-e^{-2kd})^2} = \frac{\omega^2 (v_F^2 k^2 - \omega^2)}{2 v_F^4 \kappa^2 k^2 \sinh^2 kd}. \tag{A.41}$$

For $T/\hbar \gg v_F/d$ we approximate $\mathcal{N}(\omega) \approx T/(\hbar\omega)$, straightforwardly integrate over ω between 0 and $v_F k$, then integrate over k, and arrive at

$$\begin{aligned} J_{\mathrm{hc}}(T) &= \frac{T}{2 v_F^4 \kappa^2} \int_0^\infty \frac{k\,dk}{2\pi} \frac{1}{k^2 \sinh^2 kd} \int_0^{v_F k} \frac{d\omega}{\pi} \omega^2 \left(v_F^2 k^2 - \omega^2\right) \\ &= \frac{\pi^2}{900} \frac{v_F}{d^3} \frac{T}{(\kappa d)^2}. \end{aligned} \tag{A.42}$$

For $T/\hbar \ll v_F/d$, in most of the integration region we have $\omega \sim T/\hbar \ll v_F k$, so the upper limit $\omega < v_F k$ is not important except for the narrow region $k \sim T/(\hbar v_F)$ which determines the lower cutoff of the logarithmic k integral:

$$\begin{aligned} J_{\mathrm{lc}}(T) &= \frac{\hbar}{4\pi^2} \int\limits_0^\infty \frac{\omega^3\,d\omega}{e^{\hbar\omega/T} - 1} \int\limits_{\sim T/v_F}^\infty \frac{k\,dk}{\sinh^2 kd} \\ &= \frac{\pi^2}{60} \frac{T^4}{\hbar^3 v_F^2 (\kappa d)^2} \ln \frac{v_F}{Td}. \end{aligned} \tag{A.43}$$

In the region $T/\hbar \gg 1/\tau$, $1/d \gg 1/\ell$, the clean contribution and the plasmon contribution both exist and should be added up, since they come from two distinct regions in the (k,ω) plane. Thus, to determine the dominant asymptotics, one can combine the four expressions (A.33), (A.36), (A.43) and (A.42) as $J = \max\{\min\{J_{\text{lp}}, J_{\text{hp}}\}, \min\{J_{\text{lc}}, J_{\text{hc}}\}\}$, which results in the complicated shape of the boundary between the clean and plasmonic regions in Fig. 3.1.

A.4.4 TM evanescent contribution to the local retarded calculation

As shown in Apps. A.4.1 and A.4.2, the plasmonic and diffusive contributions to the heat current in the Coulomb limit are correctly obtained with a local Drude model for the conductivity. They therefore correspond to the TM evanescent contribution to the full retarded calculation, whose other contributions were evaluated in the preceeding Apps. A.1–A.3. The corresponding expressions may be rewritten simply in terms of the dimensionless conductivity parameter $\mathcal{G} = 2\pi\sigma_{\text{DC}}/c$ by using the relation $\kappa = \mathcal{G}c/d$:

$$J_{\text{ld}}(T) = \frac{\zeta(3)}{8\pi}\frac{T^3}{\hbar^2 c\mathcal{G}d}, \tag{A.44a}$$

$$J_{\text{hd}}(T) = \frac{1}{16\pi}\frac{\mathcal{G}c}{d^3}T \tag{A.44b}$$

$$J_{\text{lp}}(T) = \frac{\zeta(3)}{4\pi}\frac{T^3}{\hbar^2 c\mathcal{G}d}, \tag{A.44c}$$

$$J_{\text{hp}}(T) = \frac{T}{16\pi\tau d^2}\mathcal{L}(\mathcal{G}c\tau/d), \tag{A.44d}$$

The domains of validity of the above contributions, shown in Fig. 3.2 in terms of κ, are similarly recast in terms of $\mathcal{G}$ in Fig. A.4. Note that expression (A.44a) equals the travelling contribution (A.9).

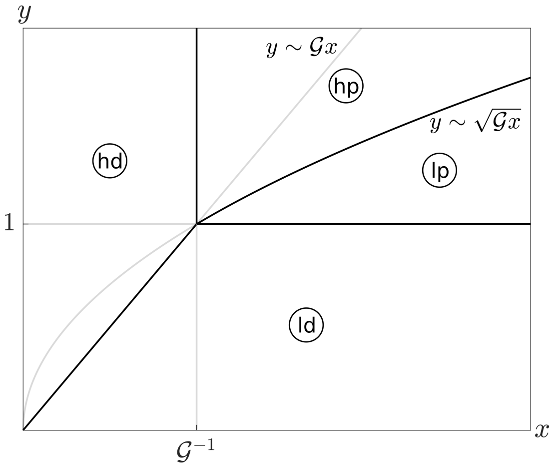

Figure A.4: Regions of validity of Eqs. (A.44a)–(A.44d) in the (x,y) plane.

B

Derivation of asymptotic expressions for the radiative heat transfer between three-dimensional metallic half-spaces

Contents

In this section we give a derivation of asymptotic expressions for the heat current between two three-dimensional semi-infinite metallic half-spaces, separated by a vacuum gap d, essentially reproducing the results obtained in Ref. [Polder71]. We take two identical metals, described by the complex dielectric functions $\varepsilon(\omega) = 1 + 4\pi i\sigma_{3D}/\omega$, where σ_{3D} is the three-dimensional dc conductivity, which can be written in terms of the bulk plasma frequency ω_p and the electron relaxation time τ as $4\pi\sigma_{3D} = \omega_p^2\tau$, and assumed to be temperature-independent. For conventional metals, $4\pi\sigma_{3D} \gg \omega_p \gg 1/\tau$, and it is natural to assume $T \ll \hbar/\tau$ (indeed, $\tau = 10^{-14}$ s corresponds to 760 K), so that for all relevant frequencies $\varepsilon(\omega) \approx 4\pi i\sigma_{3D}/\omega \gg 1$. Focusing on the local response regime, we assume to be in the normal skin effect regime, characterised by the frequency-dependent skin depth δ_ω and its value at $\omega = T/\hbar$:

$$\delta_\omega = \frac{c}{\sqrt{2\pi\sigma_{3D}\omega}}, \quad \delta_T \equiv \frac{c}{\sqrt{2\pi\sigma_{3D}T/\hbar}} \tag{B.1}$$

Since the metals are semi-infinite there can be no transmitted radiation and therefore the Joule losses are equal unambiguously to the average Poynting vector in the gap. The heat current per unit area $J(T)$ may once again be written in the form of Eq. (2.8), but without the third term in the emissivities in Eq. (2.10) (corresponding to transmission in the two-dimensional case), and with the reflectivities being just the Fresnel coefficients [Volokitin01]:

$$r_p = \frac{q_z - q_z'/\varepsilon}{q_z + q_z'/\varepsilon}, \quad r_s = \frac{q_z - q_z'}{q_z + q_z'}, \tag{B.2}$$

where $q_z' = \sqrt{[\varepsilon(\omega) - 1](\omega^2/c^2) + q_z^2}$ is the normal component of the complex wavevector describing the electric and magnetic fields inside the metal, while q_z is the same in the vacuum gap. As in the two-dimensional case, the contributions from travelling and evanescent waves for each polarisation are computed separately.

B.1 TM travelling contribution

The contribution may be written exactly as

$$J_{\mathrm{TM}}^{\mathrm{t}} = \frac{\hbar}{4\pi^2}\int_0^\infty \frac{\omega\,d\omega}{e^{\hbar\omega/T} - 1}\int_0^{\omega/c} q_z\,dq_z \frac{\left(1 - |r_p|^2\right)^2}{\left|1 - r_p^2 e^{-2iq_z d}\right|^2}. \tag{B.3}$$

The Fresnel coefficient is simplified drastically by noticing that since $cq_z < \omega \ll 4\pi\sigma_{3D}$ we may write

$$q_z' \approx \frac{\omega}{c}\sqrt{\varepsilon(\omega)}, \quad r_p \approx 1 - \frac{\omega}{cq_z}\frac{2}{\sqrt{\varepsilon(\omega)}}. \tag{B.4}$$

Focussing firstly on the case where the exponential in the denominator is oscillating fast, we may perform the same averaging according to Eq. (A.3), valid for $q_z \gg 1/d$, which translates into $d \gg \lambdabar_T$. This gives

$$J_{\text{TM}}^{\text{t}} = \frac{\hbar}{4\pi^2 c^2} \int_0^\infty \frac{\hbar\omega^3\, d\omega}{e^{\hbar\omega/T} - 1} \sqrt{\frac{\omega}{2\pi\sigma_{3\text{D}}}} = \frac{105\,\zeta(9/2)}{64\pi^{3/2}} \frac{\hbar(T/\hbar)^{9/2}}{\sqrt{2\pi\sigma_{3\text{D}}}c^2}. \tag{B.5}$$

When $q_z \ll 1/d$, the exponential in the denominator of Eq. (B.3) may be expanded as $1 - 2iq_z d$, so the denominator is approximately

$$1 - r_p^2 e^{-2iq_z d} \approx 2iq_z \left[d - (1+i)\delta_\omega \frac{\omega^2}{c^2 q_z^2} \right]. \tag{B.6}$$

This results in two expressions, depending on the relation between d and the thermal skin depth δ_T:

$$\begin{aligned} J_{\text{TM}}^{\text{t}} &= \frac{\hbar}{4\pi^2} \int_0^\infty \frac{\omega\, d\omega}{e^{\hbar\omega/T} - 1} \int_0^{\omega/c} \frac{\delta_\omega^2 q_z\, dq_z}{[(cq_z/\omega)^2 d - \delta_\omega]^2 + \delta_\omega^2} \\ &= \frac{15\,\zeta(7/2)}{128\sqrt{\pi}} \frac{\hbar(T/\hbar)^{7/2}}{\sqrt{2\pi\sigma_{3\text{D}}}cd}, \quad d \gg \delta_T, && \text{(B.7a)} \\ &= \frac{\pi^2\hbar(T/\hbar)^4}{240\,c^2}, \quad d \ll \delta_T. && \text{(B.7b)} \end{aligned}$$

Note that in the first case the q_z integral converges at $q_z \sim (\omega/c)\sqrt{\delta_\omega/d} \ll \omega/c$, so the expansion of $e^{-2iq_z d}$ is valid at $d \ll \lambdabar_T^2/\delta_T$, which is a weaker condition than $d \ll \delta_T$; this means that the small q_z contribution may coexist with that of Fabry-Perot modes, but it is subdominant. In the second case $d \ll \delta_T$, the convergence is at $q_z \sim \omega/c$, so the condition $q_z d \ll 1$ is automatically satisfied when $d \ll \delta_T$.

B.2 TE travelling contribution

The situation is quite analogous to the TM case. The TE contribution is given by Eq. (B.3), but with the replacement $r_p \to r_s$. Instead of Eq. (B.4), we have

$$q_z' \approx \frac{\omega}{c}\sqrt{\varepsilon(\omega)}, \quad r_s \approx -1 + (1-i)q_z\delta_\omega. \tag{B.8}$$

In the case of fast oscillation at $d \gg \lambdabar_T$, the denominator is again averaged using Eq. (A.3), leading to an expression, smaller than Eq. (B.5) by a factor of 3.

When $d \ll \lambdabar_T$, expanding $e^{-2iq_z d} \approx 1 - 2iq_z d$, we obtain $1 - r_s^2 e^{-2iq_z d} \approx 2iq_z[d - (1+i)\,\delta_\omega]$, which again results in two expressions:

$$\begin{aligned} J_{\text{TE}}^{\text{t}} &= \frac{\hbar}{8\pi^2 c^2} \int_0^\infty \frac{\omega^3\, d\omega}{e^{\hbar\omega/T} - 1} \frac{\delta_\omega^2(\omega)}{|d - (1+i)\delta_\omega|^2} \\ &= \frac{\zeta(3)}{4\pi^2} \frac{\hbar(T/\hbar)^3}{2\pi\sigma_{3\text{D}}d^2}, \quad d \gg \delta_T, && \text{(B.9a)} \\ &= \frac{\pi^2\hbar(T/\hbar)^4}{240\,c^2}, \quad d \ll \delta_T. && \text{(B.9b)} \end{aligned}$$

In contrast to the previous TM case, the integral is always dominated by $q_z \sim \omega/c$. In this case, analogously to Eq. (A.13), one can also take into account the contribution of the first Fabry-Perot mode:

$$J_{\mathrm{TE}}^{\mathrm{t}} = \frac{\pi^2}{4}\,\frac{cT\delta_1}{d^4}\,e^{\pi\hbar c/(Td)}, \tag{B.10}$$

where δ_1 is δ_ω corresponding to $\omega = \pi c/d$. This expression has an exponential smallness, but its prefactor is parametrically larger than Eq. (B.9a).

B.3 TM evanescent contribution

The contribution may be written exactly as

$$J_{\mathrm{TM}}^{\mathrm{e}} = \frac{\hbar}{\pi^2}\int_0^\infty \frac{\omega\,d\omega}{e^{\hbar\omega/T}-1}\int_0^\infty \tilde{q}_z\,d\tilde{q}_z\,\frac{(\operatorname{Im} r_p)^2\,e^{-2\tilde{q}_z d}}{\left|1-r_p^2 e^{-2\tilde{q}_z d}\right|^2}, \tag{B.11}$$

where the real integration variable $\tilde{q}_z$ is introduced since $q_z = i\tilde{q}_z$ is purely imaginary. Then $q_z' = \sqrt{\varepsilon(\omega)\,(\omega/c)^2 - \tilde{q}_z^2}$.

Let us first consider the case where the $\tilde{q}_z^2$ dominates over $\varepsilon(\omega/c)^2$ in the square root, that is $\tilde{q}_z\delta_\omega \gg 1$. Then

$$r_p \approx 1 - \frac{2}{\varepsilon(\omega)} = 1 + \frac{i\omega}{2\pi\sigma_{3\mathrm{D}}}, \tag{B.12}$$

and

$$\begin{aligned} J_{\mathrm{TM}}^{\mathrm{e}} &= \frac{\hbar}{4\pi^2}\int_0^\infty \frac{\omega\,d\omega}{e^{\hbar\omega/T}-1}\int_0^\infty \frac{[\omega/(2\pi\sigma_{3\mathrm{D}})]^2\,\tilde{q}_z\,d\tilde{q}_z}{\sinh^2\tilde{q}_z d + [\omega/(\pi\sigma_{3\mathrm{D}})]^2} \\ &= \frac{\pi^2}{60}\,\frac{\hbar(T/\hbar)^4}{(2\pi\sigma_{3\mathrm{D}})^2 d^2}\ln\min\left\{\frac{2\pi\sigma_{3\mathrm{D}}}{T/\hbar},\,\frac{\delta_T^2}{d^2}\right\}. \end{aligned} \tag{B.13}$$

The $\tilde{q}_z$ integral is logarithmic, and is determined by a broad interval of $\tilde{q}_z$ from the upper cutoff $\sim 1/d$ down to the lower cutoff: for $d \ll c/(2\pi\sigma_{3\mathrm{D}})$ it is $(1/d)\sqrt{\omega/(2\pi\sigma_{3\mathrm{D}})}$, while at larger distances the small $\tilde{q}_z$ cutoff is determined by the condition of $\tilde{q}_z\delta_\omega \gg 1$. The logarithmic region exists at all if $\varepsilon(\omega/c)^2$ can be neglected at $\tilde{q}_z \sim 1/d$, which translates into $d \ll \delta_T$.

In the opposite case, where we neglect $\tilde{q}_z \ll 1/\delta_\omega$ in q_z', we still assume $\tilde{q}_z \gg (\omega/c)/\sqrt{\varepsilon} \sim (\omega/c)^2\delta_\omega$, so the reflection coefficient is still close to unity:

$$r_p \approx 1 + (1+i)\,\frac{\omega}{c\tilde{q}_z}\sqrt{\frac{\omega}{2\pi\sigma_{3\mathrm{D}}}}. \tag{B.14}$$

Then the $\tilde{q}_z$ integral is determined by small $\tilde{q}_z \sim \sqrt{\omega/(cd)}[\omega/(2\pi\sigma_{3\mathrm{D}})]^{1/4} \ll 1/d$, so

$\sinh\tilde{q}_z d \approx \tilde{q}_z d$:

$$J^{\mathrm{e}}_{\mathrm{TM}} = \frac{\hbar}{4\pi^2}\int_0^\infty \frac{\omega\,d\omega}{e^{\hbar\omega/T}-1}\int_0^\infty \tilde{q}_z\,d\tilde{q}_z\left[\left(\frac{\tilde{q}_z^2 cd}{\omega}\sqrt{\frac{2\pi\sigma_{3\mathrm{D}}}{\omega}}-1\right)^2+1\right]^{-1}$$
$$= \frac{45\,\zeta(7/2)}{256\sqrt{\pi}}\,\frac{\hbar(T/\hbar)^{7/2}}{\sqrt{2\pi\sigma_{3\mathrm{D}}}cd}. \tag{B.15}$$

The conditions $\tilde{q}_z d \ll 1$, $(\omega/c)^2\delta_\omega \ll \tilde{q}_z \ll 1/\delta_\omega$ result in the requirement

$$\frac{T/\hbar}{2\pi\sigma_{3\mathrm{D}}}\,\delta_T \ll d \ll \frac{2\pi\sigma_{3\mathrm{D}}}{T/\hbar}\,\delta_T. \tag{B.16}$$

Note that the lower limit on d is smaller than δ_T, so there is an interval where Eqs. (B.13) and (B.15) are both valid, representing contributions from different regions of $\tilde{q}_z$ integration. However, when inequalities (B.16) hold, Eq. (B.15) automatically dominates over Eq. (B.13). Going to longer distances, where the assumption $(\omega/c)/\sqrt{\varepsilon} \ll \tilde{q}_z$ is violated, is not necessary since at such distances (well exceeding $\lambda\!\!\!^{-}_T$) the travelling wave contributions dominate; indeed, Eq. (B.5) exceeds Eq. (B.15) in the common wisdom region $d \gg \lambda\!\!\!^{-}_T$.

B.4 TE evanescent contribution

The TE contribution is given by Eq. (B.11), but with the replacement $r_p \to r_s$. If we try to proceed as in the TM case and assume first $\tilde{q}_z\delta_\omega \gg 1$, we obtain an integral diverging at small $\tilde{q}_z$, invalidating the assumption.

Making the opposite assumption, $q_z\delta_\omega \ll 1$, for the reflection coefficient we obtain the same approximation (B.8) with $q_z = i\tilde{q}_z$, which leads to

$$J^{\mathrm{e}}_{\mathrm{TE}} = \frac{\hbar}{4\pi^2}\int\limits_0^\infty \frac{\omega\,d\omega}{e^{\hbar\omega/T}-1}\int\limits_0^\infty \frac{\tilde{q}_z^3\,d\tilde{q}_z}{[(\sinh\tilde{q}_z d)/\delta_\omega+\tilde{q}_z]^2+\tilde{q}_z^2}. \tag{B.17}$$

At $d \gg \delta_\omega$ the $\tilde{q}_z$ integral converges at $\tilde{q}_z \sim 1/d$, and the resulting logarithmic ω integral

$$J^{\mathrm{e}}_{\mathrm{TE}} = \frac{3\,\zeta(3)}{8\pi^2 d^4}\int\limits_0^\infty \frac{\delta_\omega^2\,\hbar\omega\,d\omega}{e^{\hbar\omega/T}-1} = \frac{3\,\zeta(3)}{4\pi^2}\,\frac{c^2 T}{2\pi\sigma_{3\mathrm{D}}d^4}\ln\frac{d}{\delta_T}, \tag{B.18}$$

is cut off at low frequencies by the condition $d \sim \delta_\omega$, so that the validity condition is $d \gg \delta_T$.

For $d \ll \delta_T$ we are forced to consider $\tilde{q}_z\delta_\omega \sim 1$ and use the exact expression $q_z' = \sqrt{2i - \tilde{q}_z^2\delta_\omega^2}/\delta_\omega$; however, we can safely set $d \to 0$ as $1 \pm r_s \sim 1$. Then we obtain

$$\frac{(\mathrm{Im}\,r_s)^2}{|1-r_s^2|^2} = \frac{(\mathrm{Re}\,q_z')^2}{4|q_z'|^2} = \frac{1/2}{4+\tilde{q}_z^4\delta_\omega^4+\tilde{q}_z^2\delta_\omega^2\sqrt{4+\tilde{q}_z^4\delta_\omega^4}}, \tag{B.19}$$

which gives

$$J_{\mathrm{TE}}^{\mathrm{e}} = \frac{2\pi\sigma_{\mathrm{3D}}\hbar}{8\pi^2 c}\int_0^\infty \frac{\omega^2\, d\omega}{e^{\hbar\omega/T}-1} = \frac{\zeta(3)}{4\pi^2}\frac{2\pi\sigma_{\mathrm{3D}}\hbar(T/\hbar)^3}{c^2}, \tag{B.20}$$

the $\tilde{q}_z$ integral converging at $\tilde{q}_z \sim 1/\delta_\omega$, as expected.

C

Derivation of Caroli formula and noise spectrum via nonequilibrium Green's functions

Contents

C.1 Heat current operator

We consider a total system given by the Hamiltonian

$$\hat{H} = \hat{H}_1 + \hat{H}_2 + \hat{H}_{12}, \tag{C.1}$$

where the first two terms represent subsystems at temperatures T_1 and T_2, respectively, and the final term represents a coupling of the subsystems. The independent electronic subsystem Hamiltonians $\hat{H}_a$ are taken to be (suppressing the time argument)

$$\begin{aligned}\hat{H}_a = &\int_a d\mathbf{r}\,\Psi_a^\dagger(\mathbf{r})\left[-\frac{\hbar^2\nabla^2}{2m} + u(\mathbf{r})\right]\Psi_a(\mathbf{r}) \\ &+ \frac{1}{2}\int_a d\mathbf{r}\int_a d\mathbf{r}'\,\Psi_a^\dagger(\mathbf{r})\Psi_a^\dagger(\mathbf{r}')V(\mathbf{r}-\mathbf{r}')\Psi_a(\mathbf{r}')\Psi_a(\mathbf{r}),\end{aligned} \tag{C.2}$$

where Ψ ($\Psi^\dagger$) are the annihilation (creation) operators of electrons in the subsystems, and the three terms represent the kinetic energy, impurity scattering, and (intra-subsystem) Coulomb interactions, respectively. The coupling between subsystems is given similarly by

$$\hat{H}_{12} = \int_2 d\mathbf{r}\int_1 d\mathbf{r}'\,\Psi_2^\dagger(\mathbf{r})\Psi_1^\dagger(\mathbf{r}')V(\mathbf{r}-\mathbf{r}')\Psi_1(\mathbf{r}')\Psi_2(\mathbf{r}). \tag{C.3}$$

We seek the operator corresponding to the heat current, or energy, absorbed by subsystem 1, given by Heisenberg's equation:

$$\begin{aligned}\frac{d\hat{H}_1}{dt} &= \frac{i}{\hbar}\left[\hat{H}, \hat{H}_1\right] \\ &= \frac{i}{\hbar}\left[\hat{H}_1 + \hat{H}_{12}, \hat{H}_1\right],\end{aligned} \tag{C.4}$$

since the electron creation and annihilation operators of the two subsystems commute with each other. The only non-zero terms come from those which cannot be written in terms of the electron density, that of the kinetic energy, which results in the commutator

$$\left[\hat{H}_1 + \hat{H}_{12}, \hat{H}_1\right] = -\frac{\hbar^2}{2m}\int_1 d\mathbf{r}\int_1 d\mathbf{r}'\left[\Psi_1^\dagger(\mathbf{r})\Psi_1(\mathbf{r})\tilde{V}(\mathbf{r}), \Psi_1^\dagger(\mathbf{r}')\nabla_{\mathbf{r}'}^2\Psi_1(\mathbf{r}')\right] \tag{C.5}$$

$$= -\frac{\hbar^2}{2m}\int_1 d\mathbf{r}\,\Psi_1^\dagger(\mathbf{r})\left[\tilde{V}(\mathbf{r}), \nabla_{\mathbf{r}}^2\right]\Psi_1(\mathbf{r}) \tag{C.6}$$

where $\tilde{V}$ is the interaction term integrated over both subsystem densities:

$$\tilde{V}(\mathbf{r}) = \sum_{a=1,2}\int_a d\mathbf{r}'\Psi_1^\dagger(\mathbf{r})\Psi_a^\dagger(\mathbf{r}')V(\mathbf{r}-\mathbf{r}')\Psi_a(\mathbf{r}')\Psi_1(\mathbf{r}). \tag{C.7}$$

We arrive at the second line Eq. (C.6) simply by expanding the commutator and using the commutation relations for the fermionic operators. The final commutator may be computed by performing integration by parts once arriving at

$$\begin{aligned}\frac{d\hat{H}_1}{dt} &= -\int_1 d\mathbf{r}\,\frac{i\hbar}{2m}\left(-\Psi_1^\dagger(\mathbf{r})\nabla\Psi_1(\mathbf{r})+\nabla(\Psi_1^\dagger(\mathbf{r}))\Psi_1(\mathbf{r})\right)\cdot\nabla\tilde{V}(\mathbf{r})\\ &= -\sum_{a=1,2}\int_1 d\mathbf{r}\int_a d\mathbf{r}'\,\hat{\mathbf{j}}_1(\mathbf{r})\cdot\nabla_{\mathbf{r}}V(\mathbf{r}-\mathbf{r}')\hat{\rho}_a(\mathbf{r}')\end{aligned} \tag{C.8}$$

where we identified the particle current operator. The heat current absorbed locally at a point $\mathbf{r}$ is thus (restoring the time arguments)

$$\hat{J}_1(\mathbf{r},t) = -\sum_{a=1,2}\int_a d\mathbf{r}'\,\hat{\mathbf{j}}_1(\mathbf{r},t)\cdot\nabla_{\mathbf{r}}V(\mathbf{r}-\mathbf{r}')\hat{\rho}_a(\mathbf{r}',t), \tag{C.9}$$

where the sum represents the fact that heat absorbed at point $\mathbf{r}$ in the subsystem 1 is due to fields produced by density fluctuations either in subsystem 2, or elsewhere in subsystem 1. In the main text we omit the sum and just remember that while $\mathbf{r}$ resides in subsystem 1, the integration variable $\mathbf{r}'$ runs over the total volume of the system.

C.2 Generating functional for interacting electrons with disorder

Since we are dealing with a many body problem, the inclusion of interactions is a formidably difficult task, and an approximation scheme is necessary. Working in the framework of nonequilibrium Green's functions, we construct the generating functional for disordered electrons interacting via Coulomb interactions. The interactions are included within the random phase approximation (RPA), which is expected to be valid for high electron density systems such as the metals treated in this work. As we shall see in the following sections, the generating functional shall give us access via functional differentiation to the expectation values required for computing the average heat current and its fluctuations [first and second moments of Eq. (C.9)].

The generating functional, $\mathcal{Z}$, is defined as the weighted functional field integral over the action, $\mathcal{S}$:

$$\mathcal{Z}(V,\mathbf{A}) = \int\mathcal{D}[\bar{\psi}\psi]e^{i\mathcal{S}[\bar{\psi},\psi,V,\mathbf{A}]}, \tag{C.10}$$

where $\bar{\psi}$, ψ are independent Grassman variables necessary to describe a fermionic system. The action for interacting electrons corresponding to the Hamiltonian (C.1) with scalar and vector source fields is given explicitly by [Kamenev11]

$$\begin{aligned}\mathcal{S} = \int_{\mathcal{C}} dt\int d\mathbf{r}\Bigg\{&\bar{\psi}(\mathbf{r},t)\left[i\partial_t+\frac{\hbar^2\overrightarrow{\nabla}_{\mathbf{r}}^2}{2m}-u(\mathbf{r},t)\right]\psi(\mathbf{r},t)\\ &-\bar{\psi}(\mathbf{r},t)\left[V(\mathbf{r},t)+\frac{1}{2mi}\left(\mathbf{A}(\mathbf{r},t)\cdot\overrightarrow{\nabla}_{\mathbf{r}}-\overleftarrow{\nabla}_{\mathbf{r}}\cdot\mathbf{A}(\mathbf{r},t)\right)\right]\psi(\mathbf{r},t)\\ &-\frac{1}{2}\int d\mathbf{r}'\,\bar{\psi}(\mathbf{r},t)\psi(\mathbf{r},t)V_0(\mathbf{r}-\mathbf{r}')\bar{\psi}(\mathbf{r}',t)\psi(\mathbf{r}',t)\Bigg\}\end{aligned} \tag{C.11}$$

where the integration in time is over the Keldysh contour, $\mathcal{C}$, which begins at $-\infty$, when the interactions are adiabatically switched on, runs forwards to $+\infty$ and then runs backwards to $-\infty$. The first line of Eq. (C.11) is the free part of the theory, with the three terms representing the time evolution, the kinetic energy and interaction with an external potential, u, respectively. Through the latter one may encode disorder in the system. The second line represents the coupling to external scalar and vector source fields. The gradient operators $\overrightarrow{\nabla}$ and $\overleftarrow{\nabla}$ act in the direction of the arrow. We recognise that the scalar potential, V, couples to the fermion density, while the vector potential, $\mathbf{A}$, couples to the fermion current. We note that V and $\mathbf{A}$ are not the physical potentials, but just source fields introduced formally to access the required observables (density and current). Finally the third line represents the electron-electron interactions, where we only take into account the singlet channel and neglect triplet and Cooper channel interactions. V_0 is the fermion singlet interaction potential which for electrons is the Coulomb interaction.

We follow the standard procedure described in Ref. [Kamenev11] to separate the forward and backward parts of the Keldysh time contour, perform a Keldysh rotation of the Grassman fields using the Larkin and Ovchinnikov convention, and finally define the classical and quantum components of the bosonic density and current fields and associated sources. The Coulomb interaction in the last line of Eq. (C.11) is handled via the introduction of a Hubbard-Stratonovich bosonic field. The resulting integral over the fermionic fields becomes Gaussian and so may be performed exactly, resulting in an effective nonlinear bosonic theory. Restricting ourselves to RPA, the action is then expanded to second order in the bosonic fields and in the source terms. Then integration over the bosonic Hubbard-Stratonovich field is performed resulting in the generating functional:

$$\begin{aligned}\ln \mathcal{Z}[V,\mathbf{A}] &= -i\int dx \int dx' \Big[V^{\alpha} D^{\alpha\beta}_{\rho\rho} V^{\beta} + V^{\alpha} D^{\alpha\beta}_{\rho j_k} A^{\beta}_{k} + A^{\alpha}_{i} D^{\alpha\beta}_{j_i j_k} A^{\beta}_{k} + A^{\alpha}_{i} D^{\alpha\beta}_{j_i\rho} V^{\beta} \\ &\quad + \int dx_1 \int dx_2 \left(V^{\alpha} D^{\alpha\gamma}_{\rho\rho} + A^{\alpha}_{i} D^{\alpha\gamma}_{j_i\rho}\right) V^{\gamma\delta}_{RPA} \left(D^{\delta\beta}_{\rho\rho} V^{\beta} + D^{\delta\beta}_{\rho j_k} A_{k}\right)\Big] \\ &= -i\int dx \int dx'\, \mathcal{A}^{\alpha}_{i}(x) \tilde{D}^{\alpha\beta}_{ij}(x,x') \mathcal{A}^{\beta}_{j}(x'), \qquad \text{(C.12)}\end{aligned}$$

$$\text{where } \tilde{D}^{\alpha\beta}_{ij}(x,x') = \left[D^{\alpha\beta}_{ij}(x,x') + \int dx_1 \int dx_2\, D^{\alpha\gamma}_{ik}(x,x_1) V^{\gamma\delta}_{kl}(x_1,x_2) D^{\delta\beta}_{lj}(x_2,x')\right] \qquad \text{(C.13)}$$

where Greek superscripts represent the Keldysh space in the classical–quantum $(c-q)$ basis and $\mathcal{A} = (V, A_x, A_y)$ is the three vector of the source terms, and associated latin subscripts on the GFs refer to the corresponding observables, $\mathcal{B} = (\rho, j_x, j_y)$. The integration variables x and x' are 4-vectors of space and time. Since the interaction only couples density to density, the interaction matrix in density-current space has just one non-zero element (in the upper left corner), $V^{\gamma\delta}_{\rho\rho} = V^{\gamma\delta}_{RPA}$. The GFs themselves are defined as functional derivatives with respect to the source fields (note that we use the opposite sign convention to Ref. [Kamenev11]):

$$D_{ij}^{\alpha\beta}(x,x') = \frac{i}{2}\frac{\delta^2 \ln \mathcal{Z}[V,\mathbf{A}]}{\delta\mathcal{A}_j^{\beta}(x')\delta\mathcal{A}_i^{\alpha}(x)}\bigg|_{V=\mathbf{A}=0}. \tag{C.14}$$

Since the source fields couple to the observables, the GFs are proportional to averages of products of the corresponding observables, remembering that classical component of the source field couples to quantum component of the observable, and vice versa. Specifically, the GFs give the expectation values according to

$$D_{ij}^{\alpha\beta}(x,x') = -2i\langle\mathcal{B}_i^{\alpha'}(x)\mathcal{B}_j^{\beta'}(x')\rangle, \tag{C.15}$$

where if $\alpha = c$ then $\alpha' = q$ and vice versa. The classical and quantum field component basis is defined with respect to the Keldysh contour forward and backward basis via $\mathcal{B}^{c(q)} = (\mathcal{B}^f \pm \mathcal{B}^b)/2$. In this construction the the GFs may be collected into a triangular matrix structure

$$D = \begin{pmatrix} 0 & D^A \\ D^R & D^K \end{pmatrix}. \tag{C.16}$$

The general symmetry relations for bosonic GFs are

$$D^R(x,x') = D^A(x',x) \tag{C.17a}$$
$$D^K(x,x') = D^K(x',x), \tag{C.17b}$$

We define the Fourier transform in time of steady-state GFs (who depend only on the time difference)

$$D(\mathbf{r},\mathbf{r}',\omega) = \int_{-\infty}^{\infty} d(t-t')\, e^{i\omega(t-t')} D(\mathbf{r},\mathbf{r}',t-t'). \tag{C.18}$$

Further, the bosonic GF components for a system in thermal equilibrium at temperature T obey the relation [Kamenev11]

$$D^K(\omega) = \left[D^R(\omega) - D^A(\omega)\right]\coth\frac{\hbar\omega}{2T}. \tag{C.19}$$

In the triangular basis the screened GFs defined in Eq. (C.13) may be written in terms of the screened Coulomb interaction, which for the density-density component gives the regular matrix Dyson equation (spatial integrations over intermediate variables are implied)

$$\tilde{D}_{\rho\rho} = D_{\rho\rho} + D_{\rho\rho} V_{RPA} D_{\rho\rho}, \tag{C.20}$$

The screened interaction may itself be expressed via the iterative Dyson equation

$$V_{RPA} = V_0\sigma_1 + V_0\sigma_1 D_{\rho\rho} V_{RPA}, \tag{C.21}$$

where the first Pauli matrix, σ_1 gives the matrix structure of the bare Coulomb interaction in this basis. The screened GFs may be represented entirely in terms of noninteracting

GFs and bare interactions via

$$\begin{pmatrix} 0 & \tilde{D}^A \\ \tilde{D}^R & \tilde{D}^K \end{pmatrix} = \begin{pmatrix} 0 & D^A(\mathbb{1}-V_0D^A)^{-1} \\ D^R(\mathbb{1}-V_0D^R)^{-1} & (\mathbb{1}-D^RV_0)^{-1}D^K(\mathbb{1}-V_0D^A)^{-1} \end{pmatrix}, \tag{C.22}$$

and similarly for the screened Coulomb interaction

$$\begin{pmatrix} V^K_{RPA} & V^R_{RPA} \\ V^A_{RPA} & 0 \end{pmatrix} = \begin{pmatrix} (\mathbb{1}-V_0D^R)^{-1}V_0D^K(\mathbb{1}-V_0D^A)^{-1} & (\mathbb{1}-V_0D^R)^{-1}V_0 \\ (\mathbb{1}-V_0D^A)^{-1}V_0 & 0 \end{pmatrix}, \tag{C.23}$$

where intermediate variables are integrated over and $\mathbb{1} = \delta(\mathbf{r}-\mathbf{r}')$ is the Dirac delta function.

Aside from the density-density GF, the other current-density, density-current and current-current GFs appearing in Eq. (4.24) are related via the continuity equation,

$$\overrightarrow{\nabla}^i_{\mathbf{r}} j_i(\mathbf{r},t) + \frac{\partial\rho(\mathbf{r},t)}{\partial t} = 0, \tag{C.24}$$

which leads to the relations:

$$D_{\rho\rho}(\mathbf{r},\mathbf{r}',\omega) = \frac{1}{\omega^2}\overrightarrow{\nabla}^i_{\mathbf{r}} D_{j_ij_k}(\mathbf{r},\mathbf{r}',\omega)\overleftarrow{\nabla}^k_{\mathbf{r}'}, \tag{C.25a}$$

$$D_{j_i\rho}(\mathbf{r},\mathbf{r}',\omega) = -\frac{1}{i\omega} D_{j_ij_k}(\mathbf{r},\mathbf{r}',\omega)\overleftarrow{\nabla}^k_{\mathbf{r}'}, \tag{C.25b}$$

$$D_{\rho j_k}(\mathbf{r},\mathbf{r}',\omega) = \frac{1}{i\omega}\overrightarrow{\nabla}^i_{\mathbf{r}} D_{j_ij_k}(\mathbf{r},\mathbf{r}',\omega). \tag{C.25c}$$

Using these relations, we may derive from the generating functional expressions for the average heat current and the fluctuations.

Using the definitions written above, we may write the average of the heat current Eq. (C.9) in terms of a functional derivative of the generating functional (transforming fields from forwards-backwards basis into classical and quantum components)

$$\begin{aligned} \langle \hat{J}(\mathbf{r},t)\rangle &= \frac{1}{2}\left[\left\langle \hat{J}^f(\mathbf{r},t)\right\rangle + \left\langle \hat{J}^b(\mathbf{r},t)\right\rangle\right] \\ &= -\int d\mathbf{r}'\,\overrightarrow{\nabla}^i_{\mathbf{r}}V(\mathbf{r}-\mathbf{r}')\langle j^c_i(\mathbf{r},t)\rho^c(\mathbf{r}',t)\rangle \\ &= \frac{1}{4}\int d\mathbf{r}'\,\overrightarrow{\nabla}^i_{\mathbf{r}}V(\mathbf{r}-\mathbf{r}')\left.\frac{\delta^2\mathcal{Z}[V,\mathbf{A}]}{\delta V^q(\mathbf{r}',t)\delta A^q_i(\mathbf{r},t)}\right|_{V=\mathbf{A}=0}. \end{aligned} \tag{C.26}$$

Similarly, we may write the expression for the fluctuations in terms of functional derivatives

$$\begin{aligned}
&\left\langle \left\{ \hat{J}^f(\mathbf{r},t) \hat{J}^b(\mathbf{r}',t') \right\} \right\rangle = \frac{1}{16} \int d\mathbf{r}_1 \int d\mathbf{r}_2 \, \overrightarrow{\nabla}^i_{\mathbf{r}} V(\mathbf{r}-\mathbf{r}_1) \, \overrightarrow{\nabla}^i_{\mathbf{r}'} V(\mathbf{r}'-\mathbf{r}_2) \\
&\times \Bigg[\frac{\delta^4 \mathcal{Z}[V,\mathbf{A}]}{\delta V^q(\mathbf{r}_2,t') \delta A^q_k(\mathbf{r}',t') \delta V^q(\mathbf{r}_1,t) \delta A^q_i(\mathbf{r},t)} + \frac{\delta^4 \mathcal{Z}[V,\mathbf{A}]}{\delta V^c(\mathbf{r}_2,t') \delta A^c_k(\mathbf{r}',t') \delta V^q(\mathbf{r}_1,t) \delta A^q_i(\mathbf{r},t)} \\
&+ \frac{\delta^4 \mathcal{Z}[V,\mathbf{A}]}{\delta V^q(\mathbf{r}_2,t') \delta A^q_k(\mathbf{r}',t') \delta V^c(\mathbf{r}_1,t) \delta A^c_i(\mathbf{r},t)} + \frac{\delta^4 \mathcal{Z}[V,\mathbf{A}]}{\delta V^c(\mathbf{r}_2,t') \delta A^q_k(\mathbf{r}',t') \delta V^c(\mathbf{r}_1,t) \delta A^q_i(\mathbf{r},t)} \\
&- \frac{\delta^4 \mathcal{Z}[V,\mathbf{A}]}{\delta V^q(\mathbf{r}_2,t') \delta A^c_k(\mathbf{r}',t') \delta V^c(\mathbf{r}_1,t) \delta A^q_i(\mathbf{r},t)} - \frac{\delta^4 \mathcal{Z}[V,\mathbf{A}]}{\delta V^c(\mathbf{r}_2,t') \delta A^q_k(\mathbf{r}',t') \delta V^q(\mathbf{r}_1,t) \delta A^c_i(\mathbf{r},t)} \\
&- \frac{\delta^4 \mathcal{Z}[V,\mathbf{A}]}{\delta V^q(\mathbf{r}_2,t') \delta A^c_k(\mathbf{r}',t') \delta V^q(\mathbf{r}_1,t) \delta A^c_i(\mathbf{r},t)} \Bigg]_{V=\mathbf{A}=0} . \qquad \text{(C.27)}
\end{aligned}$$

C.3 Caroli formula for the average heat current

For the average of Eq. (C.9) the functional derivative in Eq. (C.26) may be identified as a GF via its definition

$$\langle \hat{J}(\mathbf{r},t) \rangle = -\frac{i}{2} \int d\mathbf{r}' \int_{-\infty}^{\infty} \frac{d\omega}{2\pi} \tilde{D}^K_{j_i\rho}(\mathbf{r},\mathbf{r}',\omega) \overrightarrow{\nabla}^i_{\mathbf{r}} V_0(\mathbf{r}-\mathbf{r}'), \qquad \text{(C.28)}$$

which may be conveniently split into two equal pieces:

$$\begin{aligned}
\langle \hat{J}(\mathbf{r},t) \rangle = \frac{i}{4} \int d\mathbf{r}' \int_{-\infty}^{\infty} \frac{d\omega}{2\pi} \\
\times \left[\tilde{D}^K_{j_i\rho}(\mathbf{r},\mathbf{r}',\omega) V_0(\mathbf{r}'-\mathbf{r}) \overleftarrow{\nabla}^i_{\mathbf{r}} - \overrightarrow{\nabla}^i_{\mathbf{r}} V_0(\mathbf{r}-\mathbf{r}') \tilde{D}^K_{\rho j_i}(\mathbf{r}',\mathbf{r},\omega) \right], \qquad \text{(C.29)}
\end{aligned}$$

where we now seek to express each term in terms of noninteracting GFs and RPA screened interaction terms. We have for the first dressed GF the relevant matrix Dyson equation:

$$\begin{aligned}
\tilde{D}_{j_i\rho} &= D_{j_i\rho} + D_{j_i\rho} V_{RPA} D_{\rho\rho} && \text{(C.30)} \\
&= D_{j_i\rho} + D_{j_i\rho} V_0 \sigma_1 D_{\rho\rho} + D_{j_i\rho} V_0 \sigma_1 D_{\rho\rho} V_{RPA} D_{\rho\rho} && \text{(C.31)} \\
&= D_{j_i\rho} + D_{j_i\rho} V_0 \sigma_1 D_{\rho\rho} + D_{j_i\rho} V_0 \sigma_1 \tilde{D}_{\rho\rho} V_0 \sigma_1 D_{\rho\rho}. && \text{(C.32)}
\end{aligned}$$

Performing the matrix multiplication multiplication and taking the Keldysh component gives (suppressing everywhere the dependence on ω):

$$\begin{aligned}
&\tilde{D}^K_{j_i\rho}(\mathbf{r},\mathbf{r}',\omega) = D^K_{j_i\rho}(\mathbf{r},\mathbf{r}') \\
&+ \int_{\mathbf{r}_1,\mathbf{r}_2} D^R_{j_i\rho}(\mathbf{r},\mathbf{r}_1) V_0(\mathbf{r}_1-\mathbf{r}_2) \left[D^K_{\rho\rho}(\mathbf{r}_2,\mathbf{r}') + \int_{\mathbf{r}_3,\mathbf{r}_4} \tilde{D}^R_{\rho\rho}(\mathbf{r}_2,\mathbf{r}_3) V_0(\mathbf{r}_3-\mathbf{r}_4) D^K_{\rho\rho}(\mathbf{r}_4,\mathbf{r}') \right] \\
&+ \int_{\mathbf{r}_1,\mathbf{r}_2} D^K_{j_i\rho}(\mathbf{r},\mathbf{r}_1) V_0(\mathbf{r}_1-\mathbf{r}_2) \left[D^A_{\rho\rho}(\mathbf{r}_2,\mathbf{r}') + \int_{\mathbf{r}_3,\mathbf{r}_4} \tilde{D}^A_{\rho\rho}(\mathbf{r}_2,\mathbf{r}_3) V_0(\mathbf{r}_3-\mathbf{r}_4) D^A_{\rho\rho}(\mathbf{r}_4,\mathbf{r}') \right] \\
&+ \int_{\mathbf{r}_1,\mathbf{r}_2,\mathbf{r}_3,\mathbf{r}_4} D^R_{j_i\rho}(\mathbf{r},\mathbf{r}_1) V_0(\mathbf{r}_1-\mathbf{r}_2) \tilde{D}^K_{\rho\rho}(\mathbf{r}_2,\mathbf{r}_3) V_0(\mathbf{r}_3-\mathbf{r}_4) D^A_{\rho\rho}(\mathbf{r}_4,\mathbf{r}'), \qquad \text{(C.33)}
\end{aligned}$$

where we have introduced the shorthand notation $\int_{\mathbf{r}_1,\mathbf{r}_2} = \int d\mathbf{r}_1 \int d\mathbf{r}_2$. In the second and third lines we may recognise the retarded and advanced component of the screened interaction potential, respectively, and in the final line we may replace the screened density-density sandwiched by bare interactions by the bare density-density sandwiched by screened interactions, since we have $V_0 \tilde{D}^K_{\rho\rho} V_0 = V^R_{RPA} D^K_{\rho\rho} V^A_{RPA}$. Doing so leads to

$$\begin{aligned}
&\tilde{D}^K_{j_i\rho}(\mathbf{r},\mathbf{r}',\omega) = D^K_{j_i\rho}(\mathbf{r},\mathbf{r}') \\
&+\frac{1}{\omega^2}\int_{\mathbf{r}_1,\mathbf{r}_2} D^R_{j_ij_n}(\mathbf{r},\mathbf{r}_1)\overrightarrow{\nabla}^n_{\mathbf{r}_1} V^R_{RPA}(\mathbf{r}_1,\mathbf{r}_2)\overleftarrow{\nabla}^p_{\mathbf{r}_2} D^K_{j_p\rho}(\mathbf{r}_2,\mathbf{r}') \\
&+\frac{1}{\omega^2}\int_{\mathbf{r}_1,\mathbf{r}_2} D^K_{j_ij_n}(\mathbf{r},\mathbf{r}_1)\overrightarrow{\nabla}^n_{\mathbf{r}_1} V^A_{RPA}(\mathbf{r}_1,\mathbf{r}_2)\overleftarrow{\nabla}^p_{\mathbf{r}_2} D^A_{j_p\rho}(\mathbf{r}_2,\mathbf{r}') \\
&+\frac{1}{\omega^4}\int\limits_{\mathbf{r}_1,\mathbf{r}_2,\mathbf{r}_3,\mathbf{r}_4} D^R_{j_ij_n}(\mathbf{r},\mathbf{r}_1)\overrightarrow{\nabla}^n_{\mathbf{r}_1} V^R_{RPA}(\mathbf{r}_1,\mathbf{r}_2)\overleftarrow{\nabla}^p_{\mathbf{r}_2} D^K_{j_pj_q}(\mathbf{r}_2,\mathbf{r}_3)\overrightarrow{\nabla}^q_{\mathbf{r}_3} V^A_{RPA}(\mathbf{r}_3,\mathbf{r}_4)\overleftarrow{\nabla}^s_{\mathbf{r}_4} D^A_{j_s\rho}(\mathbf{r}_4,\mathbf{r}').
\end{aligned} \tag{C.34}$$

The remaining current-density GFs are written in terms of current-current GFs via the relations (C.25), which when combined with the gradient of the bare interaction in the expression for the heat current leads to the contribution

$$\begin{aligned}
&\int d\mathbf{r}'\tilde{D}^K_{j_i\rho}(\mathbf{r},\mathbf{r}',\omega)V_0(\mathbf{r}'-\mathbf{r})\overleftarrow{\nabla}^i_{\mathbf{r}} \\
&= -\frac{1}{i\omega}\int d\mathbf{r}'\Big[D^K_{j_ij_l}(\mathbf{r},\mathbf{r}')\overleftarrow{\nabla}^l_{\mathbf{r}'} \\
&+\frac{1}{\omega^4}\int\limits_{\mathbf{r}_1,\mathbf{r}_2,\mathbf{r}_3,\mathbf{r}_4} D^R_{j_ij_n}(\mathbf{r},\mathbf{r}_1)\overrightarrow{\nabla}^n_{\mathbf{r}_1} V^R_{RPA}(\mathbf{r}_1,\mathbf{r}_2)\overleftarrow{\nabla}^p_{\mathbf{r}_2} D^K_{j_pj_q}(\mathbf{r}_2,\mathbf{r}_3)\overrightarrow{\nabla}^q_{\mathbf{r}_3} V^A_{RPA}(\mathbf{r}_3,\mathbf{r}_4)\overleftarrow{\nabla}^s_{\mathbf{r}_4} D^A_{j_sj_l}(\mathbf{r}_4,\mathbf{r}')\overleftarrow{\nabla}^l_{\mathbf{r}'} \\
&+\frac{1}{\omega^2}\int_{\mathbf{r}_1,\mathbf{r}_2} D^R_{j_ij_n}(\mathbf{r},\mathbf{r}_1)\overrightarrow{\nabla}^n_{\mathbf{r}_1} V^R_{RPA}(\mathbf{r}_1,\mathbf{r}_2)\overleftarrow{\nabla}^p_{\mathbf{r}_2} D^K_{j_pj_l}(\mathbf{r}_2,\mathbf{r}')\overleftarrow{\nabla}^l_{\mathbf{r}'} \\
&+\frac{1}{\omega^2}\int_{\mathbf{r}_1,\mathbf{r}_2} D^K_{j_ij_n}(\mathbf{r},\mathbf{r}_1)\overrightarrow{\nabla}^n_{\mathbf{r}_1} V^A_{RPA}(\mathbf{r}_1,\mathbf{r}_2)\overleftarrow{\nabla}^p_{\mathbf{r}_2} D^A_{j_pj_l}(\mathbf{r}_2,\mathbf{r}')\overleftarrow{\nabla}^l_{\mathbf{r}'}\Big] V_0(\mathbf{r}'-\mathbf{r})\overleftarrow{\nabla}^i_{\mathbf{r}},
\end{aligned} \tag{C.35}$$

where the direction of the additional gradient terms on the right hand side of all the terms in square brackets may be flipped by integration by parts, and upon factorising the final bare Coulomb interaction may be incorporated into the expression, leading ultimately to

$$\int d\mathbf{r}'\tilde{D}^K_{j_i\rho}(\mathbf{r},\mathbf{r}',\omega)V_0(\mathbf{r}'-\mathbf{r})\overleftarrow{\nabla}^i_{\mathbf{r}} = \left(\mathbb{1}+\frac{1}{\omega^2}D^R V^R_{\nabla}\right)\frac{1}{i\omega}D^K V^A_{\nabla}, \tag{C.36}$$

where the leftmost and rightmost spatial index are both $\mathbf{r}$ with Cartesian index i, while all intermediate spatial variables are integrated over. $\mathbb{1}$ is the identity operator – i.e. Dirac delta function in the spatial variables and Kronecker delta in Cartesian indices: $\mathbb{1} = \delta(\mathbf{r}-\mathbf{r}')\delta_{ik}$. The interaction terms V_{∇} are RPA screened Coulomb sandwiched by gradients on either side as seen everywhere in the above equations. The other term in the equation for the average heat current Eq. (C.29) is found in exactly the same way, leading to the general result

$$\langle \hat{J}(\mathbf{r},t)\rangle = -\frac{1}{4}\int_{-\infty}^{\infty}\frac{d\omega}{2\pi}\left[\left(\mathbb{1}+\frac{1}{\omega^2}D^R V_\nabla^R\right)\frac{1}{\omega}D^K V_\nabla^A + \frac{1}{\omega}V_\nabla^R D^K\left(\mathbb{1}+\frac{1}{\omega^2}V_\nabla^A D^A\right)\right], \tag{C.37}$$

Eq. (C.37) is general since we have not yet specified the geometry of the bodies. We just have to remember that the leftmost and rightmost spatial coordinates are both $\mathbf{r}$ which necessarily resides in body 1.

Specifying to the geometry of parallel layers amounts to specifying that the noninteracting GFs appearing in Eq (C.37) are only non-zero if their z-coordinates are either both 0 or both d. This may be taken care of by introducing a 2×2 matrix structure encoding the z-coordinate. Encoding the z-coordinate like this leads to the expression (the terms in $\mathbb{1}$ cancel due to parity for $\omega \to -\omega$)

$$\begin{aligned}\langle \hat{J}(\mathbf{r},t)\rangle = &-\frac{1}{4}\int_{-\infty}^{\infty}\frac{d\omega}{2\pi}\frac{1}{\omega^3}\int d^2\mathbf{r}_1 d^2\mathbf{r}_2 d^2\mathbf{r}_3\\ &\times\Big[D_1^R(\mathbf{r}-\mathbf{r}_1)V_{\nabla,1a}^R(\mathbf{r}_1-\mathbf{r}_2)D_a^K(\mathbf{r}_2-\mathbf{r}_3)V_{\nabla,a1}^A(\mathbf{r}_3-\mathbf{r})\\ &+V_{\nabla,2a}^R(\mathbf{r}-\mathbf{r}_1)D_a^K(\mathbf{r}_1-\mathbf{r}_2)V_{\nabla,a2}^A(\mathbf{r}_2-\mathbf{r}_3)D_2^A(\mathbf{r}_3-\mathbf{r})\Big],\end{aligned} \tag{C.38}$$

where $a = 1,2$ is summed over, and the spatial variables are now understood to be two-dimensional. All functions depend only on in-plane coordinate difference due to the in-plane translational invariance. Going to Fourier space in the in-plane spatial arguments allows us to return to density-density GFs and screened Coulomb interactions (without gradients). In doing so, we find that the 'chosen' position $\mathbf{r}$ drops out, as expected for the average (as did, indeed, the time t). Using the symmetry relations of bosonic GFs Eqs. (C.17), and the equilibrium relation for the Keldysh component Eq. (C.19), we find

$$\langle \hat{J}\rangle = \int\limits_{-\infty}^{\infty}\frac{d\omega}{2\pi}\int\frac{d^2\mathbf{k}}{(2\pi)^2}\hbar\omega\,\mathrm{Im}\,\Pi_1(\mathbf{k},\omega)\,\mathrm{Im}\,\Pi_a(\mathbf{k},\omega)\left|V_{1a}^R(\mathbf{k},\omega)\right|^2\left[\coth\frac{\hbar\omega}{2T_a}-\coth\frac{\hbar\omega}{2T_1}\right], \tag{C.39}$$

where $D_{\rho\rho}^R(\mathbf{k},\omega) = \Pi(\mathbf{k},\omega)$ and $D_{\rho\rho}^A(\mathbf{k},\omega) = \Pi^*(\mathbf{k},\omega)$. We notice that the contribution associated with heat transferred from within body 1, i.e. when $a = 1$, gives zero due to the difference of hyperbolic cotangents. The remaining contribution is the well-known Caroli formula (3.1) where V_{12}^R is the retarded component of the RPA screened inter-layer interaction term (3.3). In Ch. 3 we carefully evaluate the Caroli formula for the average heat current between identical metals using a particular model for the material density response, Π.

C.4 Fluctuations of the heat current

For the fluctuations, we seek the correlator

$$S(\mathbf{r},\mathbf{r}',t-t') = \frac{1}{2}\left\langle\left\{\hat{J}(\mathbf{r},t),\hat{J}(\mathbf{r}',t')\right\}\right\rangle - \langle\hat{J}(\mathbf{r},t)\rangle^2, \tag{C.40}$$

where in Eq. (C.27) we have already seen that the anticommutator may be found via functional differentiation of the generating functional. For each term in Eq. (C.27) we make use of the general relation valid when $\ln \mathcal{Z}$ is a quadratic functional

$$
\begin{aligned}
&\langle j_i^{\alpha}(\mathbf{r},t)\rho^{\beta}(\mathbf{r}_1,t) j_k^{\gamma}(\mathbf{r}',t')\rho^{\delta}(\mathbf{r}_2,t')\rangle \\
&= \frac{1}{16}\left.\frac{\delta^4 \mathcal{Z}[V,\mathbf{A}]}{\delta V^{\delta'}(\mathbf{r}_2,t')\delta A_k^{\gamma'}(\mathbf{r}',t')\delta V^{\beta'}(\mathbf{r}_1,t)\delta A_i^{\alpha'}(\mathbf{r},t)}\right|_{V=\mathbf{A}=0} \\
&= \frac{1}{16}\left[\frac{\delta^2 \ln \mathcal{Z}}{\delta A_k^{\gamma'}\delta A_i^{\alpha'}}\frac{\delta^2 \ln \mathcal{Z}}{\delta V_2^{\delta'}\delta V_1^{\beta'}} + \frac{\delta^2 \ln \mathcal{Z}}{\delta V_2^{\delta'}\delta A_i^{\alpha'}}\frac{\delta^2 \ln \mathcal{Z}}{\delta A_k^{\gamma'}\delta V_1^{\beta'}} + \frac{\delta^2 \ln \mathcal{Z}}{\delta V_1^{\beta'}\delta A_i^{\alpha'}}\frac{\delta^2 \ln \mathcal{Z}}{\delta V_2^{\delta'}\delta A_k^{\gamma'}}\right],
\end{aligned}
\tag{C.41}
$$

where the final term is the average heat current squared, so is subtracted when investigating the fluctuations, Eq. (C.40). Computing all the c,q combinations appearing in the expression for the correlator (C.27) leads to the expression

$$
\begin{aligned}
S(\mathbf{r},\mathbf{r}',t-t') = -\frac{1}{4}\int_{-\infty}^{\infty}\frac{d\omega}{2\pi}\int_{-\infty}^{\infty}\frac{d\omega'}{2\pi}e^{-i(\omega+\omega')(t-t')}\int d\mathbf{r_1}\int d\mathbf{r_2}\nabla_{\mathbf{r}}^{i}V_0(\mathbf{r}-\mathbf{r}_1)\nabla_{\mathbf{r}'}^{k}V_0(\mathbf{r}'-\mathbf{r}_2) \\
\times\Big[\tilde{D}^{K}_{j_ij_k}(\mathbf{r},\mathbf{r}',\omega)\tilde{D}^{K}_{\rho\rho}(\mathbf{r}_1,\mathbf{r}_2,\omega') + \tilde{D}^{R-A}_{j_ij_k}(\mathbf{r},\mathbf{r}',\omega)\tilde{D}^{R-A}_{\rho\rho}(\mathbf{r}_1,\mathbf{r}_2,\omega') \\
+\tilde{D}^{K}_{\rho j_k}(\mathbf{r}_1,\mathbf{r}',\omega)\tilde{D}^{K}_{j_i\rho}(\mathbf{r},\mathbf{r}_2,\omega') + \tilde{D}^{R-A}_{\rho j_k}(\mathbf{r}_1,\mathbf{r}',\omega)\tilde{D}^{R-A}_{j_i\rho}(\mathbf{r},\mathbf{r}_2,\omega')\Big],
\end{aligned}
\tag{C.42}
$$

where $D^{R-A} = D^R - D^A$. We first tackle the first term of the first line, which via Eqs. (C.22) and (C.23) may be written as

$$
-\underbrace{\tilde{D}^{K}_{j_ij_k}(\mathbf{r},\mathbf{r}',\omega)}_{\mathbf{r},\mathbf{r}',\omega}\underbrace{\overrightarrow{\nabla}_{\mathbf{r}}^{i}\left[\int_{\mathbf{r_1},\mathbf{r_2}}V_0(\mathbf{r}-\mathbf{r}_1)\tilde{D}^{K}_{\rho\rho}(\mathbf{r}_1,\mathbf{r}_2,\omega')V_0(\mathbf{r}_2-\mathbf{r}')\right]\overleftarrow{\nabla}_{\mathbf{r}'}^{k}}_{\mathbf{r},\mathbf{r}',\omega'}
\tag{C.43}
$$

$$
= -\tilde{D}^{K}_{j_ij_k}(\mathbf{r},\mathbf{r}',\omega)\frac{1}{\omega'^2}\int_{\mathbf{r_1},\mathbf{r_2}}\overrightarrow{\nabla}_{\mathbf{r}}^{i}V^{R}_{RPA}(\mathbf{r},\mathbf{r}_1,\omega')\overleftarrow{\nabla}_{\mathbf{r}_1}^{l}D^{K}_{j_lj_m}(\mathbf{r}_1,\mathbf{r}_2,\omega')\overrightarrow{\nabla}_{\mathbf{r}_2}^{m}V^{A}_{RPA}(\mathbf{r}_2,\mathbf{r}',\omega')\overleftarrow{\nabla}_{\mathbf{r}'}^{k}
\tag{C.44}
$$

The remaining screened current-current GF to be computed in this first term is found via its own Dyson equation

$$
\begin{aligned}
\tilde{D}_{j_ij_k} &= D_{j_ij_k} + D_{j_i\rho}V_{RPA}D_{\rho j_k} &&\text{(C.45)}\\
&= D_{j_ij_k} + D_{j_i\rho}V_0\sigma_1 D_{\rho j_k} + D_{j_i\rho}V_0\sigma_1 D_{\rho\rho}V_{RPA}D_{\rho j_k} &&\text{(C.46)}\\
&= D_{j_ij_k} + D_{j_i\rho}V_0\sigma_1 D_{\rho j_k} + D_{j_i\rho}V_0\sigma_1 \tilde{D}_{\rho\rho}V_0\sigma_1 D_{\rho j_k}. &&\text{(C.47)}
\end{aligned}
$$

Performing the matrix multiplication, taking the Keldysh component leads to (suppressing everywhere the dependence on ω):

$$\begin{aligned}
&\tilde{D}^K_{j_i j_k}(\mathbf{r},\mathbf{r}',\omega) = D^K_{j_i j_k}(\mathbf{r},\mathbf{r}') \\
&+ \int_{\mathbf{r}_1,\mathbf{r}_2} D^R_{j_i\rho}(\mathbf{r},\mathbf{r}_1)V_0(\mathbf{r}_1-\mathbf{r}_2)\left[D^K_{\rho j_k}(\mathbf{r}_2,\mathbf{r}') + \int_{\mathbf{r}_3,\mathbf{r}_4} \tilde{D}^R_{\rho\rho}(\mathbf{r}_2,\mathbf{r}_3)V_0(\mathbf{r}_3-\mathbf{r}_4)D^K_{\rho j_k}(\mathbf{r}_4,\mathbf{r}')\right] \\
&+ \int_{\mathbf{r}_1,\mathbf{r}_2} D^K_{j_i\rho}(\mathbf{r},\mathbf{r}_1)V_0(\mathbf{r}_1-\mathbf{r}_2)\left[D^A_{\rho j_k}(\mathbf{r}_2,\mathbf{r}') + \int_{\mathbf{r}_3,\mathbf{r}_4} \tilde{D}^A_{\rho\rho}(\mathbf{r}_2,\mathbf{r}_3)V_0(\mathbf{r}_3-\mathbf{r}_4)D^A_{\rho j_k}(\mathbf{r}_4,\mathbf{r}')\right] \\
&+ \int\limits_{\mathbf{r}_1,\mathbf{r}_2,\mathbf{r}_3,\mathbf{r}_4} D^R_{j_i\rho}(\mathbf{r},\mathbf{r}_1)V_0(\mathbf{r}_1-\mathbf{r}_2)\tilde{D}^K_{\rho\rho}(\mathbf{r}_2,\mathbf{r}_3)V_0(\mathbf{r}_3-\mathbf{r}_4)D^A_{\rho j_k}(\mathbf{r}_4,\mathbf{r}'),
\end{aligned} \tag{C.48}$$

where in the second and third lines we may recognise the retarded and advanced component of the screened interaction potential, respectively, and in the final line we may replace the screened density-density sandwiched by bare interactions by the bare density-density sandwiched by screened interactions, as above in the first factor. Doing so and writing everything in terms of bare current-current GFs leads to

$$\begin{aligned}
&\tilde{D}^K_{j_i j_k}(\mathbf{r},\mathbf{r}',\omega) = D^K_{j_i j_k}(\mathbf{r},\mathbf{r}') \\
&+ \frac{1}{\omega^2}\int_{\mathbf{r}_1,\mathbf{r}_2} D^R_{j_i j_n}(\mathbf{r},\mathbf{r}_1)\overrightarrow{\nabla}^n_{\mathbf{r}_1} V^R_{RPA}(\mathbf{r}_1,\mathbf{r}_2)\overleftarrow{\nabla}^p_{\mathbf{r}_2} D^K_{j_p j_k}(\mathbf{r}_2,\mathbf{r}') \\
&+ \frac{1}{\omega^2}\int_{\mathbf{r}_1,\mathbf{r}_2} D^K_{j_i j_n}(\mathbf{r},\mathbf{r}_1)\overrightarrow{\nabla}^n_{\mathbf{r}_1} V^A_{RPA}(\mathbf{r}_1,\mathbf{r}_2)\overleftarrow{\nabla}^p_{\mathbf{r}_2} D^A_{j_p j_k}(\mathbf{r}_2,\mathbf{r}') \\
&+ \frac{1}{\omega^4}\int\limits_{\mathbf{r}_1,\mathbf{r}_2,\mathbf{r}_3,\mathbf{r}_4} D^R_{j_i j_n}(\mathbf{r},\mathbf{r}_1)\overrightarrow{\nabla}^n_{\mathbf{r}_1} V^R_{RPA}(\mathbf{r}_1,\mathbf{r}_2)\overleftarrow{\nabla}^p_{\mathbf{r}_2} D^K_{j_p j_q}(\mathbf{r}_2,\mathbf{r}_3)\overrightarrow{\nabla}^q_{\mathbf{r}_3} V^A_{RPA}(\mathbf{r}_3,\mathbf{r}_4)\overleftarrow{\nabla}^s_{\mathbf{r}_4} D^A_{j_s j_k}(\mathbf{r}_4,\mathbf{r}').
\end{aligned} \tag{C.49}$$

Multiplying by the other Keldysh component as given above leads to the result for the first term of the first line of Eq. (4.24) (factorising where integration over intermediate variables is implied)

$$\underbrace{\left(1+\frac{1}{\omega^2}D^R V^R_\nabla\right) D^K \left(1+\frac{1}{\omega^2}V^A_\nabla D^A\right)}_{\mathbf{r},\mathbf{r}',\omega} \underbrace{\frac{1}{\omega'^2}V^R_\nabla D^K V^A_\nabla}_{\mathbf{r},\mathbf{r}',\omega'}, \tag{C.50}$$

where all GFs are bare current-current and the interaction terms V_∇ are RPA screened Coulomb sandwiched by gradients on either side [see Eq. (C.49)], which may be seen as dipole-dipole interactions. Note that the cartesian indices i and k always appear on the left and right hand sides, respectively, i.e. with the spatial indices $\mathbf{r}$ and $\mathbf{r}'$. Note also that the terms in brackets may be expressed entirely in terms of interactions (inverse bare and screened interaction) so the result will depend explicitly only on the imaginary part of the response function, as expected since we are computing (the square of) the dissipation.

The second term in the first line of Eq. (4.24) corresponds to sending $\tilde{D}^K \to \tilde{D}^R - \tilde{D}^A$ in the first term. We follow the same procedure and replace $V_0(\tilde{D}^R_{\rho\rho} - \tilde{D}^A_{\rho\rho})V_0 = V^R_{RPA}(D^R_{\rho\rho} - D^A_{\rho\rho})V^A_{RPA}$, while for the remaining term we find that from Eq. (C.48) we have the correspondence:

$$\tilde{D}^K_{j_i j_k} \underset{D^K \to D^R - D^A}{\longrightarrow} \tilde{D}^R_{j_i j_k} - \tilde{D}^A_{j_i j_k}, \tag{C.51}$$

and so the term gives an equivalent contribution but with the corresponding replacement, i. e. instead of Eq. (C.50) we have:

$$\underbrace{\left(1 + \frac{1}{\omega^2} D^R V^R_\nabla\right) (D^R - D^A) \left(1 + \frac{1}{\omega^2} V^A_\nabla D^A\right)}_{\mathbf{r},\mathbf{r}',\omega} \underbrace{\frac{1}{\omega'^2} V^R_\nabla (D^R - D^A) V^A_\nabla}_{\mathbf{r},\mathbf{r}',\omega'} . \tag{C.52}$$

The second line of Eq. (4.24) is approached in a completely analogous way, eventually leading to the expression for the total correlator

$$\begin{aligned} S(\mathbf{r},\mathbf{r}',t-t') = -\frac{1}{4} \int_{-\infty}^{\infty} \frac{d\omega}{2\pi} \int_{-\infty}^{\infty} \frac{d\omega'}{2\pi} e^{i(\omega+\omega')(t-t')} \\ \times \Bigg[\underbrace{\left(\mathbb{1} + \frac{1}{\omega^2} D^R V^R_\nabla\right) D^K \left(\mathbb{1} + \frac{1}{\omega^2} V^A_\nabla D^A\right)}_{\mathbf{r},\mathbf{r}',\omega} \underbrace{\frac{1}{\omega'^2} V^R_\nabla D^K V^A_\nabla}_{\mathbf{r},\mathbf{r}',\omega'} \\ + \underbrace{\frac{1}{\omega} V^R_\nabla D^K \left(\mathbb{1} + \frac{1}{\omega^2} V^A_\nabla D^A\right)}_{\mathbf{r},\mathbf{r}',\omega} \underbrace{\left(\mathbb{1} + \frac{1}{\omega'^2} D^R V^R_\nabla\right) \frac{1}{\omega'} D^K V^A_\nabla}_{\mathbf{r},\mathbf{r}',\omega'} \Bigg] + [D^K \to D^{R-A}]. \end{aligned} \tag{C.53}$$

Like Eq. (C.37) for the average, this equation (C.53) is general, since we have not yet specified the geometry of the system. In Sec. 4.3 we focus on parallel two-dimensional metallic layers in the parameter range where the heat current may be dominated by the antisymmetric surface plasmon contribution.

D

Derivation of the density response function from the Boltzmann kinetic equation

We assume the 2D electron gas to be in the good metallic regime, when the mean free path ℓ is much larger than the Fermi wavelength, so we may neglect localization effects. In this limit, and for perturbations smooth on the scale of the Fermi wavelength, the electron dynamics can be described by the semiclassical Boltzmann kinetic equation [Abrikosov88]. The electron distribution function $f_{\mathbf{p}}(\mathbf{r},t)$ is assumed to depend on the 2D momentum $\mathbf{p}$ and the 2D position $\mathbf{r}$, while the dynamics in the third dimension is assumed to be completely frozen by a tight confinement. Then the kinetic equation reads

$$\frac{\partial f_{\mathbf{p}}}{\partial t}+\mathbf{v}_{\mathbf{p}}\cdot\frac{\partial f_{\mathbf{p}}}{\partial \mathbf{r}}+\mathbf{F}\cdot\frac{\partial f_{\mathbf{p}}}{\partial \mathbf{p}}=\mathrm{St}[f], \tag{D.1}$$

where $\mathbf{F}$ is an externally applied force, and $\mathbf{v}_{\mathbf{p}}=\partial\varepsilon_{\mathbf{p}}/\partial\mathbf{p}$ is the electron group velocity determined by the energy dispersion $\varepsilon_{\mathbf{p}}$. The collision integral on the right-hand side, written in the Born approximation,

$$\mathrm{St}[f]=2\pi n_{\mathrm{i}}\int\frac{d^2\mathbf{p}'}{(2\pi)^2}\,|U(\mathbf{p}-\mathbf{p}')|^2\,\delta(\varepsilon_{\mathbf{p}}-\varepsilon_{\mathbf{p}'})\left(f_{\mathbf{p}'}-f_{\mathbf{p}}\right), \tag{D.2}$$

is determined by the impurity concentration n_{i} and the Fourier transform of the impurity potential $U(\mathbf{p}-\mathbf{p}')$. Beyond the Born approximation, $|U(\mathbf{p}-\mathbf{p}')|^2$ should be replaced by the exact scattering amplitude, properly normalized.

In the absence of perturbations, the electrons are assumed to have the Fermi-Dirac distribution determined by the Fermi energy ε_F and the temperature T:

$$f_{\mathbf{p}}^{\mathrm{eq}}=\frac{1}{e^{(\varepsilon_{\mathbf{p}}-\varepsilon_F)/T}+1}. \tag{D.3}$$

If a perturbing electrostatic potential $\varphi_{\mathbf{k},\omega}\,e^{i\mathbf{kr}-i\omega t}+\text{c.c.}$ is applied to the 2D system (again, we neglect its dependence on the third coordinate), it enters Eq. (D.1) via the associated electrostatic force $\mathbf{F}=-ie\mathbf{k}\varphi_{\mathbf{k},\omega}\,e^{i\mathbf{kr}-i\omega t}+\text{c.c.}$. To the linear order in the perturbation, the distribution function can be sought in the form

$$f_{\mathbf{p}}(\mathbf{r},t)=f_{\mathbf{p}}^{\mathrm{eq}}+e\varphi_{\mathbf{k},\omega}\,g_{\mathbf{p}}\,e^{i\mathbf{kr}-i\omega t}+\text{c.c.}, \tag{D.4}$$

where $g_{\mathbf{p}}$ is position- and time-independent and satisfies the following linear integral equation:

$$\begin{aligned}&-i\omega g_{\mathbf{p}}+i\mathbf{k}\mathbf{v}_{\mathbf{p}}g_{\mathbf{p}}-i\mathbf{k}\mathbf{v}_{\mathbf{p}}\,\frac{\partial f^{\mathrm{eq}}}{\partial\varepsilon_{\mathbf{p}}}\\&=2\pi n_{\mathrm{i}}\int\frac{d^2\mathbf{p}'}{(2\pi)^2}\,|U(\mathbf{p}-\mathbf{p}')|^2\,\delta(\varepsilon_{\mathbf{p}}-\varepsilon_{\mathbf{p}'})\left(g_{\mathbf{p}'}-g_{\mathbf{p}}\right).\end{aligned} \tag{D.5}$$

An explicit solution of this equation can be found only in the case of short-range impurities when $U(\mathbf{p}-\mathbf{p}')$ does not depend on momentum. In this case the collision integral reduces to the relaxation time approximation:

$$\mathrm{St}[f]=\frac{\overline{f_{\mathbf{p}}}-f_{\mathbf{p}}}{\tau}, \tag{D.6}$$

where the overbar denotes the average over the momentum directions on a constant energy surface,

$$\overline{f_{\mathbf{p}}} \equiv \frac{\int d^2\mathbf{p}'\, f_{\mathbf{p}'}\, \delta(\varepsilon_{\mathbf{p}'} - \varepsilon_{\mathbf{p}})}{\int d^2\mathbf{p}'\, \delta(\varepsilon_{\mathbf{p}'} - \varepsilon_{\mathbf{p}})}, \tag{D.7}$$

and the relaxation time and the density of states per unit area are given by (the factor of 2 in front of the integral takes into account two spin projections)

$$\frac{1}{\tau} = \pi \nu n_{\mathrm{i}} |U|^2, \quad \nu = 2\int \frac{d^2\mathbf{p}'}{(2\pi)^2}\, \delta(\varepsilon_{\mathbf{p}} - \varepsilon_{\mathbf{p}'}). \tag{D.8}$$

Then, Eq. (D.5) gives

$$g_{\mathbf{p}} = \frac{i\mathbf{k}\mathbf{v}_{\mathbf{p}}(\partial f^{\mathrm{eq}}/\partial \varepsilon_{\mathbf{p}}) + (1/\tau)\,\overline{g_{\mathbf{p}}}}{i\mathbf{k}\mathbf{v}_{\mathbf{p}} - i\omega + 1/\tau}. \tag{D.9}$$

Averaging both sides over the momentum directions, one obtains a closed equation for $\overline{g_{\mathbf{p}}}$ and readily finds

$$\overline{g_{\mathbf{p}}} = \frac{1 + (i\omega\tau - 1)S}{1 - S}\frac{\partial f^{\mathrm{eq}}}{\partial \varepsilon_{\mathbf{p}}}, \tag{D.10}$$

where S stands for the following angular average:

$$\begin{aligned} S &\equiv \overline{(1 - i\omega\tau + i\mathbf{k}\mathbf{v}_{\mathbf{p}}\tau)^{-1}} \\ &= \int_0^{2\pi} \frac{d\phi}{2\pi} \frac{1}{1 - i\omega\tau + i v_F k \cos\phi} \\ &= \frac{1}{\sqrt{(1 - i\omega\tau)^2 + (v_F k \tau)^2}}. \end{aligned} \tag{D.11}$$

The last two lines were written under the assumption of an isotropic dispersion $\varepsilon_{\mathbf{p}}$. Finally, since the electron density is given by

$$\rho(\mathbf{r},t) = 2\int \frac{d^2\mathbf{p}}{(2\pi)^2} f_{\mathbf{p}}(\mathbf{r},t) \tag{D.12}$$

(again, the factor of 2 takes care of the spin multiplicity), the density response function can be found as

$$\Pi(\mathbf{k},\omega) = 2\int \frac{d^2\mathbf{p}}{(2\pi)^2} g_{\mathbf{p}}. \tag{D.13}$$

Collecting all factors and assuming that $-\partial f^{\mathrm{eq}}/\partial \varepsilon_{\mathbf{p}}$ is a narrow peak around the Fermi energy of width $\sim T$, so that the energy dependence of ν and v_F can be neglected, we arrive at Eq. (3.4).

If $U(\mathbf{p} - \mathbf{p}')$ is momentum dependent, no closed solution can be obtained even in the simplest of isotropic scattering when the scattering amplitude depends only on the difference $\phi - \phi'$ of the polar angles ϕ, ϕ' associated to the 2D vectors $\mathbf{p}, \mathbf{p}'$. Indeed, in this case the solution can be sought as a sum over polar harmonics, $g_{\mathbf{p}} = \sum_m g_m e^{im\phi}$, which are the eigenfunctions of the collision integral. Different harmonics do not separate because of the second term in Eq. (D.5), which is responsible for the spatial dispersion of the conductivity $\sigma(\mathbf{k},\omega)$. Only when the spatial dispersion is neglected, the Drude conductivity $\sigma(\omega)$ can be written in terms of the transport relaxation time τ_1, determined by the first eigenvalue of the collision integral, $-1/\tau_1$. Otherwise, the result contains all eigenvalues $-1/\tau_{m>0}$. Still, qualitatively, it is τ_1 that determines the relevant time scale: in the limit of Eq. (D.6) all $\tau_{m>0} = \tau$, while in the opposite limit of small-angle scattering τ_m quickly grows with m, so high harmonics are suppressed and the result is determined by the first few τ_m's.

Théorie du transfert de chaleur dans des nanostructures : approches microscopique et phénoménologique

Theory of heat transfer in nanostructures: microscopic and phenomenological approaches

Résumé

Des objets séparés spatialement peuvent échanger de la chaleur par rayonnement. L'origine de ce mécanisme est le mouvement thermique aléatoire de charges à l'intérieur d'un corps qui induit des champs électromagnétiques qui se comportent et interagissent avec d'autres corps selon les équations de Maxwell et la réponse électromagnétique des matériaux. On sait depuis plus de 50 ans que la nature du transfert de chaleur par rayonnement est très différente pour les corps éloignés les uns des autres et pour les corps proches les uns des autres. En particulier, pour les corps proches, dans ce qu'on appelle le champ proche, le caractère ondulatoire des champs électromagnétiques est important et les ondes évanescentes peuvent renforcer le transfert de chaleur. Il y a un regain d'intérêt pour les études du champ proche en raison de la pertinence experimental relativement nouvelle des petites distances associées, ainsi que des réalisations de nouveaux matériaux et structures de taille et/ou de dimension réduite. Dans cette thèse, nous fournissons des contributions théoriques pour améliorer notre compréhension du transfert de chaleur radiatif en champ proche.

Dans ce travail, nous élucidons les rôles joués dans le transfert de chaleur radiatif par des ingrédients physiques clés qui sont communs à de nombreux systèmes. Tout d'abord, nous étudions la chaleur moyenne échangée par des couches métalliques bidimensionnelles parallèles modélisées par la conductivité de Drude. Nous effectuons un calcul analytique dans le cadre de l'électrodynamique fluctuationnelle où les contributions additives au transfert de chaleur par des ondes de type différent se séparent naturellement. Cette étude nous permet d'évaluer l'importance de retardation dans l'interaction électromagnétique en fonction de la température, de la séparation et de la conductivité des matériaux. En nous concentrant sur la limite de Coulomb valable pour les mauvais métaux à de petites séparations, nous utilisons un modèle plus riche pour la réponse du matériau afin d'étudier les rôles et les interactions du désordre, de la dispersion spatiale et des excitations collectives de densité de charge appelées plasmons de surface. A partir de nos expressions analytiques, nous montrons que dans une fenêtre paramétrique d'échelles de séparation et de température, le courant thermique radiatif est effectivement dominé par les plasmons de surface.

Nous poursuivons en étudiant les fluctuations, ou le bruit, du courant thermique radiatif autour de sa valeur moyenne. Nous abordons cette quantité beaucoup moins bien comprise car elle est censée contenir plus d'informations physiques sur les systèmes échangeant de la chaleur. En particulier, nous nous intéressons aux systèmes où la contribution dominante au transfert de chaleur provient d'excitations collectives ou résonantes, où le bruit du courant thermique peut fournir une sonde expérimentale de ces excitations. Nous étudions analytiquement deux de ces systèmes : un système effectif de dimension zéro où le courant thermique est médié par un résonateur supraconducteur, et le système familier de couches métalliques bidimensionnelles dont le transfert thermique peut être dominé par des plasmons de surface. Dans les deux cas, le spectre de bruit à fréquence finie révèle une signature du canal de transfert résonant, qui pourrait potentiellement être mesurable et donc fournir une sonde des excitations pertinentes.

Mots-clés : transfert de chaleur, interaction électron-électron, champ proche

Abstract

Spatially separated objects may exchange heat via radiation. The origin of this mechanism is the random thermal motion of charges inside a body that induce electromagnetic fields that behave and interact with other bodies according to Maxwell's equations and the materials' electromagnetic response. It has been understood for over 50 years that the nature of the radiative heat transfer is very different for bodies that are far apart than for bodies that are close together. In particular, for bodies that are close together, in the so-called near field, the wave-like character of the electromagnetic fields is significant and evanescent waves may enhance the heat transfer compared to the far field. There is a renewed interest in studies of the near field due to the relatively newfound experimental relevance of the associated small distances, as well as realisations of novel materials and structures with reduced size and/or dimension. In this thesis we provide theoretical contributions to further our understanding of near field radiative heat transfer.

In this work we elucidate the roles played in the radiative heat transfer by key physical ingredients that are common to many systems. First, we study the average heat exchanged by parallel two-dimensional metallic layers modelled by Drude conductivity. We perform an analytical calculation in the framework of fluctuational electrodynamics where the additive contributions to the heat transfer by waves of different type separate naturally. This study allows us to evaluate the importance of retardation in the electromagnetic interaction according to the temperature, separation, and the material dc conductivity. Focusing on the Coulomb limit valid for poor metals at small separations, we use a richer model for the material response to investigate the roles and interplay of disorder, spatial dispersion, and collective charge density excitations called surface plasmons. From our analytical expressions we show that in a parametric window of separation and temperature scales the radiative heat current is indeed dominated by surface plasmons.

We go on to study the fluctuations, or noise, of the radiative heat current about its average value. We approach this much less well-understood quantity because it is expected to contain more physical information about the systems exchanging heat. In particular, we are interested in systems where the dominant contribution to the heat transfer comes collective or resonant excitations, where the heat current noise may provide an experimental probe of these excitations. We study analytically two such systems: an effective zero-dimensional system where the heat current is mediated by a superconducting resonator, and the system of two-dimensional metallic layers whose heat transfer may be dominated by surface plasmons. In both cases the finite-frequency noise spectrum reveals a signature of the resonant transfer channel, that could potentially be measurable and hence provide a probe of the relevant excitations.

Keywords : Heat transport, electron-electron interaction, near field